# The Determination of the Bidomain Conductivity Tensors of Heart Tissue

Leon Simon Graham BSc. (Hons.)

Submitted in fulfilment of the requirements

for the Degree of

Doctor of Philosophy

University of Tasmania

November, 2008

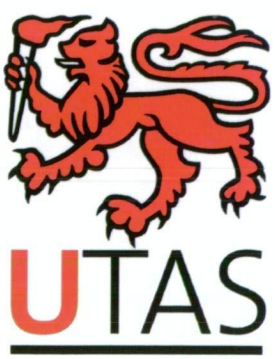

# Declaration

I declare that this thesis contains no material which has been accepted for a degree or diploma by the University or any other institution, except by way of background information and duly acknowledged in the thesis, and that, to the best of my knowledge and belief, this thesis contains no material previously published or written by another person, except where due acknowledgement is made in the text of the thesis.

Signed: Leon Graham

Date: 24/11/08

This thesis may be made available for loan and limited copying in accordance with the *Copyright Act 1968*

Signed: Leon Graham

Date: 24/11/08

# Abstract

The bidomain model is often used to simulate the electrical activity in cardiac tissue. It has applications in the inverse problem of electrocardiology, which is inferring the electric potential in the heart from non-invasive body surface potentials. Currently, the 12-lead electrocardiogram (ECG) is being used on a daily basis, though the ECG is not being used to its full potential, as the 12-lead resolution is limited. The inverse problem of electrocardiology would provide greater information; it would benefit in making predictions and clinical diagnosis, such as interpreting the relationship between ST segment changes in the electrocardiogram and ischaemia.

The electrical activity in cardiac tissue is strongly influenced by the myocardial fibre arrangement. There is strong experimental evidence which shows that current propagates much faster along the tissue fibres than across them; this directional dependence in its conduction is termed as anisotropic. When modelling this electrical activity, the bidomain conductivity tensors represent this anisotropy. These conductivities are defined for intracellular and extracellular domains, in each of the principal directions; for along, across, and perpendicular to the tissue fibres. Hence, in three-dimensions there are six conductivity parameters that describe how the electric current flows.

Several measurements of the bidomain conductivities have been obtained, but they have been inconsistent with each other, leading to a degree of uncertainty regarding the correct values. It has been shown that the different measured conductivity values produce different bidomain simulation results, which can significantly effect the outcome of the inverse problem, and so it is important to determine the correct conductivity set. One of the major difficulties in measuring the bidomain conductivity values is separating the intracellular and extracellular conductivities.

In this thesis, a method for determining the bidomain conductivity tensors is

described. It takes a different approach to the conventional four-electrode technique, as it does not require the small electrode separation needed to separate the extracellular current from the intracellular.
The method involved recording the propagation of electrical activation, initiated by point simulation, via extracellular electrodes, and time-dependent bidomain modelling to simulate the electrical phenomena. The optimum set of conductivity values were achieved by minimising the difference between the bidomain model output and measured extracellular potential, by means of inverse techniques in parameter estimation, such as Least-Squares (LS) or Singular Value Decomposition (SVD).

Overall, the LS method with the use of the Marquardt parameter, which determines how large a step the parameters are updated between optimisation iterations, seemed to work best, where as the SVD method tended to overshoot the optimum parameter set, when involving experimental data. Other parameters in the bidomain model could also be determined such as membrane capacitance and local myocardial fibre direction.

# Acknowledgements

I would like to express sincere appreciation to my supervisor, Prof. David Kilpatrick for his constant helpful suggestions, support, and encouragement throughout the course of this thesis.

I am most grateful to the following people for helping me:

Dr. Ah Chot Yong for his continuous help in the laboratory, proof reading this thesis, and his encouragement and assistance throughout the course of this work.

Mr. Frank Sainsbury for his constant help with computing, and assistance in running hardware and software used in the laboratory.

Dr. Qin Li for assistance and guidance in the laboratory, and help in medical knowledge.

Mr. Paul Waller for the building of equipment used in the laboratory, and his helpful suggestions.

Dr. John Pormann for providing numerical software for solving the bidomain equations and assistance in getting it running.

Dr. John Doherty and Matt Tonkin for providing parameter estimation software (PEST) and assistance.

Dr. Chris Johnston and the people at the Scientific Computing and Imaging Institute for providing problem solving environment software and assistance.

AProf. Peter Johnston for his helpful advice.

Mr. Leigh Gordon at the Tasmanian Partnership for Advanced Computing, for assisting in computing issues to run simulations on the supercomputer.

Capt. Digby and Mrs. Judith Longhurst for providing accommodation and support.

Geoff and Leani Read for their support.

Chona Mae Andal for her support.

My Mum and Dad.

# Publications

*The Determination of the Bidomain Conductivity Values of Heart Tissue*, L. S. Graham, D. Kilpatrick, F. Sainsbury, and A. C. Yong, Computers in Cardiology 2008, 35.

To my parents

# Contents

# Abbreviations

| | |
|---|---|
| ECG | electrocardiogram |
| ECGI | electrocardiographic imaging |
| LA | left atrium |
| LAD | left anterior Desending |
| LCX | left circumflex |
| LV | left ventricle |
| RV | right ventricle |
| RA | right atrium |
| | |
| 3D | three dimensional |
| AC | alternatining current |
| DC | direct current |
| LS | least-squares |
| FEM | finite element method |
| FDM | finite difference method |
| FVM | finite volume method |
| MRI | magnetic resonance imaging |
| CT | computer tomography |
| SVD | singular value decomposition |

# Symbols

## Bioelectric

| | |
|---|---|
| $\mathbf{J}$ | current density |
| $\sigma$ | conductivity (subscripts denote: i intracellular, e extracellular, l longitudinal, t transverse) |
| $\mathbf{E}$ | electric field |
| $\Phi$ | scalar potential |
| $\mathbf{n}$ | normal vector |
| $h(x, y, z)$ | heart surface |
| $b$ | body surface potential distribution |
| $T$ | forward transfer matrix |
| $I_m$ | transmembrane current density |
| $I_s$ | external stimulating current |
| $\mathbf{D}$ | bidomain conductivity tensor |
| $\beta$ | ratio of membrane surface area to tissue volume |
| $C_m$ | transmembrane capacitance |
| $I_{ion}$ | ionic current |
| $\mathbf{A}$ | rotation matrix |
| $\lambda$ | length constant |
| $R_m$ | membrane resistance times unit area |
| $Z_m$ | AC specific membrane impedance |
| $\theta$ | local fibre angle |
| $\theta_l$ | longitudinal conduction velocity |

| | |
|---|---|
| $\theta_t$ | transverse conduction velocity |
| $R$ | specific resistivity |
| $r$ | resistivity |
| $f_i$ | fraction of intracellular space |
| $f_e$ | fraction of extracellular space |
| $V$ | voltage |
| $\Delta$ | magnitude of transmembrane action potential |
| $a$ | radius of cell |
| $l$ | length of cell |

# Parameter Estimation

| | |
|---|---|
| **O** | objection function |
| **p** | vector containing model parameters |
| **c** | vector containing observations |
| **J** or **X** | Jacobian matrix |
| **C** | covariance matrix |
| $\sigma$ | variance |
| **m** | number of measurements/observations |
| **n** | number of parameters |
| **Q** | weighted matrix |
| **M** | model function |
| **u** | parameter upgrade vector |
| **g** | steepest decent vector |
| $\alpha$ | Marquardt parameter |
| **r** | residuals |
| $R$ or $r$ | correlation coefficient |
| **U** | $m \times m$ orthogonal matrix |
| **V** | $n \times n$ orthogonal matrix |
| **S** | $m \times n$ diagonal matrix |

# Chapter 1

# Introduction

Physicians are able to diagnose heart disorders by recognising the changes in the characteristics of the electrocardiogram, such as the ST segment changes during ischaemia. This is an empirical method of diagnosis and is used on a daily bases. One goal in cardiology is to determine the inverse problem, that is, the indirect computation of cardiac potentials from surface measurements. This would provide a deterministic approach for diagnosing and quantifying cardiac abnormalities, and thus, allow for a greater understanding and treatment of diseases. To fully utilise the inverse problem, there needs to be an understanding of the effect of disease on the hearts electrical system; and so direct potential measurements within the heart during a diseased state is of interest. In biomedical engineering there is the development of cardiac devices such as pace makers and defibrillators. To design these devices to be more effective, the resulting potentials in the heart from their application would be valuable. Though, measuring the potential within the human heart directly is usually impractical, and may be difficult with many variables involved that could significantly effect the measurements.

Another way of determining the potential is through computer simulation. Computer models are becoming more realistic, providing reliable quantities that may have otherwise been difficult to obtain physically; and revealing relationships between parameters and their effects. The bidomain model is used to determine the bioelectric potential in cardiac tissue. This model provides a tool to study

clinical and experimental investigations, in detail, for a range of different conditions. For example, bidomain computer simulation allows for investigations into pathological conditions of the heart, such as ischaemia [1, 2, 3], and arrhythmia [4]; as well as externally applied fields to the heart [5, 6, 7], such as pace makers, and defibrillators, which may then provide insight into manufacturing of these devices.

The bidomain model treats the discrete cardiac cells as two continuous domains, taking into account the intracellular and extracellular current flows. The governing equations are derived from Ohm's law and the continuity of current. There are two bidomain modelling components that influence the propagation of electric current; these are: its structural properties, and the representation of ion flow across the cell membrane [8]. The ion flow can be governed by a membrane model, to describe the shape of the action potential during depolarisation and repolarisation. With attention to the structural properties of the tissue, its fibre organisation is of importance, and greatly influences the electrical conduction. The cardiac muscle tissue is made up of a network of coronary circulation, collagen and a complex network of elongated cells that are interconnected through low-resistance channels called gap junctions; these are located at the ends of the cells at the membrane and permit the flow of ions and small molecules. The cardiac cells are arranged into fibres, and this gives rise to the anisotropy in the electrical conduction in both intracellular and interstitial space. With this arrangement, the electric current propagates faster along the tissue fibres than across them. The anisotropy is described mathematically by the set of conductivity values in the bidomain model, and they greatly influence the electrical behaviour of the tissue. There are a number of sets of conductivities available to researchers to use in their bidomain simulations; and each of these sets are different [9].

The most commonly used bidomain conductivity values have been measured experimentally by Clerc [10], and Roberts *et. al.* [11, 12]. Each of the methods employed had different mathematical modelling and experimental techniques. Clerc [10] performed in vitro experiments on tissue fibres from calf hearts, and

micro-electrodes were used to record extracellular and intracellular potentials. The conductivities were derived from a one-dimensional cable model that described the current flow. Roberts *et. al.* [11, 12] performed in vivo measurements in dogs, by recording extracellular potentials via an electrode array on the epicardium during pacing, to map the propagation of the wavefront. The conductivities were determined by their relationship with the wavefront voltage. Another bidomain conductivity measurement was performed by Le Guyader [13] *et. al.* who used the four-electrode technique. The four-electrode technique is implemented by placing two voltage recording electrodes at a known distance in the cardiac tissue, between two current injecting electrodes. The voltage between the two electrodes is measured and then the conductivity can be calculated. By adjusting the distance between the voltage electrodes, measurements can be obtained in both intracellular and extracellular space, or extracellular space in isolation [14]. Conductivities have been estimated theoretically as well, by computer models base on tissue structure at the cellular level and material constants given in the literature [15, 16, 17].

There is no general agreement as to which set of measured conductivity values is preferred. Major difficulties arise, such as knowing the tissue fibre orientation with respect to the electrode arrangement, the implementation of micro-scale electrode separation for in vivo measurements, and what measurements to make to suit the model. Another challenge is measuring the separate intracellular and extracellular conductivities. The reported sets of conductivities differ from each other for a number of reasons; factors contributing to the differences would be the different models they were derived from, the type of experiment performed, and the animal species experimented.

With the variations in the sets of conductivities there is a major dilemma; when they are used in simulations, such as, for studying ST segment shift during ischaemia, the results in simulated potentials differ significantly [18]. This makes it difficult to compare the effect of the degree of ischaemia with experimental observations. It would be beneficial if a set of conductivity values were available,

such that, the potentials produced by the bidomain model are close to physical values. Once a reliable set of conductivities have been obtained, there can be greater confidence in the results of the bidomain model, and hence, the inverse problem. Accurate bidomain conductivity values would improve cardiac stimulating devices such as pace makers and defibrillators, by testing their application through computer simulation. The bidomain model is used to study a range of cardiac diseases, and with a more reliable set of conductivities, hence more accurate simulations, there can be greater understanding between the electrical system of the heart and disease. This will lead to better diagnosis, treatment and quality of life.

An issue with the early bidomain conductivity measurements was that due to the computing power available to the researchers at the time, the conductivities were not derived from a full bidomain model, and simplifying assumptions were made. Now numerical methods are available, such as the finite element method, combined with parallel computing, to solve the partial differential equations which govern the bidomain model. There has also been development in the implementation of inverse mathematics such as in Least-Squares (LS) and Singular Value Decomposition (SVD), which have been applied to many areas of science. Parameter estimation methods were not used in the early conductivity measurements. However, there have been parameter estimation methods applied to theoretical studies involving the four-electrode technique [14, 19]. Le Guyader *et. al.* [14] estimated the conductivities by fitting the model to a range of applied voltage frequencies between 10 and 10000 $Hz$, with a modified Shor's r algorithm. Sadleir and Henriquez's [19] study estimated the conductivities and fibre angle by a Newton-Raphson method and two Tikhonov-type regularisations.

The aim of this thesis was to develop a method of measuring the bidomain conductivity values of cardiac tissue, in vivo in sheep hearts, and study how well the method can calculate the values. The bidomain conductivity parameters were determined by observing the propagation of activation in cardiac tissue from a current point stimulus. Extracellular potentials were measured via an

electrode array in sheep hearts on the epicardium. An electrode at the centre of the array was used to apply the current stimulus, which was administered by a cardiac pacemaker. To simulate the electrical phenomena, a time-dependent bidomain model was used. The optimum conductivity values were determined by parameter estimation methods (LS and SVD), by minimising the difference between experimental observations and bidomain model data output.

The method was validated by using synthetic data, which were generated from a bidomain model with known conductivity values. The method was further tested with random noise added into the synthetic data. Data reported in the literature were also used. The method was successful in determining the four conductivity values in two-dimensions; intracellular and extracellular for along and across the tissue fibres. Other parameters could also be determined, such as local fibre angle, and membrane capacitance, with the added computational cost. The method can be easily extended to three-dimensional tissue domains to determine the six conductivity values.

There were discrepancies in the initial deflections of the electrograms between the bidomain model output and experimental observations from the sheep experiments. In particular, the Q-waves of the electrograms in the experiments were more sloped than in the bidomain model, which was thought to be due to a number of factors, such as, the membrane model used, the effect of orthotropic transverse conductivity, and the reference potential. In order to achieve a closer fit between experimental observations and bidomain model data, that is, a more optimum set of conductivity values, the parameters contained in the membrane model were estimated as well.

The organisation of this thesis is composed of the literature review, methods, results, discussion, and conclusion. Chapter 2 discusses background information about the normal activation of the heart, the electrocardiogram, and the forward and inverse problem of electrocardiology. Chapter 3 defines the bidomain model and discusses the anisotropy of cardiac tissue. Chapter 4 is a review of the previous measurements of bidomain conductivity. Chapter 5 describes the

depolarisation wave which is measured and used in the parameter estimation in this study. Chapter 6 describes the parameter estimation techniques used, such as Least-Squares and SVD. Chapters 7, 8, and 9 describe the method for determining the bidomain conductivity parameters, the experimental procedures, equipment used, and data processing. Chapters 10 and 11 present the results of the parameter estimation, using synthetic data for validation, and experimental data obtained from sheep experiments. Chapter 12 is an investigation into estimating membrane model parameters to achieve a closer fit between experimental observations and model data output. Chapter 13 is a discussion on the issues that arises from the study. Chapter 14 is the concluding chapter, followed by the appendices and references.

# Chapter 2

# Electrocardiology

## 2.1 The Heart

The heart is essentially a pump, that circulates the blood around the body, via vessels, to supply oxygen and nutrients to muscles and organs in the body. The heart is a very important organ; one cannot live without it, and any problems with its function can be life threatening.

The heart contains four chambers, the left and right atrium and ventricles, with the left and right major chambers separated by the septum. Each chamber has a valve, making a total of four. The heart is enclosed in a serous-lined pericardial sac. The anatomy of the heart showing the valves, chambers and vessels is shown in Figure 2.1. All four chambers dilate and contract in a systematic order as the heart beats. The same flow of blood passes through each ventricle, even though the left ventricle wall is thicker than the right ventricular wall; their ejection volumes are the same, providing there are no leaking valves.

## 2.2 Electrical Activity of the Heart

The depolarisation and contraction of the cardiac muscle is intrinsic, it is a property of the heart itself and can function without the nervous system. A group of self-excitable cells, called pacemaker cells, are located in the right atrium, known

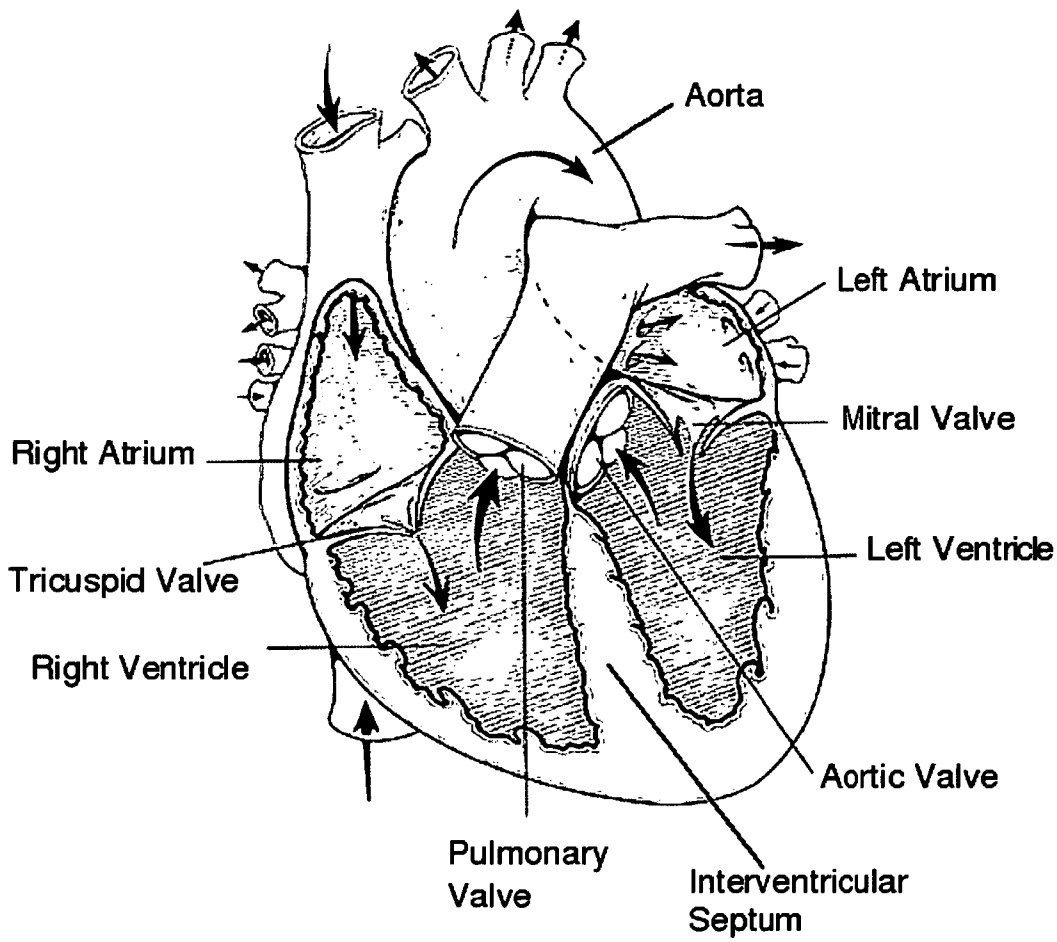


Figure 2.1: Heart diagram. Image source: reprinted with permission from the National Heart Foundation of New Zealand 2008 [20].

as the sinus node or sinoatrial node, shown in Figure 2.2. These cells generate a change in potential, or depolarise, initiating the activation, which then propagates throughout the atria. The only conducting path from the atria to the

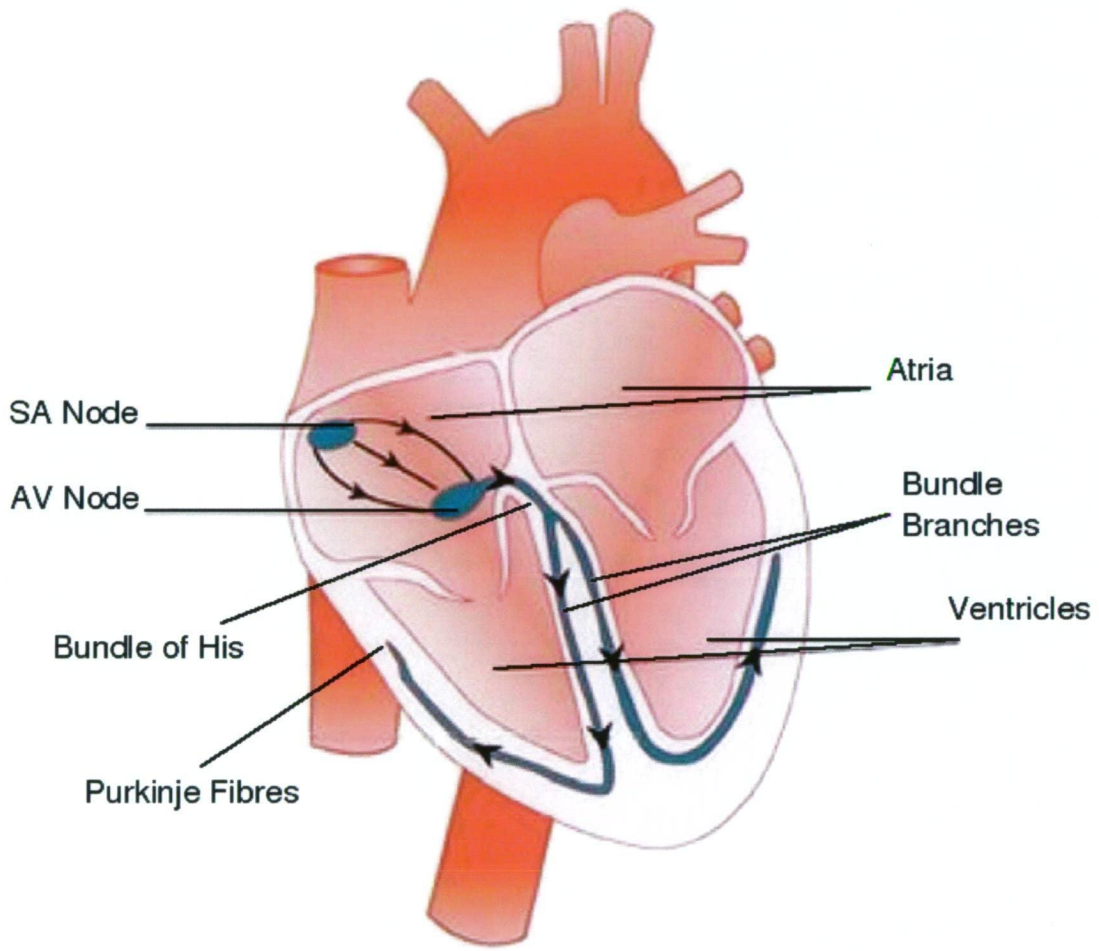


Figure 2.2: Normal conduction of the heart. Image source: reprinted with permission from the National Heart Foundation of New Zealand 2008 [21].

ventricles is via the atrioventricular node, located at the boundary between the atria and the ventricles. From then on, the excitation of the cells propagates down a conduction system, known as the bundle of His; which travels down the septum and then separates into two branches that spread out to the inner walls of the ventricles, as Purkinje fibres. Ventricular activation spreads rapidly along the endocardium, with the aid of the Purkinje fibre network, and then propagates

slower in a broad wavefront, from endocardium to epicardium [22]. This electrical activity spreads throughout the heart, followed by muscle contraction.

## 2.3 The Electrocardiogram

The electrical field generated by the heart spreads throughout the body, which can be recorded and amplified to produce a graphical representation of the field against time, known as an electrocardiogram. Recording leads are placed at different sites on the body surface to measure the potential difference between two points. It is used for clinical diagnosis, typically with 12 leads; six unipolar leads on the chest, three bipolar and three unipolar leads on the limbs [23]. A large empirical knowledge base has been acquired since its use, which matches the type of cardiac abnormality with the characteristic waveform of the electrocardiogram. In a healthy heart the morphology of the waveform tends to be consistent. Therefore, any changes in the pattern or timing of the ECG may suggest a diseased heart, since it has altered the conduction system. The theory behind these changes may not be properly understood, but they give an indication of the type of problem with the heart, and to the physician, with other factors taken into consideration for the particular case, this may be very helpful in making a diagnosis. There are a range of cardiac diseases that can be detected by the ECG, such as cardiac arrhythmia's, ischaemic heart disease, acute myocardial infarction, and pericarditis. It can be useful for helping diagnose non-cardiac diseases as well. In the field of artificial intelligence, knowledge acquisition systems for ECG diagnosis have been developed, base on the catalogue of ECG signals to the corresponding heart disorder [24].

The ECG has not been used to its full potential in diagnosing and quantifying heart conditions, due to the incomplete understanding of the relationship between body surface potentials and intracardiac events. Computer modelling is a way to gain insight into this relationship [25].

## 2.4 Equations for the Electric Field in the Body

To mathematically describe the electrical behaviour in the body, it is treated as a volume conductor. The current density, **J**, is linearly related to the electric field, **E**:

$$\mathbf{J} = \sigma \mathbf{E}, \tag{2.1}$$

where $\sigma$ is the conductivity. The electric field can be obtained from the gradient of an electric scalar potential, $\Phi$:

$$\mathbf{E} = -\nabla \Phi, \tag{2.2}$$

The electric scalar potential, $\Phi$, in an inhomogeneous isotropic thorax, is governed by Laplace's equation [26]:

$$\nabla \cdot (\sigma \nabla \Phi) = 0, \tag{2.3}$$

with no current flow through the body surface, and a specified potential distribution on the surface of the heart:

$$\nabla \Phi \cdot \mathbf{n} = 0, \quad \textit{and} \quad \Phi = h(x, y, z), \tag{2.4}$$

where **n** represents the normal vector to the surface, h(x,y,z); a given epicardial potential distribution, and $\sigma(x, y, z)$ is the conductivity for each organ. The conditions for continuous potential and current flow in an inhomogeneous thorax, between two different tissue boundaries, is stated by:

$$\Phi_1 = \Phi_2, \quad \textit{and} \quad \sigma_1 \nabla \Phi_1 \cdot \mathbf{n} = \sigma_2 \nabla \Phi_2 \cdot \mathbf{n}. \tag{2.5}$$

where the subscripts 1 and 2 refer to the different sides of the boundary.

## 2.5 Forward Problem

The forward problem is when the heart potential distribution, $h(x, y, z)$, and the conducting medium, $\sigma$, are known, but the body surface distribution $b$, is not, and must be determined. The forward problem in electrocardiology can be described mathematically as the solution to Laplace's equation, along with the appropriate boundary conditions. In general all techniques reduce to a matrix equation:

$$Th = b. \tag{2.6}$$

which relates the heart surface potential distribution, $h$, to the resulting body surface potential distribution, $b$. The matrix, $T$, is called the forward transfer matrix. This matrix is of size $m \times n$, where $m$ is the number of body surface potential measurements, and $n$ is the number of potential points on the heart surface.

The forward problem has a unique solution, and can be calculated with an accuracy based on the quality of the volume conductor modelled. Due to the complex geometry of the human body, numerical methods are applied to solve the governing equations, such as the finite element method. The forward problem does not really have any application in clinical diagnosis, since the electric field generated by the heart can be measured on the body surface [27].

The forward problem has been used to study the electric potential distribution in the human body [28, 29]. The model of the heart is placed into a volume conductor, represented by a realistic anatomical model of the human torso. This is generated by techniques of digital image processing; applied to images obtained from Cryosection, magnetic resonance imaging (MRI), and computer tomography (CT). The torso model is inhomogeneous; due to the surrounding organs, such as the lungs, bones, muscle, and fat, which form the intermediate medium between cardiac sources and the body surface. Various effects are studied, such as changes in geometry, and different tissue properties [30, 31]. Another use of the forward problem is to study the effects of ischaemia on the resulting body surface maps

[28].

## 2.6 Inverse Problem

The inverse problem is when the measured body surface potential distribution, $b$, and the properties of the conductor, $\sigma$, are known, but the potential distribution in the heart, $h$, generated by cardiac excitation and repolarisation, is unknown, and must be determined. It is known as electrocardiographic imaging (ECGI) [32]. Mathematical techniques such as regularisation and singular value decomposition have been used to invert the forward transfer matrix [26]. Solving for $h$, in terms of $T$, and $b$, using the regularisation method is represented by the following equation [33]:

$$h = (T^t T + \alpha I)^{-1} T^t b. \tag{2.7}$$

where $I$ is the appropriately sized identity matrix, $T^t$, is the transpose of matrix $T$, and $\alpha$ is a parameter that determines the amount of smoothing present in the solution.

The inverse problem has clinical importance, since a physician wants to know the electrical state of the patients heart to help make a diagnosis. The conventional ECG samples the body surface potential at a limited number of sites; providing low resolution of electrical events, resulting in a high degree of uncertainty [34]. The localisation of electrical events in the heart can then only be inferred by broad terms [35], or due to lack of sensitivity, fail to detect abnormal activity [32]. Accurate inverse solutions would provide detailed spatial and temporal information of localised cardiac electrical events; characterising nonuniformities of conduction properties, and hence, improve the non-invasive ECG evaluation of ischaemia [36], infarcts [37], and arrhythmia's [35]. The technique has the benefit of being non-invasive, so measurements can be easily obtained from patients. With the inverse problem, a physician would not have to examine a series of ECG channels, but look at the potential map of the heart, with isopotential contours

and isochrones of excitation times. This would allow a clinician to view a whole lot of information for the activation of the heart in a comprehensive form; the potential can graphically presented, so patterns are striking, and easy to distinguish [38].

The solution to the inverse problem is non-unique; that is, the potential distribution in the heart can have more than one form, that will generate potentials which are consistent with the measured body surface potentials. The inverse problem is also ill-conditioned, due to inverting a near-singular forward transfer matrix, which is made worse by increasing the number of calculated data points in the heart, and the contamination of noise. The ill-posed nature of the inverse problem has been one main area under study, since it is one major issue preventing medical implementation [39].

The inverse problem has been investigated by a number of researchers. Kilpatrick *et. al.* [38] have conducted clinical studies into the relationship between the derived epicardial potentials from body surface potentials and ischaemia. The body surface potentials were recorded by a jacket worn by patients, which had an array of 51 electrodes positioned around the body, with a concentration of electrodes over the left chest [40]. The studies confirmed that epicardial potential distributions can be used as an indicator of acute inferior infarction, which can be derived within a small amount of time of seeing a patient [41, 38]. The derived epicardial potentials are also accurate enough to predict which coronary vessel is involved in the acute infarction [42]. Patients who are at high risk, after inferior infarction, can be determined as well [36].

A direct validation of the inverse problem in electrocardiology would require the measurement of epicardial potentials, and body surface potentials, at the same time. This would be difficult to do in humans, mainly due to the obvious ethical reasons [42]. Though this study has been performed in animals. Barr and Spach [43] demonstrated the use of the inverse problem in animals, by calculating epicardial potential distributions from measured body surface potentials on dogs. This study showed that features of the potential distributions can be

inferred from body surface measurements, by using inverse techniques, and was verified with direct epicardial measurements. To make a close comparison to humans, experiments on chimpanzees have been performed [44]. An evaluation to isolated human hearts, such as measurements conducted by Durrer [22], has been performed as well [32].

# Chapter 3

# The Bidomain Model

## 3.1 Governing Equations

The complex tissue in the heart can be represented by the bidomain model, a macroscopic model that describes the behaviour of bioelectric fields. It is macroscopic, due to the assumption that the electric potentials vary over distances greater than the dimension of a single cell [45]. The bidomain model was developed by Tung [46], and is based on the interpenetrating concept by Schmitt [47], which comprises of two super-imposed continuous domains, intracellular and extracellular, which are separated by a cellular membrane, where current is only permitted to pass from one domain to the other [47]. The bidomain concept can be thought of as intracellular and extracellular domains that are represented by rows of resistors; these are coupled through parallel resistor and capacitor pairs, that act as the membrane. Figure 3.1 shows a schematic representation of a two dimensional bidomain. The intracellular and extracellular resistive domains are shown in the bottom and top networks to the left of the diagram, and are separated by parallel resistor capacitor circuits, defining the membrane. Resistivity can be defined in the $x$ and $y$ directions, for both intracellular and extracellular domains, giving a total of four resistivity values in a two-dimensional domain. The bidomain equations are derived from the continuity of current, such that, the divergence of the intracellular current density, $\mathbf{J_i}$, must be equal to the current

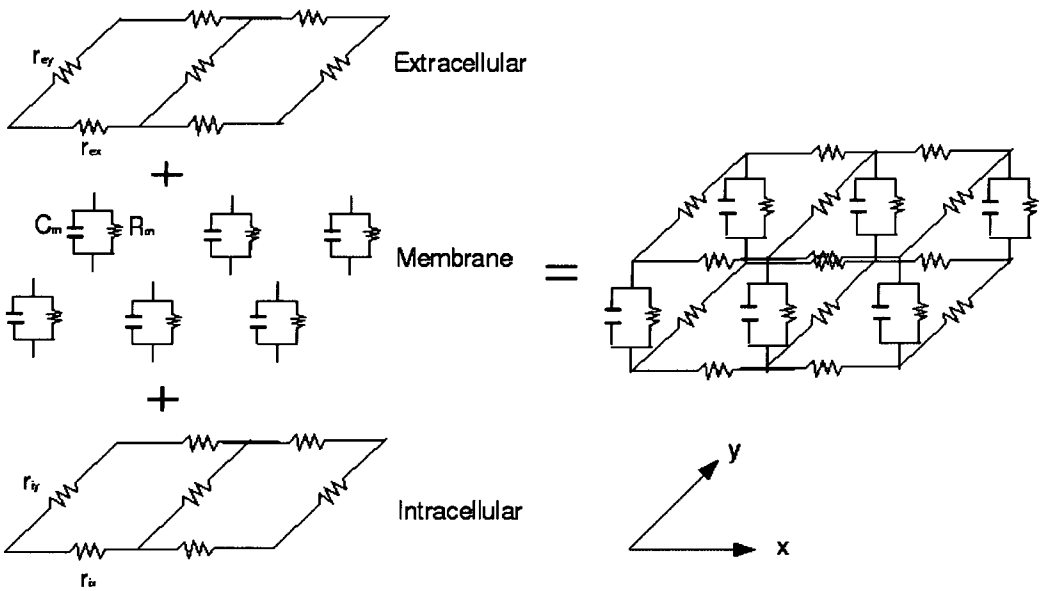


Figure 3.1: Schematic representation of the bidomain model in two dimensions. The lower and upper resistor networks in the $xy$-plane represent the electrical properties of the intracellular and extracellular domains. Between these networks are parallel resistor and capacitor circuits that join the two domains together, representing the electrical properties of the membrane. In cardiac tissue, the resistors along the $x$ and $y$ axis differ, causing anisotropy. Reproduced with permission from Roth, Dept. Physics Oakland University, Rochester, MI USA [48].

per unit volume, $I_m$, through the cell membrane [48, 49, 50, 46, 25]:

$$\nabla \cdot \mathbf{J_i} = -I_m, \tag{3.1}$$

where the minus sign indicates current leaving the intracellular domain is positive. Then, for current entering the extracellular domain:

$$\nabla \cdot \mathbf{J_e} = I_m. \tag{3.2}$$

Including externally applied point stimulus currents, $I_{si}$, in the intracellular domain, and $I_{se}$, in the extracellular domain, leads to:

$$\nabla \cdot \mathbf{J_i} = -I_m + I_{si}, \tag{3.3}$$

$$\nabla \cdot \mathbf{J_e} = I_m + I_{se}. \tag{3.4}$$

From Ohm's Law, the intracellular and extracellular current densities can be written as:

$$\mathbf{J_i} = \mathbf{D_i}\mathbf{E_i}, \tag{3.5}$$

$$\mathbf{J_e} = \mathbf{D_e}\mathbf{E_e}. \tag{3.6}$$

where $\mathbf{E_i}$ and $\mathbf{E_e}$ represent the intracellular and extracellular electric fields, and $\mathbf{D_i}$ and $\mathbf{D_e}$ define the bidomain conductivity tensors, which describes the anisotropy of the cardiac tissue properties. The bioelectric fields can be related to the gradient of the electric scalar potentials, given by:

$$\mathbf{E_{i,e}} = -\nabla \Phi_{i,e}. \tag{3.7}$$

It follows from substitution of Equations (3.5), (3.6), and (3.7), into (3.3) and (3.4), leads to:

$$\nabla \cdot (\mathbf{D_i} \nabla \Phi_i) = I_m - I_{si}, \tag{3.8}$$

$$\nabla \cdot (\mathbf{D_e} \nabla \Phi_e) = -I_m - I_{se}, \tag{3.9}$$

The transmembrane current density, $I_m$, is the sum of capacitive and ionic currents, given by the following expression:

$$I_m = \beta \left( C_m \frac{d\Phi_m}{dt} + I_{ion} \right). \tag{3.10}$$

where $\Phi_m$ is the transmembrane potential, which is defined as:

$$\Phi_m = \Phi_i - \Phi_e. \tag{3.11}$$

The $C_m$ term is the transmembrane capacitance, $\beta$ is the ratio of membrane surface area to tissue volume, and the $I_{ion}$ term is the sum of transmembrane ionic currents. Membrane models consisting of first-order, non-linear ordinary differential equations describes the behaviour of the $I_{ion}$ term, which depends on the transmembrane potential and state variables. Membrane models govern the passage of ions between the intracellular and extracellular domains. These models have been developed based upon experimental data, such as the Luo-Rudy [51, 52] and the Beeler-Reuter [53] membrane models for cardiac ventricular action potential.

By using the definition of transmembrane potential, $\Phi_m$, and adding Equations (3.8) and (3.9), the bidomain equations can be represented in a form with $\Phi_m$ and $\Phi_e$ as independent variables [54]:

$$\nabla \cdot (\mathbf{D_i} + \mathbf{D_e}) \nabla \Phi_e = -\nabla \cdot (\mathbf{D_i} \nabla \Phi_m) - I_{se}, \tag{3.12}$$

$$\nabla \cdot \mathbf{D_i} \nabla \Phi_m = -\nabla \cdot \mathbf{D_i} \nabla \Phi_e + \beta I_m. \tag{3.13}$$

Numerical methods are mostly used to solve the bidomain equations, such as the finite difference method for regularly discretized domains. For simulating realistic geometries with irregular discretized domains, the finite element method is used [54]. The finite volume method has also been used to solve the bidomain equations, and is better suited to the nature of cardiac propagation [49, 55].

One limitation of the bidomain model is that it cannot be used to study electrical activity at the cellular level, since the model is macroscopic; it calculates potentials averaged in space over many cells [56]. However, it is applicable to many cases in electrocardiology, such as, modelling the inverse problem, the shock from defibrillators, and studying cardiac conduction abnormalities. There is continual development in solving the bidomain equations and its application [57, 58, 59, 60].

## 3.2 Anisotropic Electrical Conduction

Cardiac muscle tissue consists of a dense vascular network of coronary circulation, collagen, and a complex network of cylindrical like cells that are interconnected through gap junctions. These cells are arranged into bundles of fibres which are organised into layers of sheets up to three or four cells thick (25-40 $\mu m$), which are separated by cleavage planes, and are stacked from apex to base, as shown in Figure 3.2 [61, 62]. Figure 3.3 shows a larger diagram of 3.2(a), which demonstrates the twist of the layers. Figure 3.2 is a simple model that gives insight into the laminar structure of the myocardium, though it is not the only model that can exist; a study by Arts *et. al.* [63] on the myocardial laminar structure, suggested there can be more than two populations of laminar sheet orientations, and they may occur in patches. The laminar structure has been supported by diffusion tensor MRI measurements made by Scollan [64]. The fibres are oriented spirally about the cavity of the heart, and vary transmurally, with fibre angle rotations of up to 180° from epicardium to endocardium, in the left ventricular myocardial wall (measured by Streeter *et. al.* from histological sectioning [65, 66]). Taccardi *et. al.* have measured the total transmural rotation in the left ventricle to be 110° from potential mapping at different pacing depths [67]. Diffusion tensor MRI has also verified the variation of fibre direction with transmural depth [68].

Experimental evidence has shown strongly that electric current propagates more readily along the tissue fibres than across them; hence, having anisotropic electrical conductive properties [10, 11, 12]. The conductivity tensors, $\mathbf{D_i}$ and $\mathbf{D_e}$, in the bidomain Equations (eq. 3.8 - 3.9) describes the anisotropy of the heart tissue. To describe the anisotropy in the general case, conductivity values are defined along the three principal directions, resulting in a conductivity tensor

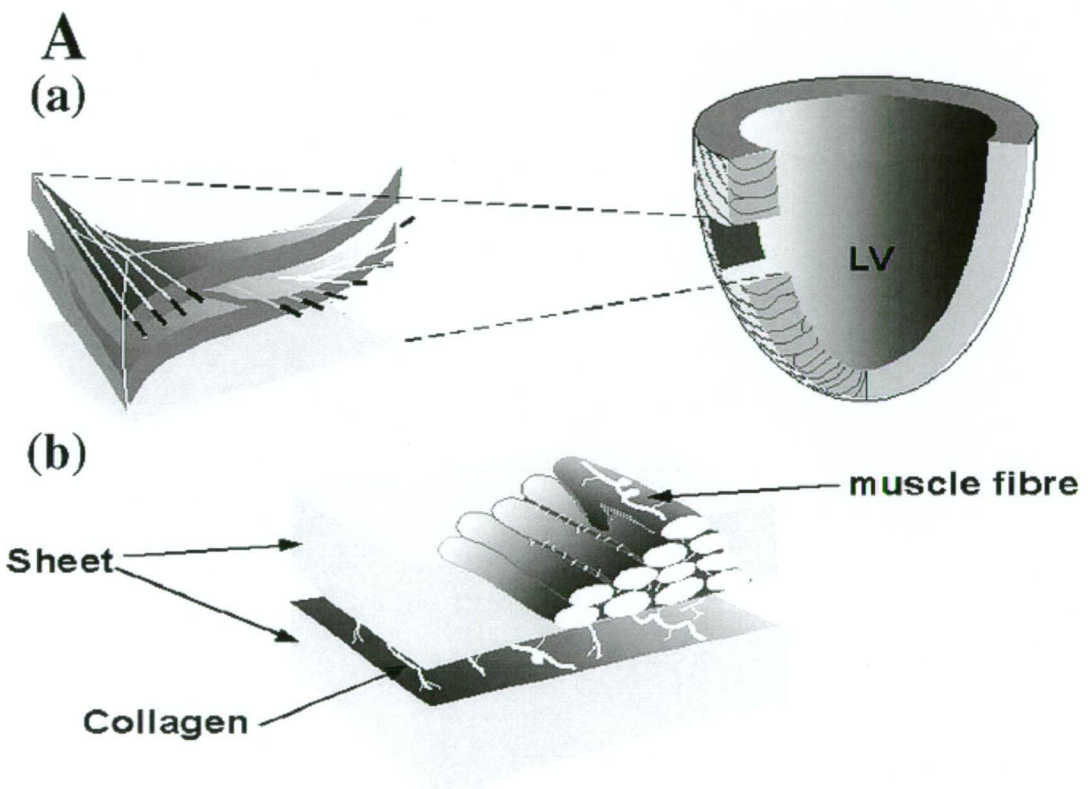


Figure 3.2: Cardiac microstructure. (a) Cross-section of heart, showing laminar sheets, stacked from apex to base. These layers rotate transmurally. (b) cellular arrangement of laminar sheets, three to four cell thick. Image source: reproduced with permission from LeGrice, Auckland Bioengineering Institute, University of Auckland, New Zealand [61].

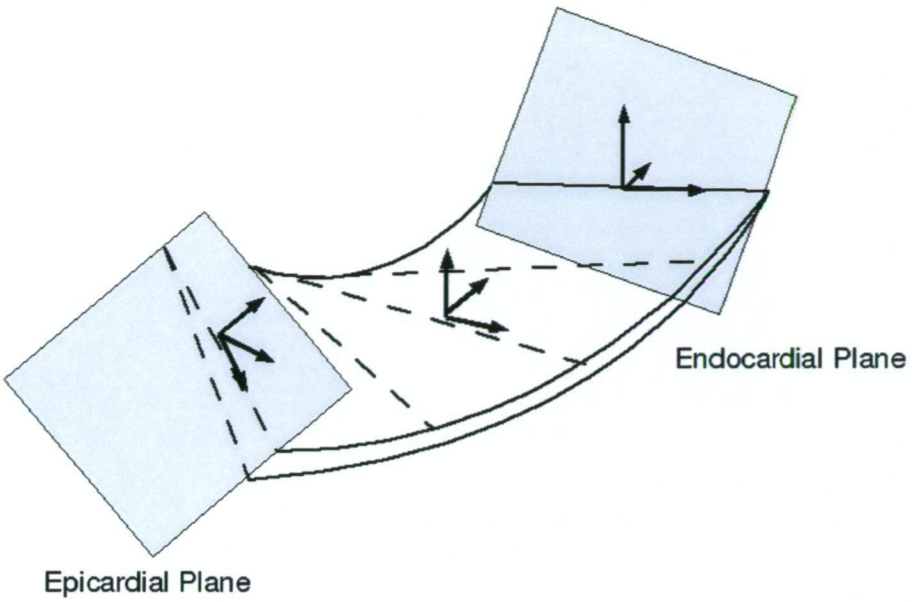


Figure 3.3: Larger diagram of 3.2 (a), showing the rotation of a laminar sheet. Three principle direction can be defined; with two directions in the plane of the sheet, and one perpendicular to it.

with only diagonal entries [69, 70, 71]:

$$\mathbf{D}^{*}_{(\mathbf{i},\mathbf{e})} = \begin{bmatrix} \sigma_l & 0 & 0 \\ 0 & \sigma_t & 0 \\ 0 & 0 & \sigma_u \end{bmatrix}. \tag{3.14}$$

$\mathbf{D}^{*}_{(\mathbf{i},\mathbf{e})}$ is the local conductivity tensor, in the fibre coordinate system, for intracellular and extracellular space [50, 72, 45], where $\sigma_l$ is the conductivity longitudinal to the fibre direction; $\sigma_t$ is the conductivity transverse to the fibre direction, in the plane of the epicardial surface; and $\sigma_u$ is the conductivity in the direction across the fibres, normal to the epicardial surface, in the epicardial to endocardial direction. These conceptual planes that rotate through the myocardium can be visualised in Figure 3.4. To incorporate the variation of fibre orientation, the local conductivity tensor $\mathbf{D}^{*}_{(\mathbf{i},\mathbf{e})}$ is transformed to the tissue's global coordinate system, by the rotation matrix $\mathbf{A}$:

$$\mathbf{D}_{\mathbf{i},\mathbf{e}} = \mathbf{A}\mathbf{D}^{*}_{(\mathbf{i},\mathbf{e})}\mathbf{A}^{\mathbf{T}} = \begin{bmatrix} \sigma_{(i,e)x} & \sigma_{(i,e)xy} & \sigma_{(i,e)xz} \\ \sigma_{(i,e)yx} & \sigma_{(i,e)y} & \sigma_{(i,e)yz} \\ \sigma_{(i,e)zx} & \sigma_{(i,e)zy} & \sigma_{(i,e)z} \end{bmatrix}. \tag{3.15}$$

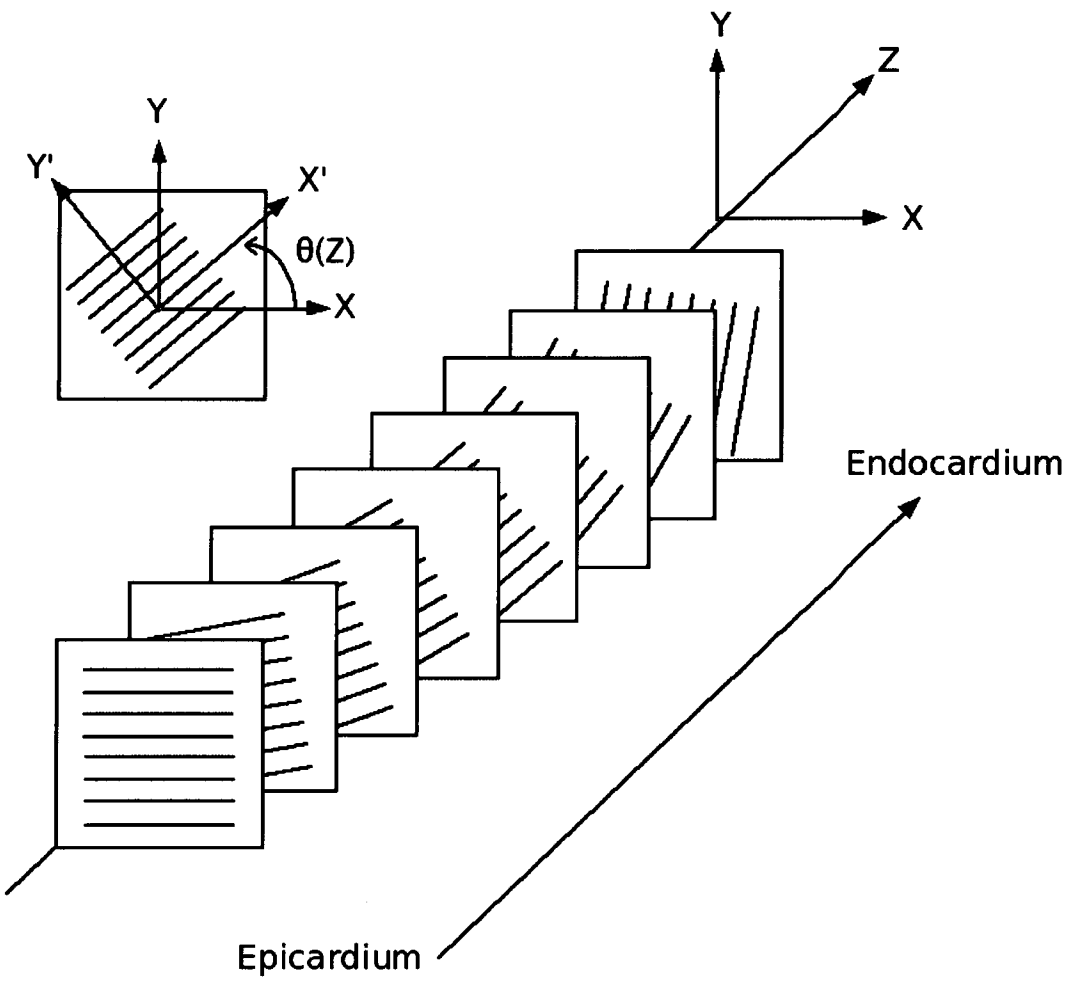


Figure 3.4: Counter-clockwise rotation of fibres from epicardium to endocardium. The planes can be thought as being tangential to the epicardial surface. The angle $\theta(Z)$ is between the X-axis and the fibre direction. Reproduced with permission from Henriquez, Biomedical Engineering, Duke University, Durham, NC USA [50].

where

$$\mathbf{A} = \begin{bmatrix} cos\theta(z) & -sin\theta(z) & 0 \\ sin\theta(z) & cos\theta(z) & 0 \\ 0 & 0 & 1 \end{bmatrix}. \tag{3.16}$$

The angle $\theta(z)$ is the angle between the fibre direction and x-axis, rotated about the z-axis as a function of depth. The conductivity tensors in Cartesian coordinates is then given by:

$$\mathbf{D_{i,e}} = \begin{bmatrix} \sigma_{(i,e)x}cos^2\theta(z) + \sigma_{(i,e)y}sin^2\theta(z) & (\sigma_{(i,e)x} - \sigma_{(i,e)y})cos\theta(z)sin\theta(z) & 0 \\ (\sigma_{(i,e)x} - \sigma_{(i,e)y})cos\theta(z)sin\theta(z) & \sigma_{(i,e)y}cos^2\theta(z) + \sigma_{(i,e)x}cos^2\theta(z) & 0 \\ 0 & 0 & \sigma_{(i,e)z} \end{bmatrix}. \tag{3.17}$$

The out-of-plane fibre angle, known as the muscle fibre imbrication angle, has been assumed to be zero in this case, since it is less than 5° in the bulk of the myocardium [71]. This has also been confirmed by Streeter [73], and by Young [74], that the angle between the fibre direction and the epicardial tangent plane is negligible. Though, it has been shown in bidomain simulations that it causes asymmetry in the magnitudes of the positive potential maxima regions of the depolarising wave [75].

On the basis that the myocardium is a discrete laminar structure, LeGrice *et. al.* [71] states that it is possible to identify three distinct material axes at any point in these planes: one in the direction of the muscle fibre axis, a second in the direction traverse to the fibre axis in the plane of the muscle layer, and the third in the direction perpendicular to that plane. These directions are shown in Figure 3.3. Though in practice, if the muscle layers are represented as transmural sheets that twist to represent local fibre direction, as in Figure 3.2, then the orientation of these planes may not be a straight forward implementation into a bidomain model. Henriquez [50] diagram of the definition of the three directions, as shown in Figure 3.4 is more simpler to model, and traditionally this coordinate system is used; with the measured bidomain conductivities by Clerc [10] and Roberts [11, 12] defined in this system, which will be used in this thesis.

## 3.3 Heart Structure

Knowledge of the myocardial fibre architecture is essential to accurately understand and interpret cardiac electrical and mechanical functions [76]. In the case of measuring the anisotropic conductivities, it is essential to obtain knowledge of the fibre direction, in relation to the measurement electrodes. There are a few ways to determine the orientation of the tissue fibres; such as histological sectioning [73, 77, 74], MRI diffusion tensor imaging, and from the orientation of the early depolarising wave on the epicardium, initiated by point stimulation [67]. Figure 3.5 shows a histological image of cardiac cells arranged into fibres. Determining the fibre direction in the heart by histological sectioning has been

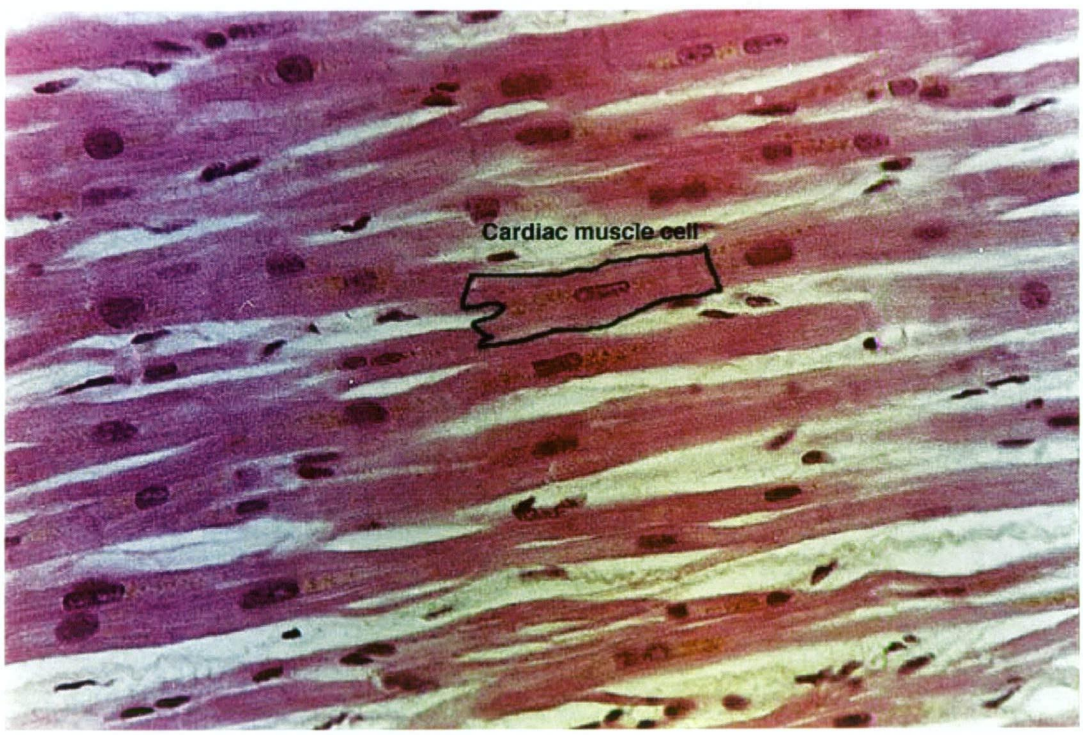


Figure 3.5: Myocytes arranged into fibres. Outline shows individual cell. Reproduced with permission from Histology World [78].

the pioneering technique [73]. Nielsen *et. al.* [69] have created a geometric anatomical model of the heart that includes the organisation of fibre direction using histological sectioning. Measurements have been made in the right and left ventricles at successive levels transmurally, and then an interpolation performed.

The disadvantage with the histological technique is that it is time consuming, and produces a large amount of data. There may be some accuracy lost when preparing and dissecting the tissue [79, 80]; with shrinkage, deformation, and imaging errors. It may be impractical to visualise the structural organisation of an entire heart in three dimensions with this technique, though it does provide detail information about the fibre architecture of large tissue samples, and at present, it is considered as the gold standard [81].

Measuring the fibre direction from the orientation of the depolarisation wavefront is based on the assumption that the electric current propagates faster along the tissue fibres than across them [10, 11, 12]. Reasonable determination of fibre orientation can be achieved in the early stages of activation. Though, in the latter stages of activation, from 20 to 30 ms onwards following stimulation, the wavefront departs from its elliptical form, becoming irregular [67]. Also, the fibre direction progressively changes as the wave propagates further out from the point of origin.

Diffusion tensor MRI is an extension of the conventional MRI, of tracking and measuring the motion of water molecules. The fibre direction can be measured since the water diffusion in the cardiac tissue is anisotropic. It is based on the hypothesis that the eigenvector of the largest MRI diffusion tensor eigenvalue coincides with the orientation of the local myocardial fibre direction [82, 83, 80, 84]. The advantage with diffusion tensor MRI, is that the true three-dimensional myofibre direction vectors can be determined [85, 80, 84]. The technique is also non-invasive, and the fibre architecture is determined for an intact heart, rather than a sectioned one by the conventional histology approach, which may introduce uncertainties. Hsu *et. al.* [82] made a direct comparison between the fibre orientation measured by diffusion tensor MRI and histological techniques, and found good correlation. Another validation was made by Scollan *et. al.* [64], which also showed good agreement between histological and diffusion tensor MRI techniques. Diffusion tensor MRI has been used to create detailed anatomical models of the human heart, for numerical simulation of electrical excitation, and

mechanical deformation [86]. Henriquez *et. al.* [55] has used the technique to determine fibre orientation in mouse hearts, for bidomain simulations. It has also been used to assess the fibre architecture of brain white matter [87, 88], spinal cord [89], kidney [90], and skeletal muscle [83, 91]. However, there are technical difficulties with diffusion tensor MRI, associated with the motion of the beating heart [92, 82], and other limitations [93, 94, 95].

# Chapter 4

# Measurement of Bidomain Conductivity

Numerous researchers have undertaken cardiac tissue conductivity measurements, such as Rush [96, 97], Weidmann [98], Chapman [99], and Kleber [100]. Typically, the conductivity is determined indirectly. With a known stimulating current, measured voltage, and a mathematical model that governs the electrical behaviour of the tissue, the unknown conductivity can be determined. Different techniques have been made; with variations of the four-electrode technique [101], measurement of wavefront conduction velocities [10, 11, 12], applications of direct current and alternating current [102, 103], and the use of different types of electrodes [104]. Determining the conductivity of cardiac muscle in vivo is a challenging problem, both experimentally and theoretically; difficulties include the knowledge of tissue fibre orientation with respect to the electrodes, and obtaining measurements with precisely known electrode separation. The measured conductivity values can be greatly influenced by the type of model used [105], and there may be difficulty in deciding what measurements to make and how to use them in a model [104].

## 4.1 The Four-Electrode Technique

The four-electrode technique has been widely used for cardiac resistivity measurements. In this technique, two voltage electrodes are placed at a known distance in the cardiac tissue, in between two current electrodes. The voltage across these two electrodes is measured, and then the resistance can be calculated [96, 106]. The advantage of this technique is that it avoids the possible electrode polarisation at the current electrodes, as experienced in the two electrode technique [107]. This technique can be used for both AC and DC voltages [108].

Rush *et. al.* [96, 97] applied the four-electrode technique to several body tissues, including heart tissue, in which anisotropic resistivities were obtained. Though only bulk conductivities were calculated, and the model used was like a monodomain. A theoretical study by Plonsey and Barr [109], applied the four-electrode technique along with the bidomain model, and were able to obtain analytical solutions by assuming constant anisotropic ratios. When the four-electrode

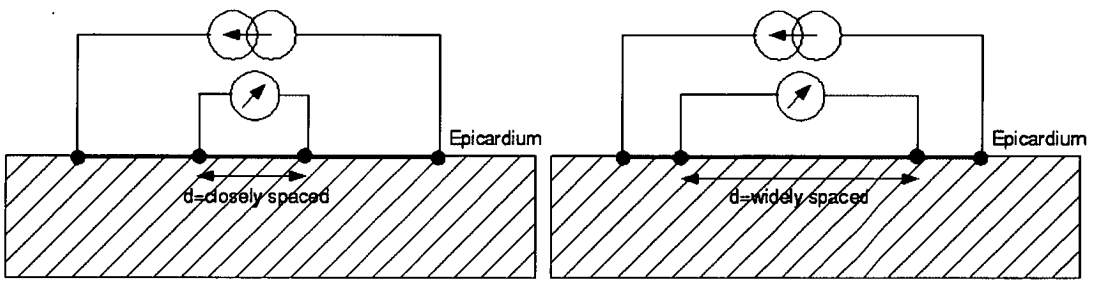


(a) Closely spaced electrodes, for current flow in only extracellular space.

(b) Widely spaced electrodes, for current flow in both intracellular and extracellular space.

Figure 4.1: The four electrode configuration applied for bidomain conductivity measurements. Two outside electrodes apply the current, while the two inner electrodes measure the voltage.

technique is applied to determine the bidomain conductivities, measurements are made to obtain potential in extracellular space in isolation, and for both intracellular and extracellular space. To measure the potential in just extracellular space, the measurement electrodes are place at a small width apart. In order to measure the potential in both intracellular and extracellular space, the measurement electrodes are spaced wider apart. Figure 4.1 shows the electrode configurations.

To determine the distances between the measurement electrodes, the so called length constants can be calculated for the longitudinal and transverse directions [110]:

$$\lambda_l = \sqrt{\frac{R_m \sigma_{il} \sigma_{el}}{(\sigma_{il} + \sigma_{el})\beta}}, \tag{4.1}$$

$$\lambda_t = \sqrt{\frac{R_m \sigma_{it} \sigma_{et}}{(\sigma_{it} + \sigma_{et})\beta}}. \tag{4.2}$$

where $\beta$ is the ratio of the membrane surface area to tissue volume, and $R_m$ is the membrane resistance times unit area. For example, using the conductivity parameters measured by Clerc [10], shown in Table 4.8, and $R_m$=0.91 $\Omega m^2$ [110], the length constants are $\lambda_l$=787 $\mu m$, and $\lambda_t$=285$\mu m$. In order to measure the potential in just extracellular space in the longitudinal direction, the separation of the measurement electrodes needs to be below 787 $\mu m$. When the separation is wider than this, the potential is measured in both intracellular and extracellular space.

The advantage of the four-electrode technique when applied to finding the two-dimensional bidomain conductivities, is that three parameters at most are needed to be estimated at one time. Firstly, measurements of the potential in extracellular space are obtained when the electrodes are close together, below the space constant. This enables the fibre direction and the two extracellular conductivities to be calculated. Then, the remaining intracellular conductivities are calculated by measuring the potential when the electrodes are widely spaced [19].

An extension of this technique by Le Guyader *et. al.* [101, 13, 14], is by applying an alternating current to change the length constant. At higher frequencies the length constant is smaller, resulting in the current flowing in both intracellular and extracellular space. At lower frequencies the space constant is wider, resulting in the current flow confined to extracellular space. Two measurement electrodes can then be held fixed at a small separation, and do not need to be increased which would sample a different larger region. The modified length

constants are given by [111]:

$$\lambda_l = \sqrt{\frac{Z_m \sigma_{il} \sigma_{el}}{(\sigma_{il} + \sigma_{el})\beta}}, \tag{4.3}$$

$$\lambda_t = \sqrt{\frac{Z_m \sigma_{it} \sigma_{et}}{(\sigma_{it} + \sigma_{et})\beta}}. \tag{4.4}$$

where $Z_m$ is the AC specific membrane impedance, which has replaced the DC membrane resistance, $R_m$, in equations (4.1) and (4.2). Le Guyander *et. al.* [14] definition of $Z_m$ is based on assumptions about gap junction resistance and capacitance.

If the myocytes are approximately 100 $\mu m$ long and 20 $\mu m$ in diameter, and judging the distance between cells, such as in Figure 3.5, then the calculated length constants seem to be large. For example, $\lambda_l$=787 $\mu m$ is more larger than the length of a myocyte by a factor of 7, and it would appear in practice, that the required closely spaced electrodes needs to be smaller. Sadleir and Henriquez [19] theoretical study used electrode spacings of 5 or 10 $\mu m$ to ensure that extracellular conductivities were independent from intracellular conductivities. Though manufacturing electrodes with small enough spacings accurately may be difficult without the necessary equipment, and they may be more prone to measurement noise [112]. Another issue that arises is that the bidomain model is a macroscopic model, with the assumption that the electric potential varies over distances greater than the dimensions of a single cell, and so it may not fully describe microscopic scales [113].

## 4.2 Estimating Bidomain Conductivities Based on Tissue Structure

Another approach to determining the bidomain conductivity values is to create a geometric model of a section of cardiac tissue, at the cellular level. Krassowska and Neu [15, 114] created a macroscopic model, based on cellular-level geometry and material constants retrieved from the literature; Table 4.1 lists the constants

used. The model represented the myocardium as a lattice of cells, electrically connected by low-resistance gap junctions; this structure resided in extracellular fluid. A continuum representation of the cellular model was derived [114]. The estimates of the intracellular conductivities in the longitudinal and transverse directions were calculated by:

$$\sigma_{il} = \frac{\sigma_i \alpha_i}{1 + \frac{1}{3}\frac{r_j}{r_c}} \quad and \quad \sigma_{it} = \frac{1}{\sqrt{3}} \frac{1}{l_c r_j}, \tag{4.5}$$

For extracellular space, the longitudinal and transverse conductivities were calculated by:

$$\sigma_{el} = \alpha_e \sigma_e \quad \text{and} \quad \sigma_{et} = \frac{\alpha_e}{2} \sigma_e. \tag{4.6}$$

where $\alpha_i$ is an intracellular area fraction, related to $\alpha_e$ by $\alpha \equiv 1 - \alpha_e$; $r_j$ is the junctional resistance, $r_c$ is the longitudinal resistance and $l_c$ is the cell length.

The results from the study found that the intracellular and extracellular conductivities in the longitudinal direction were close to experimental measurements reported in the literature; Table 4.2 presents the values obtain. However, there was a significant difference in the intracellular transverse conductivity, with the estimate from the model being much lower than the reported experimental values. The source of discrepancies between the conductivities may be from the material constants used in the model, given in Table 4.1, which may not be necessarily correct. Another reason may be since the intracellular transverse conductivity depends greatly on the junctional resistance, in which its value is uncertain. To be consistent with experimental values, changing the cell dimensions and increasing the number of junctional connections between cells is needed, but in doing so, this will change the other conductivity values, which are already close to agreement with the experimental values.

Over a decade later, Stinstra *et. al.* [16, 17] constructed a geometric cellular model based on histology images of cardiac tissue, that consisted of two domains; intracellular and extracellular space, separated by the cell membrane. Features in the two domains were included in the model, for example, interstitial fluid and capillaries for extracellular space; and then electrolyte and gap junctions for

Table 4.1: Material Constants used in the geometric tissue model by Krassowska and Neu [15].

| Parameter | Value |
|---|---|
| conductivity of cytoplasm | 4 $mScm^{-1}$ |
| conductivity of extracellular fluid | 20 $mScm^{-1}$ |
| membrane resistivity | 20 $k\Omega cm^2$ |
| membrane capacitance | 1 $\mu Fcm^{-2}$ |
| cell diameter | 15 $\mu m$ |
| cell length | 100 $\mu m$ |
| extracellular area fraction | 0.15 |
| extracellular gap width | 1 $\mu m$ |
| longitudinal cell resistance | 1.7 $M\Omega$ |
| junctional resistance | 20 $M\Omega$ |
| range of junction resistance | 1-60 $M\Omega$ |
| junctional resistivity | 3.5 $\Omega cm^2$ |
| range of junctional resistivity | 0.2-10 $\Omega cm^2$ |

Table 4.2: Comparison between the conductivities from Krassowska and Neu [15] geometric model and experimental measurements ($mScm^{-1}$).

| Parameter | Model | Experimental: Clerc [10] | Roberts *et. al.* | Roberts & Scher [12] |
|---|---|---|---|---|
| $\sigma_{il}$ | 0.7 | 1.7 | 2.8 | 3.4 |
| $\sigma_{it}$ | 0.003 | 0.19 | 0.26 | 0.6 |
| $\sigma_{el}$ | 3.0 | 6.3 | 2.2 | 1.2 |
| $\sigma_{et}$ | 1.5 | 2.4 | 1.3 | 0.8 |

intracellular space. A finite element model governed by Laplace's equations was used to calculate the currents flowing through intracellular and extracellular space due to an external applied field. From this model the bulk bidomain conductivity for intracellular and extracellular space in the longitudinal and transverse were calculated by:

$$\sigma_i = \frac{J_{ICS}}{E_{app}} \quad \text{and} \quad \sigma_e = \frac{J_{ECS}}{E_{app}}. \tag{4.7}$$

where $E_{app}$ is the applied electric field; $J_{ICS}$ and $J_{ECS}$ is the resulting net current density. The material parameters shown in Table 4.3 where used to calculate the intracellular and extracellular conductivity in the longitudinal and transverse directions; derived values are shown in Table 4.4. The results were within range of the experimentally measured values reported in the literature, however, like in Krassowska and Neu's study [15] there was disagreement with the intracellular transverse conductivity. Stinstra *et. al.* [17] reason for the discrepancy, was the value for gap junction resistance; its needed to be lower, but would then be out of range from the literature values. Another reason is due to the gap junction distribution. Gap junctions are not only located at the ends of the myocytes, but can be located on the lateral sides. The model had some simplifications: it was assumed that the myocytes were arranged into a regular grid, the sheet of interstitial fluid between the cells were of the same thickness throughout the domain, and the membrane was non-conducting. Even with these simplifications, the model had many similarities to real tissue. The conductivities derived from the model were used in a whole heart model that was based on the bidomain equations, to simulate regional subendocardial ischaemia. The advantage of using a cellular model is that the material constants can be modified to reflect changes under pathological conditions, such as during ischaemia, when there can be alterations to the cardiac cells, vascular morphology and gap junction resistance. The effect of these changes on potential distributions can then be studied in bidomain simulations [16, 115].

Table 4.3: Material Constants used in the geometric tissue model by Stinstra *et. al.* [16].

| Parameter | Value |
|---|---|
| Cytoplasm longitudinal conductivity | 0.3 $Sm^{-1}$ |
| Cytoplasm transverse conductivity | 0.15 $Sm^{-1}$ |
| Interstitial conductivity | 2.0 $Sm^{-1}$ |
| Capillary wall conductivity | 0.02 $Sm^{-1}$ |
| Blood plasma conductivity | 2.0 $Sm^{-1}$ |
| Haematocrit | 50 % |
| Gap junction resistivity | $1.45 \times 10^{-4}$ $\Omega cm^2$ |
| Cell membrane resistivity | $+\infty$ $\Omega cm^2$ |
| Average cell cross-section | 300 $\mu m^2$ |
| Average cell length | 95 $\mu m^2$ |
| Volume fraction myocytes | 84 % |
| Volume fraction interstitial space | 11 % |
| Volume fraction capillaries | 5 % |

Table 4.4: Comparison between the conductivities from Stinstra *et. al.* [17] geometric model and experimental measurements ($mScm^{-1}$).

| Parameter | Model | Experimental: Clerc [10] | Roberts *et. al.* | Roberts & Scher [12] |
|---|---|---|---|---|
| $\sigma_{il}$ | 1.6 | 1.7 | 2.8 | 3.4 |
| $\sigma_{it}$ | 0.05 | 0.19 | 0.26 | 0.6 |
| $\sigma_{el}$ | 2.1 | 6.3 | 2.2 | 1.2 |
| $\sigma_{et}$ | 0.5 | 2.4 | 1.3 | 0.8 |

Table 4.5: Resistivity measured by Clerc [10].

$$R_{il} = 402 \pm 30\ \Omega cm$$
$$R_{it} = 3620 \pm 280\ \Omega cm$$
$$R_{el} = 48 \pm 4\ \Omega cm$$
$$R_{et} = 127 \pm 38\ \Omega cm$$

## 4.3 Bidomain Conductivity Measurements

Table 4.8 provides the common conductivity values used in bidomain models [9, 27]. These were measured by Clerc [10] and Roberts *et. al.* [11, 12] more than two to three decades ago. Each investigator used different techniques. The following sections summaries their studies.

### 4.3.1 Clerc 1976

Clerc [10] performed in vitro experiments on bundles of trabeculae, from the right ventricle of calf hearts. The resistance was determined from amplitudes of intracellular and extracellular biphasic action potentials in the muscle bundles. A one-dimensional cable model was used to describe the current flow, which avoided the complexity of greater dimensions. The bundles of tissue where prepared in such a way that the longitudinal and transverse measurements were measured separately. Extracellular recordings and intracellular potential recordings were also measured separately, by different placement of micro-electrodes, which showed measured deflections of opposite polarity. Measured resistivities are given in Table 4.5. Conduction velocity was measured from the same preparation, with a longitudinal velocity, $\theta_l$, of $48 \pm 4\ cms^{-1}$, and a transverse velocity, $\theta_t$, of $16 \pm 1\ cms^{-1}$. The propagation of conduction velocity was found to be constant. Clerc's resistivity values, given as the specific resistances, $R$, are defined over a particular area of space, where as bidomain resistivities, $r$, are defined over the whole tissue area. The first column in Table 4.8 shows the converted values reported by Clerc. These values were simply obtained by the following

expressions [50]:

$$\sigma_i = f_i/R_i, \tag{4.8}$$

$$\sigma_e = f_e/R_e. \tag{4.9}$$

with the fraction of intracellular and extracellular spaces to be $f_i = 0.7$ and $f_e = 0.3$; having an extracellular space of 30 % of the tissue volume [10]. The main achievement of Clerc's work, was that he was able to measure the separate intracellular and extracellular conductivities, where as previous investigators had measured only bulk resistivity.

### 4.3.2 Roberts 1979

Due to the differences in measured resistivity values between in vitro studies such as Clerc's experiment [10] and in situ studies [97], Roberts *et. al.* [11] conducted in vivo experiments on nine dogs, and resistivity was determined by equations relating them to the wavefront voltage. He was concerned with the effects of cardiac fibre direction on conduction velocity and resistivity.

Roberts mapped the extracellular potential of propagating excitation, via an epicardial electrode array, with reference to a remote electrode located in an opening in the animal's thorax. Activation was administered by pacing the epicardium with a stimulating electrode at the centre of the electrode array.

He extended on Clerc's theoretical analysis which unified conduction velocity, resistivity, and wavefront voltage. The wavefront voltage was determined as the maximal rate of change; that is, taken as the maximal difference between two voltages recorded 2 $ms$ apart. Knowledge of fibre direction was determined, by assuming the direction of maximal conduction velocity.

Conduction velocity was measured to have a longitudinal velocity, $\theta_l$, of $58 \pm 8\ cms^{-1}$, and a transverse velocity, $\theta_t$, of $25 \pm 3\ cms^{-1}$. Resistivity values were defined differently from that of Clerc's [10], in that the resistivity was for the total tissue area. Roberts *et. al* [11] defined the resistivity in this way to avoid the assumption of the fraction of tissue that intracellular and extracellular space

Table 4.6: Resistivity measured by Roberts *et. al.* 1979 [11].

$$r_{il} = 360\ \Omega cm$$
$$r_{it} = 3800\ \Omega cm$$
$$r_{el} = 450\ \Omega cm$$
$$r_{et} = 750\ \Omega cm$$

occupies. The measured resistivities from this experiment are shown in Table 4.6, in which five dogs where used in calculating the results. Bidomain concepts were used in this study, though an anisotropic monodomain model was used in the calculations, hence, the measurement of bulk or gross resistivities were made. The separate resistivities were then derived from the assumption that the bulk resistivities are the parallel combination of the intracellular and extracellular resistivities. Bulk resistivity was determined by a method similar to the four-electrode technique; as the one used by Rush *et. al.* [97]. The pacing stimulus was used as the current source; a 3 $ms$ rectangular current pulse injected on the epicardium. With the known current $I$, measured potential $V$, and distance $D$ of the recording electrode from the current electrode, the bulk resistivities were calculated by the following expression [96]:

$$V = \frac{RI}{2\pi D}. \tag{4.10}$$

Then, the longitudinal and transverse resistivities, for intracellular and extracellular space, was obtained by the following expressions [11]:

$$r_{il} = r_l \Delta / V_{el}, \tag{4.11}$$

$$r_{it} = r_t \Delta / V_{et}, \tag{4.12}$$

$$r_{el} = r_{il} r_l / (r_{il} - r_l), \tag{4.13}$$

$$r_{et} = r_{it} r_t / (r_{it} - r_t). \tag{4.14}$$

where $r$ represents the resistivity, with subscripts $l$ and $t$ denoting the longitudinal and transverse directions, and $i$ and $e$ denoting the intracellular and

extracellular space. The symbol $r$ without the $i$ and $e$ subscripts represents the bulk resistivity. $V$ is the wavefront voltage, and the symbol $\Delta$ is the magnitude of the transmembrane action potential, which was assumed to have a value of 100 $mV$.

### 4.3.3 Roberts 1982

Later, Roberts *et. al.* [12] investigated further into measuring cardiac tissue resistivity, with more developed mathematical modelling of extracellular potential fields. Like in the previous experiment, the extracellular field was mapped during excitation of the cardiac tissue. Fibre direction was determined as the long axis of the elliptically shaped propagating wave of activation. Wavefront voltage was not determined by measuring the maximal rate of change during depolarisation, but by using least-squares to produce the best-fit between potential fields for experimental and model data. Roberts *et. al.* claimed that obtaining the wavefront voltage in this way overcomes the uncertainty of how the wavefront voltage was selected in the previous experiment. Bidomain modelling was used, and with a number of assumptions and approximations introduced, Roberts was able to deduce an expression for calculating the extracellular field, which was solved by numerical integration. Though, it was only used for obtaining the wavefront voltage; the bulk resistivity was measured with the technique used in the previous study, but this time the resistivities were calculated using the wavefront voltages determined by linear regression.

Measured conduction velocity in the longitudinal direction, $\theta_l$, was $57 \pm 6\ cms^{-1}$, and for the transverse direction, $\theta_t$, $24 \pm 3\ cms^{-1}$, similar to the values in the previous experiment. Resistivities are given in Table 4.7, for six hearts studied. Even though the measured bulk resistivities were similar to Roberts *et. al.* previously reported values [11], the bidomain resistivities were significantly different. He claimed that the difference was due to the improved method of determining wavefront voltages; affecting the calculated values.

Table 4.7: Resistivity measured by Roberts *et. al.* 1982 [12].

$$r_{il} = 291 \pm 38\ \Omega cm$$
$$r_{it} = 1677 \pm 331\ \Omega cm$$
$$r_{el} = 852 \pm 232\ \Omega cm$$
$$r_{et} = 1247 \pm 210\ \Omega cm$$

## 4.4 Differences in Measured Conductivities

The bidomain conductivities given in Table 4.8 [9] are basically the reciprocal of the resistivities from Tables 4.5 to 4.7, with the conversion for Clerc's values with the assumption of fractional volume of intracellular and extracellular space. The

Table 4.8: The Measured bidomain conductivities (mS/cm) [9].

| Symbol | Clerc(1976)[10] | Roberts(1979)[11] | Roberts and Scher(1982)[12] |
|---|---|---|---|
| $\sigma_{il}$ | 1.741 | 2.800 | 3.436 |
| $\sigma_{it}$ | 0.193 | 0.260 | 0.596 |
| $\sigma_{el}$ | 6.250 | 2.200 | 1.174 |
| $\sigma_{et}$ | 2.362 | 1.300 | 0.802 |
| $\sigma_{il}/\sigma_{it}$ | 9.021:1 | 10.77:1 | 5.77:1 |
| $\sigma_{el}/\sigma_{et}$ | 2.646:1 | 1.69:1 | 1.46:1 |
| $\sigma_{il}/\sigma_{el}$ | 0.279:1 | 1.273:1 | 2.927:1 |
| $\sigma_{it}/\sigma_{et}$ | 0.082:1 | 0.200:1 | 0.743:1 |

conductivities given in Table 4.8 have large discrepancies between each other. One difference is that the longitudinal value for extracellular space $\sigma_{el}$, in Clerc's measurements, is greater than the longitudinal intracellular value $\sigma_{il}$, when compared with Roberts' measurements. Though, there is agreement with the ratio of the longitudinal and transverse conductivities $\sigma_{il}/\sigma_{it}$ for intracellular space being greater than the extracellular space $\sigma_{el}/\sigma_{et}$; and also the transverse conductivity in extracellular space $\sigma_{et}$, being greater than intracellular space $\sigma_{it}$.

The variability between the measurements is due to the different experimental

Table 4.9: Conductivities from Colli Franzone [116] (mS/cm).

$$\sigma_{il} = 3.0$$
$$\sigma_{it} = 0.31525$$
$$\sigma_{el} = 2.0$$
$$\sigma_{et} = 1.3514$$

techniques performed; whether the experiments were performed in vivo or not, the extent and approach of the mathematical modelling, the animal species experimented on, and the type of measurements obtained.

Colli Franzone *et. al.* [116] calculated conductivity values based on measurements cited in the literature, such as conduction velocity, and applying Roberts *et. al.* [11] method. These values are shown in Table 4.9. Similarly Taccardi *et. al.* [117] made calculations in this manner, for parameter calibration for bidomain simulations. There are also a number of investigators that have selected bidomain parameters suited to their simulations [118, 119, 120, 121].

# Chapter 5

# Depolarisation Wave

The electrical excitation, referred to as the depolarisation, can be triggered by extracellular stimulus electrodes, with a current injection above threshold, at a site in the cardiac tissue. This can be applied by pacing; which delivers a frequency of DC pulses via electrodes. If this frequency is above the rate set by the heart's pacemaker cells at the sinoatrial node, and the pacing current is above threshold, then activation would occur at the site of stimulation. Furthermore, when pacing the epicardium, paced beats are produced; and when the left ventricle is paced, the normal activation sequence of transmural depolarisation can be reversed, as epicardial to endocardial propagation, rather than via the Purkinje fibre network, from endocardium to the epicardium [122, 123, 124].

## 5.1 Wavefront

Activation spreads throughout the tissue region by cell-to-cell conduction, since the cardiac cells are interconnected by low-resistance channels called gap junctions [125]. Gap junctions are located at the ends of the cells, at the membrane, and at the lateral edges; they permit the flow of ions and small molecules. The term depolarisation, or the activation of the tissue, is used to describe the sudden influx of cations $Na^{+}$ and $Ca^{++}$, which occurs when the membrane is permeable [126]. When activation occurs during pacing by point stimulation, the cardiac cells

near the stimulus electrode depolarise. This in turn, causes the depolarisation of neighbouring cells and so on. The result is a propagating wavefront, that is shaped elliptically, and is centralised over the stimulating electrode, with negative potential occupying the area inside the ellipse. This is accompanied by two positive maxima regions at both of its ends; adjacent to these maxima are two negative minima. The analogy can be thought as two collinear dipoles at 180° from one another; a diagram representing this is shown in Figure 5.1.

The wavefront can be defined as the zone where the transition from resting to the activated transmembrane potential takes place [45]; its a propagating layer, travelling less than 1 $ms^{-1}$, of approximately 1 $mm$ in width [27]. To help visualised this region, an isochrone line at the point where there is the greatest rate of change in potential can be seen as the wavefront, or as bands of densely packed negative isopotential lines [127]. In the situation of epicardial point stimulation, this gives an outline of an ellipse during the early stages of activation [11], and departs from this shape 20 to 30 $ms$ onwards after stimulation [67]. The wavefront on the epicardium propagates in all directions, until it merges with other wavefronts coming from breakthrough sites. Breakthrough sites are locations on the epicardium where the activation occurs earlier than other surrounding regions [128]; this activity is from the endocardial to epicardial activation sequence, via Purkinje fibre junctions, where individual wavefronts may come off. These breakthroughs complicate the shape of the ellipse in its later stages, and subsequently gives the appearance of increased conduction velocity; of up to 2 or 3 $ms^{-1}$ [67]. Analysis of the propagation of wavefront activation from point stimulation was first studied with epicardial mapping [129, 11]. Mapping studies of potential distributions during pacing, such as the one by Taccardi *et. al.* [67] or Watabe *et. al.* [130], have indicated that the major axis of the ellipse, that passes through both positive maxima, is mostly aligned with the tissue fibres near the stimulus site. Also, a study by Frazier *et. al.* [122] observed that the initial isochrones of the activating region were elliptical, with the major axes of the ellipse along the mean fibre direction. This occurs due to the faster conduction along the direction

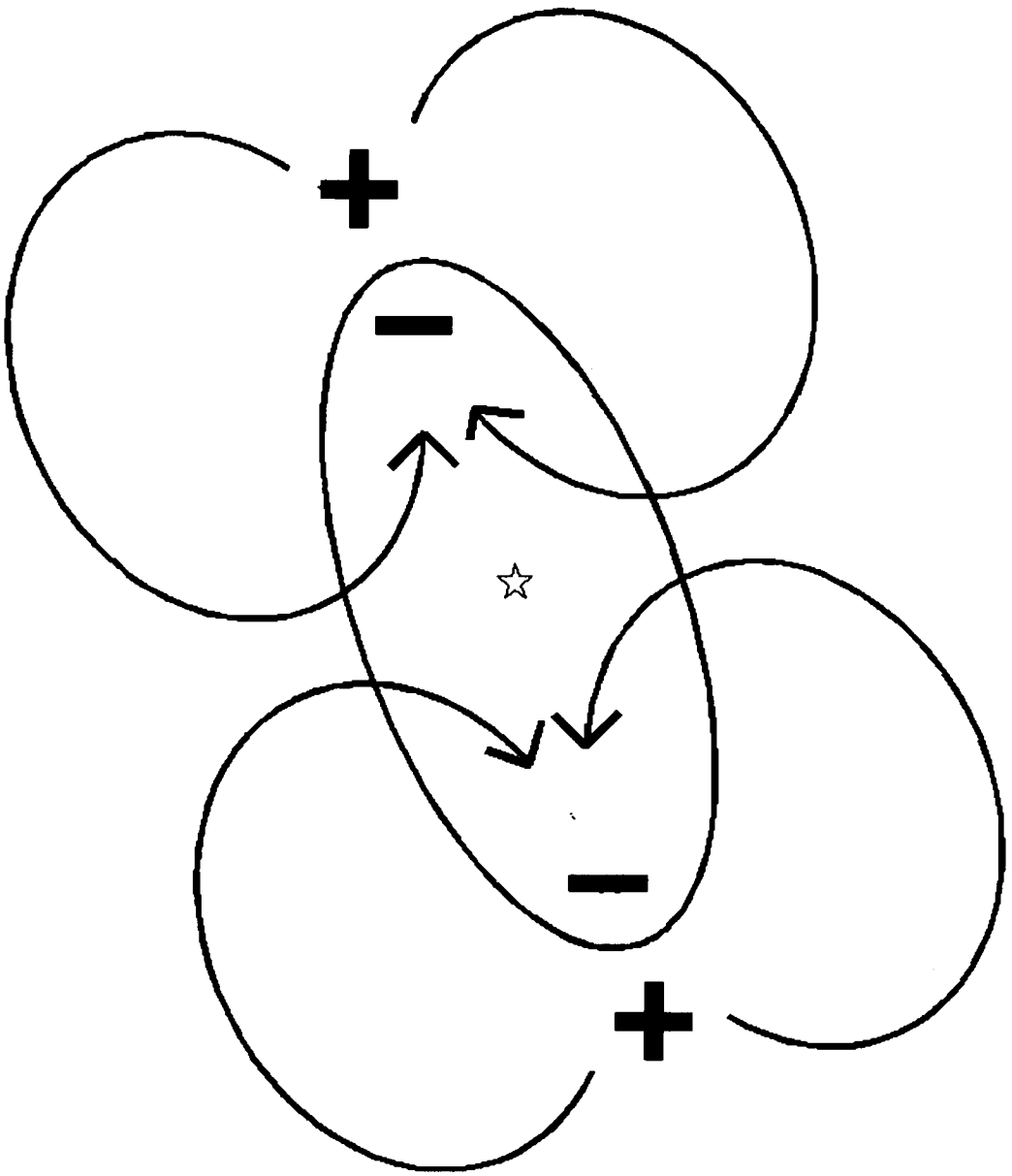

Figure 5.1: A representation of the elliptical shaped wavefront, from epicardial stimulation. Two potential maxima are located at both ends of the ellipse on the outside, and two minima are located on the inside of the ellipse at the ends. The star in the middle is the site of stimulation. Arrowed lines show the extracellular current paths, from the maxima to the minima. The orientation of the ellipse reflects fibre direction. Reproduced with permission, Taccardi *et. al.*, Effect of Myocardial Fiber Direction on Epicardial Potentials, Circulation, 90, 3076-3090 [67].

of the tissue fibres than across them [131, 98, 129, 10, 11, 8, 12]. The average conduction velocity measured, from several investigators, for mainly canine ventricular muscle, has been 56 $cms^{-1}$ and 21 $cms^{-1}$, for along and across the tissue fibres respectively [132]. Therefore, there is higher conductivity in the longitudinal direction, resulting in more current per area in the region of the wavefront travelling along the fibres than across them [133]. This exhibits the propagating wave of excitation in the form of an ellipse. Thus, from the orientation of the elliptical wavefront, the fibre direction can be revealed in situ, without histological sectioning. Colli Franzone *et. al.* [127] also defined the fibre direction in this way in simulation studies. Though, this method does have its limits; Frazier *et. al.* [122] noted that the difference between the major axis of the elliptical wavefront and the local fibre orientation, increased, as it travelled further away from the stimulation site.

## 5.2 Transmural Rotation of Depolarisation Wave

The spread of the depolarising wave from point stimulation is a three-dimensional process, which is influenced by the transmural rotation of fibres, and the distribution of Purkinje tissue [122]. In Taccardi *et. al.* [67] cardiac mapping study, they observed that the two positive maxima at both ends of the elliptical wavefront undergo an expansion and rotation in the counter clockwise direction from the epicardium to endocardium. During the study of transmural activations, Frazier *et. al.* [122] observed that the ellipse rotates in the same general direction as the fibres, with the wavefront in three-dimensions producing a helicoid. The major axes of the ellipse corresponded to the average fibre orientation, during the transmural activation, and the twist of the helicoid was less than the corresponding local rotation of the fibres.

A simulation study by Muzikant and Henriquez [134], showed that information about the fibre orientation in the cardiac tissue can be revealed by observing the potential distributions during pacing. Based on Taccardi *et. al.* [67] and Frazier's

*et. al.* [122] experimental findings, the line connecting through the two positive maxima of the depolarising ellipse on the epicardium was used to reveal the epicardial fibre orientation. Muzikant and Henriquez [134] used this technique, along with another method, for measuring the fibre orientation transmurally. Their technique involved curve fitting the isopotentials of the stimulus artifact and the contours of the depolarising ellipse, when observed on the epicardium during intramural stimulation, which gave the average of the fibre angle, $\theta_{avg}$. This assumes that these potentials reflect an average of the fibre angle, between the epicardium and the stimulus plane, and that the change in transmural fibre rotation is linear. With the epicardial fibre angle, $\theta_{epi}$, known, then the intramural fibre angle, $\theta_{depth}$, can be calculated at each intramural pacing depth by the following equation:

$$\theta_{avg} = \frac{\theta_{epi} + \theta_{depth}}{2}. \tag{5.1}$$

They concluded that extracellular potential data during and after stimulation, could be used to determine epicardial fibre angle gradients, the amount of fibre rotation per unit depth, and anisotropy. It could also be used to characterise the three-dimensional anisotropic electrical properties in situ.

When measuring the conductivity in the heart, it is important to know the fibre orientation of the tissue under study. Normally there is a geometric model with a description of fibre orientation, use to simulate electrical events, such as the Auckland geometric heart model, based on histological analysis of canine hearts by Nielsen *et. al.* [69]. Accurately matching the fibre direction at a given location in a heart from an experiment, to the corresponding fibre direction in such a model would be challenging. There is also the heart-to-heart variation between experiments to consider as well [134]. Measuring the local fibre direction from the orientation of the depolarising wave during epicardial pacing can overcome these difficulties, since the fibre direction can be determined for a particular experiment.

The depolarising wave has been use for studying the electrical activity of the heart. Oster *et. al.* [35, 135] has used it in an inverse problem study. In their study, they placed a canine heart into a human torso tank model, where direct

measurements to the heart could be obtained, and body surface potentials could be measured on the torso model. They reconstructed epicardial potentials initiated by pacing, from body surface measurements. Features of the reconstructed epicardial potential patterns included the two maxima of the depolarising wave, hence, the fibres could be derived noninvasively. This was confirmed with the direct epicardial measurements of the canine heart in the torso tank.

Muzikant and Henriquez [134] hypothesised that the eccentricity of the stimulus artifact from the pacing stimulus may be used to isolate the extracellular anisotropy ratios, so that additional information can be provided for determining the anisotropic electrical properties of cardiac tissue.

## 5.3 Electrograms

Electrograms are local samples of the potential distribution as it varies during the cardiac cycle for excitation and recovery [67, 136]. There are different electrogram morphologies that arise during the propagation of the depolarising wave, which produce Q and R waves. Figure 5.2 shows a diagram of the type of electrograms produced. R waves are associated with the positive maxima at both ends of the ellipse, hence, they are found in regions in which the activation moves along the fibre direction. This activity is shown as a positive deflection in the electrogram [67]. R waves mainly occur along fibres; and it has been confirmed by experiment [67], and computer simulations [117], that the transverse propagation of excitation between the epicardial and endocardial plane, does not generate R waves. However, from experiment and computer simulations, weak positive potentials or small R waves have been reported to appear in regions where the wavefront is spreading across the fibres. This effect is due to the presence of intracavitary blood and transmural rotation of fibres [133, 117]. Q waves are shown as a negative deflection in the electrogram. This rapidly changing component of the electrogram is known as the "intrinsic deflection" [136]. The greatest rate of change of the negative deflection can be taken as the time of local electrical

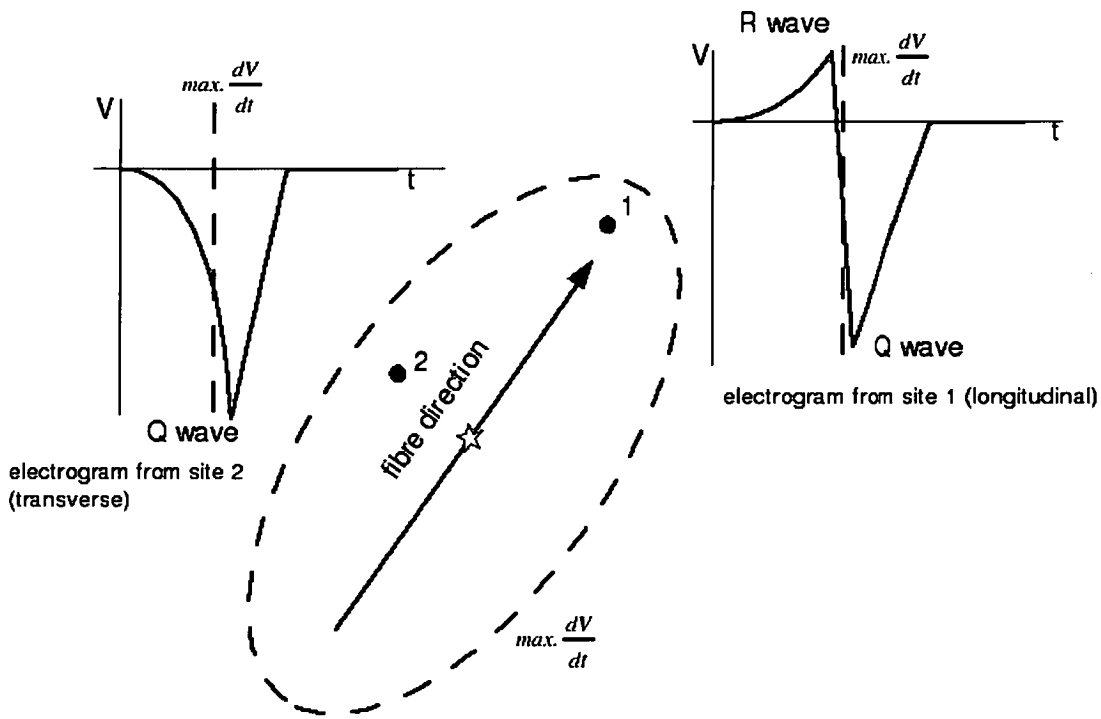


Figure 5.2: Diagram to show the types of electrograms produced during the propagation of the elliptical depolarising wave on the epicardium. The electrograms are measured at the points labelled with 1 and 2, located along and across the fibres respectively. R waves are observed along the fibre direction followed by Q waves, where as across the fibre direction only Q waves are observed. Dashed vertical lines indicate the greatest rate of change in potential, which can be used to define the outline of the ellipse, and also time of activation.

activation, which distinguishes the outline of the wavefront. Initial Q waves occur in areas where the excitation wave propagates across the fibres. When the excitation propagates along the fibres, the Q wave occurs after the initial R wave [117, 137].

Previously, the behaviour of the depolarising elliptical wavefront had been studied by the uniform double layer model [138], and later on, the oblique double layer model [139]. These models had limitations, with simplifying assumptions, and where inconsistent with experimental data [45, 117]; they are now considered to be obsolete, when compared with the bidomain model. The bidomain model has been used to study potential distributions during point stimulation by Colli Franzone *et. al.* [127], which showed similar results to Taccardi *et. al.* [67] experimental observations.

# Chapter 6

# Parameter Estimation

The parameters in the conductivity tensors, that are contained in the bidomain Equations (3.8) and (3.9), are not measured directly in this study, contrary to Clerc's [10] and Roberts *et. al.* [11] deterministic approach, but are inferred by inverse techniques, known as parameter estimation. These parameters have a physical significance, in that they describe the anisotropy of the cardiac tissue. The goal is to determined a set of these values, which gives the best-fit between model generated potential and observed potential. The determination of parameters in partial differential equations, known as parameter estimation, is generally ill-posed and non-unique, and arises in many areas of inverse problems, such as ground-water modelling [140, 141], astronomy [142], and geophysics [143].

## 6.1 Optimisation

Mathematical models are derived in many branches of physics to describe the behaviour of a system. The model equations contain variables and parameters. The parameters can describe the physical properties of a system, and it is desirable to determine their values, so that the model can produce numbers consistent with observed quantities.

Parameter estimation methods normally have two stages [143]:

1. A function $\mathbf{O}(\mathbf{p})$ is defined to represent the difference between model data

and experimental data. This function is called the objective function, a measure of fit. The smaller its value, the greater the consistency between the model and observations, and the greater confidence in the determined parameter set on the basis of the observations [143, 144]. For example, in the least-squares method for determining parameters, the sum of squares of the residuals is the objective function.

2. If $\mathbf{p}$ is an $n$-row vector containing the model parameters, then the aim is to find $\widehat{\mathbf{p}}$, an estimate of $\mathbf{p}$, such that the objective function $\mathbf{O}(\mathbf{p})$, is brought to a minimum. The process of calculating $\widehat{\mathbf{p}}$, is known as optimisation. The optimum parameters $\widehat{\mathbf{p}}$, is a local minimum of the objective function $\mathbf{O}(\mathbf{p})$. The absolute goal is to find the unique global minimum.

## 6.2 Least-squares

The least-squares method is one of the most common estimation procedures. It has been applied to a vast number of fields in science and engineering. To describe the behaviour of a system there is normally a model function, $f(x)$, that has been developed. If there are $m$ number of observations $y$, then the aim is to find a model function $f(x)$ that gives values close to the observations $y$. That is, a set of parameter values is required, to minimise the sum of the squares of the residuals:

$$\mathbf{O} = \sum_{\mathbf{i=1}}^{\mathbf{m}} (y_i - f(x_i, \mathbf{p}))^2. \tag{6.1}$$

For example, if the function was quadratic, $f(x) = ax^2 + bx + c$, then the coefficients $a$, $b$, and $c$ are to be determined, such that the objective function, $O$, is reduced to a minimum. If the model function was linear, such as the example quadratic function, then the problem simplifies considerably, essentially reducing to a system of linear equations. Though, in general, this is not the case, normally the model function is non-linear, such as the bidomain model, and the problem is more difficult to solve. Iterative gradient based parameter estimation techniques

such as the Levenberg-Marquardt algorithm [145], are used to solve the general optimisation problem.

Suppose, for a linear model, the relationship can be assumed to be:

$$\mathbf{c} = X_1 p_1 + X_2 p_2 + \cdots + X_n p_n, \tag{6.2}$$

Or in matrix form

$$\mathbf{Xp} = \mathbf{c}, \tag{6.3}$$

where

$$\mathbf{X} = \begin{bmatrix} X_{11} & X_{12} & \cdots & X_{1n} \\ X_{21} & X_{22} & \cdots & X_{2n} \\ \vdots & & & \vdots \\ X_{m1} & \cdots & & X_{mn} \end{bmatrix}, \tag{6.4}$$

$$\mathbf{p} = \begin{bmatrix} p_1 \\ p_2 \\ \vdots \\ p_n \end{bmatrix}, \tag{6.5}$$

$$\mathbf{c} = \begin{bmatrix} c_1 \\ c_2 \\ \vdots \\ c_m \end{bmatrix}. \tag{6.6}$$

$\mathbf{p}$ is a vector of order $n$, that contains the system parameters, and $\mathbf{c}$ is a vector of order $m$ representing the systems responses, which there are corresponding measurements. The matrix $\mathbf{X}$, is an $m \times n$ matrix, that contains a set of excitations, or sensitivities that gives these responses. The objective function can be represented in matrix form as:

$$\mathbf{O} = (\mathbf{c} - \mathbf{Xp})^{\mathbf{t}}(\mathbf{c} - \mathbf{Xp}). \tag{6.7}$$

where the vector $\mathbf{c}$ now contains the set of measurements. The superscript, $\mathbf{t}$, denotes the transpose operation.

To minimise the objective function, $\mathbf{O}$, the derivative with respect to $\mathbf{p}$ is taken, and the result is set equal to zero [140]:

$$\frac{\partial}{\partial p_j} O(\mathbf{p}) \mid_{\mathbf{p}=\widehat{\mathbf{p}}} = \frac{\partial}{\partial p_j} \left[ (\mathbf{c} - \mathbf{X}\mathbf{p})^{\mathbf{t}} (\mathbf{c} - \mathbf{X}\mathbf{p}) \right] \mid_{\mathbf{p}=\widehat{\mathbf{p}}} \tag{6.8}$$

$$= 0, j = 1, 2, \ldots, n. \tag{6.9}$$

where $\mid_{\mathbf{p}=\widehat{\mathbf{p}}}$ signifies that $\widehat{\mathbf{p}}$ is the set of parameters that causes the derivatives of $\mathbf{O}(\mathbf{p})$ to be zero. Following on by differentiating a product, it can be shown that the vector $\widehat{\mathbf{p}}$ that minimises the objective function is given by [144, 140]:

$$\widehat{\mathbf{p}} = (\mathbf{X}^{\mathbf{t}}\mathbf{X})^{-1}\mathbf{X}^{\mathbf{t}}\mathbf{c}. \tag{6.10}$$

A unique solution to the parameter estimation problem can be achieved by Equation (6.10), if the number of observations $m$ is greater than, or equal to, the number of parameters, $n$.

One property of the estimated parameter set, $\widehat{\mathbf{p}}$, that may be of interest, is its covariance matrix [144, 146]:

$$\mathbf{C}(\widehat{\mathbf{p}}) = (\mathbf{X}^{\mathbf{t}}\mathbf{X})^{-1}\sigma^2. \tag{6.11}$$

where $\sigma^2$ here represents the variance of each element of the vector, $\mathbf{c}$, of measurements. It can be estimated as [144]:

$$\sigma^{\mathbf{2}} = \frac{\mathbf{O}}{(\mathbf{m} - \mathbf{n})}. \tag{6.12}$$

where $(\mathbf{m} - \mathbf{n})$ is the difference between the number of measurements, and the number of parameters contained in $\widehat{\mathbf{p}}$.

From the covariance matrix, the elements $\rho_{ij}$, of the correlation coefficient matrix can be derived [144, 147]:

$$\rho_{\mathbf{ij}} = \frac{\sigma_{\mathbf{ij}}}{\sqrt{\sigma_{\mathbf{ii}}\sigma_{\mathbf{jj}}}}. \tag{6.13}$$

where $\sigma_{ij}$ represents each element in the matrix $\mathbf{C}(\widehat{\mathbf{p}})$, for a number of $i$ rows, and $j$ columns. The diagonal elements of the correlation coefficient matrix consists of ones, while the off-diagonal elements range from 1 to $-1$. The closer these off-diagonal elements are to 1 or $-1$, the higher the parameters are correlated.

## 6.3 Weighted Least-Squares

Generally, an objective function consisting of a sum of squares, like Equation (6.7), may be unsatisfactory. Measurements may be more prone to experimental errors, resulting in some observations being less reliable than others. Another issue is that the measured quantities may be of more than one type, having different physical dimensions, and hence, different magnitudes. Therefore, adding together the squares of the residuals would not be appropriate, since some measurements may dominate others.

It would be preferable, that the more accurate measurements would influence the parameter estimation process. This can be achieved by assigning a weighting factor to each measurement; the larger the weight assigned to a particular measurement, the more influence it has on the objective function. This can be implemented by multiplying a diagonal matrix, $\mathbf{Q}$ to Equation (6.7):

$$\mathbf{O} = (\mathbf{c} - \mathbf{Xp})^{\mathbf{t}}\mathbf{Q}(\mathbf{c} - \mathbf{Xp}). \tag{6.14}$$

The diagonal elements $q_{ii}$ of the weighted matrix $\mathbf{Q}$ contains the square of the weight $w_i$, for each corresponding measurement. Another form of the objective function may be given by:

$$\mathbf{O} = \sum_{i=1}^{m}(w_i r_i)^2. \tag{6.15}$$

where $r_i$ is the residual; the difference between model output and measurements. It can be shown that Equation (6.14) can be expressed by:

$$\mathbf{O} = (\mathbf{c} - \mathbf{Xp})^{t}\mathbf{P^{-1}}(\mathbf{c} - \mathbf{Xp}), \tag{6.16}$$

where

$$\mathbf{P} = \mathbf{Q^{-1}} = \frac{\mathbf{C(c)}}{\sigma^{\mathbf{2}}}. \tag{6.17}$$

The matrix $\mathbf{C(c)}$ represents the covariance matrix of the vector of measurements $\mathbf{c}$. With the weight matrix $\mathbf{Q}$ taken into account in least-squares, the vector $\widehat{\mathbf{p}}$ that minimises the objective function is then given by:

$$\widehat{\mathbf{p}} = (\mathbf{X^t Q X})^{-1}\mathbf{X^t Q c}. \tag{6.18}$$

and the parameter covariance matrix becomes:

$$\mathbf{C}(\widehat{\mathbf{p}}) = (\mathbf{X}^{\mathbf{t}}\mathbf{Q}\mathbf{X})^{-1}\sigma^{2}. \tag{6.19}$$

## 6.4 Non-linear Parameter Estimation

Usually, most models describing a system are nonlinear, and cannot be directly represented by the relationship in Equation (6.3). Since the mathematics of least-squares has been based on this relationship, nonlinear models need to be linearised. To carry this out, a Taylor series expansion is applied to the model function, and the zero and first-order terms are used, assuming local linearity. For example, let $\mathbf{M}$ represent the model function, which maps the parameter vector $\mathbf{p}$ to the measurements vector $\mathbf{c}$ [144]:

$$\mathbf{c} = \mathbf{M}(\mathbf{p}). \tag{6.20}$$

Then applying Taylor series expansion gives [148]:

$$\mathbf{c} = \mathbf{c_0} + \left\{\frac{\partial \mathbf{M_m}}{\partial \mathbf{p_n}}\right\}(\mathbf{p} - \mathbf{p_0}), \tag{6.21}$$

or

$$\mathbf{c} = \mathbf{c_0} + \mathbf{J}(\mathbf{p} - \mathbf{p_0}). \tag{6.22}$$

where $\mathbf{J}$ is the Jacobian matrix. The vector $\mathbf{c_0}$ contains the model output, and $\mathbf{p_0}$ is a vector that contains the current estimate of the parameters. The relationship of Equation (6.22) is an approximation, and it improves as $\mathbf{p_0}$ is closer to $\mathbf{p}$. By linearising the model function, the objective function by least-squares can be defined as:

$$\mathbf{O} = (\mathbf{c} - \mathbf{c_0} - \mathbf{J}(\mathbf{p} - \mathbf{p_0}))^{\mathbf{t}}\mathbf{Q}(\mathbf{c} - \mathbf{c_0} - \mathbf{J}(\mathbf{p} - \mathbf{p_0})). \tag{6.23}$$

This expression is the same as Equation 6.14, where the vector $\mathbf{c}$ is set to $(\mathbf{c} - \mathbf{c_0})$, and $\mathbf{p}$ is set to $(\mathbf{p} - \mathbf{p_0})$. In order to minimise the objective function, the parameter upgrade vector $(\mathbf{p} - \mathbf{p_0})$ needs to be calculated:

$$\mathbf{u} = (\mathbf{J}^{\mathbf{t}}\mathbf{Q}\mathbf{J})^{-1}\mathbf{J}^{\mathbf{t}}\mathbf{Q}(\mathbf{c} - \mathbf{c_0}). \tag{6.24}$$

and the parameter covariance matrix is given by:

$$\mathbf{C}(\widehat{\mathbf{p}}) = (\mathbf{J}^{\mathbf{t}}\mathbf{Q}\mathbf{J})^{-1}\sigma^{2}. \tag{6.25}$$

Due to the Taylor series expansion, the parameter upgrade vector, $\mathbf{u}$, is an approximation. Thus, the objective function would not be completely minimised by Equation (6.24). A number of optimisation iterations needs to be performed to reduce the objective function. Initially, a set of parameters is assigned for $\mathbf{p_0}$. After the calculation of the Jacobian matrix $\mathbf{J}$ and then the upgrade vector $\mathbf{u}$, a new set of parameters $\mathbf{p_0}$ are available. These are then used in the next calculation of the upgrade vector. This process is repeated a number of times until the objective function $\mathbf{O}$ has been reduced to a global minimum. Figure 6.1 shows a flow chart of this procedure.

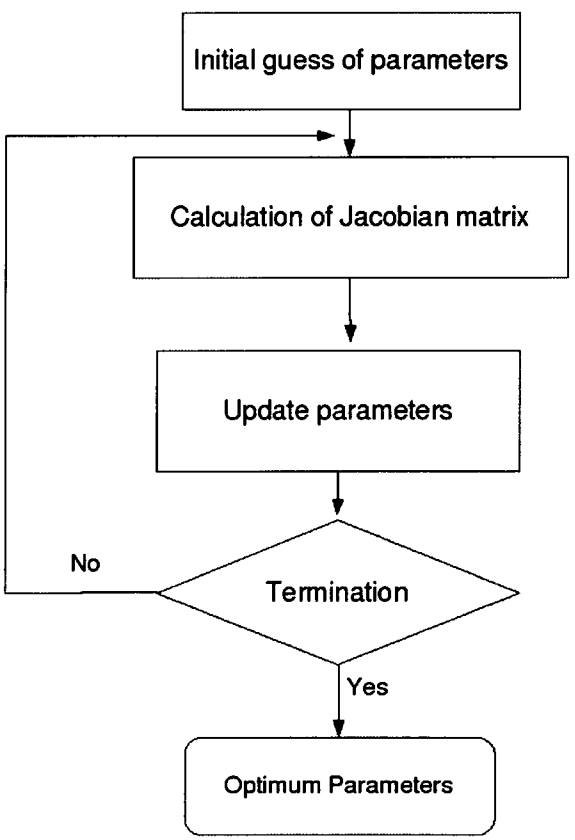


Figure 6.1: Flow chart: algorithm for parameter estimation.

## 6.5 Marquardt Parameter

One method for lowering the objective function is called the *steepest descent* method. The direction in which the objective function rapidly decreases can be determined by calculating the gradient of the objective function in parameter space [144]:

$$\nabla \mathbf{O} = \mathbf{g} = \frac{\partial O}{\partial p_1}\mathbf{i_1} + \frac{\partial O}{\partial p_2}\mathbf{i_2} + ... + \frac{\partial O}{\partial p_n}\mathbf{i_n}. \tag{6.26}$$

Unfortunately, this method is often inefficient, since it requires a large number of steps to arrive at the global minimum of the objective function, which usually terminates far from it, due to round-off effects [149], and leads to a zigzag pathway through parameter space, known as hemstitching [143]. Generally, it can be shown that the direction of the upgrade vector $\mathbf{u}$ is more effective than the direction of the steepest decent vector $-\mathbf{g}$ [144]. Although the steepest decent method is not the desirable method to minimise the objective function, it is useful in the initial stages of the parameter estimation process, when the starting values of the parameters are far from optimum. This can be done by adjusting the direction of the parameter upgrade vector $\mathbf{u}$ to more closely aligned with the direction of the vector $-\mathbf{g}$. Equation (6.24) is modified to include a parameter, known as the Marquardt parameter [148, 145]:

$$\mathbf{u} = (\mathbf{J^t Q J} + \alpha \mathbf{I})^{-1} \mathbf{J^t Q r}. \tag{6.27}$$

where $\alpha$ is the Marquardt parameter, $\mathbf{I}$ is the identity matrix, and $\mathbf{r}$ is the residual between the measured data and model data. It can be shown that the gradient vector, $\mathbf{g}$, can be given by [144]:

$$\mathbf{g} = -\mathbf{2 J^t Q r}. \tag{6.28}$$

As $\alpha$ increases, the direction of vector $\mathbf{u}$ tends towards the direction of $-\mathbf{g}$. As $\alpha$ decreases, Equation (6.27) becomes Equation (6.24). Initially it is good to set a high value of $\alpha$, then decrease it as the estimated parameters lowers the objective function. An algorithm is used for the selection of suitable values for $\alpha$ throughout the parameter estimation process.

## 6.6 Construction of the Sensitivity (Jacobian) Matrix

To evaluate the effect of each parameter has on the model output, and due to the result of linearising the model function by Taylor series expansion, the sensitivity matrix, **J**, is calculated. Its elements are the first derivative of the model function, with respect to each parameter in the set **p** [150]. It is equivalent to the Jacobian matrix for describing the forward action of the model [151, 149]:

$$\mathbf{J} = \left\{ \frac{\partial f_m(\mathbf{p})}{\partial p_n} \right\}, \tag{6.29}$$

$$\mathbf{J} = \begin{bmatrix} \frac{\partial f_1}{\partial p_1} & \frac{\partial f_1}{\partial p_2} & \cdots & \frac{\partial f_1}{\partial p_n} \\ \frac{\partial f_2}{\partial p_1} & \frac{\partial f_2}{\partial p_2} & \cdots & \frac{\partial f_2}{\partial p_n} \\ \cdots & \cdots & \ddots & \cdots \\ \frac{\partial f_m}{\partial p_1} & \frac{\partial f_m}{\partial p_2} & \cdots & \frac{\partial f_m}{\partial p_n} \end{bmatrix}. \tag{6.30}$$

where the elements of **J** are called the sensitivity coefficients. The matrix **J** can be constructed by using perturbation sensitivities. For example, a model is run with a small variation to the first parameter value in the parameter set **p**, while keeping the rest of the parameter values unchanged; this gives the first column of matrix **J**. A second model run is performed with a small variation to the next parameter in the set, while holding the others fixed; this gives the second column of matrix **J**. This process is repeated for the remaining parameter values until the Jacobian matrix is constructed. The benefit of calculating the derivatives in this way is that it is independent of how the model is implemented. Only the output values of the model are needed. There are a couple of different methods on calculating these derivatives [144]; these are described in the following sections.

### 6.6.1 Forward Differences Calculation

Calculating the derivatives with the forward differences method is done by adding an increment to the parameters current value. This is the simplest and fastest method. To form the Jacobian matrix, the model needs to run equal to the

number of parameters to be estimated, plus one more; requiring $n + 1$ model runs.

### 6.6.2 Central Derivatives Calculation

When the problem is highly non-linear, or the parameter estimation process is close to the minimum of the objective function, then the derivatives need to be calculated with greater accuracy. The next technique is the central derivative method, which calculates the derivatives using three parameter points, rather than two, giving more accuracy than the forward differences method. The calculations are performed by firstly adding, then subtracting an increment to the current parameter value. More accurate derivatives are calculated, though, twice as many model runs than the forward differences method are needed to construct the Jacobian matrix.

A consequence of calculating the Jacobian matrix is that a substantial amount of time is spent on repeatedly solving the forward problem for its construction. Time considerations may be an issue when solving complex models, such as the bidomain, or simulating three-dimensional models, resulting in more parameters to be estimated, therefore, more models runs to form the Jacobian matrix.

## 6.7 Goodness of Fit

The objective function can be used as a measure of how close the output of the model is to the measured observations. The lower the residuals between model and measurement data, the better the fit. Though, the objective function value depends on the amount of observational data used, so using it as a direct comparison between different parameter estimation runs with different sets of observational data may not be the best choice. Another measure of goodness of fit can be given by the correlation coefficient [140]. It is independent of the magnitude, and number of observations used in the parameter estimation process, so comparisons can be made between different parameter estimation runs.

The correlation coefficient is given by the following expression [144]:

$$R = \frac{\sum_{i=1}^{m}(w_i c_i - m)(x_i c_{0i} - m_0)}{\left[\sum_{i=1}^{m}(w_i c_i - m)(w_i c_i - m)\sum_{i=1}^{m}(w_i c_{0i} - m_0)(w_i c_0 i - m_0)\right]^{1/2}}. \quad (6.31)$$

where $c_i$ is the observation values, $c_{0i}$ is the model output, $m$ is the mean value of weighted observations, and $m_0$ is the mean of the weighted model output. $w_i$ is the weight associated with the corresponding observation value.

Generally, a value greater than 0.9 for $R$ is considered to be acceptable, for a good fit between model outputs and measurements [152].

## 6.8 Singularity

Due to parameter insensitivity, or correlation, a problem may occur, in that the least-squares normal matrix, the expression ($\mathbf{J^tQJ}$) in Equation (6.24), may not be invertible, due to being singular, or near singular, leading to unstable solutions.

Singularity occurs whenever the columns of the sensitivity (Jacobian) matrix $\mathbf{J}$ are linearly dependent, because this results in the rows or columns of the normal matrix ($\mathbf{J^tQJ}$) to be linearly dependent also. Linear dependence in the sensitivity matrix $\mathbf{J}$ may be stated as:

$$\mathbf{Ja} = \mathbf{0}. \quad (6.32)$$

where $\mathbf{a}$ is a vector of scalars of order $n$, which are not all zero. Multiplying Equation (6.32) by ($\mathbf{J^tQ}$) gives:

$$\mathbf{J^tQJa} = \mathbf{0}. \quad (6.33)$$

which shows that the columns or rows of, $\mathbf{J^tQJ}$, are linearly dependent, and therefore, does not have an inverse [140].

Near-singularity of the least-squares normal matrix, termed as *ill conditioned*, occurs when the columns of the sensitivity matrix $\mathbf{J}$ are close to being linearly dependent. This may be due to a strong correlation between two or more of the

estimated parameters. For example, if two columns in $\mathbf{J}$ are nearly proportional, $J_a \propto J_b$, this results in near linear dependence [140]. As the number of parameters involved in the estimation process increases, the more likely this is to occur.

Another cause of an ill-conditioned matrix is when a column in the sensitivity matrix, $\mathbf{J} = [J_1, J_2, J_3, ...J_n]$, approaches zero. Therefore the derivatives in that column are small, having no effect on the objective function. This is a result of parameter insensitivity, and the parameter responsible may be omitted from the parameter estimation process.

The accumulation of round-off error due to solving an ill-conditioned normal matrix can have adverse effects on the outcome of the estimation process. The parameter covariance matrix, which is also calculated by the normal matrix, can be effected as well.

## 6.9 Truncated Singular Value Decomposition (SVD)

The problem of singularity can be overcome by using Singular Value Decomposition (SVD). It decomposes an arbitrary $m \times n$ matrix $\mathbf{A}$, of rank $k$, into three component matrices[153, 147]:

$$\mathbf{A} = \mathbf{USV^t}. \tag{6.34}$$

where $\mathbf{U}$ is an $m \times m$ orthogonal matrix, $\mathbf{V}$ is an $n \times n$ orthogonal matrix, and $\mathbf{S}$ is an $m \times n$ diagonal matrix, with its entries positive, in descending order.

Calculating the SVD of matrix $\mathbf{A}$ consists of finding its left and right eigenvectors. The eigenvectors of $\mathbf{AA^t}$ make up the columns of $\mathbf{U}$, and the eigenvectors of $\mathbf{A^tA}$ make up the columns of $\mathbf{V}$. The diagonal entries of $\mathbf{S}$ are the singular values of $\mathbf{A}$, which are the positive square roots of the nonzero eigenvalues of $\mathbf{AA^t}$ or $\mathbf{A^tA}$ [154].

Applying SVD to the least-squares normal matrix ($\mathbf{J^tQJ}$), when the Marquardt parameter $\alpha$ is set to zero, gives:

$$\mathbf{J^tQJ} = \mathbf{USV^t}. \tag{6.35}$$

Substituting this expression into Equation (6.27), the parameter upgrade vector becomes:

$$\mathbf{u} = (\mathbf{USV^t})^{-1}\mathbf{J^tQr}. \tag{6.36}$$

The normal equation is a square and symmetric matrix, resulting in $\mathbf{U}$ being equivalent to $\mathbf{V}$. It is also positive semi-definite, with $\mathbf{V^t} = \mathbf{V^{-1}}$. The parameter upgrade vector then becomes [141]:

$$\mathbf{u} = \mathbf{VS^{-1}V^tJ^tQr}. \tag{6.37}$$

From this expression, it can be seen that applying SVD to the normal matrix avoids the task of inverting it, which would be helpful when it is near-singular, resulting in more stable solutions.

When computing the singular values in matrix $\mathbf{S}$ for an estimation problem, some of these values may be very small compared to others, and may not contribute to the solution. These values may also be affected by noise present in the observational data, which can be amplified when inverting $\mathbf{S}$ [141]. To attend to this issue, the singular values that are below a certain threshold, are set to zero; this method is known as Truncated Singular Value Decomposition (TSVD).

A decision needs to be made as to when the singular values are to be truncated; if they are truncated at really small values, keeping most of them, a greater match between experimental observations and the features of the model output can be achieved. However, it can have adverse affects, such as over-fitting, and the solution can become unstable due to the presence of noise. Conversely, setting the truncation threshold at larger singular values, resulting in fewer of them, can result in the solution lacking details about the model [155, 26].

## 6.10 Prior Information

Knowing information about the parameter values before an estimation process can be very helpful. In that convergence to the optimum values would be achieved quicker, by narrowing down the search, or even if the outcome of the process was successful or not.

Prior information on the bidomain conductivities can include their range; a simple assumption could be, that the conductivities are always positive and non-zero, and that the longitudinal conductivities are larger than the transverse conductivities. More information on parameter range can be acquired by judging the measured values reported in the literature, such as the measurements conducted by Clerc [10] and Roberts *et. al.* [11, 12]. These measured values, that vary between the different experiments, can give an estimate on the lower and upper bounds of the parameters. Placing these bounds restrict the estimation process on not going under or over the intended values, so that unnecessary optimisation iterations can be avoided, resulting in faster estimation times. The imposed lower and upper bounds can also help not to go over values that causes the numerical solution of the forward model to become unstable, and cause the solver to max its iteration limit. Initial starting values can be important in whether or not the estimation process is successful or not as well. For example, if the initial values were very far from the optimum parameter values in parameter space, it may take many optimisation iterations to reach the desired values. Or it may not even reach the intended values at all, if the model is highly non-linear.

The measured values in Table 4.8 can be used to select the initial values, for a start. Then after a parameter estimation of the current experimental data is achieved, these values can be used in the next parameter estimation process and the lower and upper bounds can be reset accordingly.

# Chapter 7

# Solution Method

## 7.1 Forward Model

CardioWave [156] software was used to simulate the electric potential in a model of an isolated section of heart tissue. The software performs the forward solution of the bidomain Equations (3.8) and (3.9). It is a modular system of individual programs, in which users have the choice to select these different components, to form one program. The different program modules categories are membrane kinetic models, mesh types, boundary conditions, stimulation methods, matrix solvers, time-integration schemes, preconditioners, and data output formats. These modules are selected and compiled to form an executable. CardioWave can be run on parallel computers to significantly reduce the computational time, and to have access to larger memory space [157, 158, 159, 160, 156].

SCIRun, a general purpose problem solving environment [161, 162, 163], was used to setup finite element stiffness matrices, for the discretization of the elliptical operators in the bidomain Equations (3.8) and (3.9). It has a bioelectric field modelling package known as BioPSE [164], which provides components for a volume conductor model, governed by Poisson's equations. SCIRun allows users to form a data flow network comprised of program modules connected by data pipelines, for a problem solution customised to the users application. It also provides visualisation tools such as isosurfacing and surface potential mapping.

Weinstein [165], and Henriquez [55] have integrated CardioWave into SCIRun, for simulation and visualisation of three-dimensional mouse heart propagation.

### 7.1.1 Computational Mesh

The finite element method (FEM) was mostly used to construct the stiffness matrices, though for simple simulations, finite difference techniques were used. The tissue domain in the model was a regular mesh, discretised into either finite hexahedral elements for three-dimensional domains, or triangular finite elements for two-dimensional domains. Spatial discretization (node spacing) was chosen to be 100 $\mu m$, for adequate resolutions of the membrane kinetics [156]. Mesh types are shown in Appendix F, Figures F.1 and F.2.

### 7.1.2 Local Fibre Direction

It is common for transmural fibre rotation to be included in bidomain models [127, 75, 134, 3]. For three-dimensional simulations, the change in transmural fibre direction was described by the following expression:

$$\theta(z) = \theta_{rot}(z_{depth} - z) + \theta_{start}. \tag{7.1}$$

where $\theta_{rot}$ is the amount of rotation the fibre direction undergoes from epicardium to endocardium, $\theta_{start}$ is the starting fibre angle on the epicardium with respect to the x-axes, and $z_{depth}$ is the thickness of the tissue in the $z$ direction. This expression assumes that the fibre direction varies in a linear sequence, transmurally in the myocardium, as measured by Streeter [65, 66]. Note, that 2D bidomain simulations do not include transmural fibre rotation.

### 7.1.3 Conductivity Tensors

To describe the anisotropy of the tissue, each element in the mesh was assigned with a corresponding conductivity tensor, based upon the local fibre angle and Equation (3.17). The FEM resulted in two stiffness matrices representing the

elliptical operators in Equation (3.8) and (3.9), one for each domain; intracellular and extracellular. These matrices were saved as sparse-banded matrices in NSPCG (Nonsymmetric Preconditioned Conjugate Gradient) format [166, 156], and where then loaded into CardioWave.

### 7.1.4 Applied Current Stimulus

Simulations for the propagation of cardiac excitation from point stimulation were performed, to mimic experimental observations in wave mapping [11, 12, 67]. To act as a pacing stimulus, a DC current was applied to a point in the tissue domain, to initiate activation. Current densities of 1000 $\mu Acm^{-2}$, was set to a group of nodes in the mesh to act as the stimulus site; and applied for a duration of about 1 $ms$. To keep the numerical solution stable, and for faster convergence times, current injection of opposite polarity was applied in both domains at the stimulus nodes; 1000 $\mu Acm^{-2}$ for intracellular and -1000 $\mu Acm^{-2}$ extracellular. This was usually set to a group of nodes in the centre of the mesh.

### 7.1.5 Boundary Conditions

For the boundary conditions, at some point in the domain, away from the stimulus site, the potential was grounded to provide a reference, by assigning a group of nodes to zero. This acquired a unique solution [55], and to help with convergence [156]. Usually, four nodes located in the bottom left corner of 2D meshes were set to zero; and similarly, for a 3D slab of tissue, eight nodes at the bottom corner of the mesh were set to zero.

### 7.1.6 Tissue Parameters

As well as the bidomain conductivity values, there are other parameters that need assigning, such as the surface-to-volume ratio, $\beta$, and the membrane capacitance, $C$. Like the bidomain conductivities, these values vary in the literature, and they also have an effect on the simulated potentials. Henriquez [50, 55] calculated the

surface-to-volume ratio, $\beta$, by treating the fibres to have a circular cylindrical form, and by assuming the fraction of intracellular space. The surface-to-volume ratio, $\beta$, can be calculated by the following expression:

$$\beta = \frac{total\ membrane\ area}{total\ tissue\ volume} = \frac{2\pi al}{\frac{\pi a^2 l}{f_i}} = \frac{2f_i}{a}. \tag{7.2}$$

where $a$ is the radius of the cell, $l$ is the length of the cell, and $f_i$ is the fraction of cross-sectional area occupied by intracellular space. With a cell radius of 8.4 $\mu m$, and the fraction of intracellular space to be 0.7, the surface-to-volume ratio, $\beta$, has a value of 1666 $cm^{-1}$ [55]. This value may be lower than the actual value, since the contributions of membrane folding or sub-cellular membranes such as traverse tubules are ignored [119]. However, a value of 2000 $cm^{-1}$ is used in most bidomain simulations reported in the literature [118, 116, 75, 134].

A number of measurements of membrane capacitance, $C_m$, has been reported [98, 99, 100]. Usually, a value of 1 $\mu F cm^{-2}$ is used in simulations [167, 168, 169]. Since these values have been calculated on the bases of assumptions, and they vary in the literature, they too, may also be determined during the inversion process of estimating the bidomain conductivity parameters.

### 7.1.7 Time Integration

The discretised form of the system of bidomain equations can be given by:

$$\frac{dq}{dt} - F_q(q, v_m) = 0, \tag{7.3}$$

$$M_i\phi_i = \beta A C_m \frac{d\phi_m}{dt} - \beta A F_v(q, v_m) - I_i, \tag{7.4}$$

$$M_e\phi_e = -\beta A C_m \frac{d\phi_m}{dt} + \beta A F_v(q, v_m) - I_e. \tag{7.5}$$

where $M_i$ and $M_e$ are the matrix approximations of the elliptical operators. Subscripts $i$ and $e$ denote the intracellular and extracellular space. $A$ is a term to scale the area or volume in the domain, $\phi_m$ is the transmembrane voltage, $q$ is a vector of state variables, $I$ is an external stimulus, and $t$ is time. $F_v$ and $F_q$

are the functions describing the membrane model. The time discretization was performed by a semi-implicit method, at time-step $t + h$, given by [170, 54, 156]:

$$\begin{bmatrix} K - \alpha M_i & -K \\ -K & K - \alpha M_e \end{bmatrix} \begin{bmatrix} v_i^{i+h} \\ v_e^{i+h} \end{bmatrix} = \begin{bmatrix} Kv_m^t + \beta A F_q(q^t, v_m^t) + \beta A I_i + (1-\alpha) M_i v_i^t \\ -Kv_m^t - \beta A F_q(q^t, v_m^t) + \beta A I_e + (1-\alpha) M_e v_e^t \end{bmatrix}. \tag{7.6}$$

where $K = \frac{\beta C_m A}{h}$. When $\alpha = 1$, the expression is the semi-implicit method, and when $\alpha = 1/2$ it becomes a Crank-Nicholson scheme. The time-stepper used in the forward solution was the Crank-Nicholson method. Depending on the complexity of the membrane model used, the time steps were set to 1 or 2 $\mu s$ [158]. The linear solver used was a Jacobi Preconditioned Conjugate Gradient algorithm, set to a tolerance of $10^{-6}$ to $10^{-3}$ mV. Simulations were performed on an SGI Altix 4700 supercomputer, with 128 Itanium2 1.6 GHz processors, and 320 GB of memory. Message Passing Interface (MPI) software was used to run the simulation in parallel. Normally 4 to 16 CPUs were used; the simulation run-time depended on the complexity of the model, whether it was for 2D or 3D tissue domains, and the duration of electrical activity simulated.

### 7.1.8 Bidomain Simulation Data

For the simulation output, extracellular potential at each node in the mesh was written out into a binary file. For nodes at the location of the measurement electrodes, extracellular potential was written to file in text format. For the analysis, binary data was used to display potential maps in SCIRun [161] or MAP3D [171]. Text output was used for plotting graphs in MATLAB, and as observations into the parameter estimation software (PEST) for the calculation of the bidomain conductivity parameters.

## 7.2 Inverse Method

The bidomain conductivity parameters were estimated by PEST (Parameter ESTimation) *Watermark Numerical Computing* [144]. This software determines the

parameters based on the mathematics described in Chapter 6. It is independent of the forward model, and so, it does not need to know how the bidomain equations are solved, just the potential values in the output file are required. PEST was setup to run CardioWave iteratively, as many times necessary, to build the sensitivity matrix, **J** (Jacobian). The derivatives in the Jacobian matrix were calculated from the differences in extracellular potential output from CardioWave, for given parameter increments. PEST adjusted the parameters in the model based on the calculated upgrade vector at each optimisation iteration, to reduce the objective function, **O**, such that the discrepancies between model and experimental data came to a minimum. The inverse techniques implemented in the PEST software are Least-squares and SVD (Singular Value Decomposition).

In this thesis, the depolarising elliptical wave was used as the tissue's response to measure the bidomain conductivity parameters. From this wave the local fibre direction could be obtained. Bidomain simulated extracellular potential distributions were fitted to experimental observations by PEST. A unique parameter set could be achieved since the features of the depolarising wave, such as the two positive maxima, the anisotropy and magnitudes depends greatly on the set of bidomain conductivities used; each producing a different pattern.

Any parameter in the forward model could either be held fixed or estimated; for example, the membrane capacitance, or the parameters within the membrane model could be estimated. However, the more parameters that are estimated, the harder the inversion becomes, and the greater the computational times required. There are a number of settings that can be initialised at the beginning of the parameter optimisation run, which can lead to different outcomes. For example, parameter change limits can be imposed; which is the amount a parameter is permitted to change in any one optimisation iteration. More information on the settings in PEST can be found in the Appendix G. The termination criteria of the parameter estimation process was on the basis of either:

1. For a number of optimisation iterations the following condition was met:

$$\frac{(\mathbf{O_i} - \mathbf{O_{min}})}{\mathbf{O_i}} \leq stop\_factor. \tag{7.7}$$

   where $\mathbf{O_i}$ being the objective function value at the end of the current optimisation iteration, and $\mathbf{O_{min}}$ being the lowest objective function calculated.

2. The number of optimisation runs had exceeded its limit and terminates, even though the objective function had not fully been reduced. A number of 30 to 40 optimisation runs was normally set.

3. The objective function had not been significantly reduced for a given number of optimisation runs (usually four).

The progress of the parameter estimation process was monitored by observing the changes in the objective function and parameters each optimisation iteration. PEST could be restarted if it had stopped prematurely. At the end of the run the results such as parameter estimates, standard deviations, and correlation were printed to file for analysis.

# Chapter 8

# Experimental Methods

## 8.1 Animal

Unipolar electrogram recordings were performed in vivo, on sheep, of Polwarth/Comeback cross breeds. All sheep were bred at the University of Tasmania's animal farm. Sheep were weighed to be between 30-50 Kg, and both genders were used.

## 8.2 Surgical Procedures

Experiments were performed as an open-chest preparation; surgical procedures were carry out similar to the experiments conducted by Li *et. al.* [172, 173, 174]. At the beginning of each experiment, the animals were weighed for calculating respiratory and anaesthesia requirements. Wool was shorn in the neck and chest area to make way for incisions. Anaesthesia was induced intravenously through the jugular vein, with sodium pentobarbital (30 mg/kg). With a syringe pump, the pentobarbital was continuously infused at a rate of 3-12 mg/kg/hr throughout the experiment, depending on sheep's weight, to achieve adequate anaesthesia. The dosage of pentobarbital was adjusted, judged by signs of eyelid reflexes and pedal reflexes. The animal was intubated and artificially ventilated at a rate of 12 breaths per min, with room air, using an Engstrom Erica respirator (Engstrom Medical, Sweden) at a tidal volume of 12-15 ml/kg. Once set, tidal volume and

respiratory were kept constant during each experiment. A left thoractomy was performed in the fourth and fifth intercostal space, and the heart was suspended in the pericardial cradle, giving access to the left side of the heart. Gauze material was placed over the chest opening, to prevent exposure to the air.

Carotid arterial pressure was measured by a 7F pigtail catheter (Tarcon NB® Advantage), introduced into the left carotid artery. When measuring the effects of ischaemia, the left circumflex (LCX) or the left anterior descending (LAD), depending on accessibility, were isolated proximally, to attach a Doppler Ultrasound Triton® flow transducer, for blood flow measurements. Then 10-20 mm distally from this, a hydraulic occluder was placed around the vessel, to induce coronary artery stenosis, or total occlusion.

## 8.3 Potential Recording

Extracellular potentials were recorded during normal heart activity. The propagation of the depolarising wave was initiated by pacing the epicardium, using the technique similar to other wavefront mapping experiments [11, 67, 12]. When pacing the epicardium, there is no early involvement of the purkinje fibre network, and activation propagates in all direction from the site of the pacing electrode [35]. The pacer used was a Medtronic® 5364 demand pulse generator (Medtronic Inc. Minneapolis, USA). It was set to a rate of 150 ppm (pulses per min), and the current output was adjusted to the lowest possible, to reduce the pacing spike artifact, but still achieving ventricular capture. The resting heart rate of the sheep was normally around 120 beats/min. With the pacer set at 150 ppm, the heart would be paced at this rate from the central stimulus. The negative lead of the pacer was positioned at the centre of the electrode array; acting as the pacing site, while the positive lead was position far away from the pacing site, on the heart, or on one of the animal's hind legs. By observing the pacing spike recorded on the electrograms, the current pulse peaked at about $2ms$, after the initial rise of the pulse.

Most potentials were recorded with reference to an electrode located subcutaneously on the animals leg. Different reference positions were tried; at the aortic root, and at the opening of the chest, and there was no significant difference in waveforms. Electrograms were taken at 2 kHz for half a second. With the pacer set at 150 ppm, two QRS waveforms could be sampled. Normally, samples were save to file when two waveforms were present, with the pacing spike at the beginning of the cycle. An example of the display for viewing the recorded electrograms is given in the appendix, Figure D.2.

### 8.3.1 Epicardial Electrode Array

Epicardial potentials were recorded by an array of 194 silver electrodes. It consisted of 15 rows and 13 columns of electrodes, and had dimensions of 17 mm wide and 24 mm long. This gave a spacing of 1.42 mm between the columns, and 1.71 mm between the rows. Figure 8.1 shows the electrode spacing width of the array. The electrode position at the middle of the array was allocated for the pacer. The electrode array was hand made, and was based on a technique by Macchi [175], who developed high-density precision electrode arrays, for in vivo epicardial mapping in rat hearts.

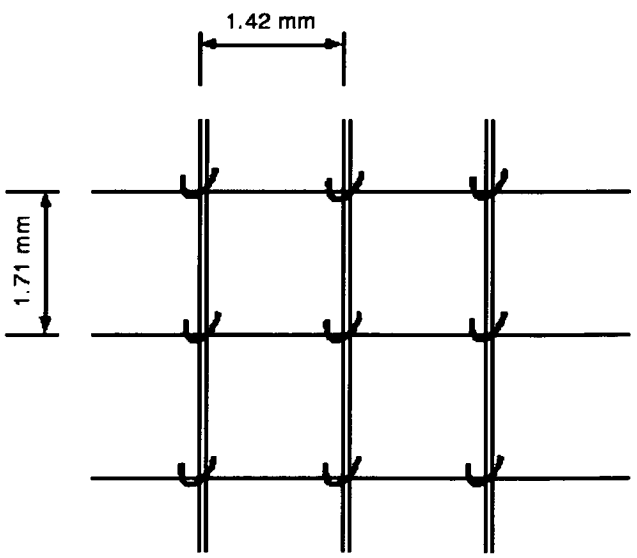


Figure 8.1: Electrode spacing. Silver wire was looped around the cross sections of the mesh.

The silver wire used had an outer diameter of 0.0059" ( 0.015 mm), which was insulated by polyimide. It was produced by the Californian Fine Wire Company. To keep the electrodes evenly spaced, phifertex material was used as the base; this fabric was obtained from a local yachting materials store. It is machine made, with a rectangular mesh, giving reliable spacing for the electrodes. The relative stiffness of the material kept the electrode spacing fixed, but was flexible enough to conform to the epicardial surface of the sheep's heart; as seen in Figure 8.4.

Each silver wire of the electrodes was tied at the cross sections of the fibres of the mesh. The wire around the knot was lubricated with Vaseline, and a pair of forceps was used to make the knot tight. The short end of the wire was twisted a few times to make the knot secure, and was cut flush. With the aid of a maggylamp and a scalpel, the insulation located at the loop of the knot was removed; this made the electrode contact surface. Figures 8.2 and 8.3 show both sides of the electrode array. The end of the silver wire was then soldered to a 37-pin connector, which could be plugged into ribbon cables, leading to the data recorder. Rubber hose was used at the ends of the connectors to secure the bundle of silver wires, to prevent them from pulling at the solder cups on the connectors.

The electrode array was superficially sutured to the epicardium to hold it in position, as shown in Figure 8.4, preventing it from dislodging from the motion of the beating heart, and to keep the orientation of array with respect to the fibre direction as consistent as possible between data samples. The pericardium was also used to secure the electrode array in place.

### 8.3.2 Needle Electrodes for Transmural Measurements

To measure the transmural extracellular potential, fibreglass plunge needle electrodes were used. The technique used to construct the electrodes was based on Rogers' technique [176]. These electrodes are much thinner than other needles, such as the ones used in Li's study [174], and therefore, can be packed in more denser arrays. The smaller diameter can minimise the disruption to the electrical

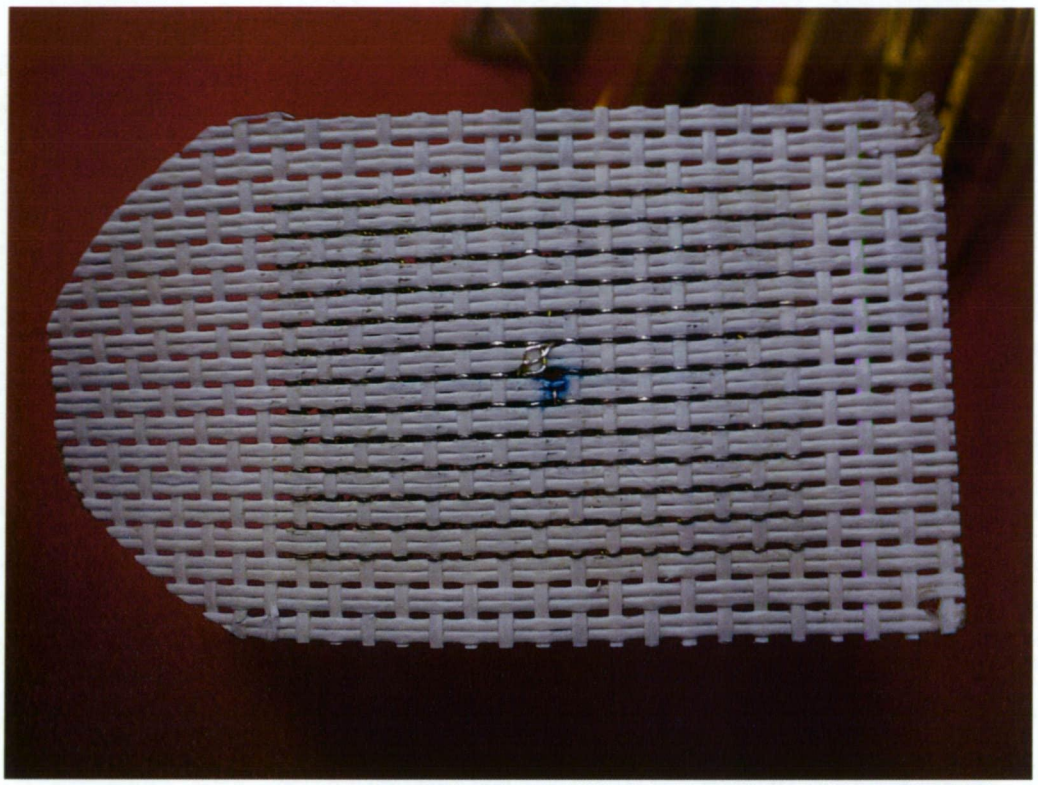

Figure 8.2: Electrode array surface to be in contact with the epicardium

patterns, when the electrodes are densely packed in an array [176]. Their smaller diameter also reduces injury, sustained when inserting them into the myocardium, and so, injury potentials are resolved more quickly.

The needles have 8 electrodes with 1 mm spacings, and are 0.5 mm in diameter; Figure 8.5 shows these dimensions. The electrodes are constructed from readily available materials, and no special equipment is required. They are fabricated from fibreglass reinforced epoxy, and are strong enough to easily insert into a beating heart. To make the needles, heat-shrink tubing was used as a mould, which had an inside diameter of 1.5 mm, and a shrink ratio of 1:3. Electrode sites were carefully marked on the tubing by pricking it with a fine needle, under a maggylamp. Silver wire of 0.075 mm, was threaded through a hypodermic needle, and this was used as a guide to insert into the tubing, through the marked electrode locations. After this, a few strands of fibreglass were then inserted into the tubing. Once they were in place, heat from the flame of a candle was used

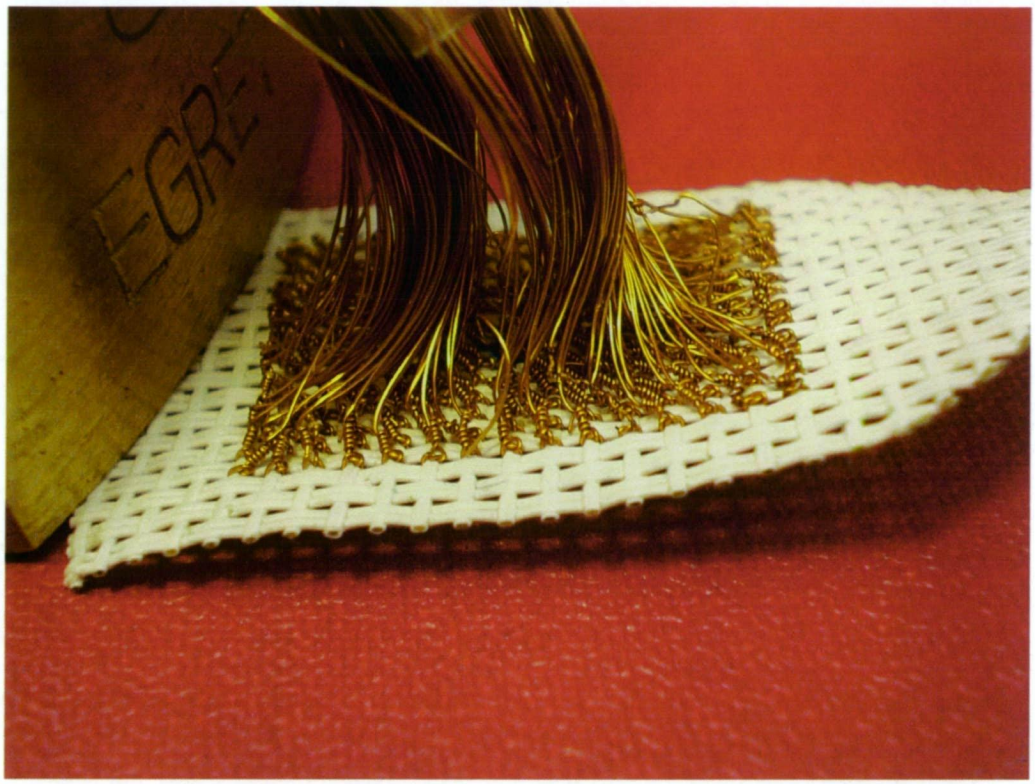

Figure 8.3: The back of the electrode array

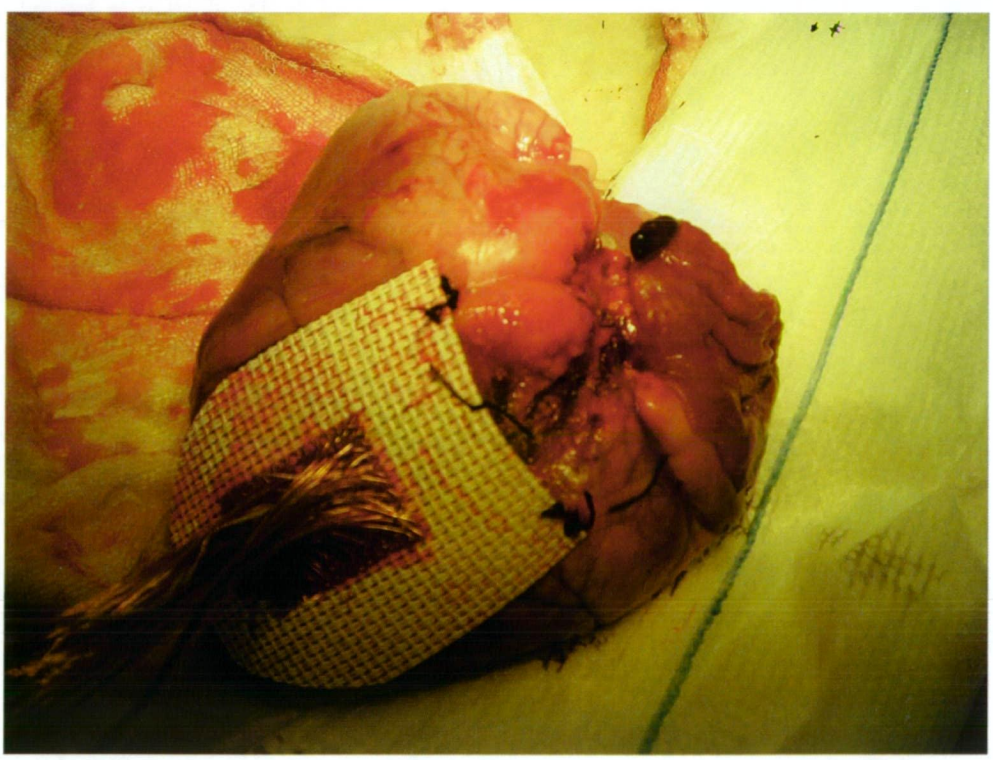

Figure 8.4: Epicardial electrode array fixed in position to left side of heart

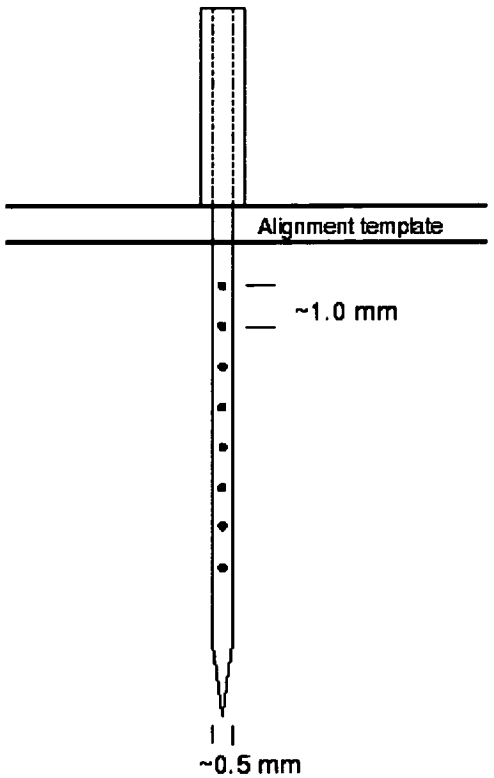


Figure 8.5: Fibreglass Plunge Needle Electrode

to shrink the tubing, giving a tight fit around the fibres and silver wires. Epoxy resin was then injected into the distal end of the mould; the syringe used in the injection was heated with warm water to lower the viscosity of the epoxy resin for easier injection. The moulds were then held fixed with aluminium blocks to keep them straight until the epoxy cured. After the epoxy had cured, the mould was removed and the end of the needle was sharpened with a scalpel. Tubing of about 1 cm from the proximal end was left untouched, partly for electrode reinforcement, and for ease of holding. The silver wires at the electrode positions were cut flush, and the wires coming out of the proximal end of the needle were soldered to connectors. Figures 8.6 and 8.7 show photographs of the finished fibre glass plunge needle electrodes. In order to have consistent separation between each needle electrode when inserting them into the myocardium, an alignment template was used, for placing them into an array. This technique had been used by Rogers, when making potential recordings in pig hearts, during fibrillation

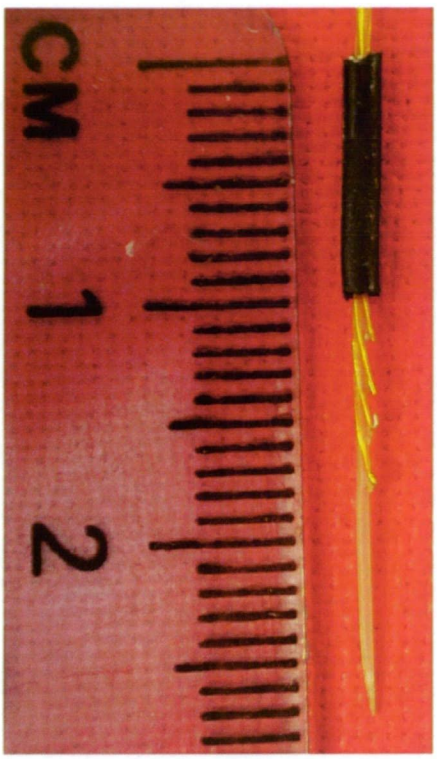


Figure 8.6: Fibreglass Plunge Needle, with four electrodes, approximately 2 *mm* apart.

[177]. The mesh material used for the template was the same phifertex material used for the electrode array. This was sutured to the epicardium to be held in place, while the needle electrodes where inserted into the myocardium. Similar to the electrode array, an electrode at the centre of the template was for the pacing stimulus.

When the needles were inserted into the myocardium, ST elevation was observed initially, but settled soon after. ST segment shift from the injury current settled down to normal activity within a period of 10-20 minutes following the plunge needles insertion.

### 8.3.3 Silver Chloriding Electrodes

The electrodes were silver chlorided to Ag/AgCl, to reduce the noise in the data. Silver chloriding the electrodes reduces their low-frequency impedance, and is commonly done to electrodes when making physiological measurements

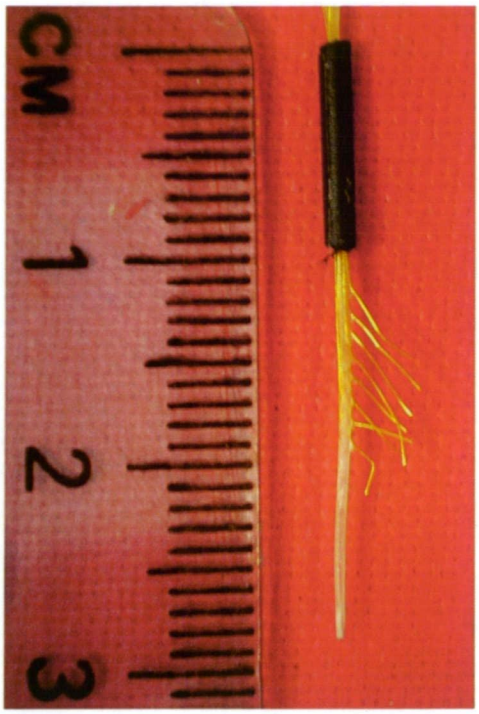


Figure 8.7: Fibreglass Plunge Needle, with 8 electrodes, approximately 1 *mm* apart. Ends of silver wires yet to be cut flush

[175, 176, 178, 179]. Electrolysis was used to silver chloride the electrodes. The technique can be easily fabricated [180]. The electrodes were immersed into a beaker of 9% saline (sodium chloride) solution, and current was passed through it. The electrodes served as the cathode, while a silver spoon, also immerse in the solution, acted as the anode. A battery was used to supply a current, which was controlled by a resistor in series, to provide the optimum current for the reaction. The optimum current was calculated based on a report by Geddes [181], to prevent over silver chloriding the electrodes, which could increase their impedance. A comparison between silver chlorided electrodes and non-silver chlorided electrodes was made for electrogram recordings, and there was improvement in noise reduction.

### 8.3.4 Recording System

The output of the recording electrodes were connected to the '256 Channel Switch and Signal Generator Unit'; made at the Central Science Laboratory, University of Tasmania [182]. The unit was designed to enable 256 electrodes to be switched through to a data acquisition system, or to have a stimulating waveform of constant voltage applied between different electrodes. It also has a calibration voltage signal to be supplied to the data logger. The intended use of the unit was to make measurements for the four-electrode technique [183, 184, 113, 185], but with a different approach to determining the bidomain conductivity parameters, the function of the unit was to supply the calibration signal, and for a junction between the electrodes and the multichannel data acquisition system.

The data acquisition system was a 256-channel system Binary Data Delivery Device (BDDD), suitable for high resolution electrocardiographic potential recordings [186]. It was controlled by a Field Programmable Gate Array (FPGA), a logic device, that has programmable amplifier gains and sampling rates. It has one analog-to-digital (A/D) converter, which provides 800 ns conversion time with 12 bits. Simultaneous sampling of 256 channels at 2 kHz per channel can be obtained from the device.

The data acquisition device was connected to a host computer; a SPARC Sun system, by the S11W, which is a 16 bit, parallel input output (I/O) interface for the SBus. Software on the computer allowed the user to selected the appropriate voltage gain, and take samples of the data. The electrocardiographic signals for all channels could be viewed; and individual channels could be selected for a larger display for closer inspection. The data was saved to file, which could be later used for analysis with software such as MATLAB.

## 8.4 Marking of Electrode Positions and Coronary Arteries

At the end of each experiment, the heart was carefully removed from the chest cavity. If measurements were made during ischaemia, the ischaemic tissue area was marked with dye. This was injected into either the LAD or LCX. The heart was then cut open and laid flat. Clear plastic wrapping was placed over the flattened heart, and the outline of the ventricles were traced. The coronary arteries, and the region of injected dye were marked. The position of the electrode array was marked, and the fibre direction seen by eye was noted. These markings were not used to produce potential maps as done by Li [174], but were used as references.

# Chapter 9

# Data Processing

In one experiment, there can be 10 to 50 samples of the 194 electrograms that are recorded to file. Processing the data had been semi-automated, which included the calibration and interpolation of electrode points. The data processing was semi-automated, since any channel that had substantial noise, or that did not pick up a waveform, was omitted manually. Electrograms for all channels were viewed for any inconsistencies at the start of the data processing. Fourier transforms of the noisy channels could be performed with a low bandpass filter to remove the noise, but this was not applied to the electrograms.

The baseline was chosen to be the potential at the moment just before the current pulse of the pacer, which had been chosen as the baseline in Roberts [11] study. This current pulse from the pacer showed up as a spike, recorded in the electrograms, and the beginning of this stimulus artifact was taken as the zero time reference for the start of stimulation, as defined in Kleber's study [187]. It was determined by calculating the rate of change of the potential; then choosing the time instant of the first greatest rate of change. Figure 9.1 shows an example recording for channel 1.

A text file of the samples was made with the calibration applied and the bad channels taken out. This text file had the potential for each channel printed in columns, with each row as successive time steps. The number of time steps was 1024, which were 0.5 ms apart. This file was used for the parameter estimation

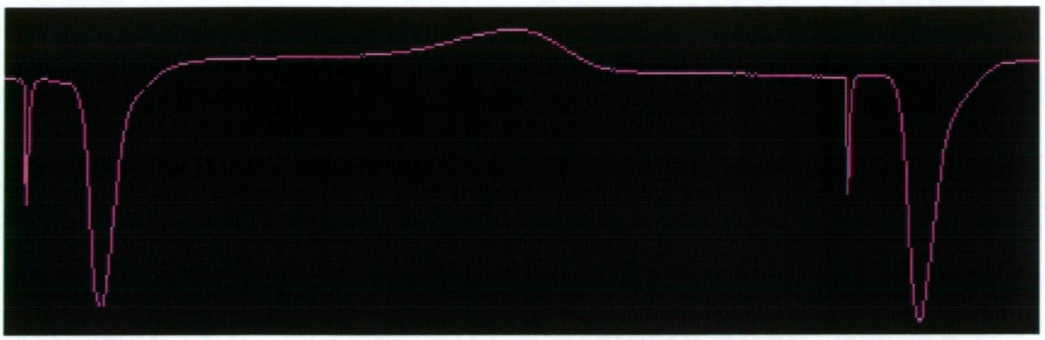

Figure 9.1: Electrogram recorded during pacing; for a length of 0.5 $s$. The first negative spike is the stimulus artifact, before the Q wave deflection. The onset of the pacing spike was used at the time of activation.

process.

## 9.1 Calibration

To calibrate the electrogram recordings, a sinusoidal waveform of 2 Hz, with a peak-to-peak voltage amplitude of 10 mV was used. This signal was generated by the 256 channel switch and generator unit. The calibration was applied to the recorded voltages; by scaling the signals to the correct magnitude. No calibration was applied to the frequency of the data recording, but it was ensured that the error would be negligible [186].

The calibration signal was supplied to the data acquisition system by the '256 Channel Switch and Signal Generator Unit', and a sample was taken. The saved data was converted into ASCII format to be loaded into MATLAB, where the data processing was carried out. A Fourier transform was applied to each of the recorded channels, with a low bandpass filter to remove the noise. Figure 9.2 shows the recorded calibration signal, for channel 1, with its Fourier transform.

For each channel, the peak-to-peak voltage was then determined by finding the minimum and maximum peaks of the Fourier transform signal. Then, with the known 10 mV signal, the electrograms were scaled:

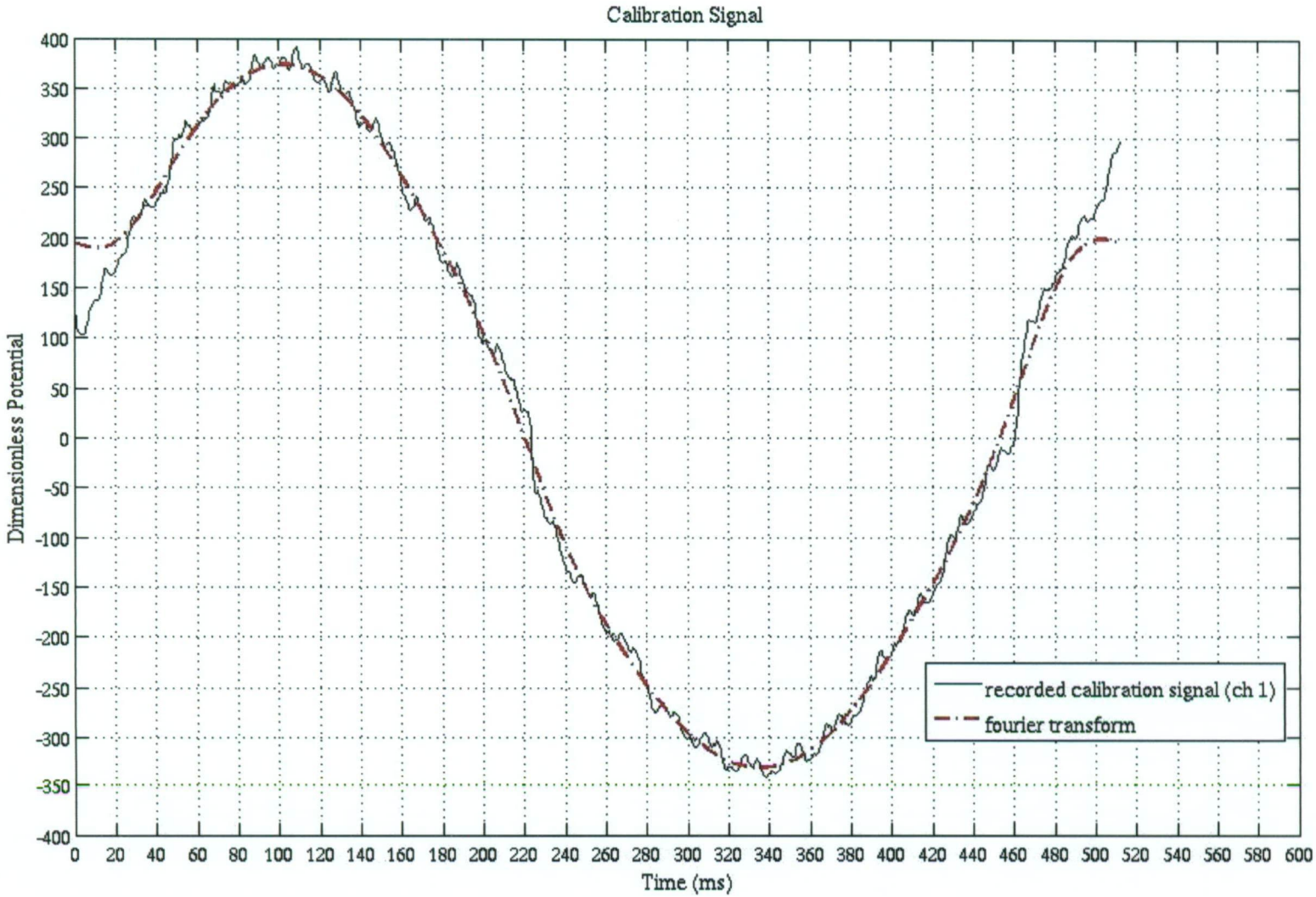


Figure 9.2: Sinusoidal calibration signal; recorded by channel 1, sampled for 500 ms. A Fourier transform was applied to remove the noise.

$$\text{calibration factor} = \frac{\text{recorded signal}}{\text{calibration signal}}. \tag{9.1}$$

The calibration factor was fairly consistent for the majority of the channels. There were a few channels where the calibration could not be calculated, due to problems with their gain, being fixed too high, such that the waveforms were cut off. This problem was a hardware issue related to the digital switches being unresponsive, and the few channels were omitted from the data.

## 9.2 Potential Maps

To present the data in a form which was easy to comprehend, potential maps were produced. An interpolation of the data at the electrodes was performed on a triangulated mesh, consisting of $51 \times 51$ nodes, about the size of the measured domain; that is, the area of the electrode array. The locations of the electrodes were easily obtained by the known spacing of the electrode array, or the spacing of the needle electrodes in the alignment template.

The interpolation scheme used was a method described by Oostendorp *et. al.* [188]. It has been tested by MacLeod *et. al.* [189], for interpolating body surface potentials, with acceptable results. It consists of two stages; the first involves describing the geometry of the mesh, that the data would be interpolated on; this requires the calculation of the Laplacian, the second spatial derivative, of the mesh. The second involves the mapping of each electrode location to the corresponding node in the mesh, and then the interpolation is performed.

The interpolation of the data was saved as MATLAB matrix files. These could be loaded into interactive visualisation software, such as MAP3D [171] and SCIRun [161], where colour coded potential maps with contours could be viewed. In the software, the electrograms could be stepped through the time-series, showing the changes in potential with time.

# Chapter 10

# Preliminary Results

In this chapter the parameter estimation method is tested with synthetic data, and experimental data from the literature. Firstly, 2D bidomain simulations for different sets of conductivities are presented to show the differences in potential distributions. The effect of transmural fibre rotation on the epicardial potentials is shown in Section 10.2. For the validation of the parameter estimation method in Section 10.3, synthetic data from a bidomain simulation for a known set of conductivities is used as observations in the parameter estimation. Other parameters are estimated, such as membrane capacitance and fibre angle. Contour plots of the objective function in parameter space are shown to observe its behaviour with respect to the conductivities. Experimental data from Roberts *et. al.* [11] and Baruffi *et. al.* [129] are used as observations into the parameter estimation; the results are presented in Section 10.4. CardioWave software was used for the bidomain simulations and PEST software was used to estimate the conductivity parameters; the general setup of these are described in Chapter 7.1.

## 10.1 Differences in conductivity values

The effect of different conductivity values on simulated potential distributions has been shown by Johnston and Kilpatrick [18, 190], when studying ST depression. To demonstrate the effect of conductivity on potential distributions during cardiac

activation from point stimulation, simulations were performed using the sets of conductivity values in Table 4.8. The general description of the bidomain setup can be found in Chapter 7.1, but the following describes the specific setup of the bidomain model used in this section.

### 10.1.1 Bidomain Model

#### Computational Mesh

The tissue domain for the simulations was an area of $1 \times 1\ cm^2$, with its triangular mesh consisting of $101 \times 101$ nodes. This resulted in 100 $\mu m$ separation between the nodes. The simple domain geometry was chosen to only demonstrate the effect of conductivity on potential distributions.

#### Fibre Direction

Fibre direction was set along the horizontal axes (x-axis). Since the domain was 2D, there was no transmural fibre rotation.

#### Membrane Model

The membrane model used was the Luo-Rudy model. It was chosen to produce realistic potential distributions.

#### Current Stimulus

To act as the pacing stimulus, current injection of opposite polarity was applied in both domains; with a magnitude of 1000 $\mu A cm^{-2}$ for intracellular and -1000 $\mu A cm^{-2}$ extracellular. The location of the stimulus site was at the centre of the domain, where the current was assigned to a group of four nodes. The duration of the current stimulus was 1 $ms$.

### Boundary Conditions

For the boundary conditions, the potential was grounded at a site in the domain to provide a reference. For the simulations here, a group of four nodes in the bottom left-hand side of the domain was assigned to zero.

### Solver and Time Integration

The time stepping method used to solve the time-dependent bidomain was the Crank-Nicholson scheme. The time step size was chosen to be 1 $\mu s$. 10 $ms$ of activation time was simulated. The linear solver used was a Jacobi Preconditioned Conjugate Gradient algorithm, set to a tolerance of $10^{-3}$ mV.

### Bidomain Model Output

The values of extracellular potential at each node in the computational mesh was written to binary file, every 0.1 $ms$, starting at $t$=0 $ms$ and finishing at $t$=10 $ms$. These data were used for producing potential maps. Extracellular potentials at the measurement electrode sites were written to file in ASCII format, every 1 $ms$, from $t$=0 $ms$ to $t$=10 $ms$. These data were used to plot electrograms.

## 10.1.2 Simulation Results for Different Conductivities

Figures 10.1 to 10.5 show the potential distributions at every 2 ms intervals, up to 10 ms, with Clerc's [10], Roberts(1979) [11], and Roberts(1982) [12] conductivity values. The simulations shows the excitation of the tissue, with the depolarising wave propagating from the middle stimulus electrode; travelling outward in all directions. The propagating wave of excitation is shaped elliptically, with its major axes aligned with the fibre direction, reflecting the anisotropy of the tissue. The outline of the wave is associated with crowded isopotential contour lines. Throughout the simulations, the elliptical wave has two maxima on each end, and although not as apparent, there are two minima in the inside region of the wave, at both ends. These features have been identified in simulation and

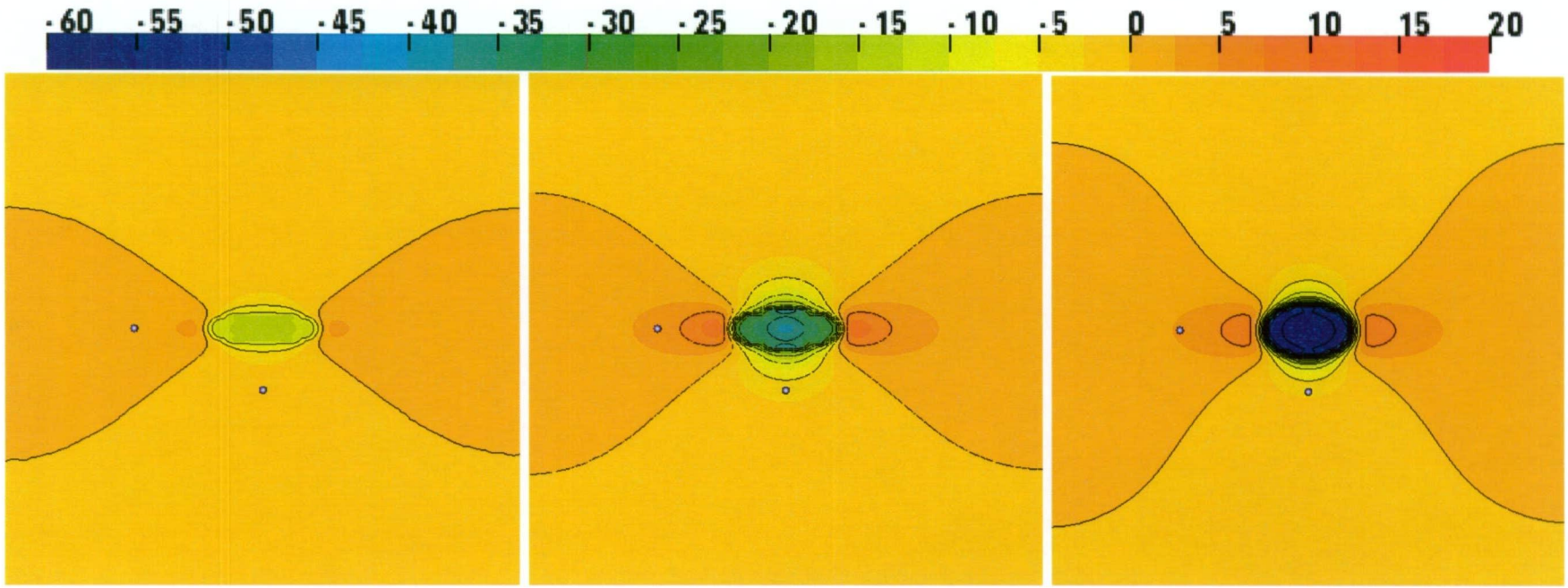


(a) (b) (c)

Figure 10.1: Bidomain simulations of excitation, initiation by a central stimulus, in an area of $1 \times 1$ cm$^2$ of tissue. Different conductivity values from Table 4.8 were used in the simulations; Clerc (a), Roberts(1979) (b), and Roberts(1982) (c), to demonstrate the differences in resulting potential distributions. Fibre direction was along the horizontal axes. Time after stimulation was at t=2 $ms$. The colour scale is in $mV$, and the isopotential spacing is 5 $mV$. The two dots in the potential maps indicate the sites of electrogram recordings, for along and across fibres.

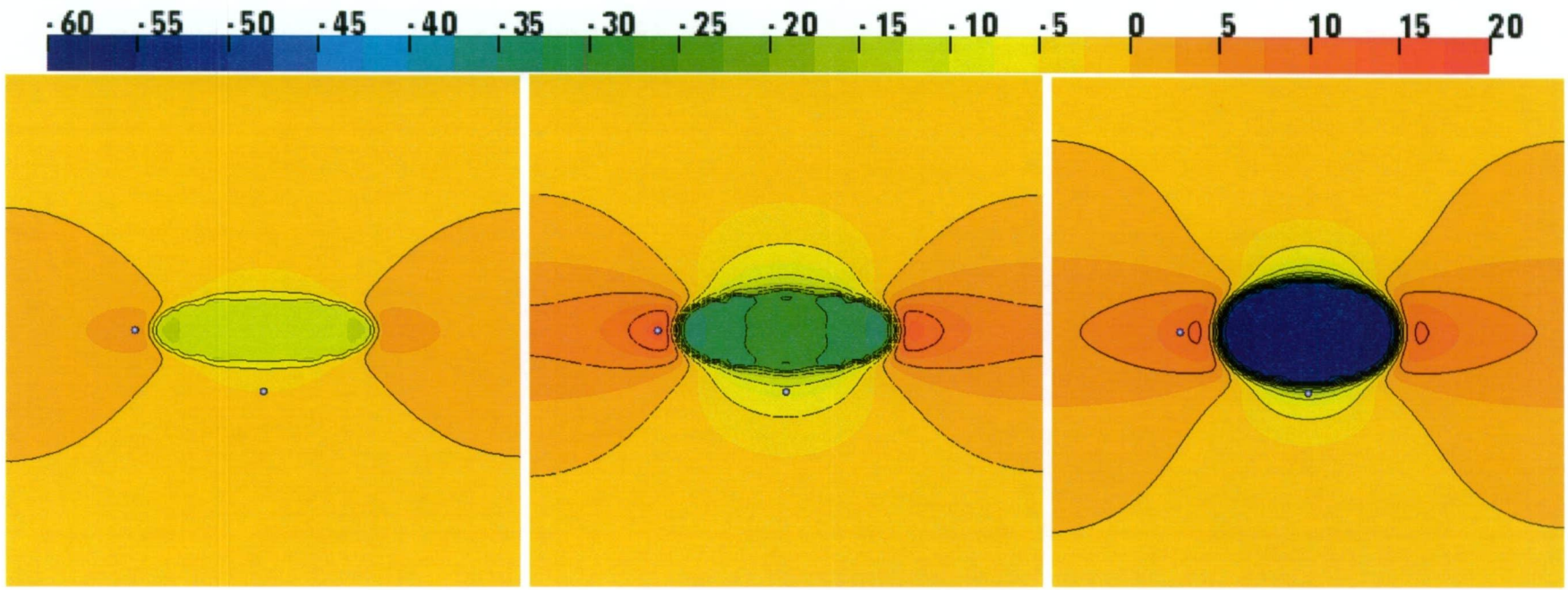


(a) (b) (c)

Figure 10.2: Bidomain simulations of excitation, at t=4 *ms*.

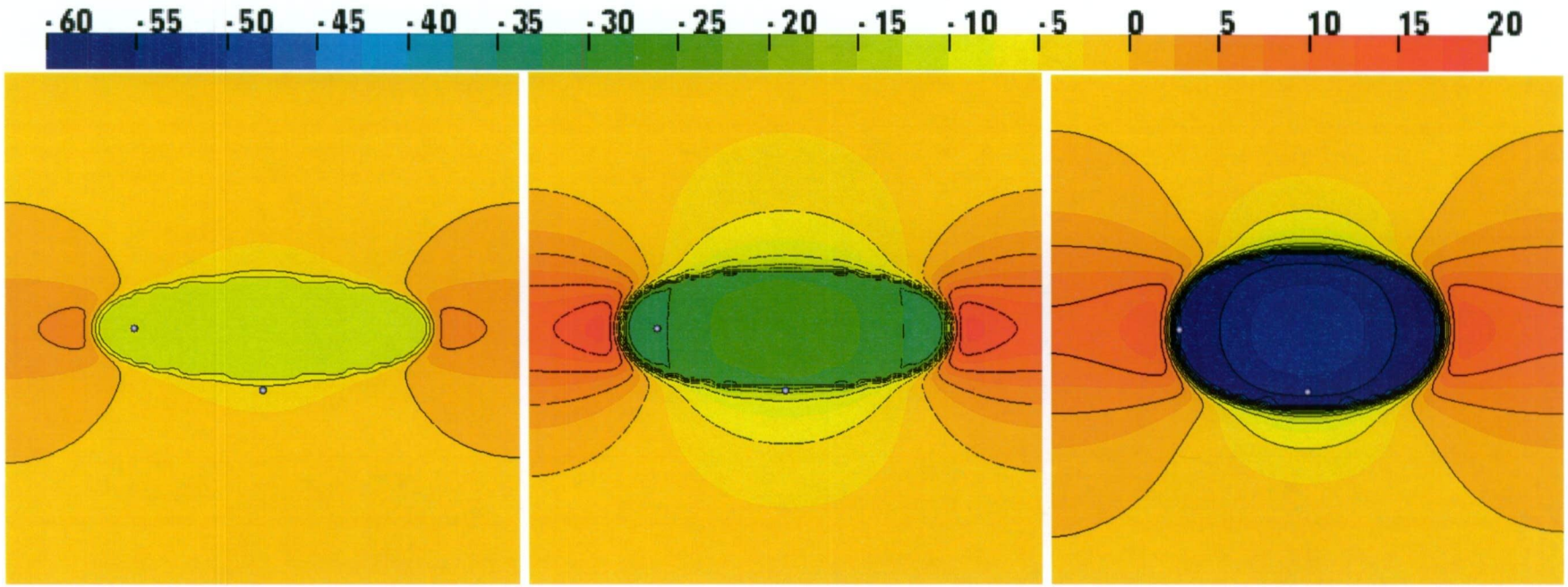


(a) (b) (c)

Figure 10.3: Bidomain simulations of excitation, at t=6 $ms$.

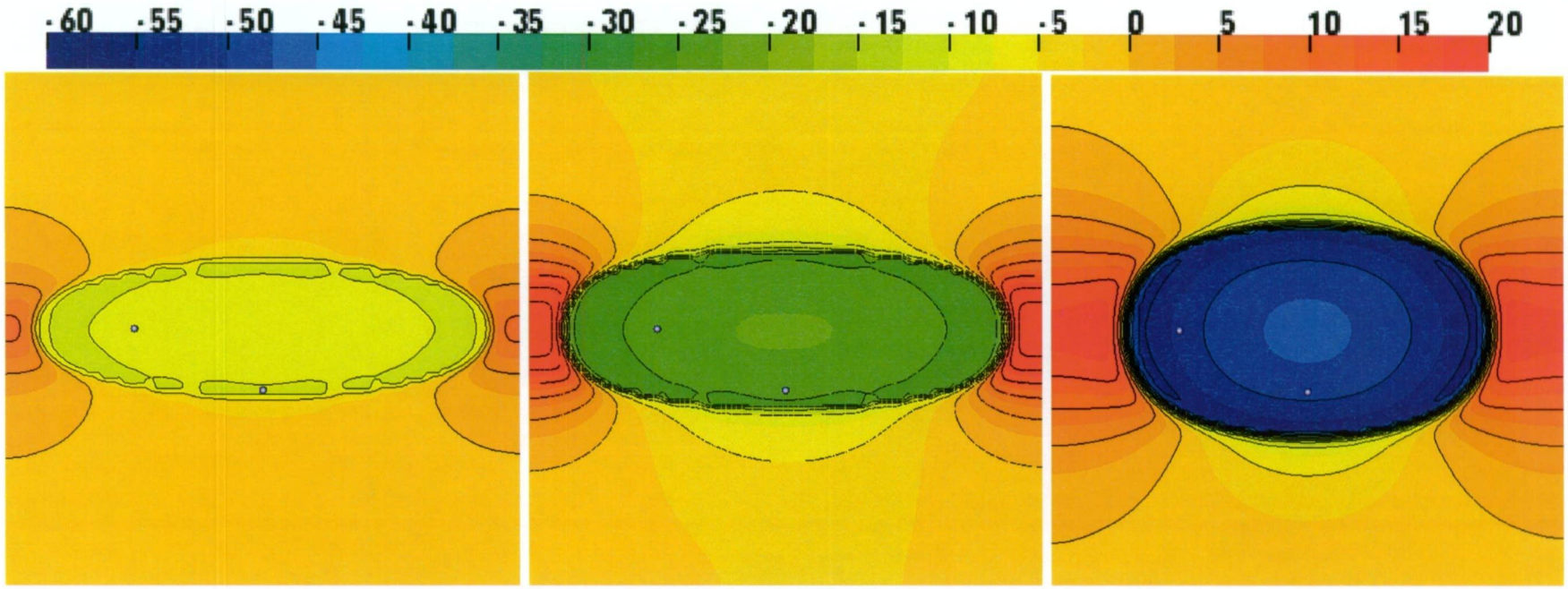


(a) (b) (c)

Figure 10.4: Bidomain simulations of excitation, at t=8 $ms$.

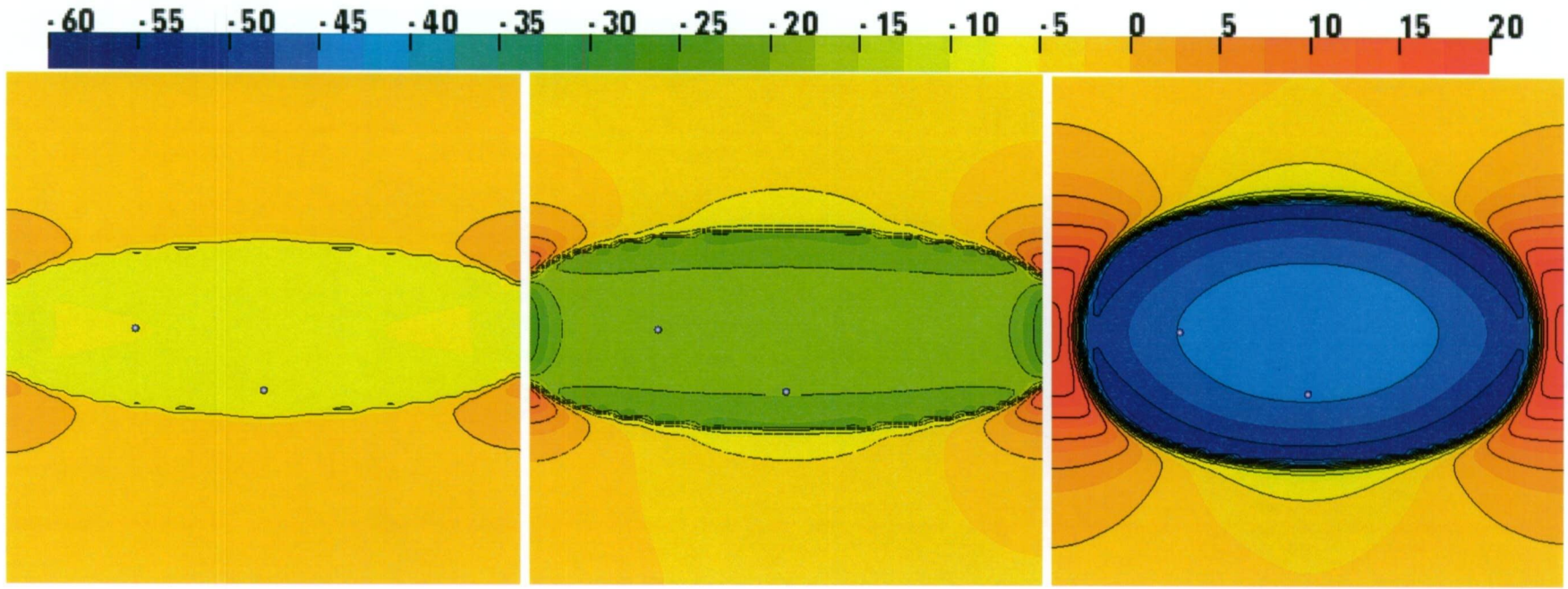


(a) (b) (c)

Figure 10.5: Bidomain simulations of excitation, at t=10 $ms$.

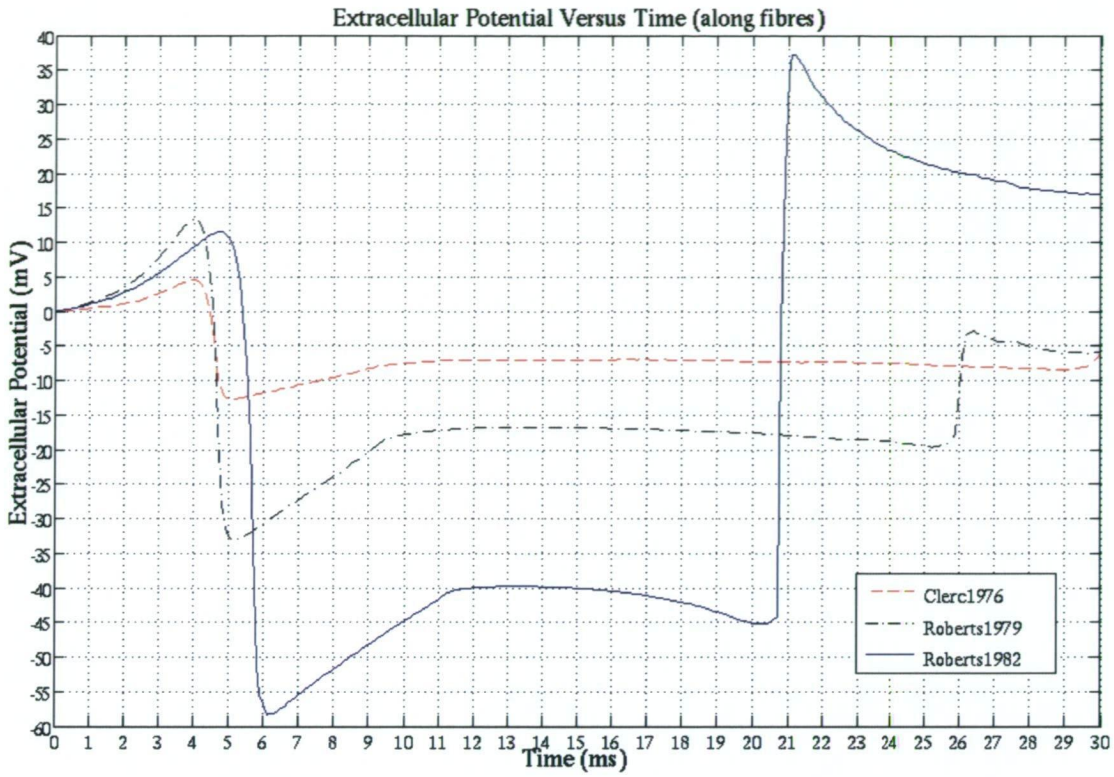


(a)

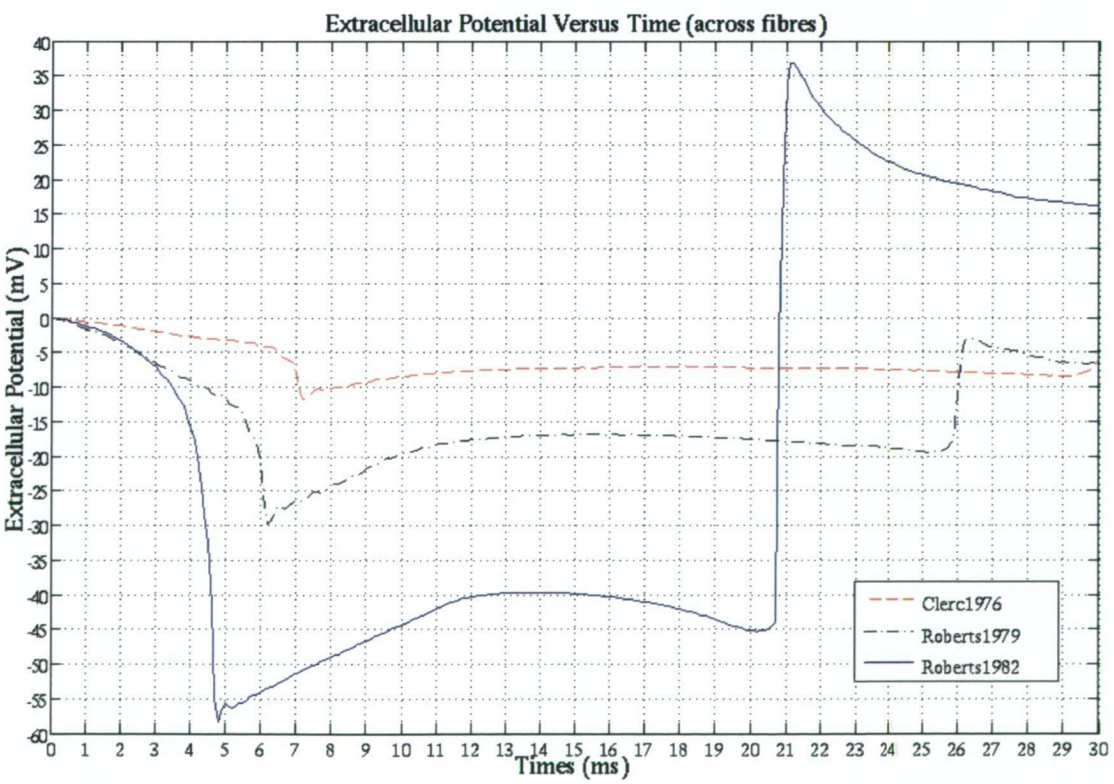


(b)

Figure 10.6: Plot of extracellular potential versus time, for the simulations using different conductivity values. The potential was taken at sites in the tissue marked by the two dots in Figures 10.1 to 10.5, for along and across the fibre direction.

experimental studies [67, 127, 117].

The differences in the potential distributions from the different conductivity values can be recognised by these key features in the depolarising wave. Firstly, the propagating wave is shaped differently between the three simulations; noticeably, Roberts(1982) values produces a wave that is more rounded, with Clerc's being the most elongated; the different anisotropies are clearly responsible for these differences. When comparing the magnitudes in the region inside the wave, each simulation was different; with Clerc's being the lowest and Roberts(1982) being the highest. There are also differences in the size and magnitudes of the two maxima at each end of the ellipse as well; with Roberts(1979) simulation having the highest magnitude, and Roberts(1982) simulation having the larger sized ones. When observing the isopotential lines, larger potential gradients occur in Roberts(1982) simulation, with more crowding at the wavefront of activation. Variations in the features such as the minima and maxima are enhanced with the isopotential lines. Differences can also be seen in studying the electrograms; by plotting a graph of extracellular potential versus time. Figure 10.6 shows electrograms from two sites in the domain, located along and across the tissue fibre direction, marked by the two dots in Figures 10.1 to 10.5. The behaviour of the potential with time can be observed. In the fibre direction in Figure 10.6(a), the initial rise in potential is associated with R waves. These R waves correspond to the passing of the maxima of the ellipse. In the across fibre direction in Figure 10.6(b), no initial R waves are present, but instead, initial Q waves occur. It can be seen that the different conductivity values have an affect on these electrogram characteristics.

The only changes in the simulation parameters was the conductivity values, resulting in marked differences in potential distributions, which has been encountered by Johnston and Kilpatrick [18, 190]. The variations are difficult to explain, since the effect of changing the combination of the parameters is not easy to interpret. Though the main point is, that the different anisotropies produce significant variations in the features of the potential distributions, and these features can be

taken into consideration when matching simulated data with experimental data.

## 10.2 Three-Dimensional Simulation of Epicardial Stimulation

In this section three-dimensional simulations of excitation from epicardial point stimulation were investigated. The purpose of the study is not directly related to the validation of the parameter estimation method, but to show the influence of the transmural fibre rotation on epicardial potential distributions. The simulation results are used as a reference for a source of model to experimental observation miss-match and the issue of orthotropic transverse conductivity, later discussed in Chapter 13.

### 10.2.1 Bidomain Model

#### Computational Mesh

The tissue domain was represented by a slab of $2\times2\times0.97\ cm^3$, consisting of a $60\times60\times60$ node hexahedral mesh. Ideally the mesh spacing would have a node spacing of 100 $\mu m$, but due to computer memory constraints for building the stiffness matrices, the node spacing was restricted to 333 $\mu m$. This mesh resolution still gave reasonable results, for the purpose of showing the effect of transmural fibre rotation on epicardial potential distributions.

#### Fibre Direction

The total rotation of fibres from epicardium to endocardium was 180°, starting at 30° with respect to the x-axis on top of the tissue slab (epicardium).

#### Membrane Model

The Beeler-Reuter [53] membrane model was used. This model was chosen as an alternative to the Luo-Rudy membrane model.

### Current Stimulus

To act as the pacing stimulus, current injection of opposite polarity was applied in both domains; with a magnitude of 1000 $\mu Acm^{-2}$ for intracellular and -1000 $\mu Acm^{-2}$ extracellular. The location of the stimulus site was on top of the slab, at the centre, where the current was assigned to a group of eight nodes. The duration of the current stimulus was 1 $ms$.

### Boundary Conditions

For the boundary conditions, the potential was grounded at a site in the domain to provide a reference. For the simulation here, a group of eight nodes in the bottom left-hand side of the slab was assigned to zero.

### Solver and Time Integration

The time stepping method used to solve the time-dependent bidomain was the Crank-Nicholson scheme. The time step size was chosen to be 1 $\mu s$. 30 $ms$ of activation time was simulated. The linear solver used was a Jacobi Preconditioned Conjugate Gradient algorithm, set to a tolerance of $10^{-3}$ mV.

### Bidomain Model Output

The values of extracellular potential at each node in the computational mesh was written to binary file, every 1 $ms$, starting at $t$=0 $ms$ and finishing at $t$=30 $ms$. These data were used for producing potential maps.

## 10.2.2 Simulation Results for Epicardial Stimulation

Figure 10.7 shows the extracellular potential 15 $ms$ after point stimulation; isopotential surfaces and current vectors are displayed. The activating wavefront propagates from the central stimulus location, in all possible directions, and gives an appearance of half an ellipsoid in three-dimensional space, with its major axis oriented along the fibre direction. The wavefront travels the same distance into

the depth of the tissue as across the epicardial surface in the transverse direction, since the conductivity has been assigned the same values. The flow of extracellular currents can be observed to emanate from the two potential maxima, and travel outwards from the wave, then travel back towards the negative depolarised region, where the the two negative potential minima reside, analog's to Figure 5.1.

Figures 10.8 and 10.9 show slices through the epicardial plane (z-plane), showing the effect of fibre rotation with depth on potentials. The cross-sectional planes begin at the surface of the tissue domain (Figure 10.8(a)), and are sectioned for every 1 *mm* of depth. Asymmetry in the two positive maxima can be observed by their gradual counter-clock-wise rotation about the centre; this can be easily seen in Figure 10.9(a), at a depth of 2 *mm*. It can been seen in 10.8(a) that the fibre direction on the surface does not exactly align with the major axis of the ellipse, as well as not being directly aligned through the two maxima, which is due to the fibre rotation [127]. The major axis appears to be ahead of the local fibre direction of around 4°. This has also been observed in other investigators simulations [127, 117, 191]. Figure 10.8(b) shows the z-plane at 1 *mm* from the surface; here the major axis of the ellipse is lagging the local fibre direction, at approximately 5°. The two maxima are also just starting to deviate from the major axis in the counter-clock-wise direction, as well as the two minima. In Figure 10.9(a) at 2 *mm* depth, the maxima and minima are rotated further more, and no longer coincide with the major axis of the ellipse, becoming more distorted from the ones observed on the surface. The major axis lags even more from the local fibre direction, suggesting that the rotational effect on the wave becomes attenuated with depth. Figure 10.9(b) at 3 mm depth shows that this region is located just outside the wavefront.

From these simulation results, the fibre rotation has a significant effect on the transmural potential distributions. Even on the potentials on the epicardial surface, the fibre rotation has an effect.

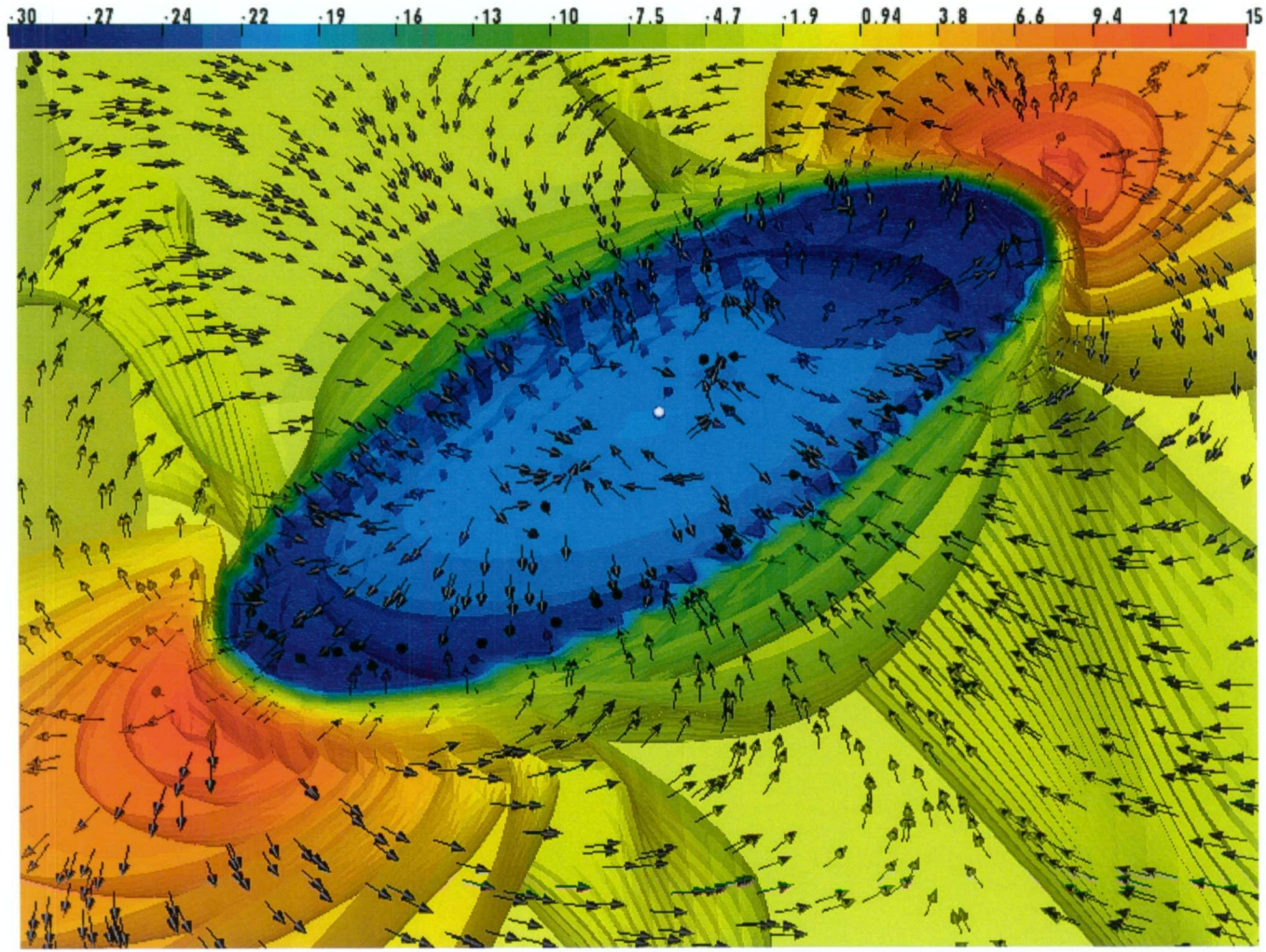


Figure 10.7: Close up view of simulated potentials over looking the surface of the tissue block, with extracellular isopotential surfaces and current vectors. Positive isopotentials are at every 1 $mV$ increments, and negative isopotentials are at every -1 $mV$ up until -5 $mV$, then -5 $mv$ increments after that. Colour bar in $mV$.

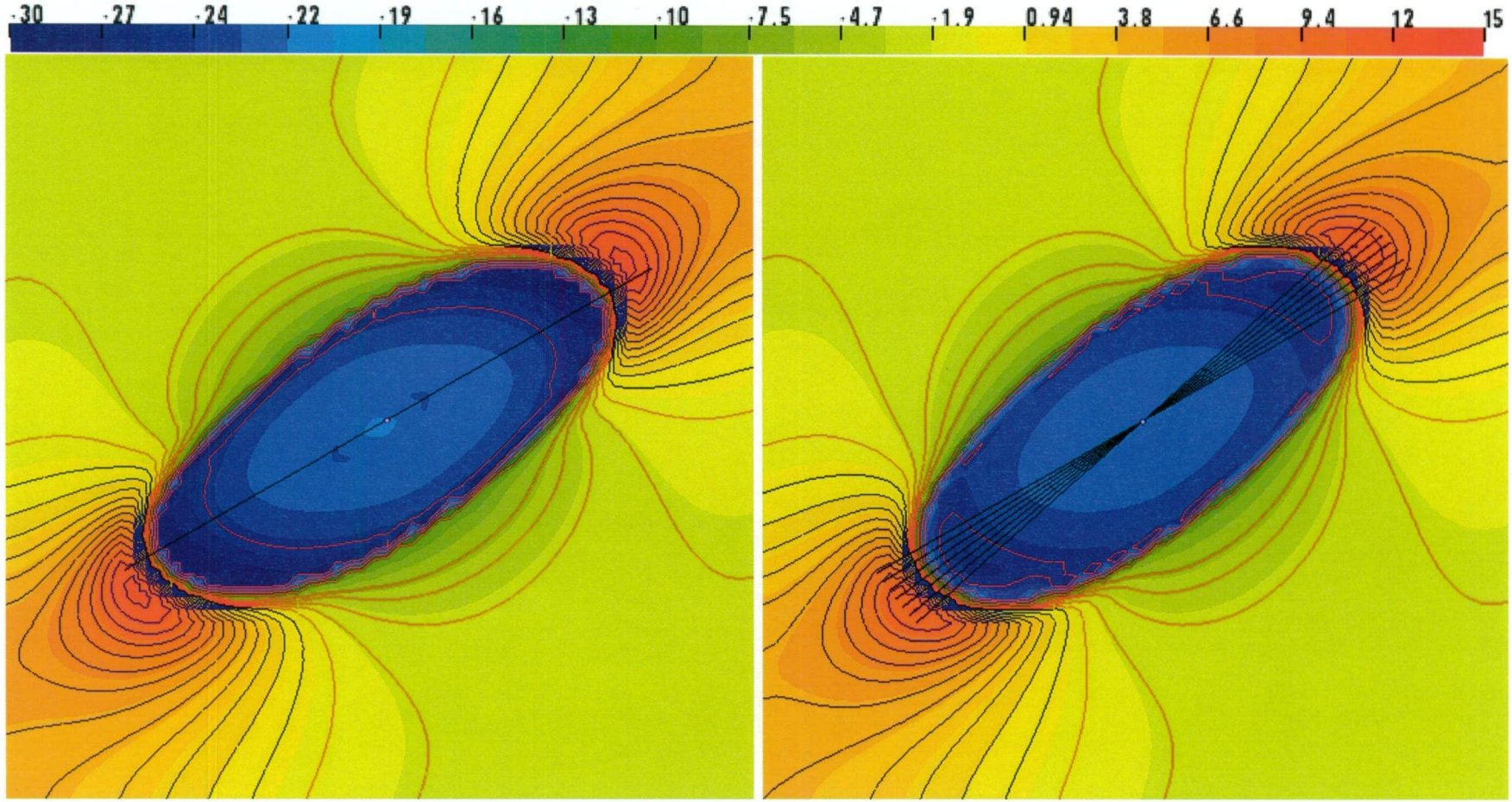


(a) epicardial surface

(b) 1.0 mm depth

Figure 10.8: Influence of transmural fibre rotation on potential distribution. Black straight lines about the centre of the ellipse, at the stimulus site indicates the variation in transmural rotation of the fibres at 2° intervals. Positive isopotentials are represented by blue lines, with 1 $mV$ increments, negative isopotentials are red lines, with -1 $mV$ increments up until -5 $mV$, then -5 $mV$ increments after that. The zero isopotential line is represented by the curved black line.

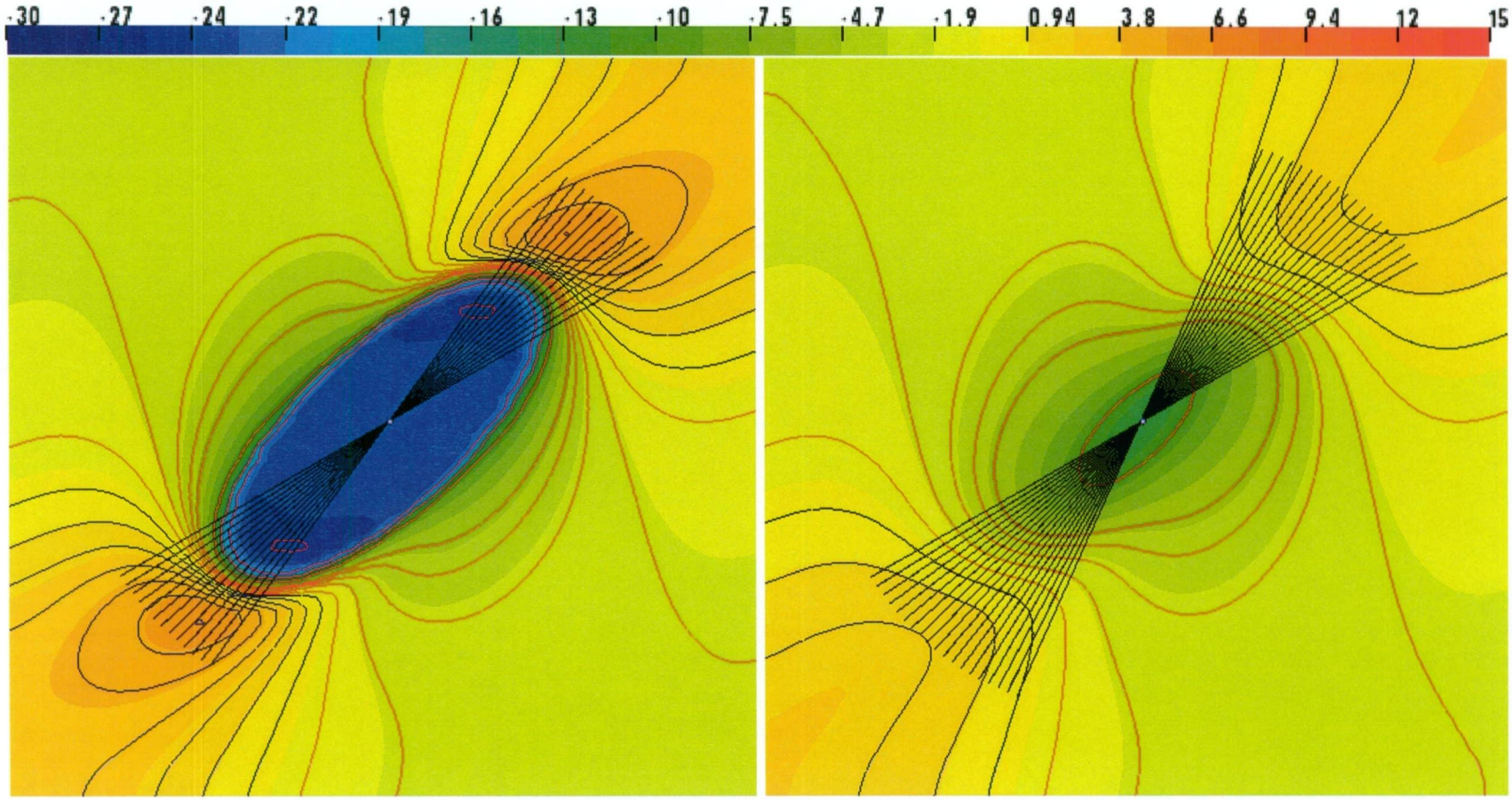


(a) 2.0 mm depth

(b) 3.0 mm depth

Figure 10.9: Influence of transmural fibre rotation on potential distribution.

## 10.3 Inversion from Synthetic Data

This section presents a study on the validation of the parameter estimation method. Before the parameter values calculated from the inversion method can be trusted, one should test it with synthetic data produced from a bidomain simulation with known conductivity parameter values. The inversion method can be tested to see how well the conductivity parameters are calculated back. It can be further tested with artificial random noise added into these data. The synthetic data used was the extracellular potential distributions, measured at the recording electrodes. The extracellular potential distributions were produce from a 2D bidomain simulation for activation initiated by point stimulation. The activation phenomena was simulated to replicate the spread of activation that is measured in experiments [11]. The recording electrode locations were arranged into an array over the tissue domain. The array consisted of 6×12 electrodes, with spacings of 1.5 $mm$. The central electrode acted as the pacing site. The electrode array points are shown in Figure 10.10.

### 10.3.1 Bidomain Model

#### Computational Mesh

The tissue area was 1.2×1.9 $cm^2$. This provided a 1.5 $mm$ overhang from the edge of the electrode array on all sides. The triangular mesh had 121×191 nodes, therefore the node spacing was 100 $\mu m$. The dimensions of the tissue domain was chosen to suite the tissue area that was measured by the electrode array used in Roberts *et. al.* experiment [11]. The same mesh is used later for the estimation of the bidomain conductivities from Roberts *et. al.* experimental data.

#### Fibre Direction

The fibre angle was set to 121° from the horizontal.

### Current Stimulus

To act as the pacing stimulus, current injection of opposite polarity was applied in both domains; with a magnitude of 1000 $\mu Acm^{-2}$ for intracellular and -1000 $\mu Acm^{-2}$ extracellular. The location of the stimulus site was at the centre of the domain, where the current was assigned to a group of four nodes. The duration of the current stimulus was 1 $ms$.

### Boundary Conditions

For the boundary conditions, the potential was grounded at a site in the domain to provide a reference. For the simulation here, a group of four nodes in the bottom left-hand side of the domain was assigned to zero.

### Solver and Time Integration

The time stepping method used to solve the time-dependent bidomain was the Crank-Nicholson scheme. The time step size was chosen to be 1 $\mu s$. Simulation of activation was for a duration of 10 $ms$. The linear solver used was a Jacobi Preconditioned Conjugate Gradient algorithm, set to a tolerance of $10^{-4}$ mV. The solver tolerance was more lower than what was set in the previous simulations. This was to calculate accurate derivatives for the construction of the Jacobian matrix in the parameter estimation.

### Bidomain Model Output

The values of extracellular potential at each node in the computational mesh was written to binary file, every 0.1 $ms$, starting at $t$=0 $ms$ and finishing at $t$=10 $ms$. These data were used for producing potential maps. Extracellular potentials at the measurement electrode sites were written to file in ASCII format, every 1 $ms$, from $t$=0 $ms$ to $t$=10 $ms$. These data were used as synthetic data into the parameter estimation software, and as model observations for calculating the derivatives for the construction of the Jacobian matrix.

### 10.3.2 Data Used in Parameter Estimation

In this validation, the conductivity parameters chosen was the set measured by Roberts 1979 experiment [11], shown in Table 4.8. The noise introduced into the synthetic data was generated from a Gaussian distribution, with a zero mean, and its standard deviation calculated by the following expression [147]:

$$b = (\sqrt{2}/2)u_{max}p. \tag{10.1}$$

where $u_{max}$ is the absolute maximum potential in the model output, taken from the sites of the measurement electrodes, and $p$ is the percentage of noise contamination; for example, $p = 0.05$ gives 5% noise level. The percentage of noise introduced into the data was 5%, 10% and 15%. To gauge how much noise this was, Figure 10.10 shows the potential map of the synthetic data with and without noise. Similarly, an electrogram located at a site somewhere in the region along the major axis of the depolarising wave, is shown in Figure 10.11, with different amounts of noise in its data points. The observations put into the PEST software was the extracellular potential values at the electrode recording sites. The frequency of the data used was at every 1 $ms$, for a duration of 10 $ms$, from the start of activation. The values were written to file from a bidomain simulation, noise was added, and then read by PEST.

### 10.3.3 Parameter Estimation

The conductivity values were set to a value of 1 $mScm^{-1}$, as initial values for the parameter estimation runs. Both Least-Squares and SVD methods were used in the validation. The mathematics of the methods are discussed in Chapter 6; use of the software is mentioned in Section 7.2. The observations used in the parameter estimation was discussed above.

### 10.3.4 Results of Parameter Estimation Validation

Table 10.1 shows the estimated conductivity values using two techniques; Least-Squares (LS), and Singular Value Decomposition (SVD), for a certain level of

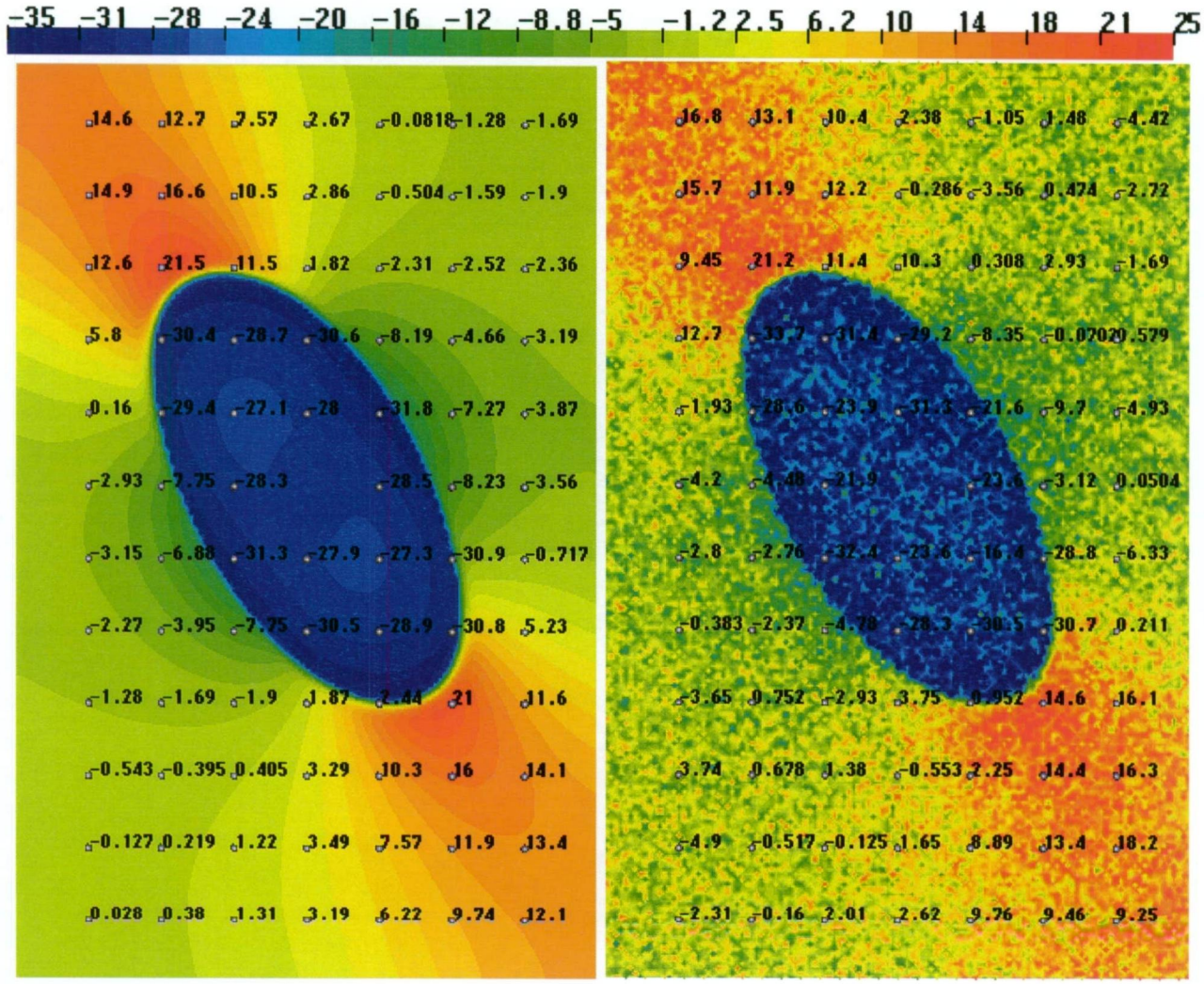


(a) 0% noise

(b) 15% noise

Figure 10.10: Synthetic data, shown without, and with 15 % random noise. Potential map shows activation at 10 $ms$ after stimulation. Fibre direction is at 121° from the horizontal. Electrode recording points are shown with corresponding extracellular potential values ($mV$). The values at the electrode sites were used as observations in the parameter estimation; at a frequency of 1 $kHz$, for a duration of 10 $ms$, from the start of activation.

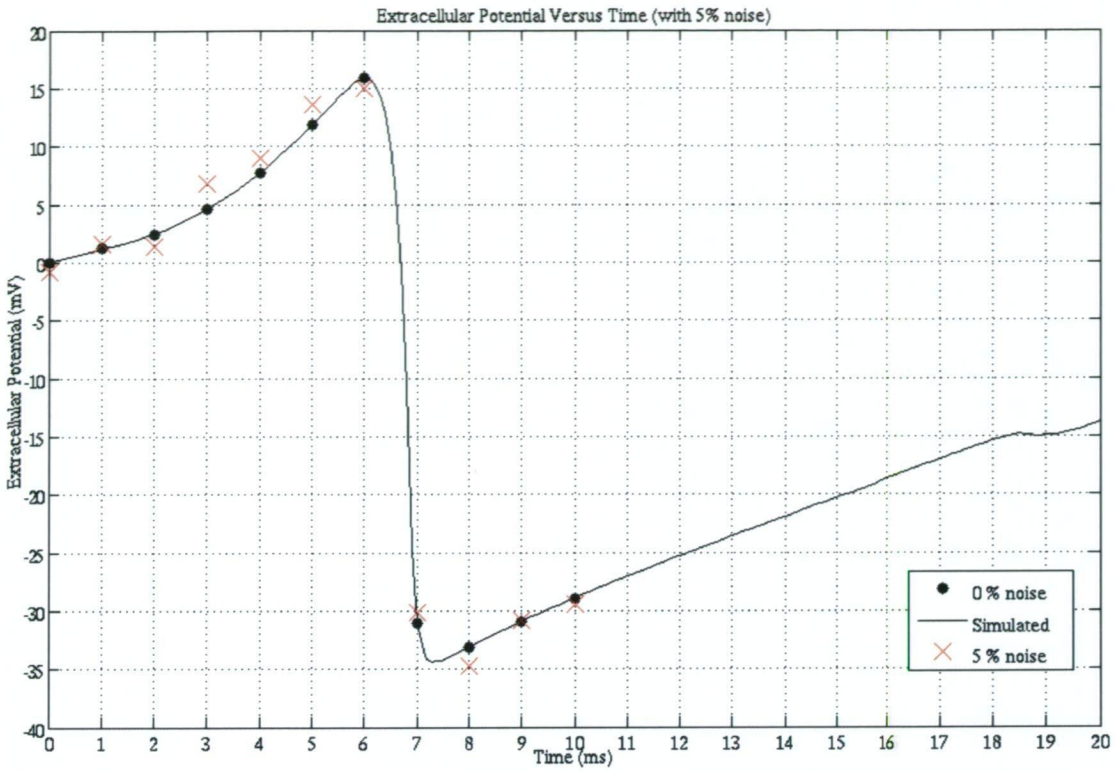


(a) 5% noise

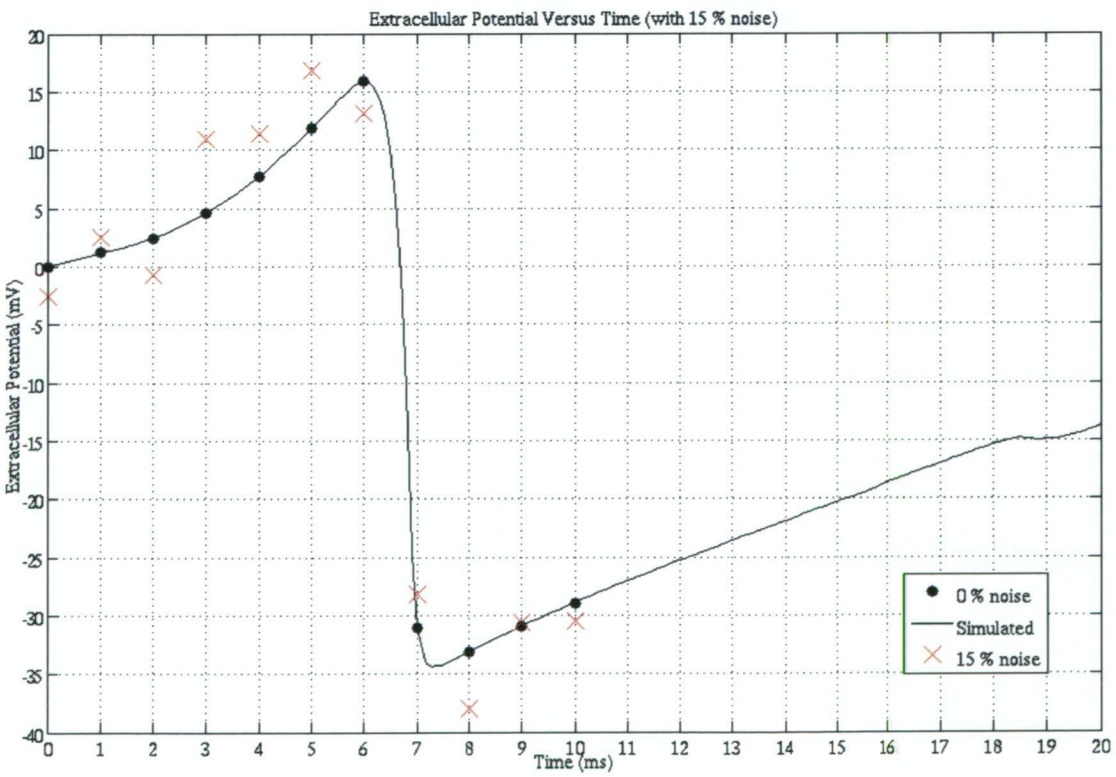


(b) 15% noise

Figure 10.11: Synthetic data; an electrogram recorded at a site in the domain along the fibre direction. Frequency of data points made at 1 $kHz$. Electrograms show data points with a percentage of random noise added.

noise added into the synthetic data. Statistical values such as the sum of squared weighted residuals (objective function) $\Phi$, the correlation coefficient $r$, number of optimisation iterations, and the number of forward model calls made during the estimation process, are also presented. Standard deviations were taken from the parameter covariance matrix, calculated from Equation (6.25). The third and fourth columns of Table 10.1 shows the estimated parameters, using the synthetic data with 0 % noise; both LS and SVD methods retrieved the values back successfully. As expected, the increase in noise level, 5%, 10%, and 15%, increases the uncertainty in the estimated parameters; for example, increases in standard deviations, increases in residuals, and lower correlation values. However, for all noise levels up to 15 %, the parameters were retrieved back to reasonable values. Even at 20 % noise, the parameters that were calculated back were reasonable (not included in Table 10.1). Both methods, LS and SVD, recovered the parameter values with the same accuracy; though, as the noise levels increased, it took SVD less model calls than LS, hence, less run time. This depends on a number of factors, such as, how soon the estimation process goes into central derivatives calculation, which takes twice as many model runs; usually when the optimisation function has not been reduced significantly between optimsation iterations. Also, in the LS method, there may be extra model runs to try out different Marquardt parameter values, in order to lower the objective function.

To observe the objective function's dependence on the conductivity values, Figure 10.12 shows a surface plot of it in parameter space. The plot is for the variation in intracellular conductivity parameters, for longitudinal and transverse directions, whilst holding the extracellular conductivity parameters fixed. The contours show equal objective function values. The goal is the objective function minimum, at values $\sigma_{il} = 2.8$ and $\sigma_{it} = 0.26\ mSCm^{-1}$, which is located in a valley. Changes in $\sigma_{il}$ for either lower or higher values results in moving away from this minimum; in the uphill direction. Changes in $\sigma_{et}$ results in moving through the valley, but still goes up hill in either direction. The crosses connected by the red line marks each optimisation iteration, for its objective function value.

Table 10.1: Estimated conductivities from synthetic data with added noise (mS/cm).

| Symbol | Orig. | LS 0% | SVD 0% | LS 5% | SVD 5% | LS 10% | SVD 10% | LS 15% | SVD 15% |
|---|---|---|---|---|---|---|---|---|---|
| $\sigma_{il}$ | 2.800 | 2.799 | 2.800 | 2.801 $\pm$ 0.178 | 2.800 $\pm$ 0.017 | 2.793 $\pm$ 0.038 | 2.795 $\pm$ 0.038 | 2.788 $\pm$ 0.056 | 2.785 $\pm$ 0.056 |
| $\sigma_{it}$ | 0.260 | 0.260 | 0.260 | 0.264 $\pm$ 0.003 | 0.264 $\pm$ 0.003 | 0.257 $\pm$ 0.007 | 0.256 $\pm$ 0.006 | 0.255 $\pm$ 0.010 | 0.256 $\pm$ 0.009 |
| $\sigma_{el}$ | 2.200 | 2.200 | 2.200 | 2.199 $\pm$ 0.017 | 2.199 $\pm$ 0.017 | 2.211 $\pm$ 0.038 | 2.211 $\pm$ 0.038 | 2.212 $\pm$ 0.057 | 2.211 $\pm$ 0.056 |
| $\sigma_{et}$ | 1.300 | 1.300 | 1.300 | 1.289 $\pm$ 0.014 | 1.291 $\pm$ 0.014 | 1.331 $\pm$ 0.032 | 1.332 $\pm$ 0.032 | 1.358 $\pm$ 0.049 | 1.358 $\pm$ 0.049 |
| | | | | | Stat. Values | | | | |
| $\Phi$ | - | 0.016 | 0.088 | 1298 | 1298 | 5874 | 5874 | 13217 | 13222 |
| $r$ | - | 1.000 | 1.000 | 0.991 | 0.991 | 0.959 | 0.959 | 0.913 | 0.913 |
| Opt. Iter. | - | 12 | 13 | 11 | 12 | 12 | 12 | 13 | 10 |
| Mod. Calls | - | 73 | 97 | 95 | 88 | 105 | 84 | 114 | 62 |

The intracellular conductivities start at 1 $mScm^{-1}$, with a high objective function, and with each optimisation iteration, it lowers, until the minimum has been reached. Note, that initially, big steps are taken to reduce the objective function, with steepest descent, using large Marquart values, then when the minimum is approached, smaller steps are taken with smaller Marquart values, to not over shoot the minimum and for a more refined estimation. Similarly, Figure 10.13 shows the behaviour of the objective function in parameter space, with respect to the extracellular conductivities. Its more of a steeper canyon than the intracellular parameter space in Figure 10.12. It can been seen that for values less than 1 $mScm^{-1}$, for both longitudinal and transverse directions, the residuals rapidly increase, shown by the steep surfaces, accompanied by closely spaced contour lines. Two dimensional contour plots can be found in Appendix B for alternative viewing.

One of the major difficulties in determining the bidomain conductivities is separating the intracelluar and extracellular values. It has been shown in Section 10.1 that different sets of conductivity values produce marked differences in the elliptical wave. In observing the objective function in parameter space for the longitudinal conductivities in Figure 10.14, there appears to be one minima, which gives the reassurance that the intracellular and extracellular conductivities can be determined as unique separate values, or as the true values. Figure 10.15 is for the transverse conductivities, and there is also one minimum. Table 10.2 shows estimation results with additional parameters, such as membrane capacitance and fibre angle. The level of noise in the synthetic data was 5 %. Values of the conductivity parameters started at 1 $mScm^{-1}$, and membrane capacitance started at a value of 1.5 $\mu F$. Looking at the third column, the parameters did not go back to their original values, even though the residuals and the correlation had similar values to column 5 in Table 10.1. The reason for this, is that the membrane capacitance parameter degraded the performance of the estimation. Table 10.3 shows the parameter correlation coefficient matrix, and it can be seen between the membrane capacitance, $C_m$, and the intracellular longitudinal conductivity, $\sigma_{il}$,

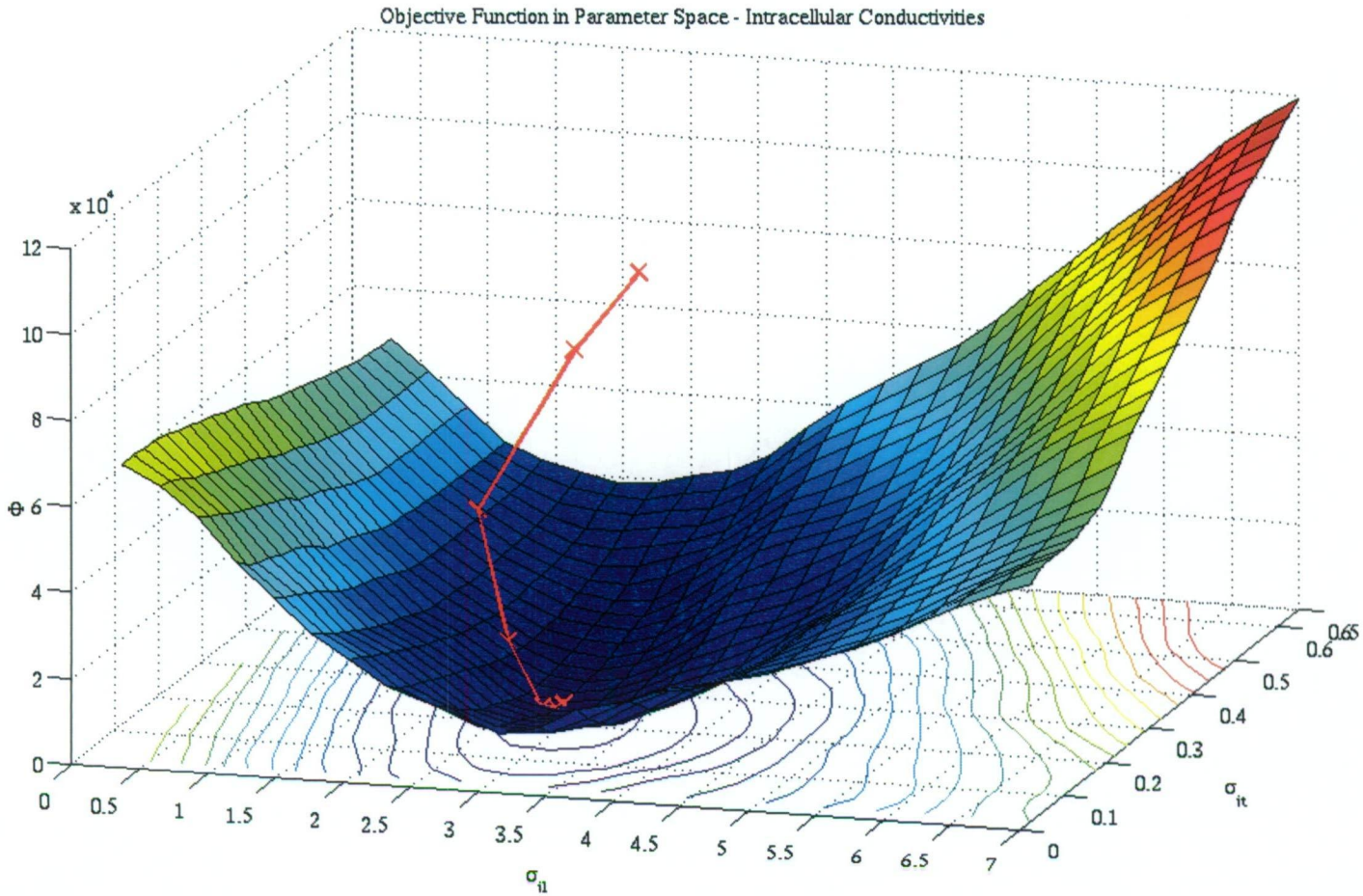


Figure 10.12: Surface plot of objective function in parameter space; for variation in intracellular conductivity values, whilst holding the extracellular conductivities fixed. The cluster of red crosses indicates the region of the objective function minimum, corresponding to $\sigma_{il} = 2.8$ and $\sigma_{it} = 0.26$ $mScm^{-1}$. Contour spacing is 5000.

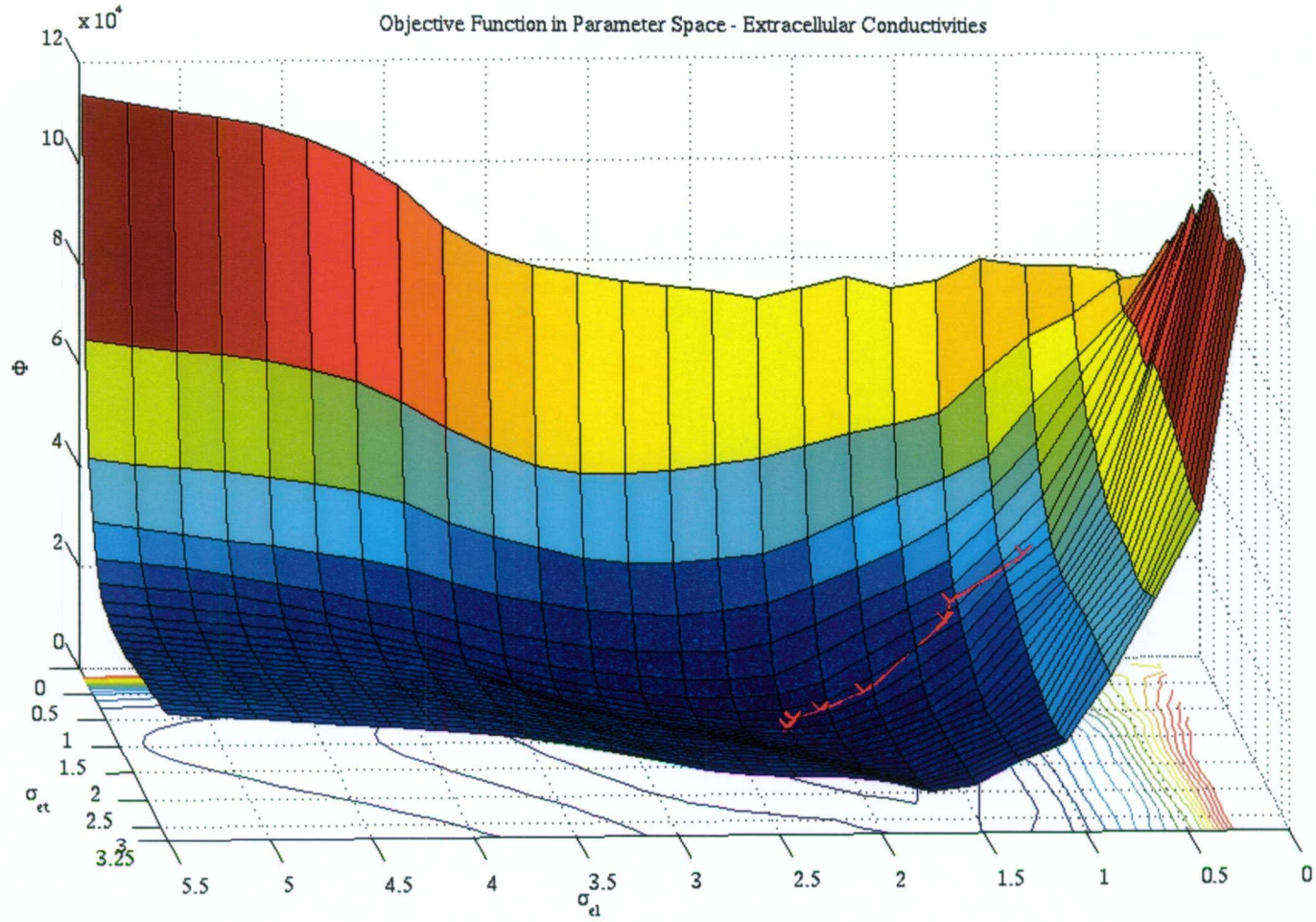


Figure 10.13: Surface plot of objective function in parameter space; for variation in extracellular conductivity values, whilst holding the intracellular conductivities fixed. Objective function minimum at $\sigma_{el} = 2.2$ and $\sigma_{et} = 1.3\ mScm^{-1}$.

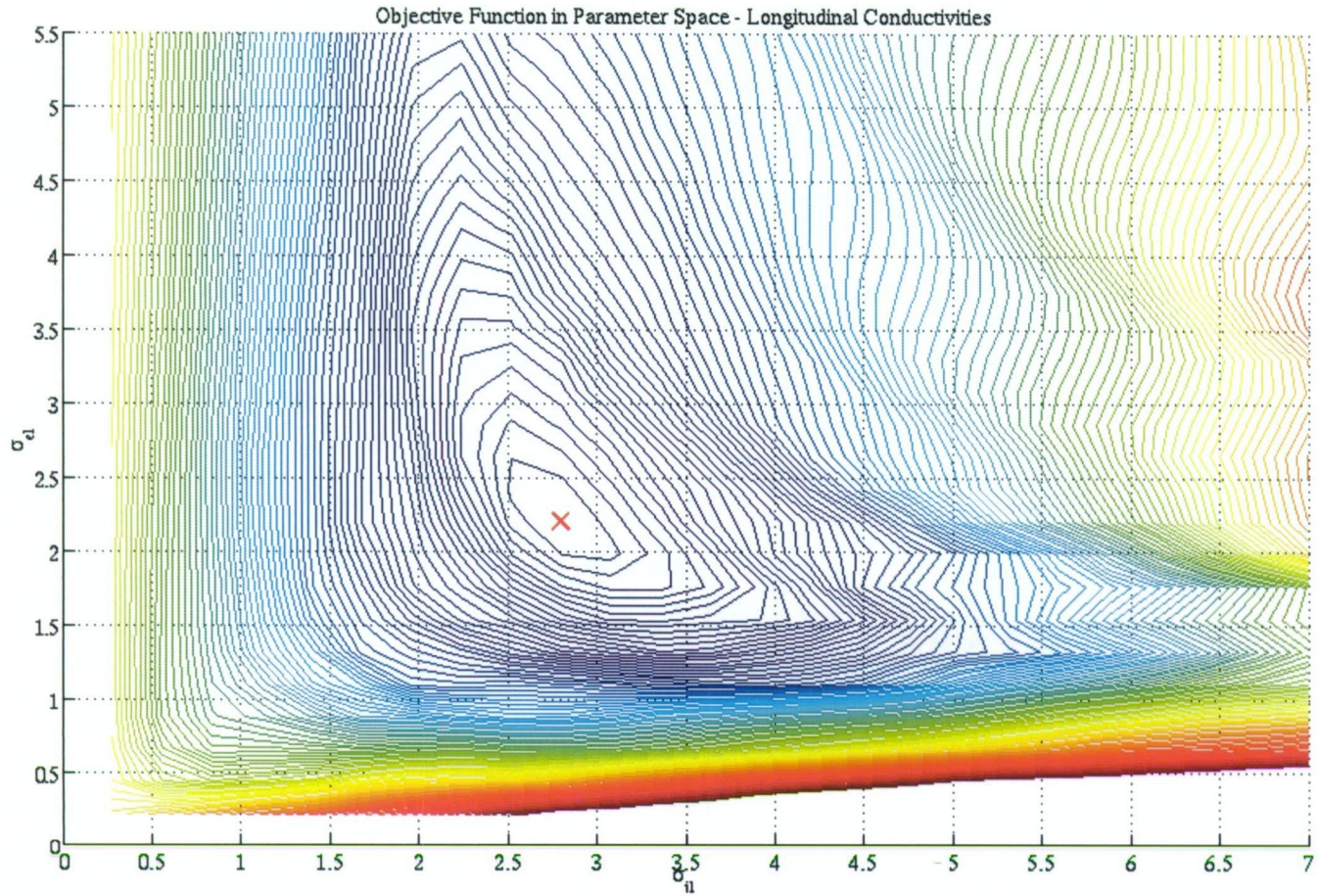


Figure 10.14: Contour plot of objective function in longitudinal parameter space, with spacings of 1000. Objective function minimum at $\sigma_{il} = 2.8$ and $\sigma_{el} = 2.2\ mSm^{-1}$.

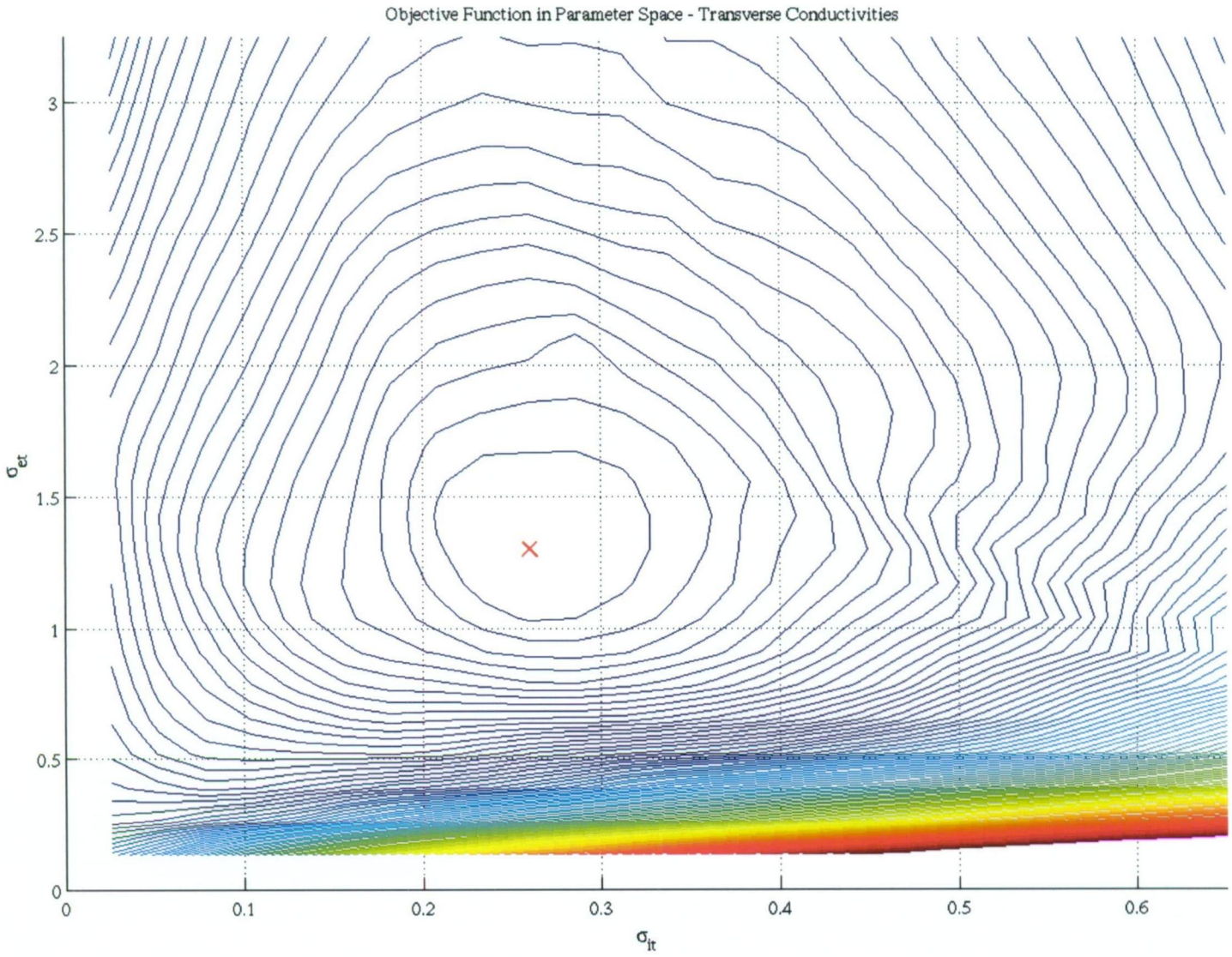


Figure 10.15: Contour plot of objective function in transverse parameter space, with spacings of 1000. Objective function minimum at $\sigma_{it} = 0.26$ and $\sigma_{et} = 1.3\ mScm^{-1}$.

Table 10.2: Estimated conductivities, membrane capacitance, and fibre angle, from synthetic data with 5 % noise (mS/cm).

| Symbol | Orig. | LS (estimate $C_m$) | LS (estimate $C_m$) stricter termination criterion | LS (estimate $\theta$ with fixed $C_m$) |
|---|---|---|---|---|
| $\sigma_{il}$ | 2.800 | 1.791 ± 0.020 | 2.668 ± 0.036 | 2.804 ± 0.018 |
| $\sigma_{it}$ | 0.260 | 0.162 ± 0.002 | 0.250 ± 0.003 | 0.264 ± 0.003 |
| $\sigma_{el}$ | 2.200 | 1.534 ± 0.018 | 2.115 ± 0.025 | 2.199 ± 0.018 |
| $\sigma_{et}$ | 1.300 | 0.839 ± 0.009 | 1.227 ± 0.014 | 1.291 ± 0.015 |
| $C_m$ | 1.000 | 0.769 ± 0.004 | 0.972 ± 0.005 | 1.000 (fixed) |
| $\theta$ | 121.000 | 121.000 (fixed) | 121.000 (fixed) | 121.033 ± 0.149 |
| | | | Stat. Values | |
| $\Phi$ | - | 1347 | 1297 | 1299 |
| $r$ | - | 0.990 | 0.991 | 0.991 |

the correlation was high with a value of 0.8347. As a comparison, Table 10.4 shows the correlation coefficient matrix for estimating without membrane capacitance, which has lower values; the parameters from this estimation are given in the fifth column of Table 10.1. An estimation including membrane capacitance was performed with SVD, however it failed to lower the objective function at all.

In the fourth column of Table 10.2, the results are much closer to the true values, due to stricter termination criterion; such as the one set in Expression (7.7) in Section 7.2. However the trade off was many more optimisation runs, hence, an increase in run time. In the last column of Table 10.2, fibre angle was estimated while holding the membrane capacitance fixed; the fibre angle started at 130°, being 9° out. In this estimation, the conductivity parameters and the fibre angle were retrieved back, without difficulty. Normally, noise in the electrograms recorded in experiments would be minimal, and so, it would be safe to say, that it does not really pose a major problem. Judging from published data [67], and measurements made in this study, the noise would be mostly below 5%. At this stage, SVD seems to handle noise better, as it takes less forward model

Table 10.3: Parameter correlation coefficient matrix, when estimating $C_m$.

| Symbol | $\sigma_{il}$ | $\sigma_{it}$ | $\sigma_{el}$ | $\sigma_{et}$ | $C_m$ |
|---|---|---|---|---|---|
| $\sigma_{il}$ | 1.000 | -0.226 | 0.502 | -0.205 | 0.835 |
| $\sigma_{it}$ | -0.226 | 1.000 | 0.200 | -0.017 | 0.171 |
| $\sigma_{el}$ | 0.502 | 0.200 | 1.000 | -0.187 | 0.712 |
| $\sigma_{et}$ | -0.205 | -0.017 | -0.187 | 1.000 | 0.032 |
| $C_m$ | 0.835 | 0.171 | 0.712 | 0.032 | 1.000 |

Table 10.4: Parameter correlation coefficient matrix, without estimating $C_m$.

| Symbol | $\sigma_{il}$ | $\sigma_{it}$ | $\sigma_{el}$ | $\sigma_{et}$ |
|---|---|---|---|---|
| $\sigma_{il}$ | 1.000 | -0.594 | -0.414 | -0.354 |
| $\sigma_{it}$ | -0.594 | 1.000 | 0.172 | 0.103 |
| $\sigma_{el}$ | -0.414 | 0.172 | 1.000 | -0.237 |
| $\sigma_{et}$ | -0.354 | 0.103 | -0.237 | 1.000 |

calls to arrive at the objective function minimum, giving shorter run times. It has been shown that if other parameters are estimated as well, such as membrane capacitance, the determined parameter set may be entirely different from the set that generated the artificial data. Even though the residuals and the correlation values may seem reasonable. This could be due to a number of reasons, such as those mentioned in Chapter 6.8, such as parameter correlation, and parameter insensitivity, resulting in nonuniqueness. Signs of this happening can be seen by inspecting the correlation coefficient matrix, and the eigenvector matrix. The membrane capacitance is insensive to parameter increments when calculating derivatives, in relation to the conductivity values, causing singularity in the normal matrix in Equation (6.24). It is also of different type to the conductivity parameters, and so its derivatives may behave differently. It would be thought that SVD would be benificial in this situation, but it was unsucessful. Another validation test that could be performed on the parameter estimation method could be done by adding uncertainty in the position of measurement electrodes,

which may be occur to a certain degree in practice. Though, it will be seen later on, that experimental to model data miss-match poses more of a concern.

In the next section the parameter estimation method will be tested with experimental data that has been published in the literature. Due to availability, only data for one time instance during activation (one potential map) is used as observations into the parameter estimation. The validation of the parameter estimation method just presented was with data for more than one time instance, which were the potentials at the measurement electrodes from $t$=0 to $t$=10 $ms$, at every 1 $ms$ time steps. To have confidence in the estimated values in the next section, estimation runs were performed with observations for one time instance only. The bidomain model setup was the same as in the previous validation. The synthetic data was also the same, but for activation at $t$=10 $ms$ only. For example, the data points in the potential map in Figure 10.10(a). No noise was added into the synthetic data. The Least-Squares method was used for the estimation, and the starting values of the parameters were set to 1 $mScm^{-1}$. Table 10.5 shows the results from the parameter estimation, which retrieved back the parameters successfully closed to their original values. It was found later on that when using experimental data for more than one time instance, it was more difficult to fit due to satisfying a number of data points in time. This was due to the different rate-of-rise in the action potential in the experimental data than that produced by the membrane model in the bidomain model. In the case for data with one time instance, the changes in potential with time are not an issue in the estimation, and so its less constrained, leading to an easier estimation.

## 10.4 Inversion from Published Experimental Data

With the parameter estimation method applied to noise contaminated synthetic data, it was then tested on real data reported in the literature. Potential maps for epicardial pacing in canine hearts from Roberts *et. al.* [11] and Baruffi *et. al.* [129] experiments were used. Due to availability, data was only for one instant

Table 10.5: Estimated conductivities from synthetic data for just one time instance (one potential map), at 10 $ms$ after stimulation, with no noise (mS/cm).

| Symbol | Orig. | LS (estimate for one time instance |
|---|---|---|
| $\sigma_{il}$ | 2.800 | 2.798 |
| $\sigma_{it}$ | 0.260 | 0.260 |
| $\sigma_{el}$ | 2.200 | 2.201 |
| $\sigma_{et}$ | 1.300 | 1.299 |
| $C_m$ | 1.000 | 1.00 (fixed) |
| $\theta$ | 121.000 | 121 (fixed) |
| | | Stat. Values |
| $\Phi$ | - | 0.035 |
| $r$ | - | 1.000 |

in time. In these experiments, epicardial electrode arrays were used to measure unipolar electrograms, and pacing was applied to a central location in the arrays, thus, causing a propagating elliptical depolarising wave.

### 10.4.1 Roberts 1979 Experiment

The epicardial electrode array used in the Roberts 1979 experiment had a total of 83 measurement electrodes, with spacings of 1.5 $mm$, which covered an area of $0.9\times1.65$ $cm^2$. An electrode located at the centre of the array was allocated for the stimulus. The bidomain model setup used here is the same model that was used in Section 10.3.1, with the same 2D computational mesh ($1.2\times1.9$ $cm^2$ with $121\times191$ nodes) and boundary conditions; except it had a different fibre angle and the extracellular data output used in the parameter estimation was for one instant in time, at 10 $ms$ after activation. The data used in the parameter estimation from Roberts *et. al.* [11] experiment is presented in Figure 10.16, which shows the interpolated extracellular field at 10 $ms$ after stimulation; the values used are at the electrode points. Roberts *et. al.* choice of fibre direction was assumed to

correspond to the maximal epicardial conduction velocity; indicated by the black straight line shown in Figure 10.16. Note that it does not directly pass through the major axis of the ellipse, or through the two maxima. From the potential map, asymmetry in the maxima can be seen. Figure 10.17 shows a surface and contour plot of the interpolation, to help visualise the relation of potential regions; such as the magnitudes of the minima and maxima. Table 10.6 shows the estimated conductivity values for a number of estimation runs, under different conditions. Least-Squares (LS), and Singular Value Decomposition (SVD) inverse techniques were used. Additional parameters such as membrane capacitance, $C_m$, and fibre angle, $\theta$, were estimated as well. It was advantageous that membrane capacitance could be estimated, since its value varied in the literature.

The second and third columns were estimation runs for determining membrane capacitance, while holding the fibre angle to the value chosen by Roberts *et. al.* [11], of 72°. In these runs, SVD gave smaller model parameter values than LS. The fourth and fifth columns were estimations runs while keeping the membrane capacitance fixed, to a value of 1.00. In the LS case, the fibre angle was estimated. The outcomes of both estimation methods were very similar. The sixth column was for choosing the reference potential far away from the stimulus electrode, in the top left-hand corner of the domain, while holding the fibre angle fixed, which resulted in different parameter values. The seventh column was for estimating both fibre angle and membrane capacitance. Note that the standard deviation values were more higher for estimation runs that determined membrane capacitance. Suggesting that the parameters were calculated with greater uncertainty when estimating this parameter. The ratio between longitudinal and transverse conductivities, for intracellular and extracellular space are shown between the different estimation runs; the values where consistent, with a intracellular ratio of around 6.0, and an extracellular ratio of 3.0. Figure 10.18 shows the potential map produced by the bidomain model, using the conductivity parameters estimated from SVD, shown in Table 10.6, fifth column. Comparing this with the experimental data, in Figure 10.16, the elliptical wave appears to have the same

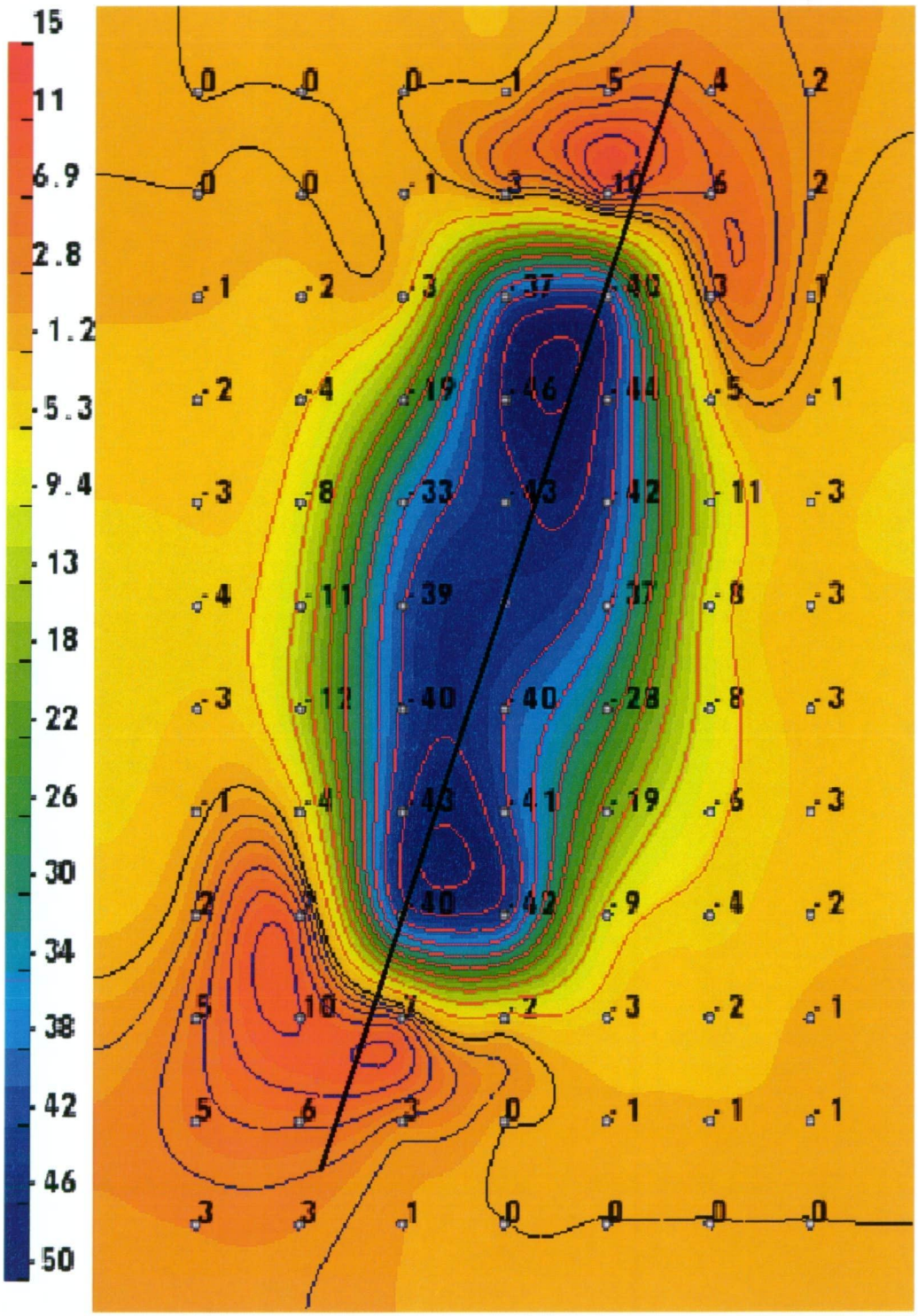


Figure 10.16: Extracellular potential map obtained by Roberts *et. al.* [11]. Potential distribution is at 10 $ms$ after stimulation. Extracellular potential values are shown at each electrode location. Positive isopotential lines are in blue with 2 $mV$ increments, negative isopotentials are in red with -5 $mV$ increments, and the zero isopotential is in black. Colour bar is in $mV$. The black straight line indicates the fibre direction, of 72° from the horizontal, chosen by Roberts *.et al.* [11].

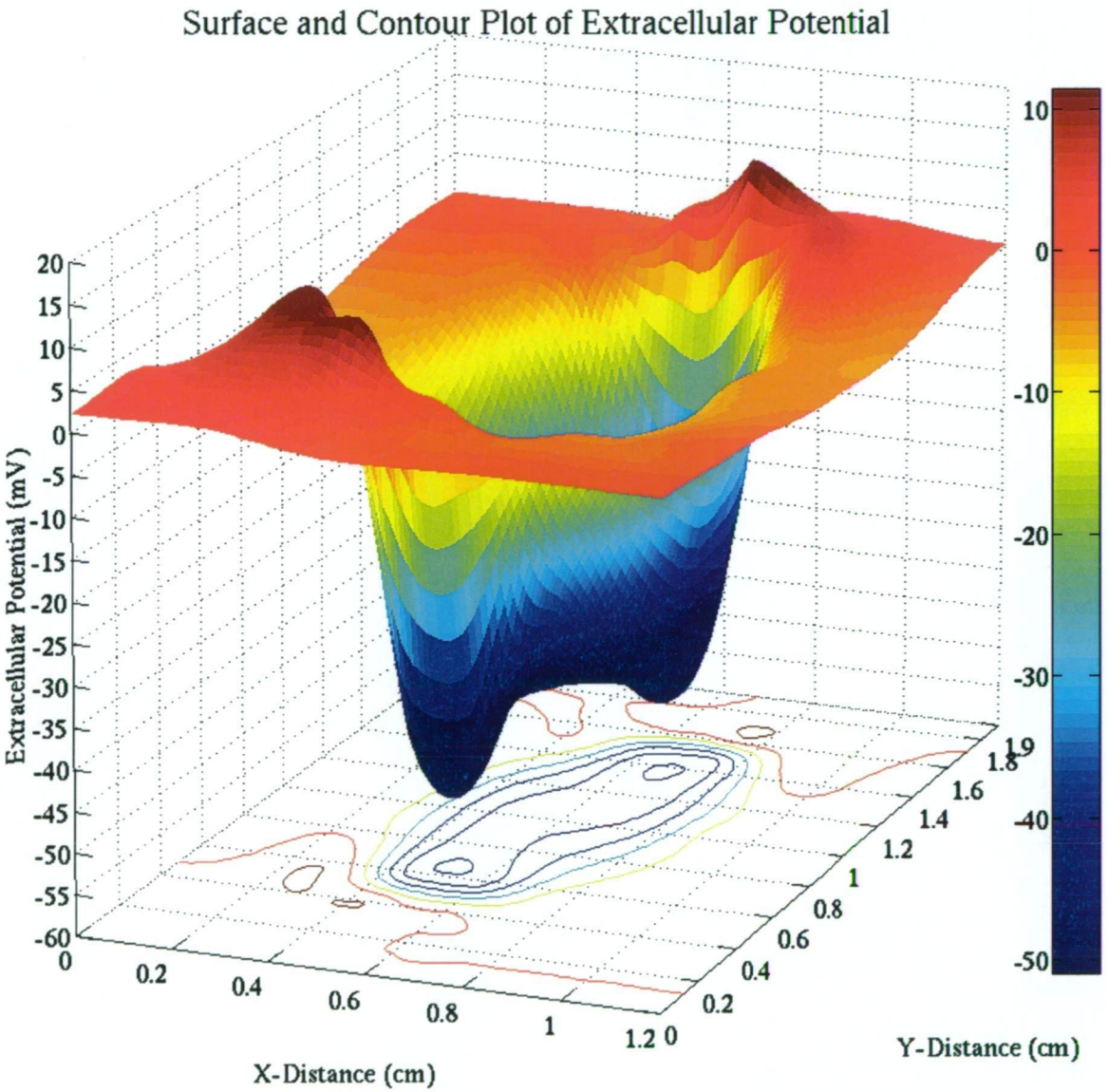


Figure 10.17: Surface and contour plot of the interpolated extracellular field from Roberts *et. al.* [11] data, showing the minima and maxima.

Table 10.6: Estimated conductivities from Roberts(1979) [11] experimental data (mS/cm).

| Symbol | SVD (estimate $C_m$) | LS (estimate $C_m$) | LS (estimate $\theta$ & fixed $C_m$) | SVD (fixed $C_m$ & $\theta$) | LS (corner reference & estimate $C_m$) | LS (estimate $\theta$ & $C_m$)) |
|---|---|---|---|---|---|---|
| $\sigma_{il}$ | 1.735 ± 0.620 | 2.344 ± 1.137 | 2.587 ± 0.069 | 2.586 ± 0.071 | 4.015 ± 2.365 | 4.121 ± 3.463 |
| $\sigma_{it}$ | 0.303 ± 0.110 | 0.398 ± 0.197 | 0.417 ± 0.017 | 0.420 ± 0.016 | 0.684 ± 0.397 | 0.638 ± 0.512 |
| $\sigma_{el}$ | 2.072 ± 0.689 | 2.733 ± 1.227 | 2.557 ± 0.094 | 2.568 ± 0.091 | 3.803 ± 1.940 | 3.796 ± 2.747 |
| $\sigma_{et}$ | 0.636 ± 0.218 | 0.822 ± 0.361 | 0.904 ± 0.040 | 0.903 ± 0.039 | 1.109 ± 0.841 | 1.327 ± 0.892 |
| $\sigma_{il}/\sigma_{it}$ | 5.726 | 5.889 | 6.204 | 6.157 | 5.870 | 6.459 |
| $\sigma_{el}/\sigma_{et}$ | 3.258 | 3.325 | 2.829 | 2.844 | 3.429 | 2.861 |
| $C_m$ | 0.782 ± 0.179 | 0.929 ± 0.268 | 1.000 (fixed) | 1.000 (fixed) | 1.206 ± 0.379 | 1.289 ± 0.569 |
| $\theta$ | 72.00 (fixed) | 72.00 (fixed) | 76.185 ± 0.524 | 76.00 (fixed) | 72.00 (fixed) | 76.274 ± 0.704 |
| | | | Statistical Values | | | |
| $\Phi$ | 1113 | 1054 | 935.2 | 935.9 | 1204 | 911.1 |
| $r$ | 0.977 | 0.973 | 0.980 | 0.981 | 0.9786 | 0.981 |

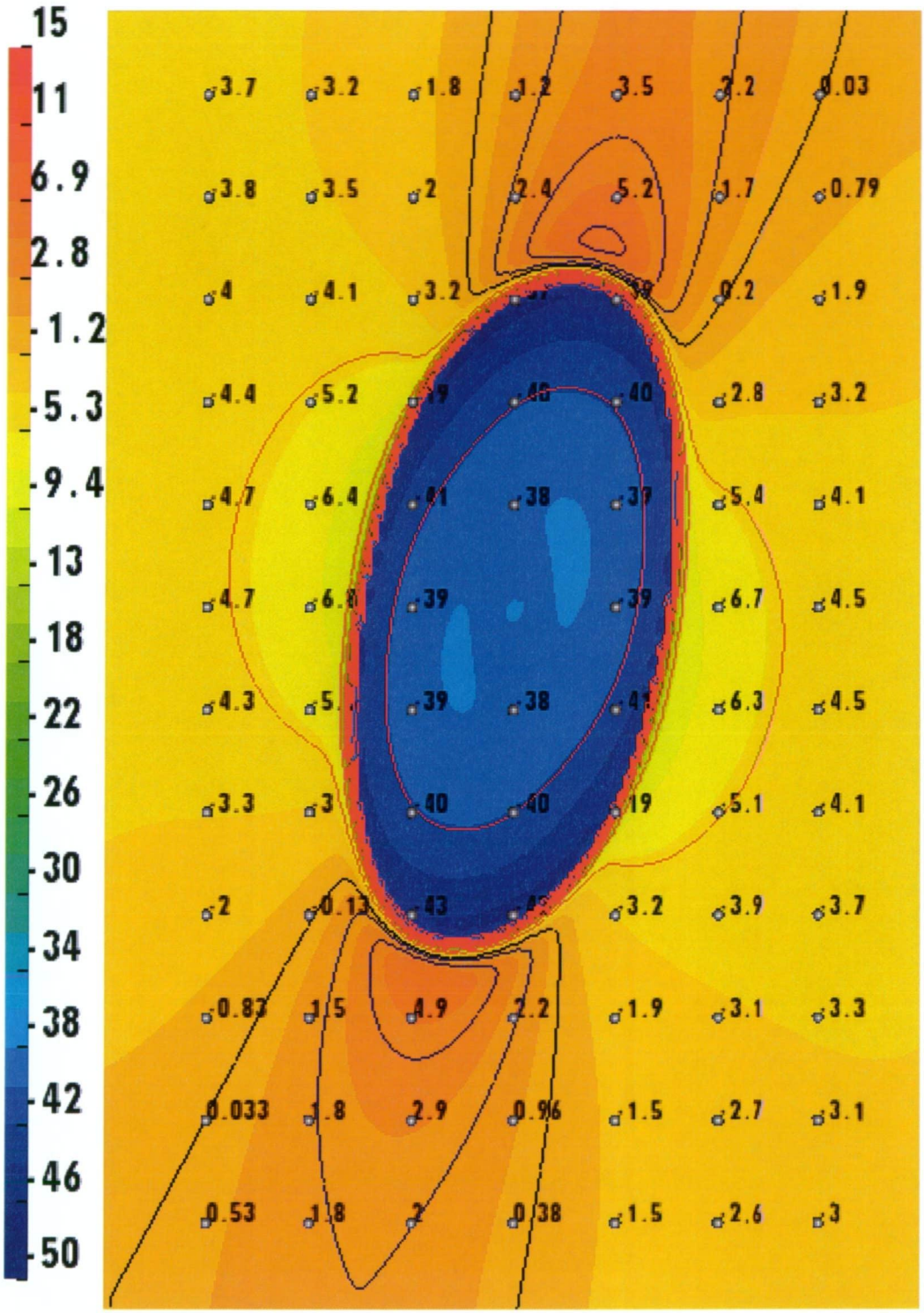


Figure 10.18: Extracellular potential map produced by the bidomain model using the conductivity parameters estimated from Roberts *et. al.* [11] data, shown in Figure 10.16. Parameter values used are presented in Table 10.6, fifth column. Positive isopotential lines are in blue with 2 $mV$ increments, negative isopotentials are in red with -5 $mV$ increments, and the zero isopotential is in black. Colour bar in $mV$.

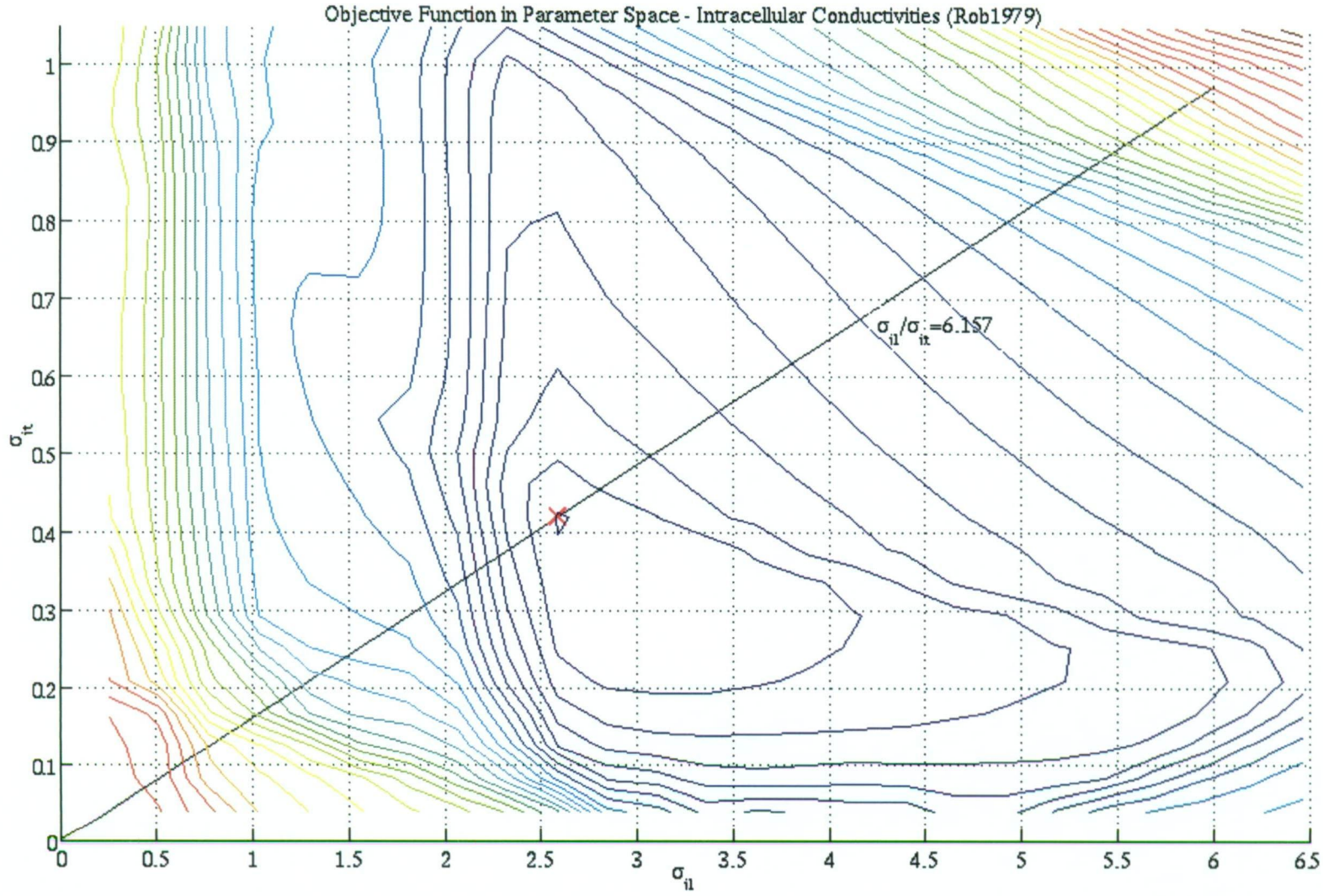


Figure 10.19: Contour plot of objective function in intracellular parameter space, with spacing intervals of 1000. The conductivity values that give the minimum are from the estimation run in Table 10.6, fifth column. The red cross marks the objective function minimum at $\sigma_{il}$=2.586 and $\sigma_{et}$=0.42 $mScm^{-1}$. Extracellular conductivities are held fixed at $\sigma_{el}$=2.568 and $\sigma_{et}$=0.903 $mScm^{-1}$. The diagonal black line passing through the minima is where there is the equal conductivity ratio of $\sigma_{il}/\sigma_{it}$=6.157.

shape, with similar length and width. The fibre direction was estimated to be at 76°, which aligned more with the semi-major axes of the ellipse outlined by the isopotential lines, rather than passing through the two maxima. The negative potentials inside the ellipse are similar in magnitude, with potentials of around -40 $mV$, however, the two potential maxima in the bidomain output are smaller in magnitude and are tucked closer into the ends of the ellipse. The differences in the maxima may be partly due to their asymmetry in the experimental observations; from the transmural fibre rotation, and fibre gradients, causing the offset of the maxima from the major axis. Another cause is that the isopotentials outlining the ellipse in the bidomain output are packed much closer together than in the experimental observations, indicating that the rate of depolarisation is faster. This is dependant on the membrane model incorporated in the bidomain, and it causes the positive maxima to be closer into the ends of the ellipse.

In other differences, the potentials furthest away from the point of stimulation, in the top left-hand and bottom right-hand corners of the domain in the experimental observations, are zero, where as in the bidomain output, the potentials in those regions are around -3 $mV$. There are also differences in potential in the regions traverse from the ellipse. The shape and location of the minima also differ. These differences are perhaps due to the membrane model used, intramural fibre rotation, orthotropic transverse conductivity, and the choice of reference potential. A contour plot of the objective function is given in Figure 10.19. The objective function here behaves differently than the one produced for the synthetic data shown in Figures B.1 (Appendix); there appears to be more flexibility in the intracellular longitudinal values, $\sigma_{il}$, to give low residuals, since the contours are widely spaced, for values in the range of 2.5 to 6.0 $mScm^{-1}$. Similarly, Figure 10.20 shows the objective function in extracellular space, showing widely spaced contour lines, implying greater variability in parameters. However, there is one minima, suggesting there are unique values for the two parameters, as long as the termination criterion is strict enough to converge to it.

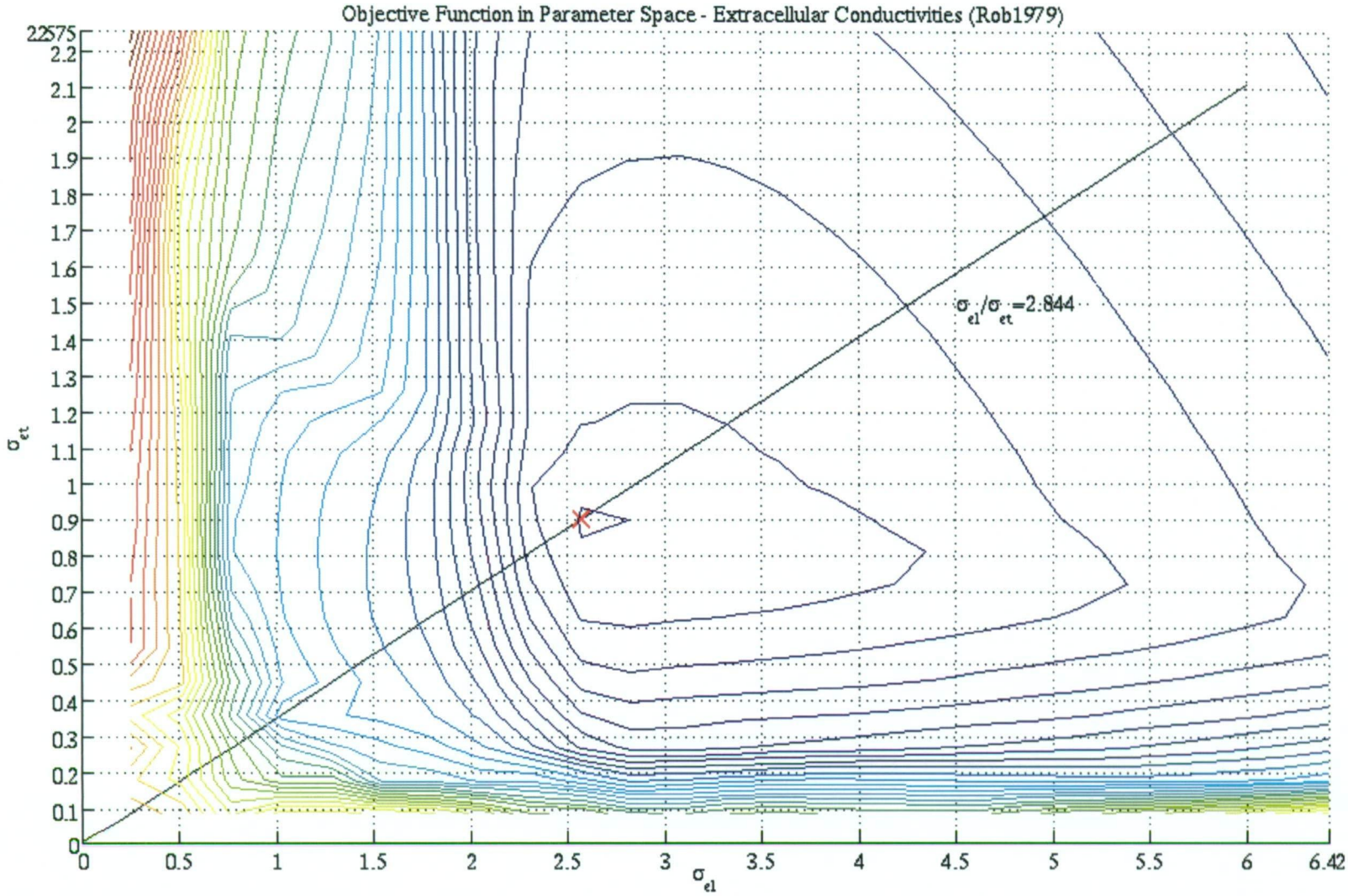


Figure 10.20: Contour plot of objective function in extracellular parameter space, with spacing intervals of 1000. The conductivity values that give the minimum are from the estimation run in Table 10.6, fifth column. The red cross marks the objective function minimum at $\sigma_{el}$=2.568 and $\sigma_{et}$=0.903 $mScm^{-1}$. Intracellular conductivities are held fixed at $\sigma_{el}$=2.586 and $\sigma_{et}$=0.420 $mScm^{-1}$. The diagonal black line passing through the minima is where there is the equal conductivity ratio of $\sigma_{el}/\sigma_{et}$=2.844.

Table 10.7: Estimated conductivities from Baruffi *et. al.* 1978 [129] experimental data (mS/cm).

| Symbol | LS fixed $C_m$ & $\theta$ | SVD fixed $C_m$ & $\theta$ | LS estimate $C_m$ with fixed $\theta$ |
|---|---|---|---|
| $\sigma_{il}$ | 3.484 ± 0.239 | 3.684 ± 0.230 | 3.464 ± 0.260 |
| $\sigma_{it}$ | 0.366 ± 0.012 | 0.359 ± 0.011 | 0.360 ± 0.013 |
| $\sigma_{el}$ | 2.123 ± 0.094 | 2.049 ± 0.082 | 2.076 ± 0.092 |
| $\sigma_{et}$ | 0.596 ± 0.025 | 0.600 ± 0.025 | 0.588 ± 0.030 |
| $\sigma_{il}/\sigma_{it}$ | 9.519 | 10.436 | 9.622 |
| $\sigma_{el}/\sigma_{et}$ | 3.562 | 3.415 | 3.531 |
| $C_m$ | 1.000 (fixed) | 1.0 (fixed) | 0.990 ± 0.011 |
| $\theta$ | 81 (fixed) | 81 (fixed) | 81 (fixed) |
| | | Statistical Values | |
| $\Phi$ | 5281 | 5293 | 5282 |
| $r$ | 0.934 | 0.934 | 0.934 |

### 10.4.2 Baruffi 1978 Experiment

In the Baruffi *et. al.* [129] experiment, a larger area on the epicardial surface was measured than in Roberts experiment; a 11×11 electrode array, with 2 $mm$ spacing was used. On the outside of this array, around the perimeter, there was a series of electrodes with 4 $mm$ spacing. The tissue area measured was 2.8×2.8 $cm^2$. A central electrode was used to deliver the current stimulus. The array was placed on the anterior left ventricular surface. Figure 10.21 shows the interpolated extracellular field at 20 $ms$ after stimulation. Due to the resolution, limited by the electrode spacing, the shape of the elliptical wave is more irregular, and the two negative minima and positive maxima are not as well defined, than in Roberts *et. al.* potential map, in Figure 10.16. Also, since the measurements were recorded for a larger tissue area, the effects of varying fibre direction and tissue geometry (curvature of epicardium) may have had an effect. The fibre angle was chosen to be the line that coincided with the major axis of the ellipse, defined by the isopotential lines, which had a value of 81° from the horizontal.

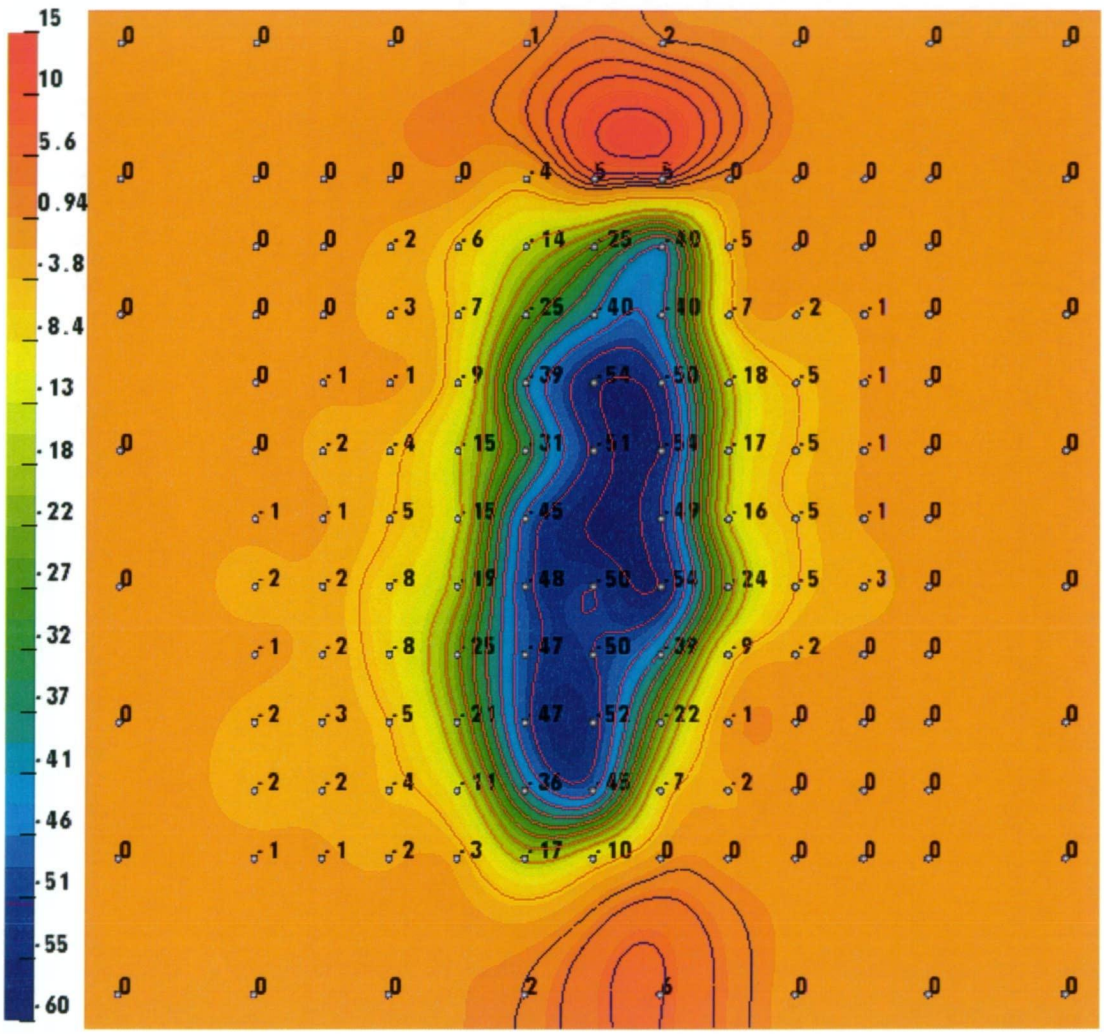


Figure 10.21: Extracellular potential map obtained by Baruffi *et. al.* [129]. Potential distribution is at 20 $ms$ after stimulation. Positive isopotential lines are in blue with 2 $mV$ increments, negative isopotentials are in red with -5 $mV$ increments. The 11×11 array of electrodes in the middle of the tissue domain have 2 $mm$ spacings; outside this array there is a series of electrodes around the perimeter, with spacings of 4 $mm$. The extracellular potential values at the electrodes points were used in the parameter estimation.

The bidomain model used in this parameter estimation is the same as in the previous section, but with different tissue domain size. The node spacing in the computational mesh was still the same at 100 $\mu m$, since the mesh had an area of 3.2×3.2 $cm^2$, with 321×321 nodes. There was an over-hang of 2 $mm$ from the outside electrodes. Simulation of activation was for 20 $ms$. Similarly to Roberts *et. al.* experiment, only one time instance of extracellular potentials were used in the parameter estimation; the values at the electrode points in Figure 10.21.

Table 10.7 shows the results of the estimation run using the data. The second and third columns are estimation runs whilst holding membrane capacitance and fibre angle fixed. The residuals were more higher for these results than from the results from Roberts 1979 data, since there were more measurements, and also greater experiment to model miss-match. In the last column, membrane capacitance was estimated, though it did not beneficially change the conductivity parameters, and statistical values. Figure 10.22 presents the bidomain model output potential, using the parameters given in the second column of Table 10.22. As seen previously, there are some inconsistencies between the model and experimental data. Such as the asymmetries of the potential maxima, differences in potentials in certain regions, and the spacing of the isopotential lines.

The correlation values in estimations for Roberts 1979 and Baruffi gave values greater than 0.9, which is generally considered acceptable for a good fit between model and experiment [152]. Though, there are still inconsistencies, such as asymmetry, and the rate of depolarisation. The parameter values were only estimated with data at one time instance (10 $ms$ or 20 $ms$).

Caution should be made when estimating additional parameters such as membrane capacitance. Selection of initial parameter values may be important to reduce the amount of computational time spent on searching for the objective function minimum. The bidomain model used here was only for a 2D tissue domain, and so there was no rotation of fibre direction with depth. Since the transmural fibre rotation has an effect on the epicardial potential distribution, as seen in simulations like in Section 10.2, then for a closer match it would need to

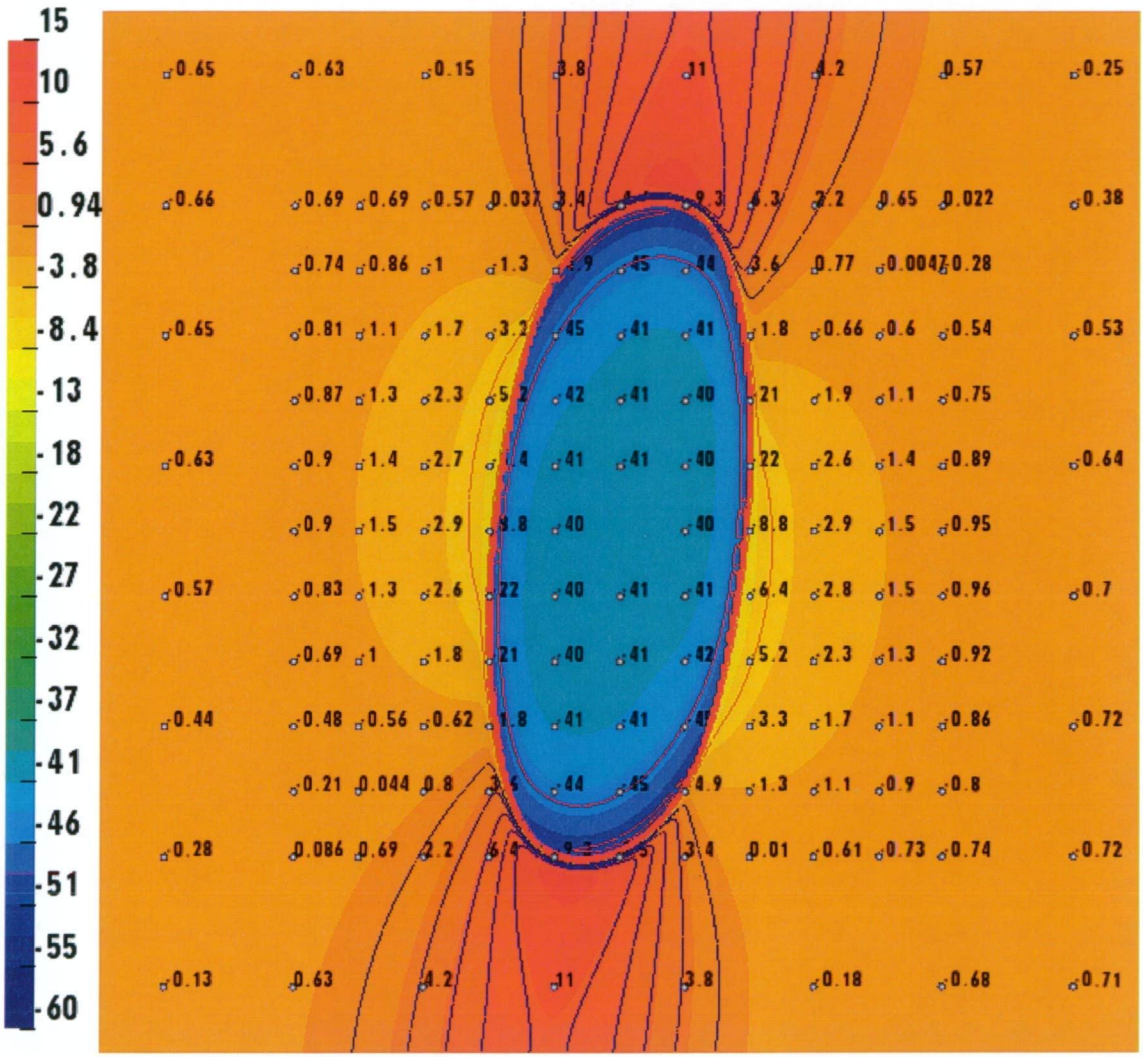


Figure 10.22: Extracellular potential map from bidomain model, using the conductivity parameters estimated from Baruffi *et. al.* [129] data, in Figure 10.21. Estimated parameters used are given in Table 10.7, second column. Positive isopotential lines are in blue with 2 $mV$ increments, and negative isopotentials are in red with -5 $mV$ increments.

be included into the model. This would mean a 3D bidomain model would be used, with additional parameters to estimate, which would require longer computational time to solve.

# Chapter 11

# Experimental Results

## 11.1 Experimental Method

Unipolar electrogram recordings were performed in vivo, on sheep. The details of the experiment is described in Chapter 8, but is briefly described here. Sheep weighing around 30 to 50 $kg$ were anaesthetised with sodium pentobarbital (30 $mg/kg$). Additional amounts of anaesthetic were administered during the experiment as needed, based on signs of eyelid and pedal reflexes. The heart was exposed through a left thoractomy performed in the fourth or fifth intercostal space and was suspended in the pericardial cradle. The unipolar electrograms were recorded via an electrode array. The electrode array used in the experiment is described in Section 8.3.1; it had a total of 194 silver electrodes (13×15), with 1.42 $mm$ spacing between the columns and 1.71 $mm$ spacing between the rows. The electrode array was placed in the left ventricular epicardium and was sutured on each corner to hold it into place. Gauze material was placed over the chest opening to prevent exposure of the heart to air. A unipolar cathodal stimulus, administered by a Medtronic® 5364 demand pulse generator (Medtronic Inc. Minneapolis, USA), was delivered to the central electrode in the array; the return electrode was embedded superficially under the skin of the sheep, either on the hind leg or on the chest wall. The stimulus duration was for 2 $ms$, and the stimulus strength was just above threshold to achieve ventricular capture. The

pacing rate was set to 150 *ppm* (pulses per minute), just above rest rate. The electrograms were recorded at 2 $kHz$ for half a second. This meant that at least one waveform could be recorded, since the average rest rate of sheep is around 2 beats per second.

The output of the recording electrodes were connected to a '256 Channel Switch and Signal Generator Unit' (Central Science Laboratory, University of Tasmania) [182]. This unit supplied the calibration signal, and provided the junction between the recording electrodes and the multichannel data acquisition system. The data acquisition system was a 256-channel system Binary Data Delivery Device (BDDD) [186]. It was connected to a host computer; a SPARC Sun system, by an S11W, which is a 16 bit, parallel input output (I/O) interface for the SBus. The electrogram data was saved to file for processing.

For the viewing of the data, potential maps were created by interpolating the values at the electrodes to a 51×51 mesh. The interpolation scheme used was a method described by Oostendorp *et. al.* [188]. Since the electrogram data was recorded at 2 $kHz$, interpolated potential maps could be created for every 0.5 $ms$. The baseline potential was chosen to be the time before the Q wave intrinsic deflection, determined by the greatest rate of change in potential. The interpolation of the data was saved as MATLAB matrix files. These could be loaded into interactive visualisation software, such as MAP3D [171] and SCIRun [161], where colour coded potential maps with contours could be viewed. In the software, the electrograms could be stepped through the time-series, showing the changes in potential.

## 11.2 Potential Maps

This section presents extracellular potential maps, recorded on the epicardium for normal sinus rhythm and for epicardial pacing. The differences in potential distributions between normal sinus rhythm and epicardial pacing can be seen. Normal sinus rhythm produces complex irregular pattern of potential on the

epicardial surface, and would be difficult to utilise for measuring the bidomain conductivities. The activating wave that propagates across the epicardium is much easier to model; and so it was used for the observations in the parameter estimation.

### 11.2.1 Normal Activation

Figure 11.1 shows three extracellular potential maps for normal sinus rhythm, at 5 $ms$ intervals. Electrode points are indexed in the map. Measurements were made in the left ventricle of the sheep's heart. Figures 11.2(a) and 11.2(b) shows electrograms measured at electrodes 51 and 149.

The negative potential at the top left hand side of Figure 11.1(a) moves through, with positive potentials laying ahead, possibly related to the fibre direction. Depending on the location, there were slight R waves produced, for example, of around 0.3 $mV$ in amplitude, such as in Figure 11.2(a). There were also R waves that were quite pronounced, at 4 $mV$, as in Figure 11.2(b). The potentials were irregularly distributed; Arisi *et. al.* [192] described this potential distribution as mosaic like. Breakthrough sites were observed, such as in the regions where electrodes 43 and 56 are located. The distribution of the potentials is reflected by the structural properties of the ventricular wall, such as the branches of the Purkinje network underneath, causing breakthrough sites on the epicardium [192, 128].

### 11.2.2 Activation from Pacing

Extracellular potential maps are shown in Figure 11.3, for epicardial pacing. The maps show the propagation of the depolarising elliptical wave from the central electrode, reflecting anisotropic conduction. The location of the electrode array was the same as for the measurements of normal activation, in Figure 11.1. Electrograms during epicardial pacing are shown in Figure 11.4, for different sites in the measured domain. An initial positive spike was observed in the electrograms,

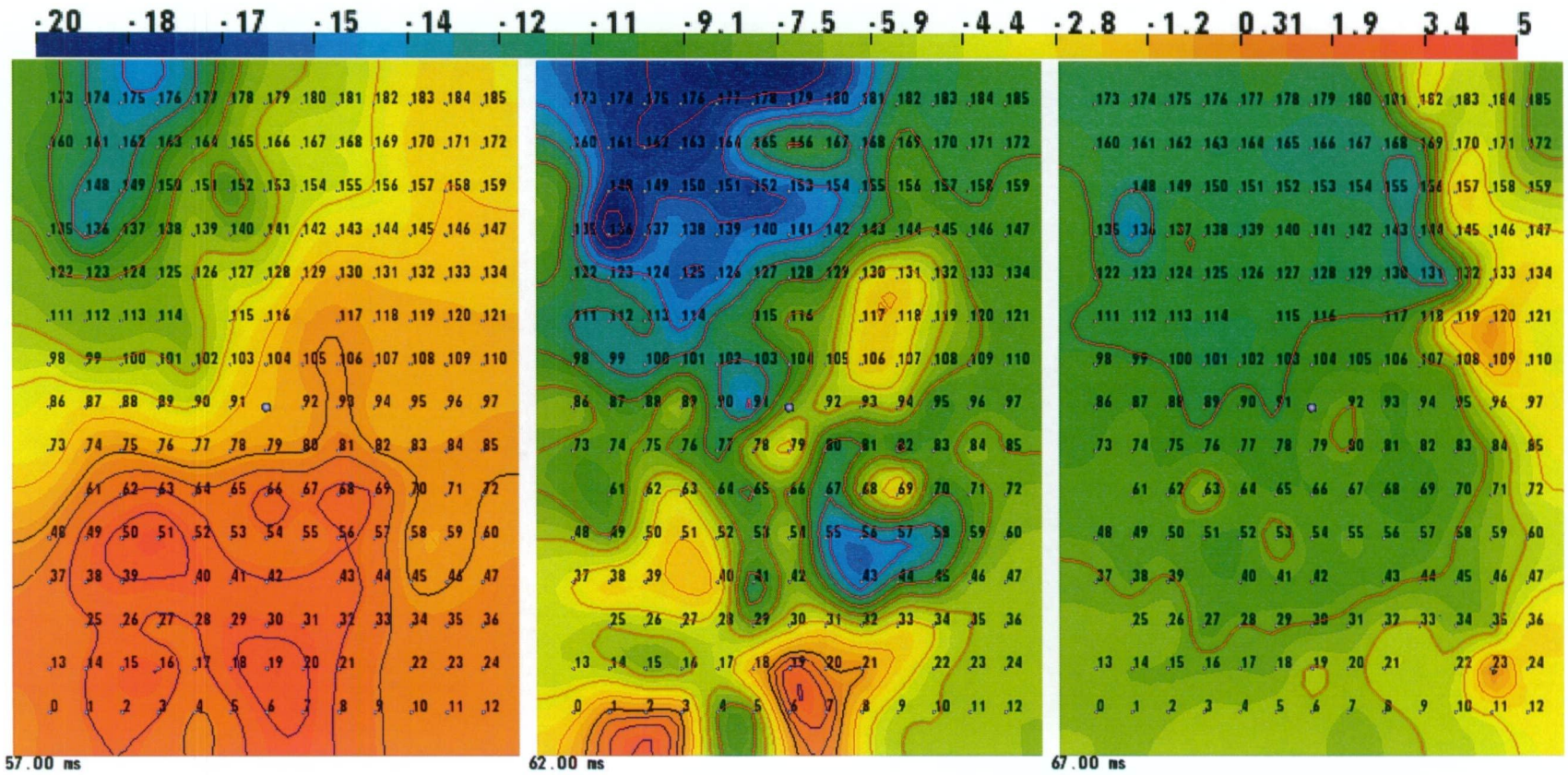


(a) (b) (c)

Figure 11.1: Potential maps of normal activation in the left ventricle from experiment 5. Electrode numbering starts from zero, at the bottom left hand corner of the domain. The electrodes that produced bad electrograms were omitted. Positive isopotential lines are in blue with 1 $mV$ increments, negative isopotential lines are in red with -2 $mV$ increments, and the zero isopotential line is in black. Maps are at 5 ms intervals.

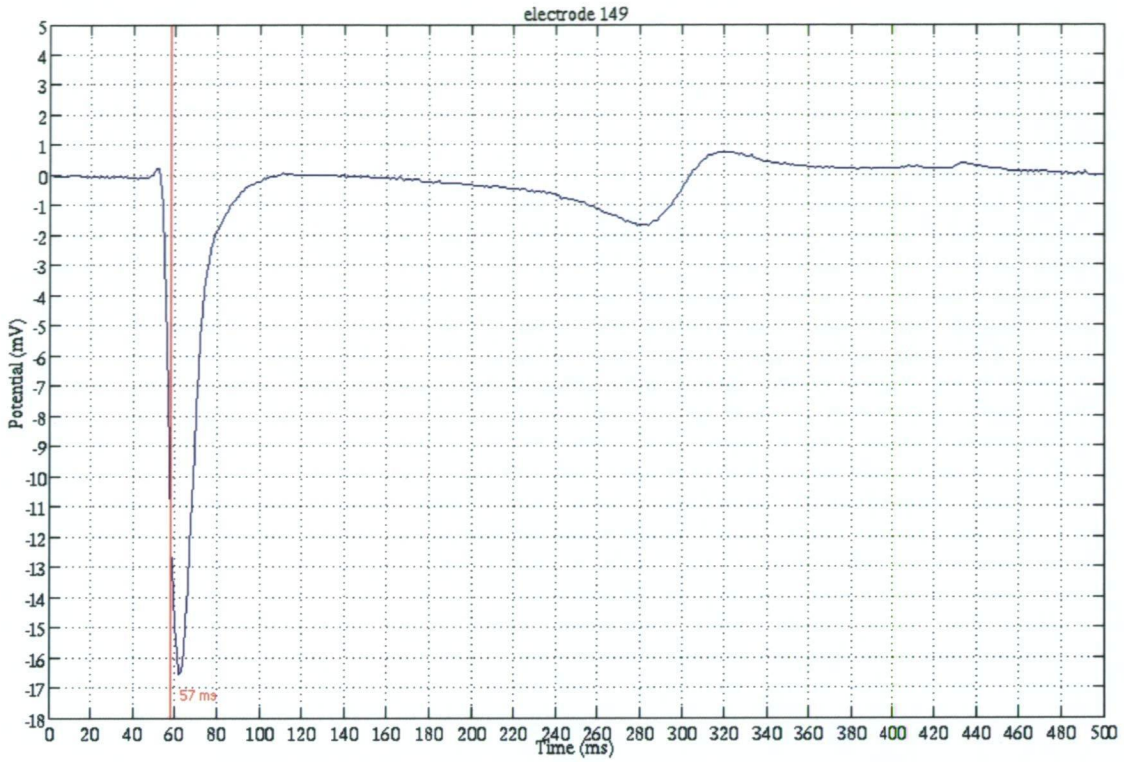


(a)

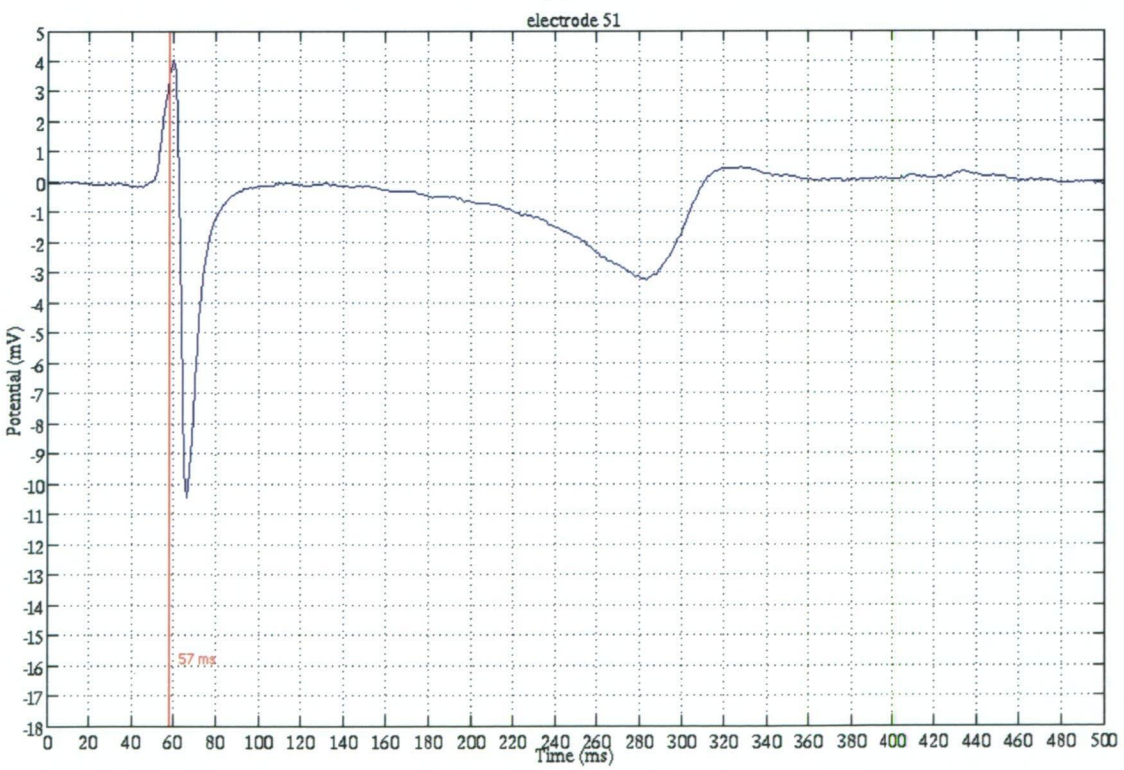


(b)

Figure 11.2: Electrograms from experiment 5, during normal sinus rhythm. Electrograms correspond to two electrode points in Figure 11.1, indexed 51 and 149. The red vertical line indicates the time instance of the potential map in Figure 11.1(a), at 57 ms.

since the positive pacing lead was at the central electrode.

For this particular experiment, the depolarising wave was initially spherical for the first 10 ms after stimulation; possibly due to the amount of tissue area stimulated, but later formed into an ellipse. The elliptical shape of the wave held until 20 ms, and then afterwards it started to become irregular, probably due to it reaching the Purkinje fibre network [67]. The propagating elliptical wave was accompanied by two maxima, however due to asymmetry, one of the maxima was significantly weaker, and only one minima was apparent. This asymmetry in the maxima may have been caused by the imbrication fibre angle [75]; which is the out-of-plane fibre angle, mentioned in Chapter 3. The orientation of the wave reflected the direction of the myocardial fibres, and was normally in the same general direction for most experiments with similar electrode array positions. Where the depolarising wave travelled along the fibres, an initial R wave occurred, followed by the intrinsic deflection of the Q wave. In the across fibre direction, no R waves occurred, only Q waves. Compared to other experiments [11, 12], the R waves were shifted down, relative to the baseline potential, that is, the potential the moment before stimulation. When the positive pacing spike had dropped down after it had peaked, it passed the baseline and became negative, at that point an R wave occurred; this can be seen in Figures 11.4(a), 11.4(d), and 11.5. This passing below the baseline may have been due to the large positive stimulus current applied, and this effect became more extreme as the current stimulus was increased. The pacing spike in Figure 11.4 seemed relatively large compared to other experiments [67]. A lower current stimulus was tried, but ventricular capture could not be achieved, and normal sinus rhythm took over.

Figure 11.5 shows an electrogram recorded at electrode 136, located in a region along the fibre direction. It did have a larger R wave compared to the other electrograms in Figure 11.4(a) and 11.4(d), since a maxima passed straight by the recording electrode, and was further away from the stimulus; but the initial rise in the R wave still started from below the baseline, like in Figures 11.4(a) and 11.4(d). The shift in the R waves below the baseline may explain the absence

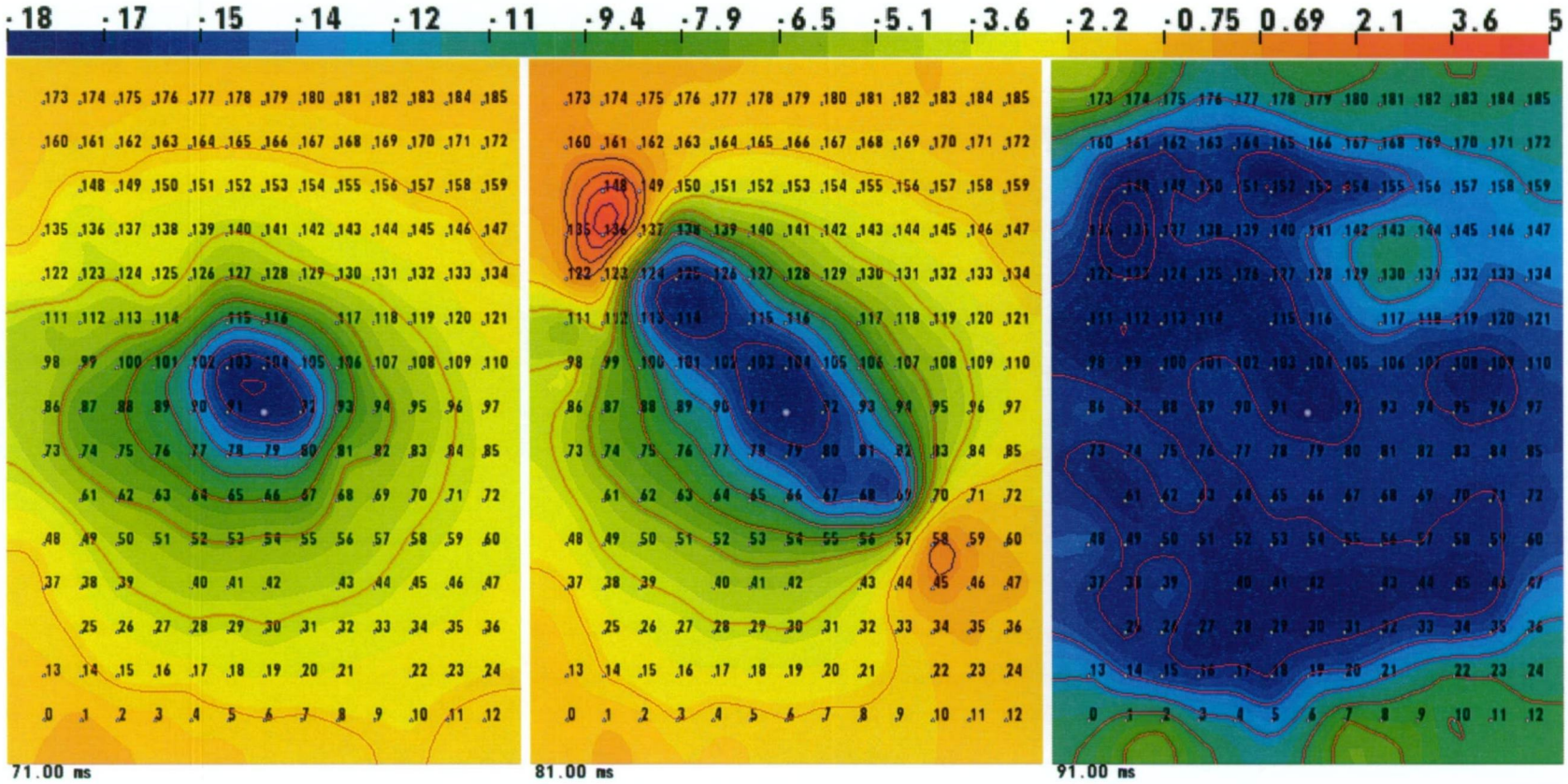


(a) 10 ms after stimulation.

(b) 20 ms after stimulation.

(c) 30 ms after stimulation.

Figure 11.3: Potential maps during epicardial pacing, at 10 ms intervals, from experiment 5. From the line passing through the ellipse outlined by the isopotential lines, the fibre direction was estimated to be around 130° from the horizontal. In the early stages of activation the wave was elliptical, but later on, became irregular.

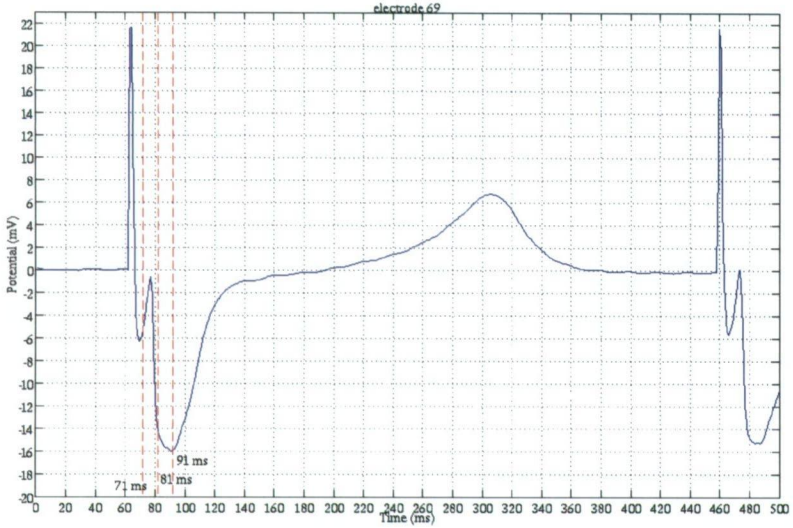


(a) electrode 69

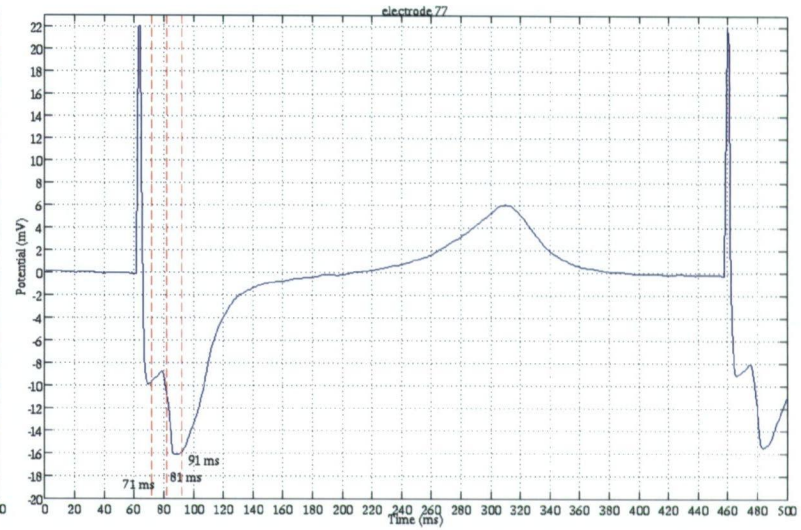


(b) electrode 77

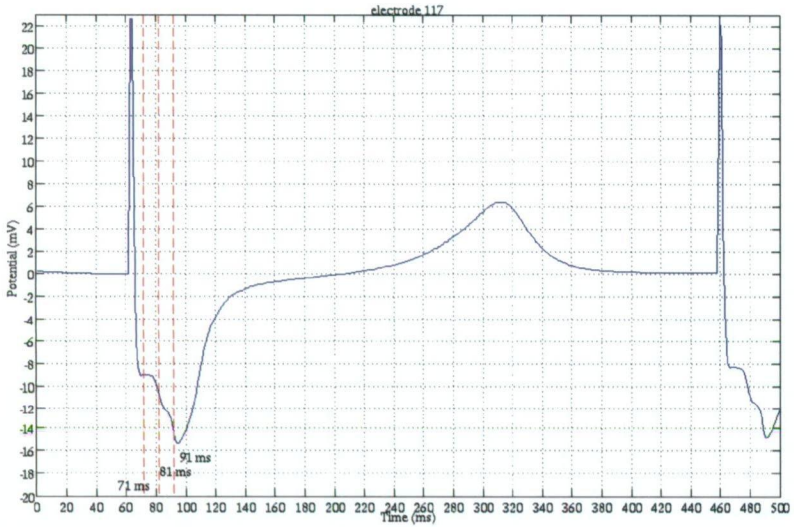


(c) electrode 117

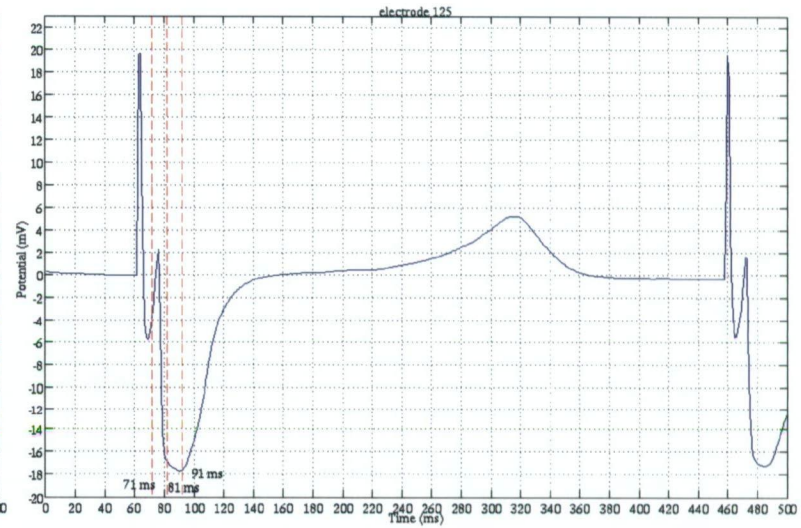


(d) electrode 125

Figure 11.4: Electrograms from experiment 5, during epicardial pacing. The positions of the electrodes that recorded these electrograms are indicated in the potential map; Figure 11.3. Electrode 77 and 117 are located in the transverse direction, while electrodes 69 and 125 are located in the longitudinal direction. The red vertical dashed lines indicates the time intervals of the maps in Figure 11.3.

of the two maxima in the first 10 *ms* after stimulation in the potential map in Figure 11.3(a).

Another feature in the electrograms was the presence of a notch in the Q waves, as observed in Figures 11.4(b) and 11.4(c), which were in the across fibre direction. This had not been seen in electrograms from other experiments of epicardial pacing [67]. The notch in the Q waves was not reproducible in two-dimensional bidomain simulations in Chapter 10, Figure 10.6(b). This may be an effect of transmural fibre rotation and orthotropic transverse conductivity [137].

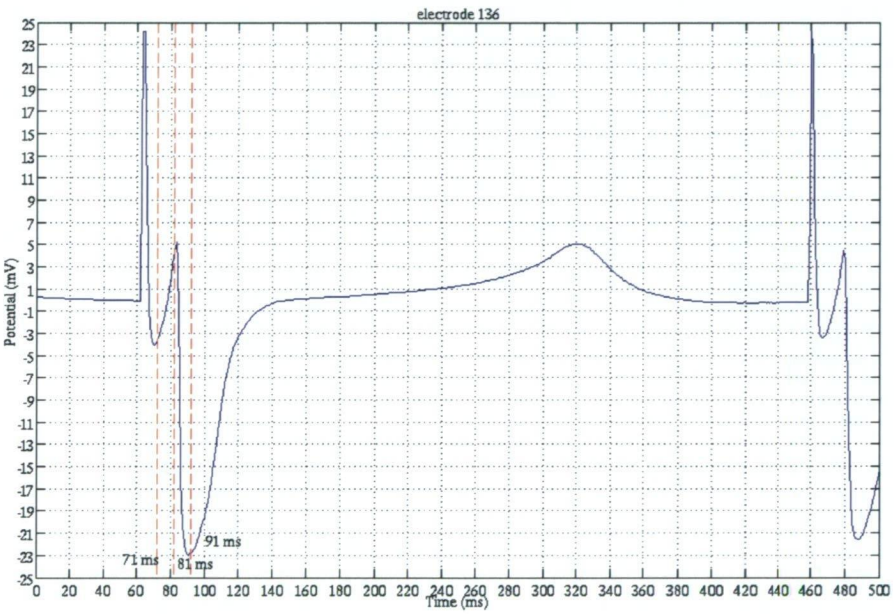


Figure 11.5: An electrogram recorded in a region where the depolarising wave travelled along the myocardial tissue fibres, at electrode 136. An initial R wave was exhibited, since a positive maxima passed by electrode 136, as shown in Figure 11.3(b). After the rise and fall of the pacing spike, an R wave occurred while still below the baseline.

## 11.3 Conductivity Estimation From Sheep Experiments

This section reports the conductivity values calculated from the data obtained from the sheep experiments. The method of solving the bidomain model and the

parameter estimation process is described in Chapter 7. The setup here is similar to the validation study in Section 10.3, but with a different sized tissue domain (still 2D), fibre direction and set of observations. The bidomain model and the observations used in the parameter estimation will be described here.

### 11.3.1 Bidomain Model

#### Computational Mesh

The tissue area was 1.98×2.74 $cm^2$. This provided a 1.42 $mm$ overhang from the left and right edges of the electrode array, and an over-hang of 1.71 $mm$ from the top and bottom. The triangular mesh had 200×276 nodes, therefore the node spacing was approximately 100 $\mu m$.

#### Fibre Direction

The fibre angle was estimated by the orientation of the major axis of the elliptical wavefront; normally when the wave had formed around 10 to 15 $ms$ after stimulation. A line was drawn through the ellipse, along the major axis, and then the angle between the major axis and the horizontal axis (x-axis) was measured with a protractor. This provided a good starting value for when it was determined in the parameter estimation.

#### Current Stimulus

To act as the pacing stimulus, current injection of opposite polarity was applied in both domains; with a magnitude of 1000 $\mu A cm^{-2}$ for intracellular and -1000 $\mu A cm^{-2}$ extracellular. The location of the stimulus site was at the centre of the domain, where the current was assigned to a group of four nodes. The duration of the current stimulus was 1 $ms$. In the experiments the duration of the current stimulus was 2 $ms$ and its strength varied between sheep, which depended on the stimulus threshold for ventricular capture (lowest was desired). The pacing device output was in $mA$ and the capture range was 0.5 to 1.5 $mA$. However,

bidomain simulations showed that the duration and the stimulus strength had no significant effect on the resulting potential distributions for activation, so the current strength of 1000 $\mu Acm^{-2}$ applied in both domains for a duration of 1 $ms$ was set for consistency in the bidomain simulations.

#### Boundary Conditions

For the boundary conditions, the potential was grounded at a site in the domain to provide a reference. For the simulation here, a group of four nodes in the bottom left-hand side of the domain was assigned to zero.

#### Solver and Time Integration

The time stepping method used to solve the time-dependent bidomain was the Crank-Nicholson scheme. The time step size was chosen to be 1 $\mu s$. Simulation of activation ranged from 15 to 20 $ms$, depending on how long the wavefront was intact after stimulation. The linear solver used was a Jacobi Preconditioned Conjugate Gradient algorithm, set to a tolerance of $10^{-4}$ mV.

#### Bidomain Model Output

The values of extracellular potential at each node in the computational mesh was written to binary file, every 0.1 $ms$ for the duration of activation. These data were used for producing potential maps. Extracellular potentials at the measurement electrode sites were written to file in ASCII format, every 0.5 $ms$. These data were used as model observations into the parameter estimation software for the calculation of the Jacobian matrix.

### 11.3.2 Data Used in Parameter Estimation

The data used as observations into the parameter estimation software was the extracellular potentials at the recording electrodes (the electrograms). The data acquisition was at 2 $kHz$, and so the data was at every 0.5 $ms$. The time of

activation was taken as the occurrence of the pacing spike, as seen in Figure 9.1. Due to the artifacts produced by the shock from the central pacing electrode, data before the first 10 *ms* of activation was not used. As mentioned above, the elliptical wavefront was intact for at least 15 to 20 *ms*. Therefore the data put into the parameter estimation software were the electrogram data from 10 to 20 *ms*, at every 0.5 *ms*. For example, the total number of observations for the 194 electrode array, for 10 to 20 *ms* of activation time, would be 3880. Though the number of observations may had been less than this because the electrogram channels which had substantial noise were omitted from the parameter estimation. As a comparison, the validation of the parameter estimation method in Section 10.3 had a total of 830 observations, for an array of 83 electrodes, for 10 *ms* of activation, and data every 1 *ms*.

### 11.3.3 Parameter Estimation

The conductivity parameters were set to values reported in the literature first, such as the values by Roberts *et. al.* [11], as initial values for the parameter estimation runs. When there were conductivity values available from the sheep data, these values were used as initial values in the next parameter estimations. Only the Least-Squares method was used in the parameter estimation, as it was found to be more robust than the SVD method. The mathematics of the Least-Squares method is described in Chapter 6; use of the software is mentioned in Section 7.2. The observations put into the PEST software was discussed above.

### 11.3.4 Results of Parameter Estimation From Sheep Experiments

Table 11.2 and 11.1 shows the results of the estimated conductivity values using Least-Squares estimation. In the first few experiments data was not usable, due to technical difficulties, so parameter estimations started from experiment 5. There were also other cases when the data were not suitable, and so, were excluded.

Table 11.1: Estimated conductivities from sheep experiment data, with positive pacing (mS/cm).

| Symbol | exp 5 | exp 7 | exp 9 |
|---|---|---|---|
| $\sigma_{il}$ | 1.186 ± 0.006 | 1.286 ± 0.006 | 0.850 ± 0.004 |
| $\sigma_{it}$ | 0.186 ± 0.002 | 0.197 ± 0.002 | 0.137 ± 0.001 |
| $\sigma_{el}$ | 8.014 ± 0.140 | 6.760 ± 0.100 | 7.963 ± 0.116 |
| $\sigma_{et}$ | 2.296 ± 0.044 | 1.701 ± 0.028 | 2.159 ± 0.036 |
| $\sigma_{il}/\sigma_{it}$ | 6.376 | 6.528 | 6.204 |
| $\sigma_{el}/\sigma_{et}$ | 3.490 | 3.974 | 3.688 |
| $\theta$ | 128.662 ± 0.183 | 130.093 ± 0.150 | 147.013 ± 0.171 |
| $r$ | 0.782 | 0.848 | 0.841 |

Positive pacing at the central electrode was used from experiments 5 to 9, with the results shown in Table 11.2. All other results used negative pacing, with the results presented in Table 11.1.

As an example, the potential output from the estimated bidomain model that used the data in experiment 5, is given in Figure 11.6. When comparing the bidomain model output to the corresponding data in Figure 11.3(b), the magnitudes of the two potential maxima are smaller, as well as the potential inside the area of the ellipse. This could be due to the asymmetry of the maxima in the elliptical wave. Looking at Figure 11.3(b) the central electrode was not locate in the centre of the ellipse, which would have effected the outcome of the estimated conductivities.

In inspecting the electrograms produced in the simulation and experiment, in Figure 11.7, there were some differences. Especially in the electrograms that were recorded in the regions where the depolarising wave travelled across the tissue fibres. The simulated electrograms were not as continuous as the measured electrograms, which was partly due to the membrane model used. The downstroke of the Q waves in the simulated electrograms did not become as negative as the experimental ones, such as in Figures 11.7(a) and 11.7(d). These discrepancies caused difficulty in fitting the model to the observations. The estimated

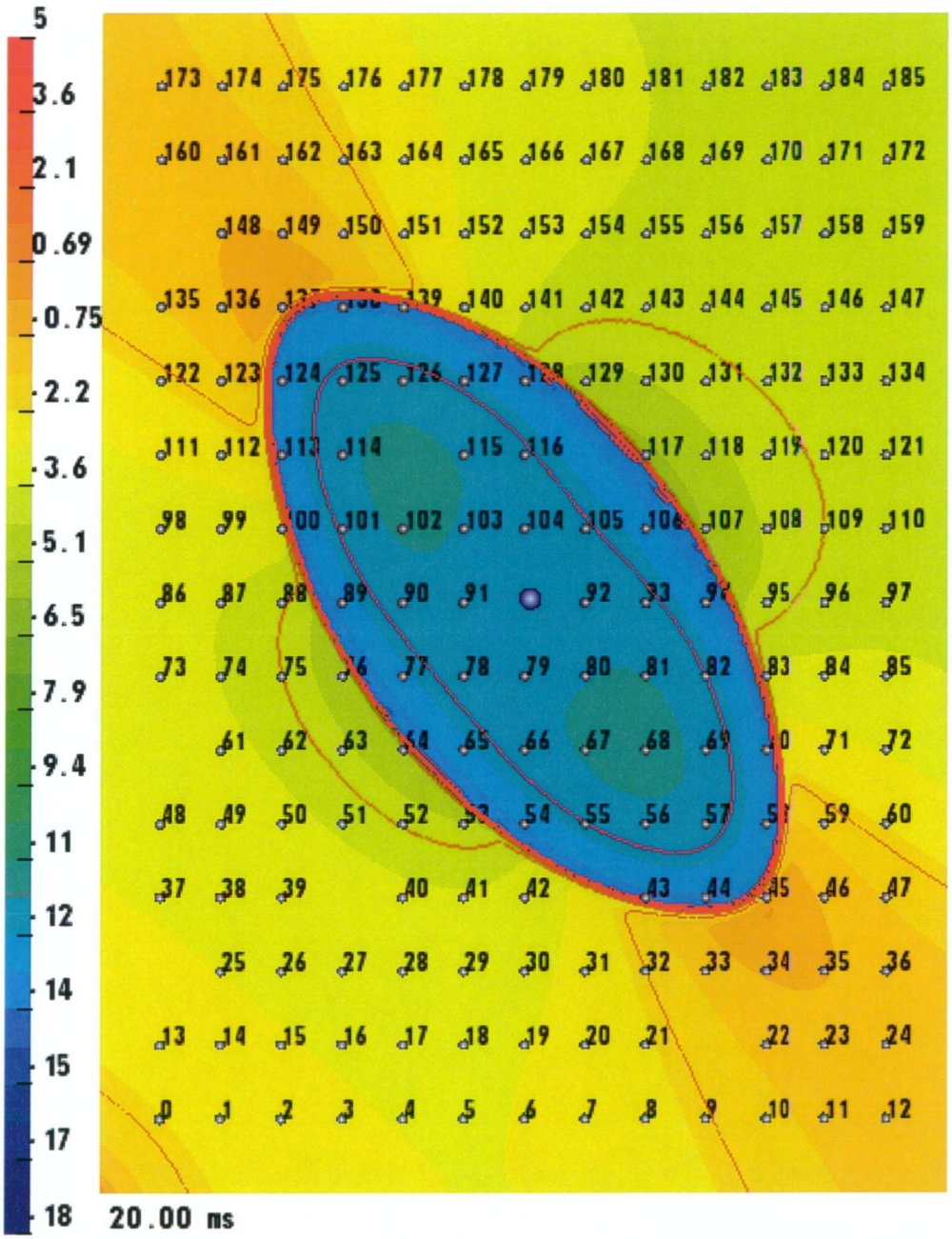


Figure 11.6: Potential map from estimated bidomain model, which used the data from experiment 5. Time was at 20 $ms$ after the onset of stimulation.

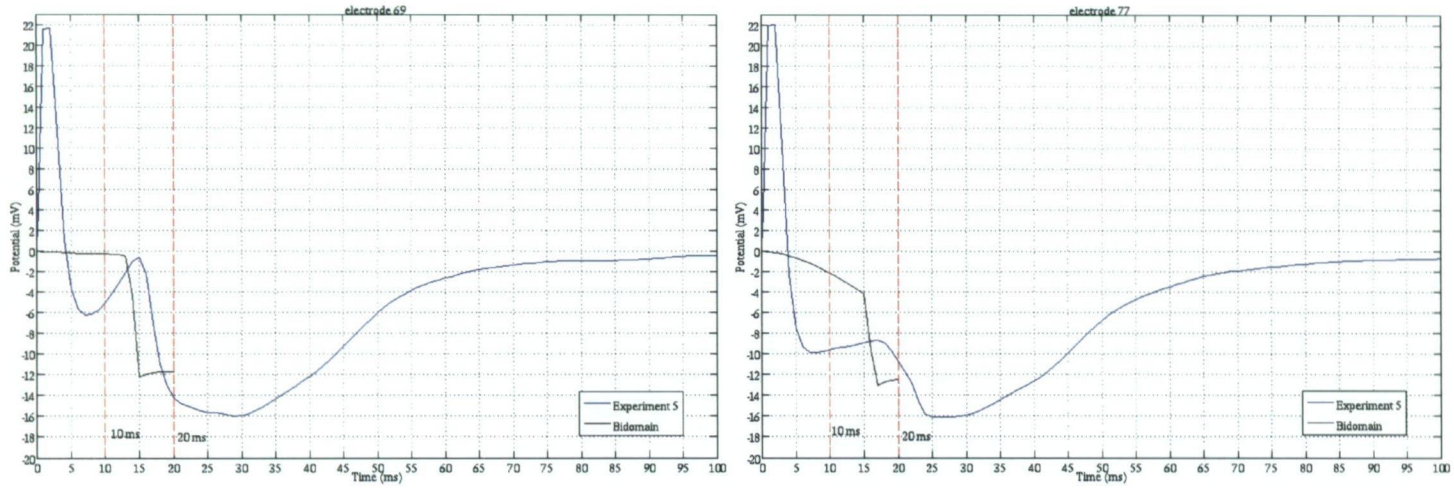


(a) electrode 69




(b) electrode 77

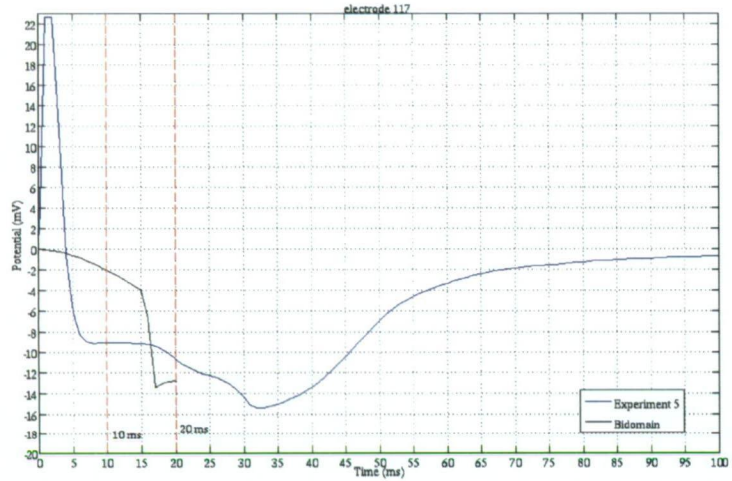


(c) electrode 117

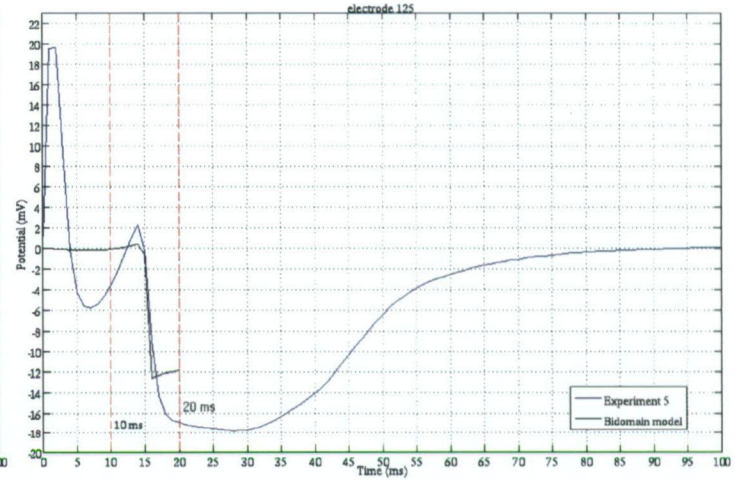


(d) electrode 125

Figure 11.7: Comparison of simulated and experimental electrograms for experiment 5. The positions of the electrodes that recorded these electrograms are indicated in the potential map; Figures 11.3 and 11.6. Electrodes 77 and 117 are located in the transverse direction, while electrodes 69 and 125 are located in the longitudinal direction. The red vertical dashed lines indicates the time intervals of the data used in the estimation of the conductivity values.

Table 11.2: Estimated conductivities from sheep experiment data, with negative pacing (mS/cm). Symbol * indicates parameter reached upper bound

| Symbol | exp. 10 | exp. 12 | exp. 13 | exp. 14 | exp. 16 | exp. 18 | exp. 19 |
|---|---|---|---|---|---|---|---|
| $\sigma_{il}$ | 0.679 ± 0.003 | 0.462 ± 0.002 | 0.741 ± 0.003 | 0.917 ± 0.005 | 1.077 ± 0.005 | 1.139 ± 0.006 | 1.032 ± 0.004 |
| $\sigma_{it}$ | 0.043 ± 0.0003 | 0.053 ± 0.0003 | 0.057 ± 0.001 | 0.070 ± 0.001 | 0.119 ± 0.001 | 0.210 ± 0.002 | 0.233 ± 0.001 |
| $\sigma_{el}$ | 3.787 ± 0.048 | 3.610 ± 0.060 | 6.470 ± 0.111 | 5.643 ± 0.093 | 6.338 ± 0.097 | 2.570 ± 0.029 | 4.930 ± 0.067 |
| $\sigma_{et}$ | 2.191 ± 0.094 | 3.000 ± 0.082 * | 3.000 ± 0.071 * | 3.000 ± 0.081 * | 2.830 ± 0.054 | 1.300 ± 0.020 | 2.809 ± 0.041 |
| $\sigma_{il}/\sigma_{it}$ | 15.790 | 8.717 | 13.000 | 13.100 | 9.050 | 5.424 | 4.429 |
| $\sigma_{el}/\sigma_{et}$ | 1.728 | 1.203 | 2.157 | 1.881 | 2.240 | 1.977 | 1.755 |
| $\theta$ | 159.443 ± 0.158 | 133.523 ± 0.208 | 146.562 ± 0.203 | 143.816 ± 0.216 | 142.643 ± 0.172 | 138.164 ± 0.140 | 165.055 ± 0.179 |
| $r$ | 0.853 | 0.815 | 0.781 | 0.776 | 0.841 | 0.890 | 0.895 |

conductivity values for the sheep experiments presented in Tables 11.1 and 11.2 are fairly different to the measured conductivities reported in the literature, shown in Table 4.8. Perhaps the estimated values are more closer to Clerc's [10] measured values. The results from the sheep data are also different to the values presented in Table 10.6 and 10.7, that were estimated from data measured by Roberts *et. al.* [11] and Baruffi *et. al.* [129] for canine hearts; described in Chapter 10. There was difficulty in estimating the conductivity values from the sheep experiment data; in some estimation runs, the extracellular transverse conductivity, $\sigma_{et}$, had values that were unrealistic, and so its upper bound was set to 3.0 $mScm^{-1}$.

When observing the potential maps from Roberts [11] and Baruffi [129], shown in Figures 10.16 and 10.21, and the potential map from experiment 5, shown in Figure 11.3, the magnitudes of the potentials in Roberts' and Baruffi's data was larger. For example, in the two maxima, and the area inside the ellipse. The isopotential lines in Roberts' and Baruffi's data were also closer together, which indicated that the downstroke of the Q waves were more rapid, and so, was more suited to the Luo-Rudy membrane model. All these factors would have contributed to the different values estimated from the sheep experiment data. The correlation coefficient was normally around 0.8, though would not be acceptable if a value of 0.9 was required for a good fit between observations and model [152]. For further comparison, another example of the potential output from an estimated bidomain model is given in Figure 11.9, for experiment 16 (negative pacing). When comparing these data to the interpolated potential map from experiment, in Figure 11.8, there appeared to be smaller potential magnitudes inside the area of the ellipse, at 15 $ms$ and 20 $ms$ after stimulation. The isopotential lines that outlined the ellipse were also more tightly packed than observed in experiment. When looking at both of the bidomain estimated and experimental electrograms in Figure 11.10, the Q waves in the experimental electrograms were more sloped. Since the parameter estimation was based on observations for 10 to 20 $ms$ after the onset of stimulation, the Q waves had not reach its minimum value yet, since its deflection was more gradual, and so the

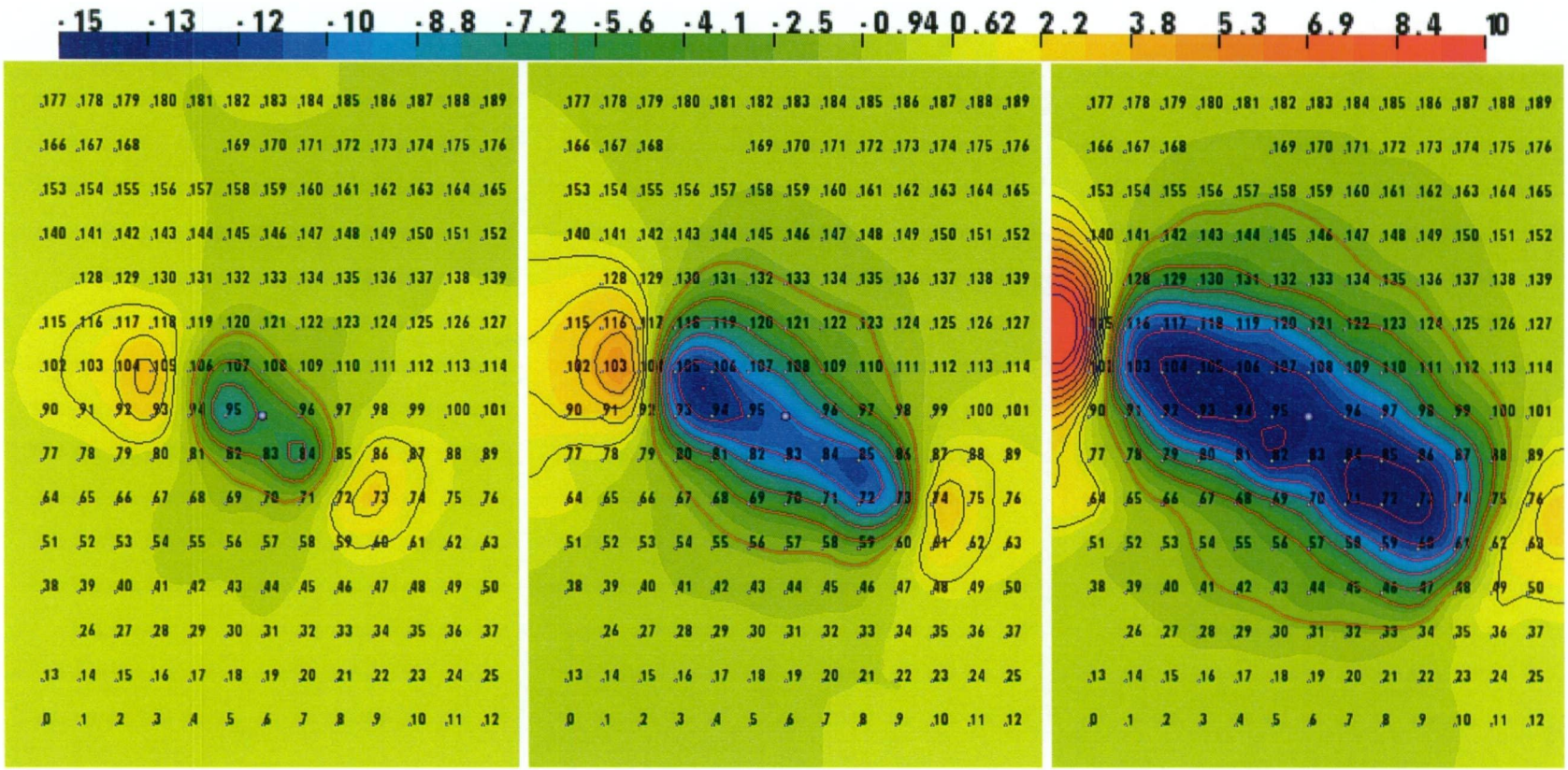


(a) 10 ms after stimulation. (b) 15 ms after stimulation. (c) 20 ms after stimulation.

Figure 11.8: Potential maps during negative epicardial pacing, at 5 ms intervals, from experiment 16.

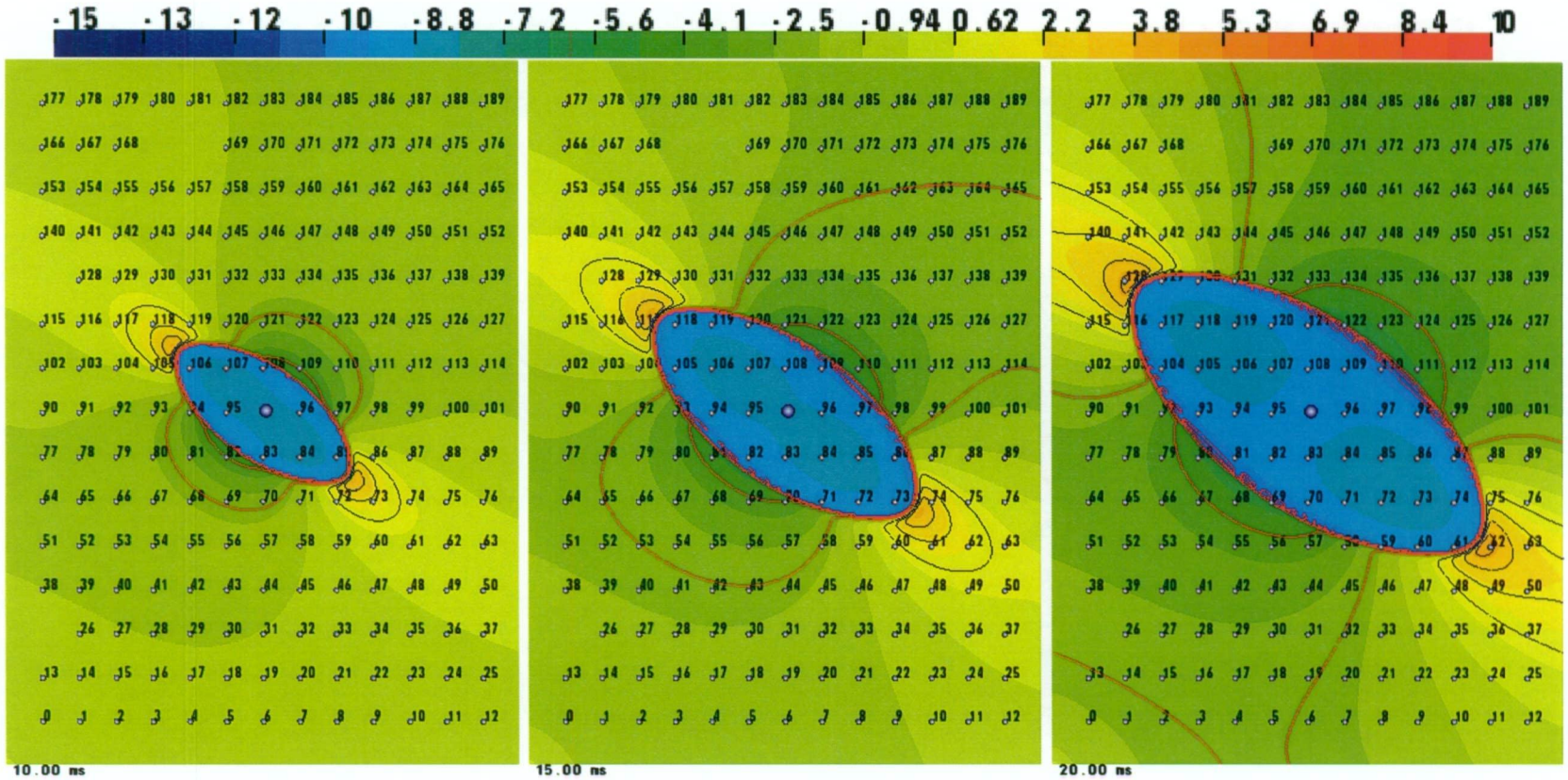


(a) 10 ms after stimulation.

(b) 15 ms after stimulation.

(c) 20 ms after stimulation.

Figure 11.9: Potential maps, at 5 ms intervals, from estimated bidomain model, for experiment 16.

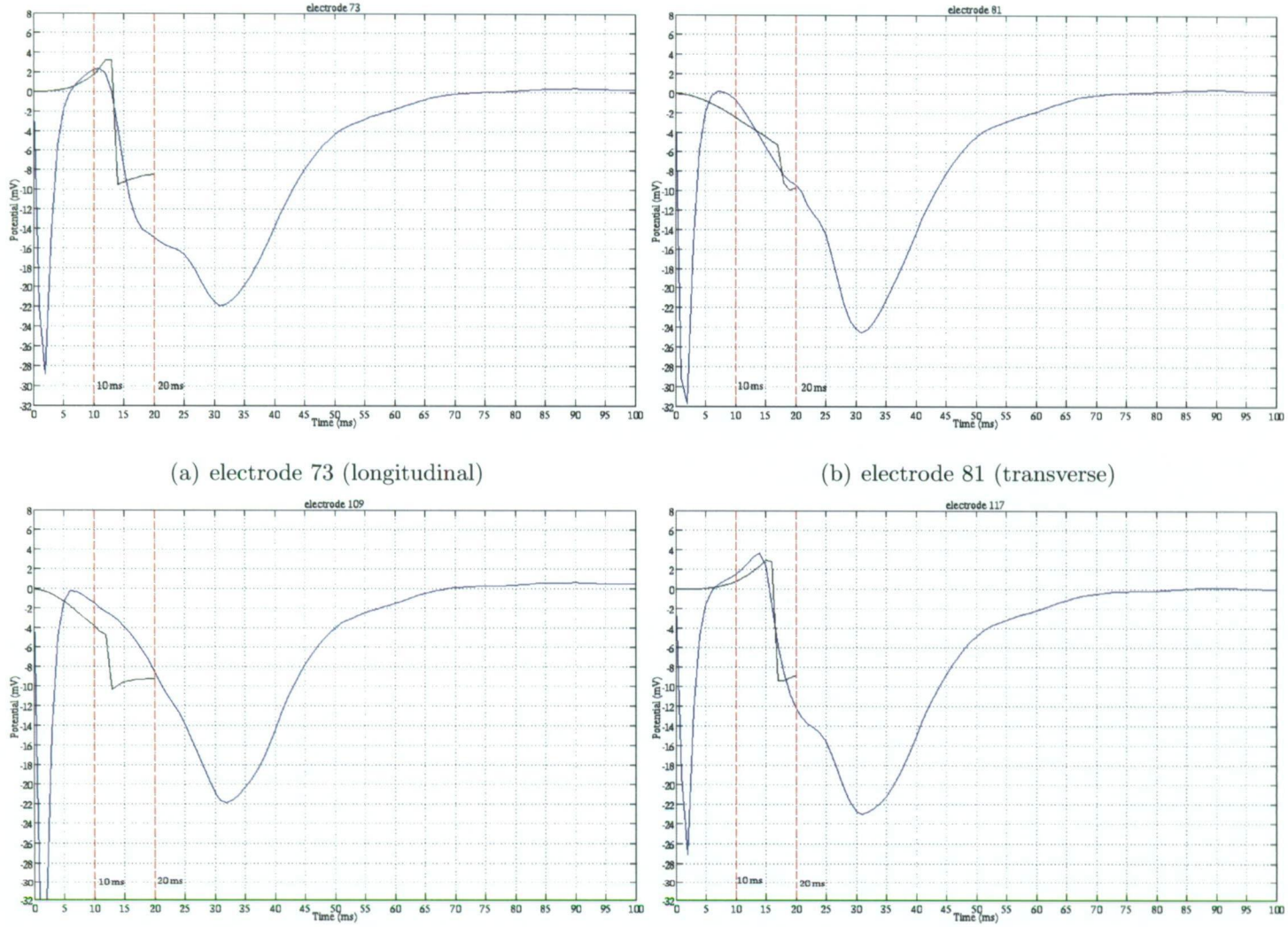


(a) electrode 73 (longitudinal)

(b) electrode 81 (transverse)

(c) electrode 109 (transverse)

(d) electrode 117 (longitudinal)

Figure 11.10: Comparison of simulated and experimental electrograms, for experiment 16. The positions of the electrodes that recorded these electrograms are indicated in the potential map; Figures 11.8 and 11.9. Electrodes 81 and 109 are located in the transverse direction, while electrodes 73 and 117 are located in the longitudinal direction. The red vertical dashed lines indicates the time intervals of the data used in the estimation of the conductivity values.

conductivity values were estimated such that the bidomain model produced less negative potentials. It can be seen in Figure 11.10 that the recovery phase occurs earlier in the estimated bidomain electrograms, resulting in the magnitude of the negative potentials to be lower. Parameter estimations for longer periods of time were tried, so that the Q waves had enough time to reach its minimum value, but they did not perform well, since the elliptical depolarising wave became irregular, and so did not properly reflect the anisotropy.

Most of the experiments produced electrograms with Q waves that were more gradual than the model. However there was one experiment, experiment 18, which produced Q waves with more rapid downstrokes, which gave observations more closer to Roberts' [11] and Baruffi's [129] measurements. Hence, the parameter estimation from these data produced values more similar to the ones estimated from Roberts data [11], shown in Table 10.6; with similar anisotropy ratios. When observing the depolarising wave from experiment 18, in Figure 11.11, it can be seen that the magnitudes of potential were higher than the other experiments, with attention to the two maxima, and the area inside the ellipse. The isopotential lines that outlined the ellipse were also more tightly packed. In looking at the comparison between model estimated and experimental electrograms in Figure 11.13 it can been seen that there was a closer match, especially for the electrograms in the longitudinal directional Figures 11.13(a) and 11.13(d). However there was still considerable miss-match in the electrograms for the transverse direction, and generally, the minimum of the Q waves in the model electrograms were not as negative.

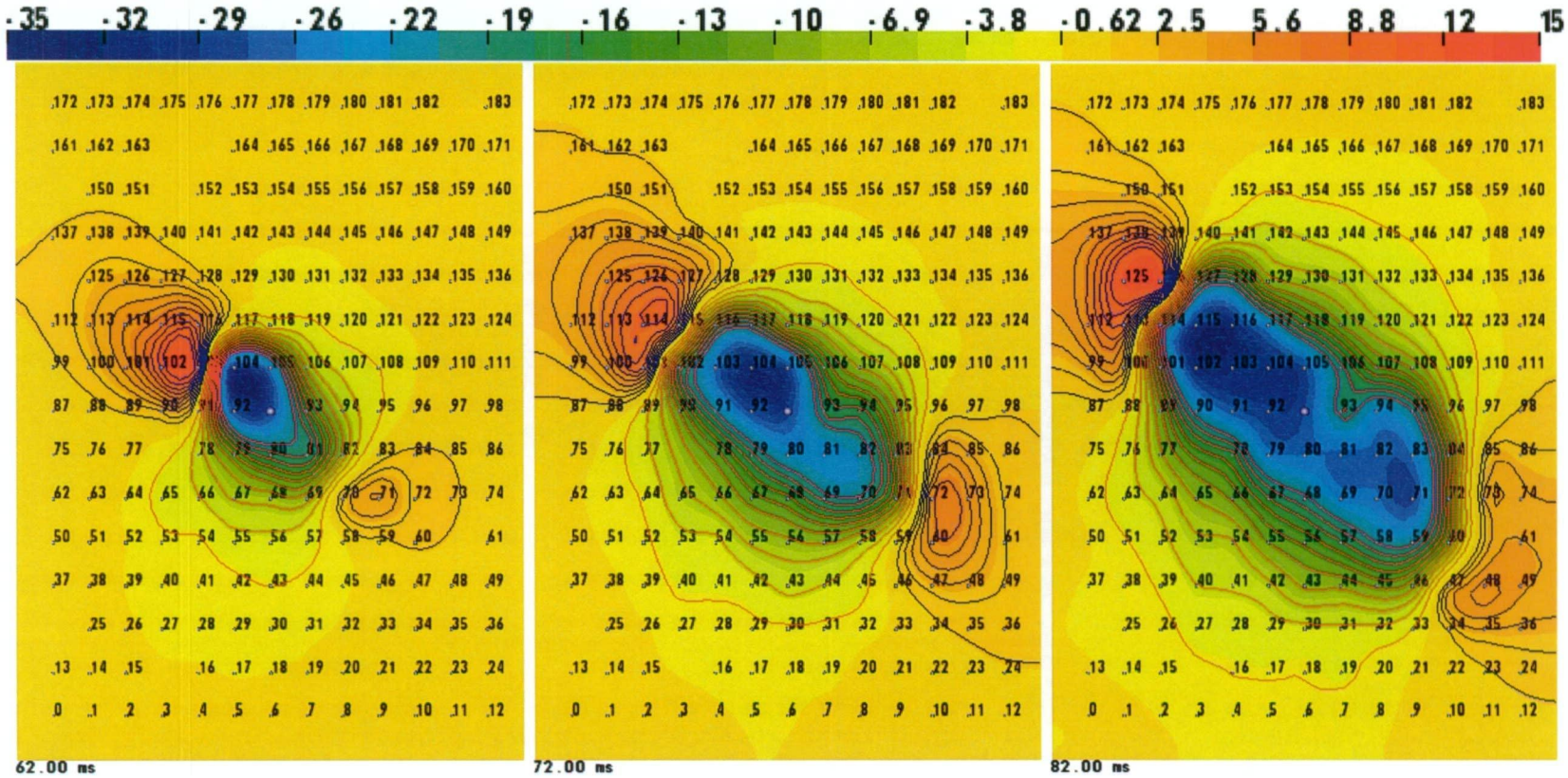


(a) 10 ms after stimulation. (b) 15 ms after stimulation. (c) 20 ms after stimulation.

Figure 11.11: Potential maps during negative epicardial pacing, at 5 ms intervals, from experiment 18.

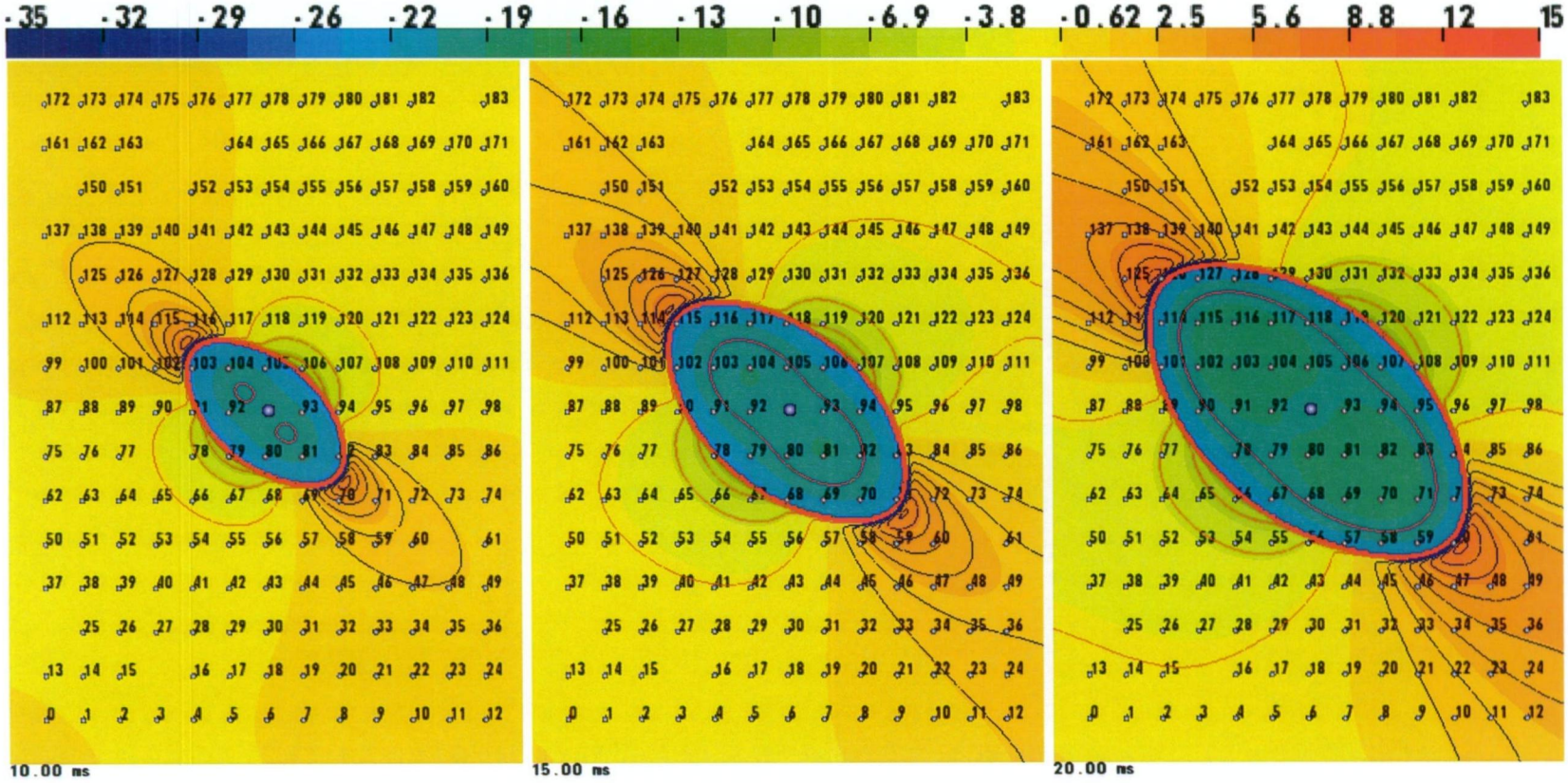


(a) 10 ms after stimulation. (b) 15 ms after stimulation. (c) 20 ms after stimulation.

Figure 11.12: Potential maps, at 5 ms intervals, from estimated bidomain model, for experiment 18.

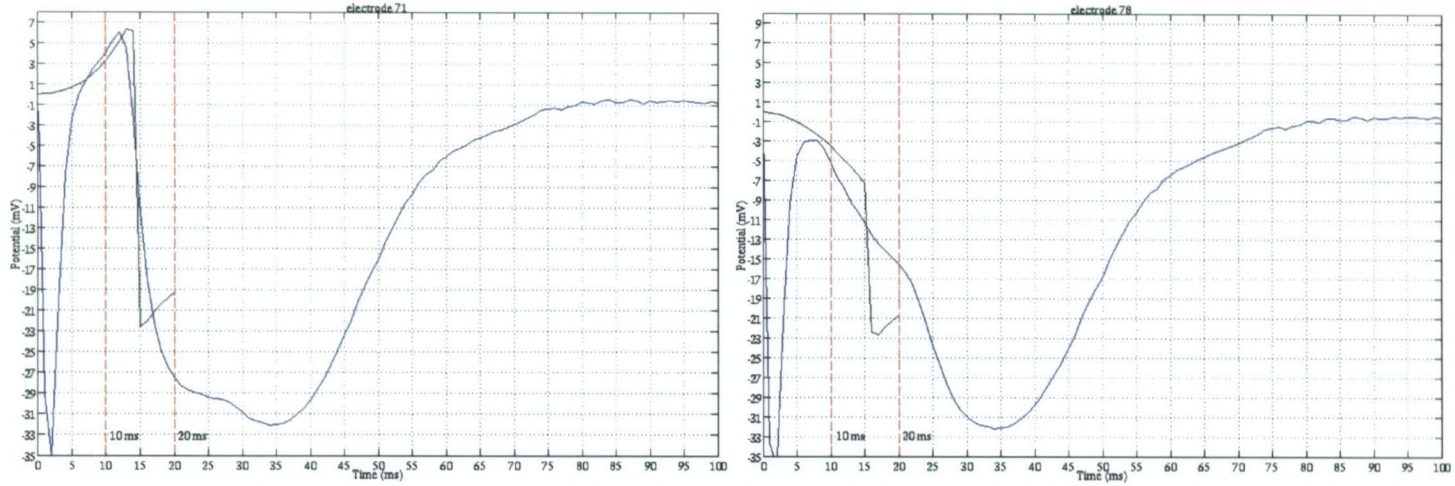


(a) electrode 71 (longitudinal)




(b) electrode 78 (transverse)

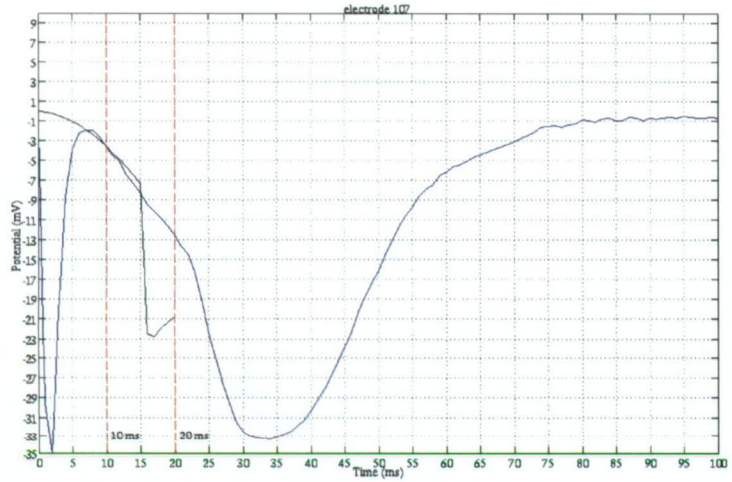


(c) electrode 107 (transverse)

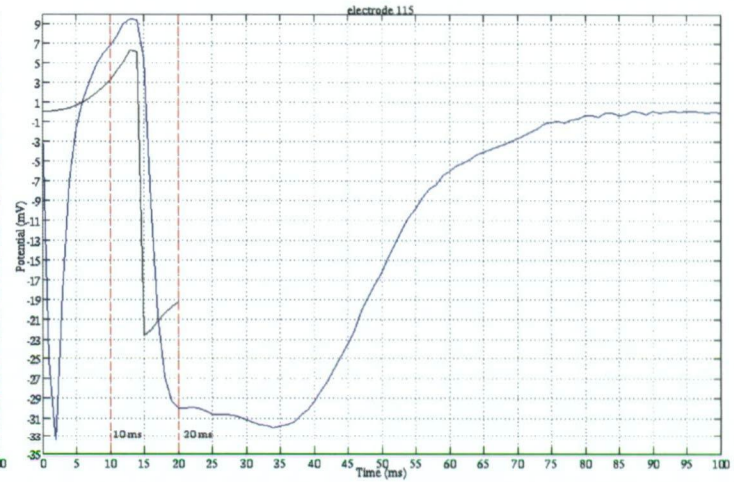


(d) electrode 115 (longitudinal)

Figure 11.13: Comparison of simulated and experimental electrograms, for experiment 18. The positions of the electrodes that recorded these electrograms are indicated in the potential map; Figures 11.11 and 11.12. Electrodes 78 and 107 are located in the transverse direction, while electrodes 71 and 115 are located in the longitudinal direction. The red vertical dashed lines indicates the time intervals of the data used in the estimation of the conductivity values.

# Chapter 12

# Investigations

## 12.1 Estimating Membrane Parameters

The parameter estimation results from the sheep experiment data in Chapter 11 were perhaps, not convincing. There was considerable miss-match between model and observations for the majority of the experiments. The major problem was the slope of the Q waves in the electrograms from the experiment being more gradual than the ones produced in the computational model. The slope is mainly determined by the membrane model, which is incorporated into the bidomain model. The membrane model contains parameters which govern the rate-of-rise of the action potential. This lead to an investigation into including the membrane model parameters in the estimation.

### 12.1.1 Modified FitzHugh-Nagumo Membrane Model

The Luo-Rudy membrane model [51, 52] is a sophisticated model, which contains many parameters; it is difficult to determine which combination of parameters to adjust, for the rate-of-rise of the action potential. Therefore, a simpler model, a modified version of the FitzHugh-Nagumo [193] was used. This model is governed by a reaction-diffusion system of two equations, which mimic the flow of sodium and potassium ions across the cell membrane. A modified FitzHugh-Nagumo

membrane model for cardiac tissue can be given by [194, 191]:

$$\frac{d\Phi_m}{dt} = C_1\Phi_m\left(\frac{\Phi_m}{\Phi_{m(thresh)}} - 1\right)\left(1 - \frac{\Phi_m}{\Phi_{m(peak)}}\right) - C_2\Phi_m w, \tag{12.1}$$

$$\frac{dw}{dt} = C_3(\Phi_m - C_4 w). \tag{12.2}$$

where $\Phi_{m(thresh)}$ is the threshold transmembrane potential (5 $mV$ from rest), $\Phi_{m(peak)}$ is the peak transmembrane potential (100 $mV$ from rest), and $w$ is a recovery variable. The parameters in the equations can be selected to give the shape of action potential upstroke and recovery of choice. Parameters $C_3$ and $C_4$ were set to 0.015 and 0.005 respectively [191]; the parameters $C_1$ and $C_2$ were estimated. To obtain a more desired upstroke in the action potential, with the control of parameters $C_1$ and $C_2$, Equation (12.1) was modified by including a *tanh* function, similar to the Fenton-Karma membrane model of three variables [195, 196, 197]:

$$\frac{d\Phi_m}{dt} = C_1 tanh(\Phi_m)\left(\frac{\Phi_m}{\Phi_{m(thresh)}} - 1\right)\left(1 - \frac{\Phi_m}{\Phi_{m(peak)}}\right) - C_2 tanh(\Phi_m) w. \tag{12.3}$$

The *tanh* function allowed for flexibility in adjusting the slope of the action potential upstroke.

### 12.1.2 Estimating Parameters from Synthetic Data

To test if the parameter estimation method could successfully calculate the $C_1$ and $C_2$ parameters in the modified FitzHugh-Nagumo membrane model, parameter estimation runs were performed with synthetic data, similar to the validation in Section 10.3; with the same bidomain model. The only modelling feature that had changed was that the simpler modified FitzHugh-Nagumo membrane model was used instead of the Luo-Rudy membrane model. Synthetic data used in the estimation were the potentials at the recording electrodes, for a duration of 10 $ms$ into activation, from $t$=0 to $t$=10 $ms$, for every 1 $ms$ time steps. No random noise was added into the synthetic data. In the model for generating the synthetic data, the bidomain conductivity values used were the ones measured by Roberts

Table 12.1: Estimated conductivities and membrane parameters by Least-Squares from synthetic data with 0 % noise $mScm^{-1}$.

| Symbol | Orig. | LS |
|---|---|---|
| $\sigma_{il}$ | 2.800 | 2.789 ± 0.009 |
| $\sigma_{it}$ | 0.260 | 0.268 ± 0.001 |
| $\sigma_{el}$ | 2.200 | 2.198 ± 0.013 |
| $\sigma_{et}$ | 1.300 | 1.286 ± 0.005 |
| $C_1$ | 2.200 | 2.211 ± 0.016 |
| $C_2$ | $1.00\times10^{-4}$ | $1.049\times10^{-4} \pm 1.077\times10^{-5}$ |
| $r$ | - | 0.981 |

*et. al.* [11]; these were used in the previous validation. The membrane parameter values for $C_1$ and $C_2$ where 2.20 and $1.00\times10^{-4}$; these were chosen since they give a rate-of-rise similar to what was observed in the sheep experiments. At the beginning of the estimation the conductivity values started at 1 $mScm^{-1}$; the membrane parameters started at 2.00 for $C_1$ and 0.001 for $C_2$. The results from the estimation is presented in Table 12.1. The estimation was sucessful at arriving to the original values.

### 12.1.3 Estimating Parameters from Sheep Data

Estimations were performed on the sheep data. The bidomain model used was the same as in the previous Chapter, with the changes to the membrane model. The same data was used. The results from the estimation runs, for determining the conductivities, local fibre angle, membrane capacitance, and membrane model parameters, are shown in Table 12.2. Data from experiment 16 and 18 were used as an example. The estimated bidomain model output, for the experiment 18 data, is shown in Figure 12.1. It can be seen that the isopotential lines were spaced more widely when compared with the data using the Luo-Rudy membrane model in Figure 11.12. In looking at the electrograms in the Figure 12.2, it can be seen that the slopes of the Q waves were more gradual. A greater fit was

achieved with correlation values above 0.9. Though, there were still discrepancies between model and experiment; the model seemed to produce Q waves that were too gradual in the longitudinal direction, and too steep in the transverse direction, as shown in Figures 12.2(d) and 12.2(b). The Q waves were also not as negative as the experimental ones. When observing an electrode far away from the stimulus, for example, electrode 168 in Figure 12.1, the bidomain simulated electrogram appeared to become negative earlier than the one in the experiment. This was thought to be an effect of the drift in the reference potential [117, 198], since in the bidomain, the potential was referenced to a ground, while in the experiment, the potential was referenced to a remote electrode a finite distance away, located on the animals body. Therefore, estimations were run for bidomain simulations referenced to an electrode located in the right hand corner of the domain; electrode 183. A general positivity was added to the electrograms when referenced to a remote electrode; in Figure 12.3 the bidomain model electrogram referenced to a corner electrode was a closer match to the experimental electrogram. Though, it was more positive, since the reference electrode was confined to the model domain, where as in the experiment, it was located further away. The estimated parameters were different when referenced to the corner electrode, but the change in correlation was not significant. The estimated electrograms in Figures 12.2 and 12.3 were generally more positive.

Table 12.2: Estimated conductivities and membrane parameters $mScm^{-1}$.

| Symbol | exp. 16 | exp. 18 | exp. 16 (ref) | exp. 18 (ref) |
|---|---|---|---|---|
| $\sigma_{il}$ | 1.369 ± 0.029 | 2.413 ± 0.377 | 1.259 ± 0.021 | 2.178 ± 0.342 |
| $\sigma_{it}$ | 0.259 ± 0.004 | 0.439 ± 0.069 | 0.248 ± 0.003 | 0.595 ± 0.100 |
| $\sigma_{el}$ | 7.416 ± 0.130 | 4.510 ± 0.698 | 9.662 ± 0.149 | 5.076 ± 0.815 |
| $\sigma_{et}$ | 2.931 ± 0.045 | 2.502 ± 0.393 | 2.729 ± 0.044 | 2.586 ± 0.422 |
| $\sigma_{il}/\sigma_{it}$ | 5.286 | 5.497 | 5.077 | 3.661 |
| $\sigma_{el}/\sigma_{et}$ | 2.530 | 1.803 | 3.540 | 1.963 |
| $\theta$ | 146.655 ± 0.394 | 140.238 ± 0.291 | 141.980 ± 0.292 | 137.854 ± 0.423 |
| $C_m$ | 0.144 ± 0.003 | 0.440 ± 0.066 | 0.337 ± 0.004 | 0.390 ± 0.066 |
| $C_1$ | 0.434 ± 0.016 | 2.166 ± 0.366 | 2.068 ± 0.048 | 1.783 ± 0.366 |
| $C_2$ | $2.697\times10^{-3} \pm 4.077 \times 10^{-5}$ | $1.042 \times10^{-4} \pm 2.221 \times 10^{-5}$ | $6.685 \times10^{-3} \pm 2.584 \times 10^{-3}$ | $1.510 \times10^{-4} \pm 3.965 \times 10^{-6}$ |
| $r$ | 0.921 | 0.939 | 0.894 | 0.931 |

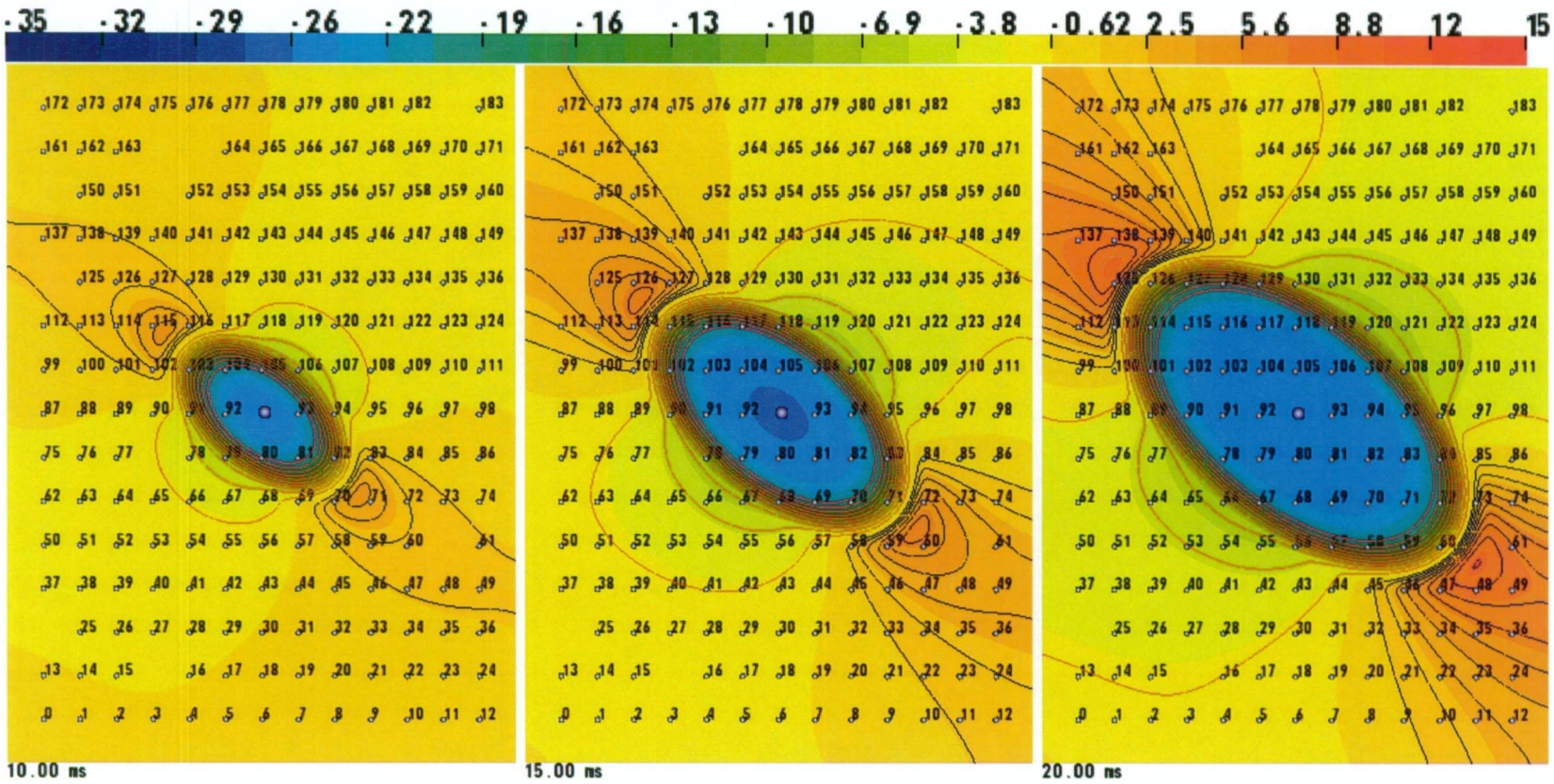


(a) 10 ms after stimulation.

(b) 15 ms after stimulation.

(c) 20 ms after stimulation.

Figure 12.1: Potential maps, at 5 ms intervals, from estimated bidomain model, for experiment 18. Membrane parameters were also estimated for the modified FitzHugh-Nagumo membrane model.

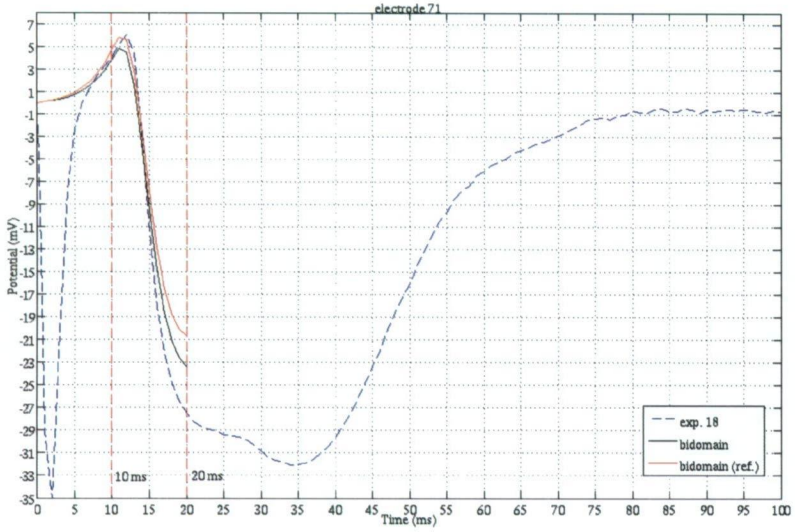


(a) electrode 71 (longitudinal)

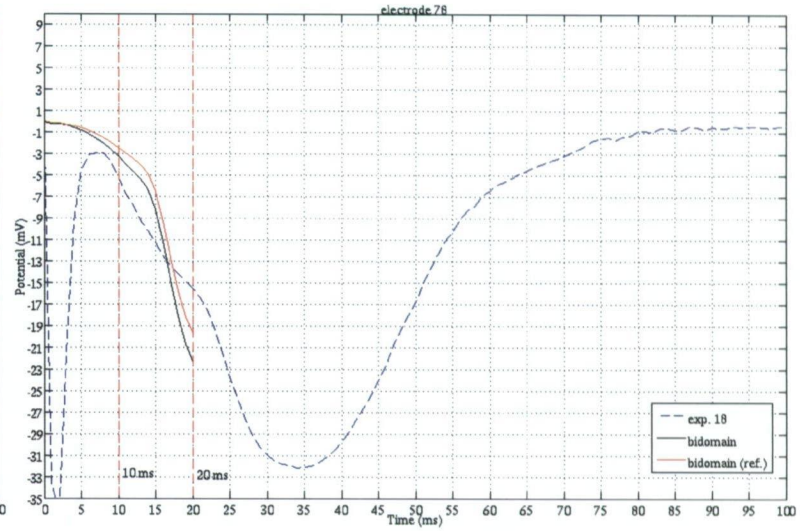


(b) electrode 78 (transverse)

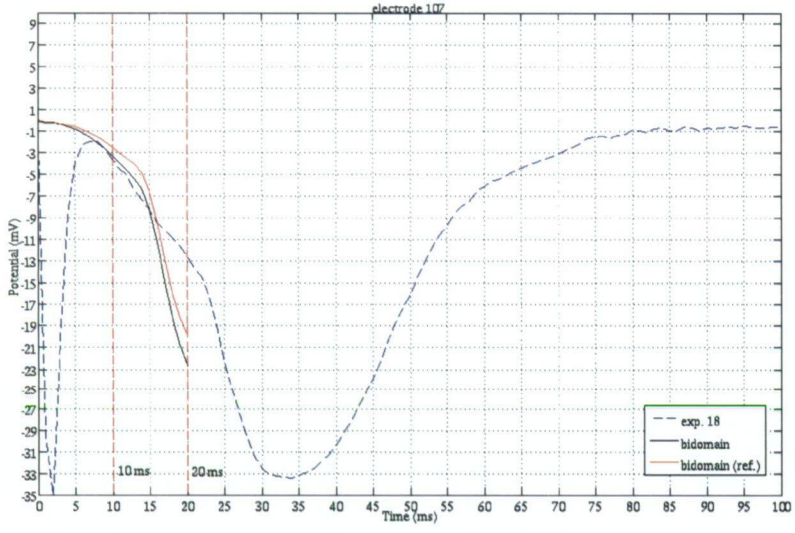


(c) electrode 107 (transverse)

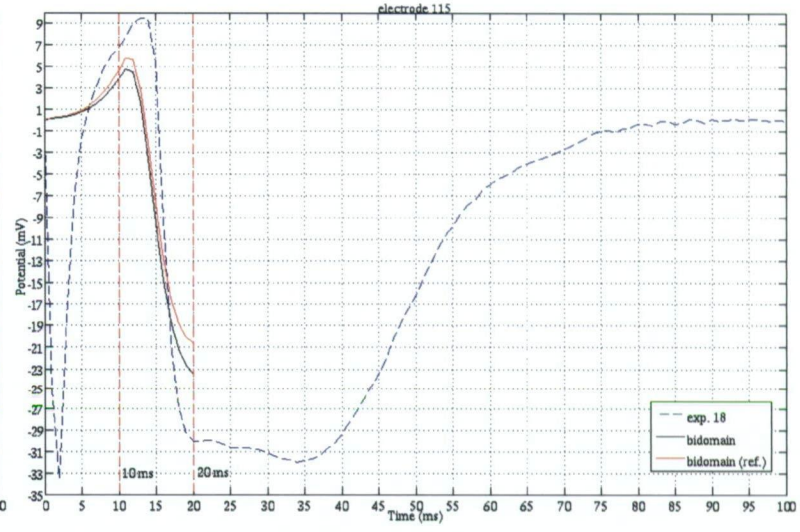


(d) electrode 115 (longitudinal)

Figure 12.2: Comparison of simulated and experimental electrograms, for experiment 18, using the FitzHugh-Nagumo membrane model. Electrograms with reference to a electrode located in the top right hand corner of the domain were also shown.

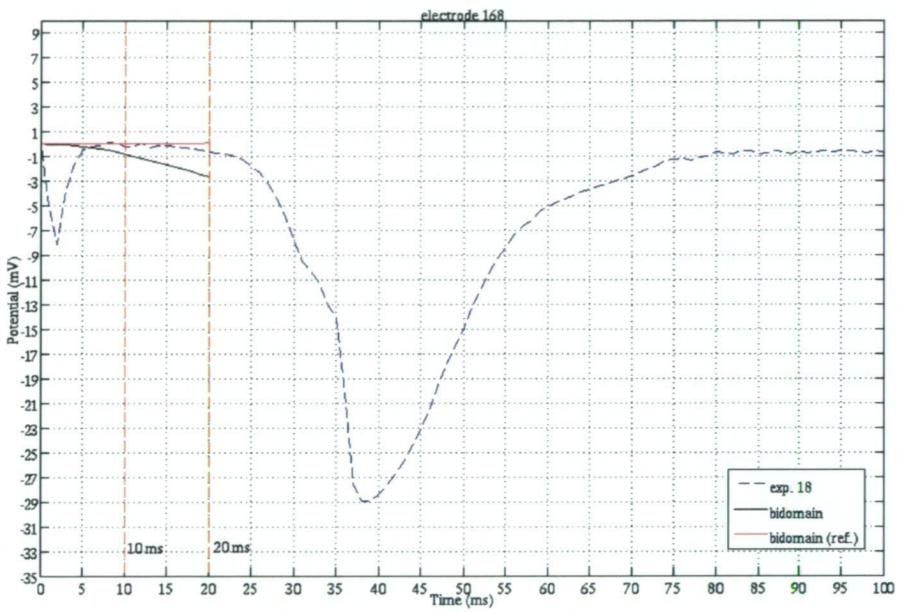


Figure 12.3: Comparison of simulated electrograms with reference to zero, and to a corner electrode, for experiment 18, using the FitzHugh-Nagumo membrane model. The electrograms were recorded at electrode 168, far away from the point of stimulation. The blue dotted line was experiment, black solid line was the bidomain model referenced to ground, and the red solid line was the bidomain model referenced to a remote electrode.

# Chapter 13

# Discussion

The reason for determining the bidomain conductivities was that there are several different sets of values reported in the literature; when they are used in bidomain simulations they each produce significantly different results in potential distributions [18, 190]. It is important to determine a set of conductivity values that produce data consistent with observations; the inverse problem of electrocardiology, the study of heart diseases, and the development of medical devices would benefit from a set of accurate bidomain conductivity values.

It was confirmed in Section 10.1 that different sets of conductivity values produced significantly different simulation output. Features such as the shape of the elliptical wave, and the potential maxima were influenced by the set of conductivities used. Information such as the local fibre direction was reflected by the orientation of the elliptical wave. When inspecting the electrograms, the R and Q waves differed in magnitude and time for different sets of conductivity values. The simulation study in Section 10.2 showed that intramural fibre rotation has a significant effect on the potential distribution; causing the propagation of the elliptical activating wave to undergo transmural rotation. It also contributes to the asymmetries observed, such as the offset of the two positive maxima from the major axes of the ellipse.

A validation for the parameter estimation method was described in Section 10.3. Least-Squares and Singular Value Decomposition methods were used in the

estimation of the bidomain conductivities. For the validation, synthetic data, generated from a bidomain model with a set of known conductivity values, was used with a percentage of random Gaussian noise. The conductivity values were able to be retrieved back, close to their original values. Other parameters in the bidomain model could also be estimated, such as the local fibre direction, and membrane capacitance. Data from experiments reported in the literature were also used to test the method.

In Chapter 11, results of parameter estimation runs from sheep data were presented. Unipolar electrograms were recorded, while pacing the epicardium of the sheep's heart. The results raised concerns with miss-match between model output and experimental observations. Attempts were made to achieve a closer fit, such as taking into account the reference potential, and modifying the rate of rise of the action potential. The following sections discuss the issues that came about when determining the bidomain conductivities of heart tissue.

## 13.1 Parameter Estimation

Normally the four-electrode method is applied to determine the bidomain conductivities, and has had recent attention in theoretical [14, 19, 113, 184, 185, 183], and experimental [101, 13] studies. This method requires small electrode separation to ensure that current is only measured in extracellular space. It was thought that with the current resources at hand to develop electrodes with small separations, and then applying them in in vivo experiments, would have been difficult. Also, since small electrode spacings are needed in the micro range [19], the bidomain model may not properly represent the bioelectric potential at this level, since it is based on macroscopic scales.

In this thesis, a new approach has been developed, which involves measurement of extracellular potential at macroscopic scales, with techniques of potential mapping that have been around for many years [11, 67]. Data can be obtained with electrodes that could be easily made, with materials available at

hand [176, 175], and a full time-dependent bidomain model is used. The inverse problem is overly-posed, since there are many more observations than estimable parameters [147]. The method takes advantage of parallel computing [158, 160], developments in bidomain modelling [170, 54], and computer visualisation [165, 55], which would have not been available at the current level to investigators measuring cardiac resistivity before [10, 11, 12].

The bidomain conductivity values were determined by finding the optimum set, which minimised the difference between model output and experimental observations. The effect of each parameter had on the residuals was determined by running the forward model a number of times to construct a Jacobian matrix. With Least-Squares or SVD methods, parameters were able to be estimated, as explained in Chapter 6. Determining conductivity and local fibre angle, from synthetic data, for a two-dimensional bidomain with Least-Squares was successful. Though, when membrane capacitance was included into the estimation, all the parameters were not retrieved back to their original values, since the inverse problem was more ill-posed. However, with a tighter convergence criterion, the estimated parameters were closer to their original values. The tradeoff was a longer computational time; this may be a problem when determining more parameters such as for a three-dimensional bidomain, when simulation times are significantly longer.

Shorter run times would be desirable for three-dimensional simulations, but it is important to calculate reliable derivatives for the Jacobian matrix. Accurate derivative calculation depends on accurate calculation of model output, and so, the parameter estimation would benefit. It would be best to set the numerical solver tolerance to a more stricter condition, but the compromise is greater convergence times. Setting the solver tolerance less stricter would result in model output with less precision, therefore the calculated derivatives would be degraded. This may effect the success of obtaining the optimum set of parameters. Even if the optimum set may be found, many more model runs would be needed for more optimisation iterations, to make up for the imprecision of derivatives.

Other ways of reducing computational time could be achieved by reducing the coarseness of the computational mesh, and by increasing the time-step size, though it may result in numerical instability, and degradation of simulation output. Faster simulation times may also be achieved by incorporating a less complex membrane model into the bidomain, such as the FitzHugh-Nagumo membrane model [193], instead of the complex Luo-Rudy membrane model [51, 52]. Though, the membrane kinetics may be too simple and not accurately represent the electrophysiological behaviour. Then the estimated parameters may only be as accurate as the model it was derived from.

## 13.2 Transverse Orthotropic Conductivity

It is a common assumption that the conductive properties of the heart are transversely isotropic; that is, the direction transverse and perpendicular to the laminar plane of fibres, are the same [199]. This assumption is due to limited data available[109]. Though, LeGrice *et. al.* believes that this assumption is not consistent with the apparent structural anisotropy of the ventricular muscle [61]. If it is assumed that muscle layers are electrically insulated by the cleavage planes, and current can only spread to adjacent layers only via the muscle branches, hence having a more convoluted path, LeGrice *et. al.* estimates that the conduction velocity transverse to the fibres, would be two to three times faster in the plane of a muscle layer than perpendicular to it. Unfortunately, transmural myocardial potentials were not recorded via the fibreglass needle electrodes to test this out in this thesis, due to focusing on fitting the data to the bidomain model.

A simulation study by Colli-Franzone studied the effects of isotropic and orthotropic transverse conductivity on wavefronts and potentials [137]. Isotropic means that the transverse bidomain conductivities are equal, while orthotropic means they are unequal. The study showed that there were differences in the potential distributions and electrograms. The Q waves in the orthotropic electrograms were more gradual in the transverse direction than in the isotropic case;

simulations using the bidomain model used in this thesis also confirmed this. Hooks *et. al.* [200] also observed that the downstroke duration was considerably longer when the cleavage planes inbetween the laminar muscle layers were taken into account in their bidomain simulations. Orthotropic anisotropy may be an explanation for the more sloped Q waves measured in the sheep experiments. The slope of the electrograms measured in the sheep experiments may be due to both the rate of rise of the action potential, and orthotropic conductivity.

## 13.3 Reference Potential

Taccardi *et. al.* [133, 117] identified a drift component in the reference potential, for unipolar electrograms. The extracellular potential generated by the heart travels throughout the surrounding tissue in the body. The drift occurs since the indifferent electrode or reference lead senses this electrical excitation passing by it. If the reference lead was located at infinity away from the measurement electrodes, the reference potential could be taken as zero, but the reference lead is contained within the body a finite distance away from the measurement electrodes, normally located on the animals leg or chest. Therefore, the reference lead picks up the presence of the excitation travelling through the body tissue; and progressively develops during the QRS interval. Negative drift occurs when depolarisation reaches the reference electrode, introducing a positive trend into the unipolar electrograms, while the opposite occurs for repolarisation [117]. Taccardi *et. al.* [117] stated that the drift in the reference voltage affects the slope of both the excitation and recovery phases of the electrograms. Taking this drift component into account provides consistency between simulated and experimental electrograms. The potential distribution remains the same, since when subtracting the reference potential, all the electrograms are affected by a constant [201].

In bidomain simulations, when modelling the whole heart or sections of tissue, the choice of the reference potential is limited, since it can only reside in the

model domain. The simulated electrogram is the potential difference between a node in the mesh and a reference potential. Usually a group of nodes somewhere away from the stimulus site is assigned to zero, to act as the grounded reference potential, but with the presence of the drift potential, this may not be adequate. The potential at a remote site in the domain can be chosen as the reference potential. Another type of reference potential can be calculated by averaging the potential values over the whole surface of the domain; such as the epicardium [202]. This has been shown to be close to the potential of Wilson's central terminal [133], and has been used as the reference potential in simulations by a number of investigators [117, 198, 191].

The choice of reference may be important; Muzikant's [191] study of comparing simulated and experimental electrograms, showed that the choice of reference effected the correlation between them. They used three different reference schemes; (1) a site at the aortic root for experimental recordings, and a grounded plane of nodes below the blood cavity in their model; (2) the average of four electrode sites at each corner in the electrode array; (3) and a reference made up of the average of all recording electrodes. Their results indicated that the four corner reference scheme provided the best correlation. This gives a good approximation to the reference potential since it is far away from the pacing site; the potential gradients there are small, and so the electrogram at that point represents pure drift in the reference potential. This reference scheme can produce drift-free electrograms when used in an isolated tissue model without transmural fibre rotation [117].

## 13.4 Asymmetries in Elliptical Wave

A direct comparison between bidomain simulated and experimentally recorded electrograms has been reported a few times in the literature [117, 191, 198]. Muzikant *et. al.* [191] suggested that there was significant difference between their simulated and experimentally recorded electrograms, due to the simple membrane

model used and the reference potential being limited to be at a point in the cardiac tissue model.

One limitation of the method used in this thesis, is that only a small region region of tissue can be studied in an experiment, since the ventricular geometry is curved on the epicardium, and the fibre direction does not remain straight over a large region, which may have an affect on the recorded potentials.

The potentials recorded in the sheep's heart during pacing showed an asymmetric propagating ellipse of activation. The asymmetry is due to a number of factors. One of these main factors is the cardiac structure, with the effect of fibre curvature, intramural fibre rotation, fibre inclination with respect to the epicardial plane, and abrupt changes in fibre direction. There may be other factors such as inhomogeneities in the tissue, for example, the presence of blood vessels, collagen, and sporadic fatty tissue, producing nonuniformities in the propagating wavefront [75, 191]. The asymmetry of the positive maxima, shown as the weakening or total disappearance of one of the two maxima, was observed in most of the sheep experiments. Taccardi *et. al.* [67] suggested that this may be due to the imbrication fibre angle, known as the tipping of the intramural fibres out of the plane parallel to the epicardium and endocardium. Bidomain simulations by Henriquez *et. al.* [75] with fibre angle tipping of 5°, showed significant asymmetry of the magnitudes of the positive regions. Measurement of this angle has been reported to be less than 5° [71], and is normally assumed to be zero in bidomain models [203, 3]. Judging from the asymmetry observed in the Henriquez *et. al.* [75] simulation studies, as well as observations from the Taccardi *et. al.* experiment, and common occurrences in this study, the incorporation of fibre angle tipping would be beneficial, in giving a closer match between model and experiment. However, in the Muzikant *et. al.* [191] comparison of experimental and bidomain simulated electrograms, the correlation between the two did not improve when the fibre tipping was taking into account.

Given the size of the area recorded by the electrode array, the assumption that the fibres are parallel would not be completely valid over the distance the

depolarising wave would have travelled. It would be expected that the fibre direction would be curved, resulting in an asymmetric elliptical wavefront. Simulation studies have shown that fibre curvature in the epicardial plane causes the wavefront to propagate along the curved path, resulting in the bending of the ellipse [75, 134]. There is the curved geometry of the epicardial surface to consider as well, which could contribute to the asymmetry. This was not taken into account in this study since the recorded potentials where mapped to a flat surface in the bidomain model. To minimise the effect of the curvature of the heart surface, a smaller electrode array could be used.

In some of the wavefronts measured from the sheep experiments, the two positive maxima were slightly twisted in the counter-clockwise direction. This is due to the intramural fibre rotation, and was reproduced in simulations in Section 10.2; it has also been observed in other experiments [67], and bidomain simulations [75, 191]. It would be beneficial to include this into the model. When estimating the bidomain conductivity values in three-dimensions the intramural fibre rotation would be expected to be estimated. The local fibre direction was estimated successfully, and it would be possible to estimate intramural fibre rotation, fibre curvature, and fibre tipping, to take into account the asymmetric features of the elliptical wavefront, to better fit the model to experimental observations. The consequences of estimating these extra angles would be increased computational time, and parameter correlation leading to singularity, as discussed in Section 6.8.

## 13.5 Action Potential Rate of Rise

The differences between canine and sheep unipolar electrograms were unexpected, as there is only canine data reported in the literature [11, 129]. Now with the possession of sheep data, it is reasonable to suggest that there may be a species difference; in particular, the slope of the Q waves was not as steep in the sheep electrograms than the ones published in the literature for canine measurements

[11, 67, 117], and even for porcine hearts [187]. It is uncertain what is the cause of the different electrograms, perhaps there are some anatomical features in the sheep's ventricular wall that is responsible, such as the amount of transmural fibre rotation, or the insulating cleavage planes between the laminar sheets of cardiac muscle having an effect on the orthotropic conductivity. Another cause could be the different membrane kinetics between the animals. Dogs are a carnivorous animal which requires hunting down prey, while sheep are a herbivorous animal and are less active, so it is reasonable to suggest that dogs would have faster membrane kinetics than sheep for hunting requirements, resulting in a faster action potential upstroke.

The membrane model used in the bidomain model can have a significant affect on the slope of the downstroke, and it has been shown in simulations that the Luo-Rudy model gives a sharper downstroke than in the experimental electrograms. These models contain a number of parameters, and have been measured for a particular animal species, reflecting the membrane characteristics. The parameters in these models can be modified to the change the rate-of-rise of the membrane action potential, to give the desired downstroke in the electrograms. This could be achieved either by direct measurement [51], parameter estimation [194], or trial and error [196, 197].

In Section 12.1, membrane model parameters were estimated, along with the conductivity parameters, to consider the slope of the electrograms. A modified version of the FitzHugh-Nagumo was used; only two parameters were needed to adjust the action potential rate-of-rise. A closer fit was achieved, with higher model-to-experiment correlation values than when the Luo-Rudy model was used. The benefit of using the FitzHugh-Nagumo model is, it is less complex than the Luo-Rudy model, and so, faster bidomain simulations can be performed. Since the data for the first 20 to 30 $ms$ after stimulation is used in the parameter estimation, only depolarisation is of importance, and the complex currents of repolarisation do not have to be modelled in detail. Therefore, using membrane models such as the Luo-Rudy model would be unnecessary.

A blood bath in contact with the endocardial surface was not including in the model. It was assumed, that since pacing was initiated at the epicardial surface, the main focus would be the potential distribution propagating from this point. Simulation studies of epicardial pacing showed that the blood volume had negligible effect on potentials near the epicardial surface [117, 204].
Another modelling aspect that could be considered is the fluid layer in contact with the epicardium; studies have shown that this can have an effect on electrograms [137]. The Purkinje fibre network could also be considered [137].

## 13.6 Comparison with the Four-Electrode Technique

In this section, a comparison will be discussed between the method used in this thesis and the four-electrode technique. In the four-electrode technique, two voltage electrodes are placed at a known distance in the tissue, in between two current electrodes. The distance of the voltage electrodes can be chosen such that extracellular potential can be measured separately from the intracellular. The technique has had recent attention in theoretical studies [19, 113, 184, 185], but its application in experiments for measuring the bidomain conductivities has not fully been implemented [101, 13]. The technique used in this thesis maps the spread of activation (depolarisation), initiated by point stimulation. Extracellular potentials are recorded by an electrode array. This method and the implementation of the four-electrode technique by Sadleir and Henriquez [19], both use parameter estimation techniques; which work by minimising the difference between experimental observations and bidomain model output to obtain the optimum parameter set. Both techniques also use extracellular electrodes to obtain the measurements.

With the four-electrode technique, a smaller portion of the tissue is sampled than the wave mapping technique, which would have the advantage of measuring a section of tissue with more uniform fibre direction; and avoid less irregularities

caused by blood vessels and fat. Modelling would be more simpler, and perhaps a greater fit could be achieved between experimental observations and bidomain model output. Also, less computation for solving the bidomain equations would be gained, due to the smaller tissue domain to simulate. The advantage with the four-electrode technique in a 2D domain, is that at most, 3 parameters need to be estimated at one time (longitudinal and transverse conductivity in extracellular space; and fibre angle), since the measured extracellular potential can be separated from the intracellular. This results in less computational effort to estimate the parameters. A range of different AC frequencies can be applied with the four-electrode technique, which can be used to reduce the space constant, needed to separate the intracellular and extracellular current flows, and extracting additional information from the tissue [14]. An issue that remains to be investigated with the four-electrode technique is that the bidomain model is based on a macroscopic concept. The electrode separation used in this technique (5-10 $\mu m$) [19] is smaller than the length of a cardiac cell (100 $\mu m$). At this level the tissue may no longer behave as anisotropic, and the longitudinal and transverse conductivities may not be properly measured.

The advantage with the wave mapping technique is that the fibre angle can be determined by the orientation of the wave. It can be used as a starting value in the parameter estimation process, which would result in less computation to arrive at the optimum parameter set. The electrode spacing with the wave mapping technique is significantly larger than what is used in the four-electrode technique; 1-1.5 $mm$, compared with 5-10 $\mu m$. Electrodes with larger separation are easier to make, and can be made by hand, without the need for special tools. They are also less prone to measurement noise compare with micro-electrodes [112]. The anisotropy can be easily recognised with the wave mapping technique by observing the shape and orientation of the depolarising wave. Bidomain simulations for modelling the propagation of activation for different conductivity values showed significant changes in potential distributions; where as for simulating a source and sink electrode pair, it was found that the changes in potential distributions

was not as apparent, especially in close proximity to the current electrodes; only far away there were noticeable changes in magnitude. From the validation studies in this thesis, the method seems to handle random measurement noise more robustly than the four-electrode technique [19]. The technique benefits from having a larger data sample, since the potentials can be measured with time, and simulated with a time-dependant bidomain model. Where as in the four-electrode technique, constant current is applied and steady state potentials are measured (one instance in time). The issue with the wave mapping technique is that it depends on how well the bidomain model can produce potential distributions similar to experimental observations, so that a better fit can be achieved. The potential distributions can be quite complex, and is significantly influenced by the membrane model. The membrane model determines the movements of the ion currents, influencing the action potential rate-of-rise, and repolarisation. Within the membrane model there are parameters, and their values can differ between animal species and under certain conditions. If the membrane model is not suited to the animal species then there would be uncertainty in the estimated conductivity parameters. The membrane parameters may be estimated to provide a greater fit, but depending on the membrane model there can be many parameters. This may lead to non-uniqueness or uncertainty in the parameters obtained. In the wave mapping technique the measured tissue region is much larger than what is measured by the four-electrode technique. The issues encountered are the variation in fibre direction, for example, across the epicardial surface, and less simpler tissue geometry. This would require more complex modelling than what would be required with the four-electrode technique, and introduce more uncertainty in the estimated parameters.

The two methods each have a different way of measuring the response from the tissue stimulation. The four-electrode technique applies a current source between two electrodes which produces a potential distribution, as a source and sink pair. The technique used in this thesis stimulates the tissue to cause depolarisation, and the resulting potential distribution is measured. The later is measuring the

passive properties of the cardiac tissue; the flow of ions across the cell membrane, while the other method is active; current flow without depolarisation. These differences need further investigation.

Out of the two methods, the wave mapping technique seems to be the easiest to apply experimentally, since mapping methods have been widely used [11, 12, 67], and the electrode arrays can be easily made [175]. In regards to modelling issues, the four-electrode technique would avoid the complex tissue structure modelling; in terms of fibre direction and tissue geometries. Its experimental application needs further investigation, so that further comparisons can be made.

# Chapter 14

# Conclusion

This thesis has described a new method for determining the bidomain conductivity parameters. This method takes a different approach to the four-electrode method; as it does not require small electrode separation. Only extracellular potential needs to be measured, with techniques of cardiac mapping already available. No simplifying assumptions were made about the relationship between intracellular and extracellular conductivity, only certain parameters were held fixed during the parameter estimation process, such as the membrane surface-to-volume ratio and membrane capacitance. The technique takes advantage of parallel computing, inverse mathematics, and developments in bidomain modelling.

To determine the bidomain conductivity parameters, the propagation of the depolarising wave from epicardial point stimulation was measured in vivo. An epicardial electrode array and fibreglass plunge electrode needles were made to map this electrical activity. A time-dependent bidomain model was used to describe the electrical behaviour of the cardiac tissue. Then the optimum set of conductivity parameters were obtained when the difference between model output and experimental observations came to a minimum. Parameter estimation methods such as Least-Squares and SVD were used. Other parameters could be determined as well, such as membrane capacitance and local fibre angle.

As well as statistical measures, features in the elliptical depolarising wave

could be used to compare between experiment and model, such as the positive maxima, shape and orientation of the wave, and isopotential lines. Electrogram characteristics were also inspected, by comparing Q and R waves.

The method was validated by using synthetic data generated from a bidomain model with known parameter values, with random noise. Both Least-Squares and SVD methods retrieved back the parameters to acceptable values, though SVD took less computation than Least-Squares when the amount of noise was increased. Fibre angle was estimated without much effort, but parameters such as membrane capacitance had an effect on the performance of the estimation run, requiring many more forward model calls. Parameter estimations that were performed on data reported in the literature were successful. Overall, the Least-Squares method with the use of the Marquart parameter seem to work best; as a more refined optimisation could be achieved, where as the SVD method tended to overshoot the objective function minimum for estimations involving experimental data, as a result of the highly nonlinear problem.

Conductivity values were estimated from sheep data, though there was miss-match between experimental and model observations, with differing potential regions and electrograms. The main discrepancy was in the slope of the Q wave in the electrograms; in that the Luo-Rudy model produced sharper downstrokes than in experiment. An attempt was made to achieve a closer fit between model and experiment by estimating a membrane model that suited to the sheep's cardiac membrane characteristics. Modifying the rate-of-rise of the action potential for the Luo-Rudy model was not straight forward due to its many parameters. Also, its complexity was unnecessary for modelling the early stages of activation, resulting in longer simulation times. Therefore, a modified FitzHugh-Nagumo membrane model was used, which had a couple parameters that controlled the action potential rate of rise. A closer fit was then achieved.

## 14.1 Future Investigations

To achieve a greater fit between model and experiment, therefore, better estimated parameters, more realistic modelling could be included. Such as, the myocardial fibre architecture, with transmural fibre rotation, and fibre gradients, which cause asymmetries in the depolarising wave, as observed in experiments. This information could be obtained by MRI diffusion tensor imaging. Though, simple fibre architecture could still be used; if the fibre direction was assumed to not change over a short distance, then an electrode array with smaller spacings and measurement area may be sufficient.

In this study, only a two-dimensional tissue domain for the bidomain model was used for estimating the conductivity parameters from experimental data. Investigations using a three-dimensional model of the heart tissue are quite possible with the computing power available. If a three-dimensional model is used, then transmural potential could be measured by needle electrodes, and the transverse conductivity in the epicardial to endocardial direction could be determined. From studies of the cardiac tissue structure, both transverse conductivities may be different; termed as orthotropic. It would be interesting to validate this.

Throughout the sheep experiments, changes in the electrograms were observed. The strength of the pacing stimulus also needed to be increased to achieve ventricular capture. Studies have shown that different methods of pacing can cause changes in the action potential upstroke, and so this may need further investigation.

Potential mapping during epicardial point stimulation for ischaemic tissue was investigated in sheep experiments, which showed significant changes in the electrograms. Determining the bidomain conductivities during ischaemia is the next step.

# Appendix A

# SCIRun Networks

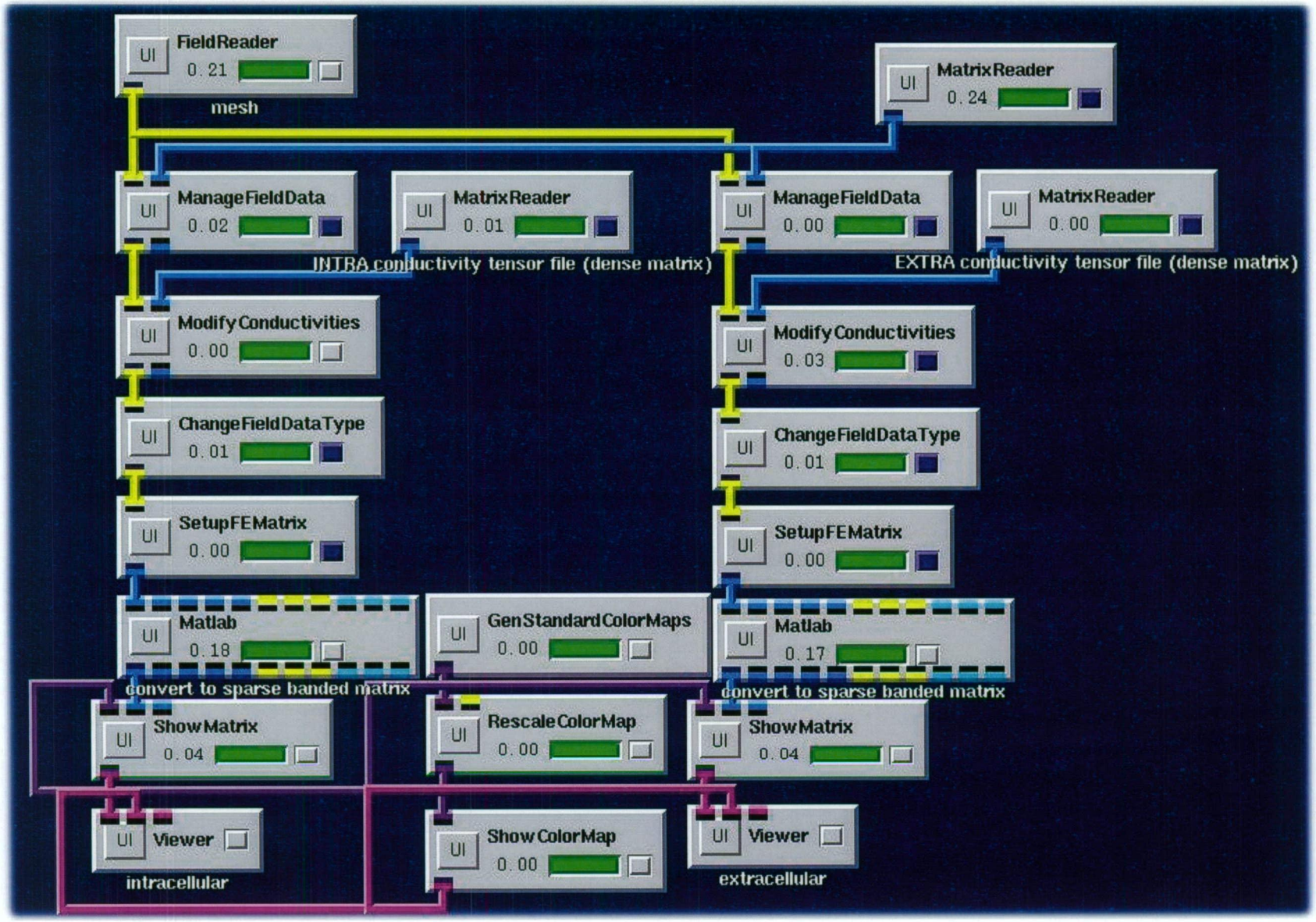


Figure A.1: Screenshot of SCIRun network for constructing FEM matrices.

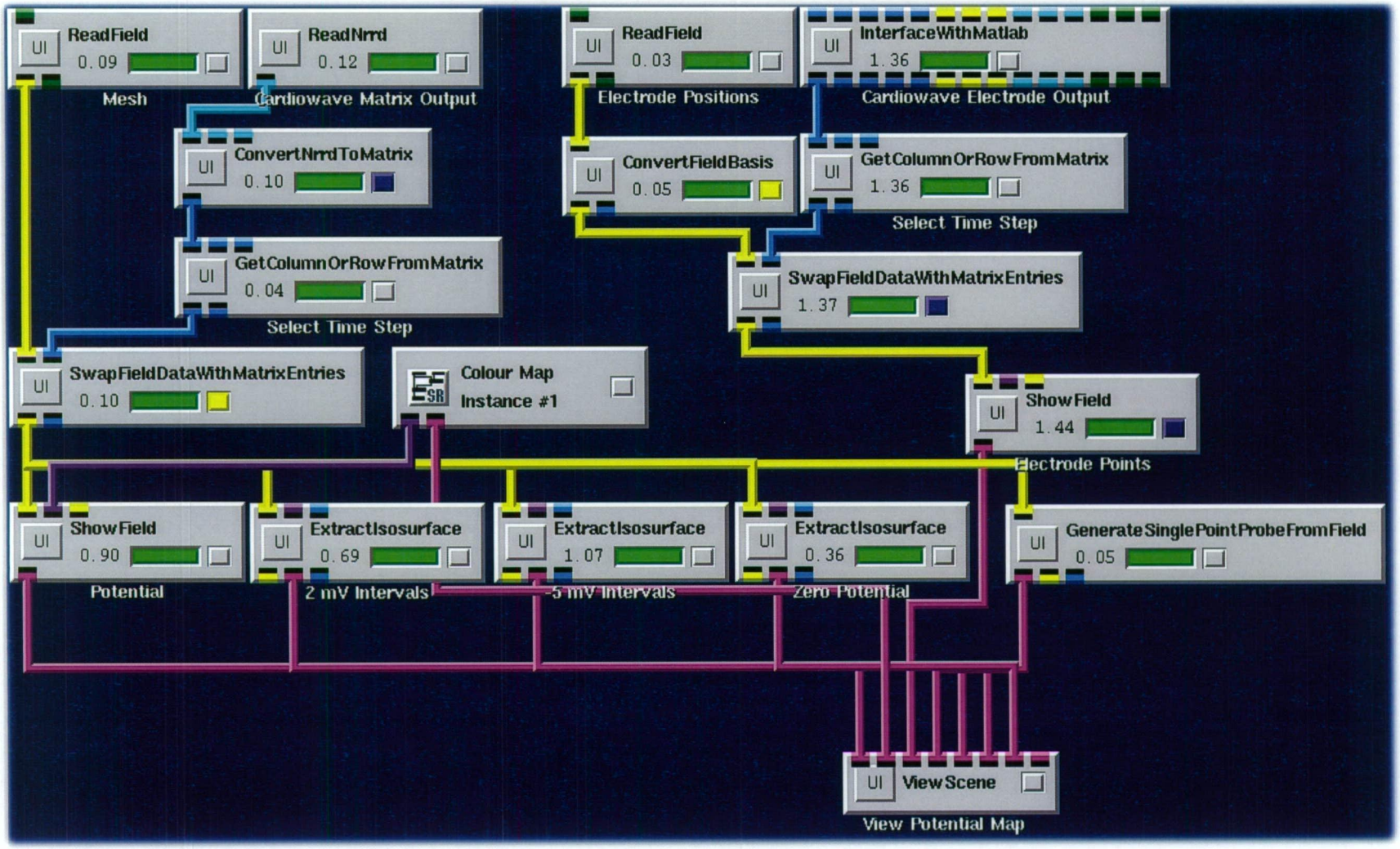


Figure A.2: Screenshot of SCIRun network for viewing Bidomain model output.

# Appendix B

# Objective Function in Parameter Space

Contour plots of the objective function in parameter space are presented for alternative viewing to the surface plots in section 10.3; figures 10.12 and 10.13. Contours represent equal objective function values, at 1000 spacings. The red line connecting the red crosses trace out the progress of lowering the objective function, throughout optimisation iterations till the minimum had been reached.

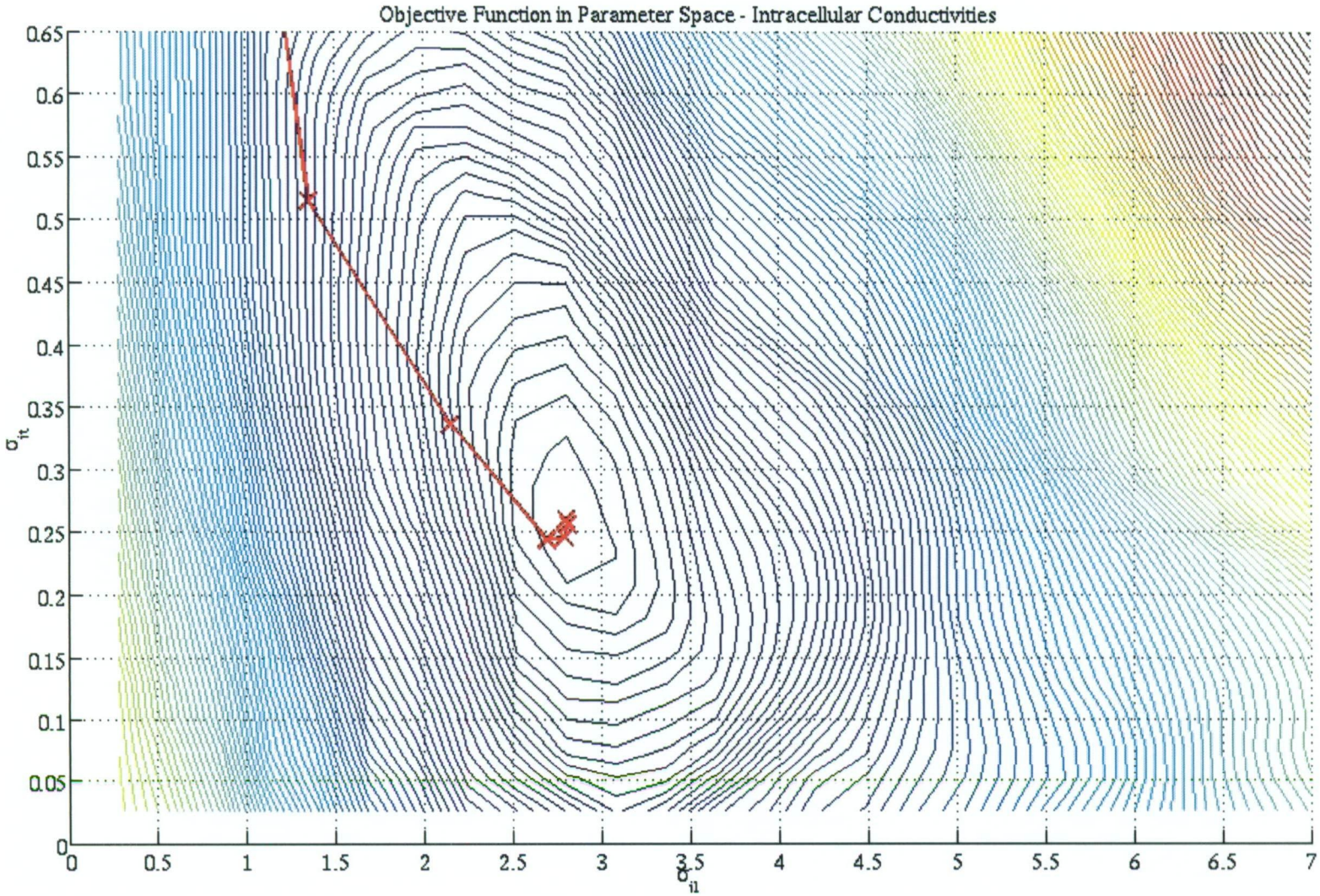


Figure B.1: Minimum at $\sigma_{il} = 2.8$ and $\sigma_{it} = 0.26\ mScm^{-1}$.

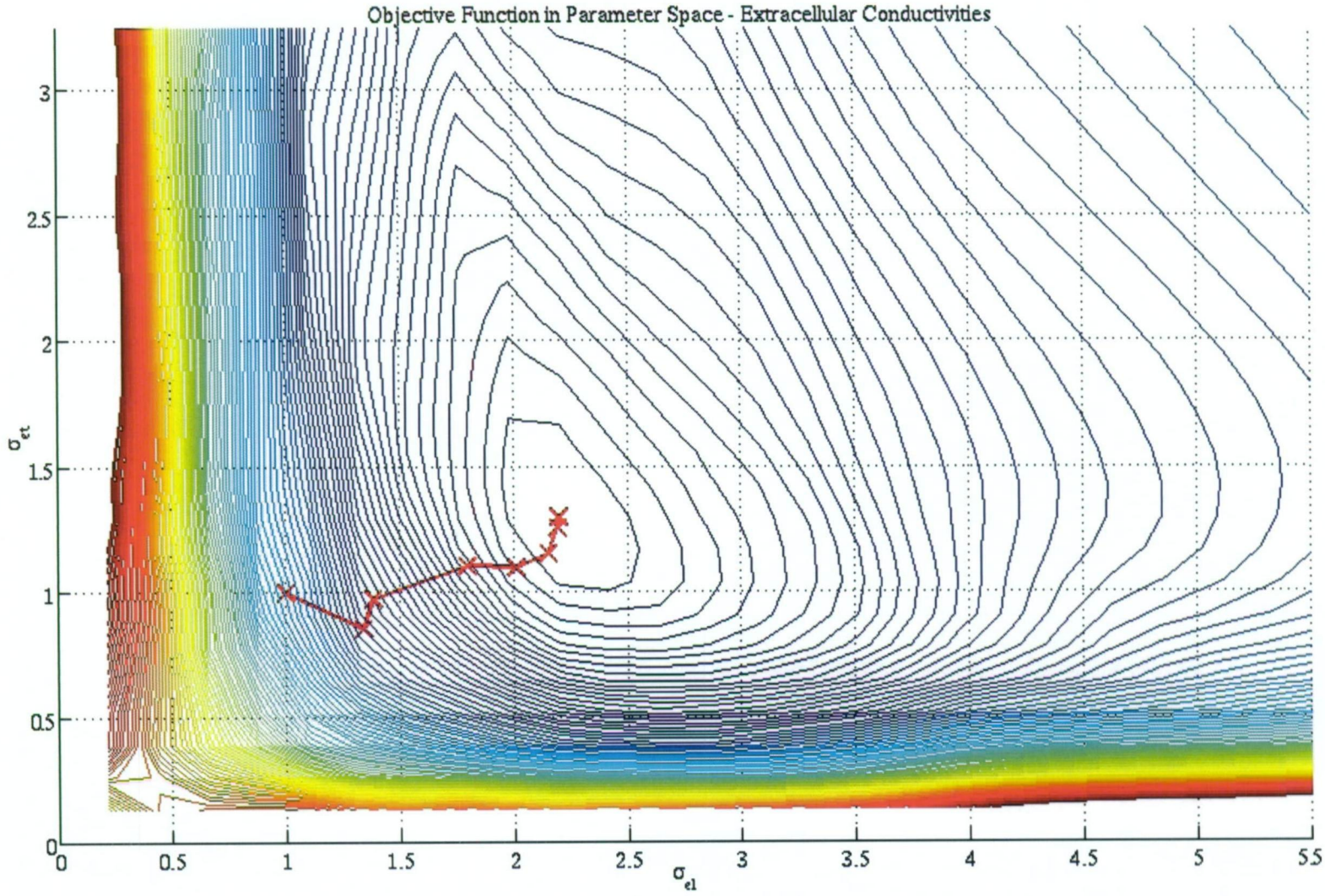


Figure B.2: Minimum at $\sigma_{il} = 2.2$ and $\sigma_{it} = 1.3\ mScm^{-1}$.

# Appendix C

# Electrodes

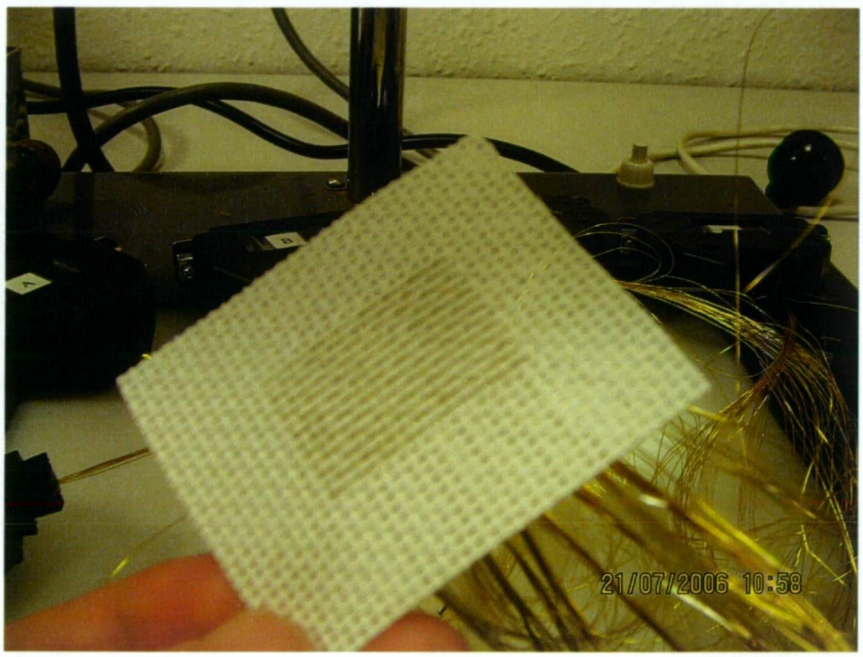


Figure C.1: Electrode array surface to be in contact with the epicardium.

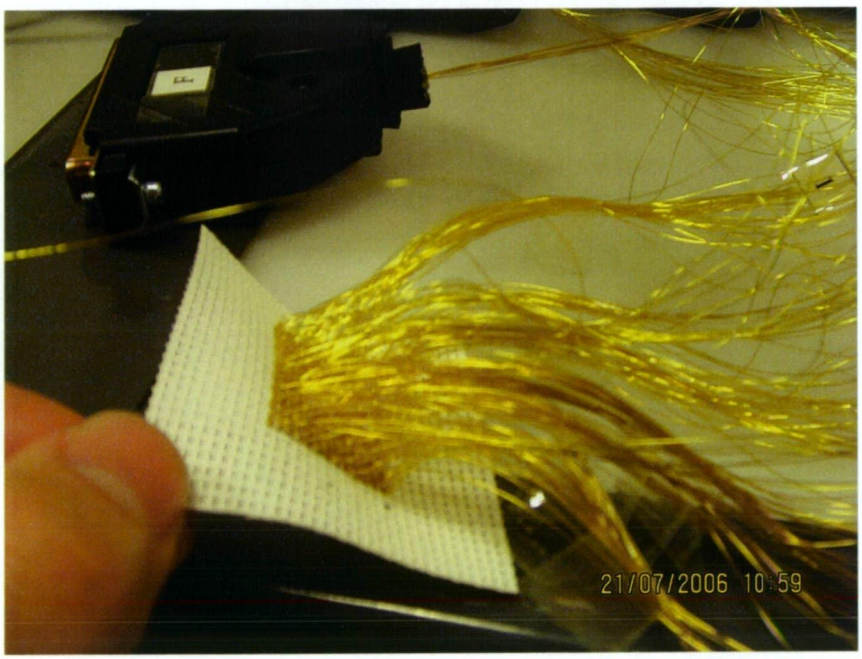


Figure C.2: The back of the electrode array; with connector in the background.

# Appendix D

# Electrogram Data

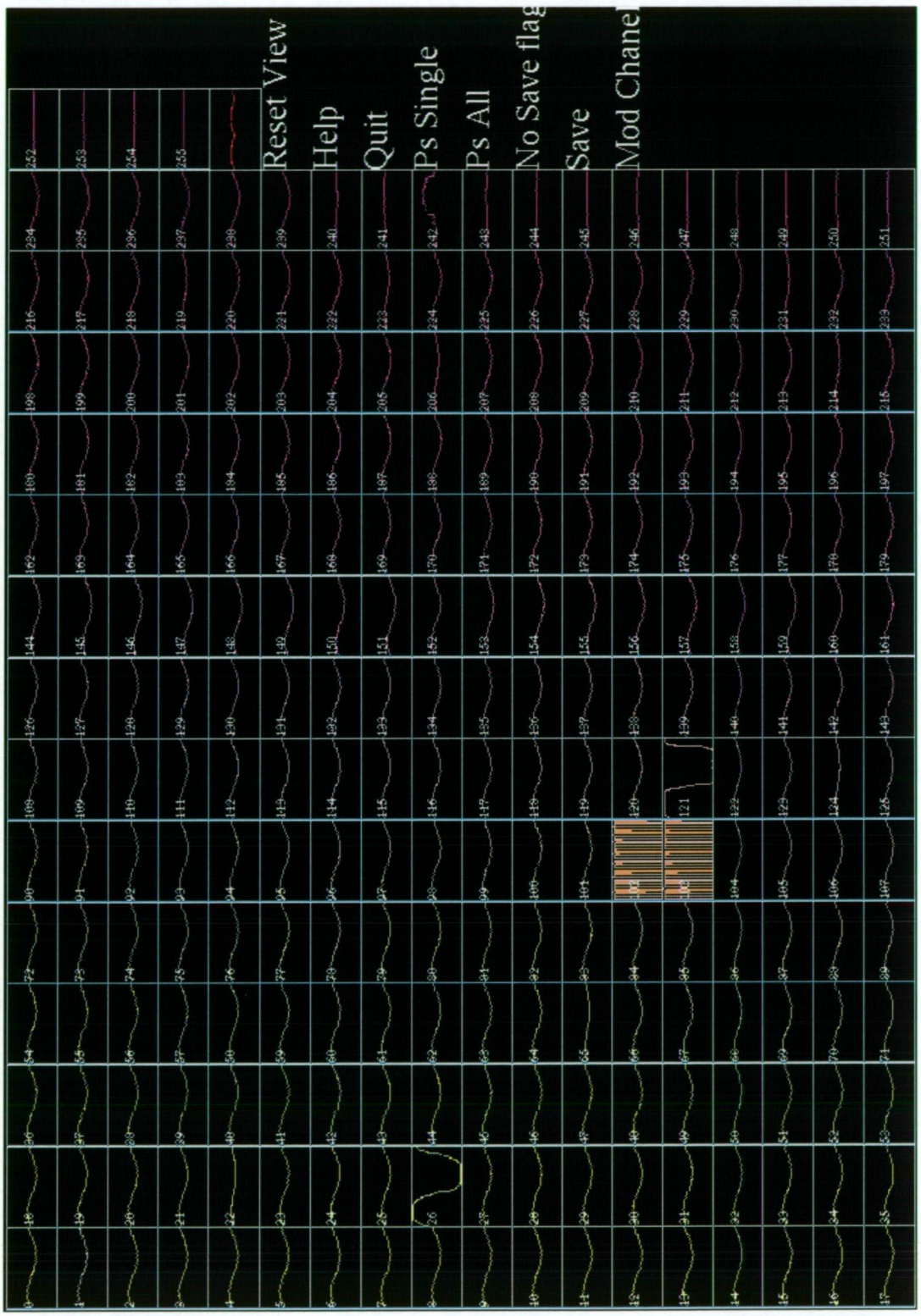


Figure D.1: Display of recorded calibration signal for all channels. Note that channels 102 and 103 are on high gain levels, which were omitted from the data set.

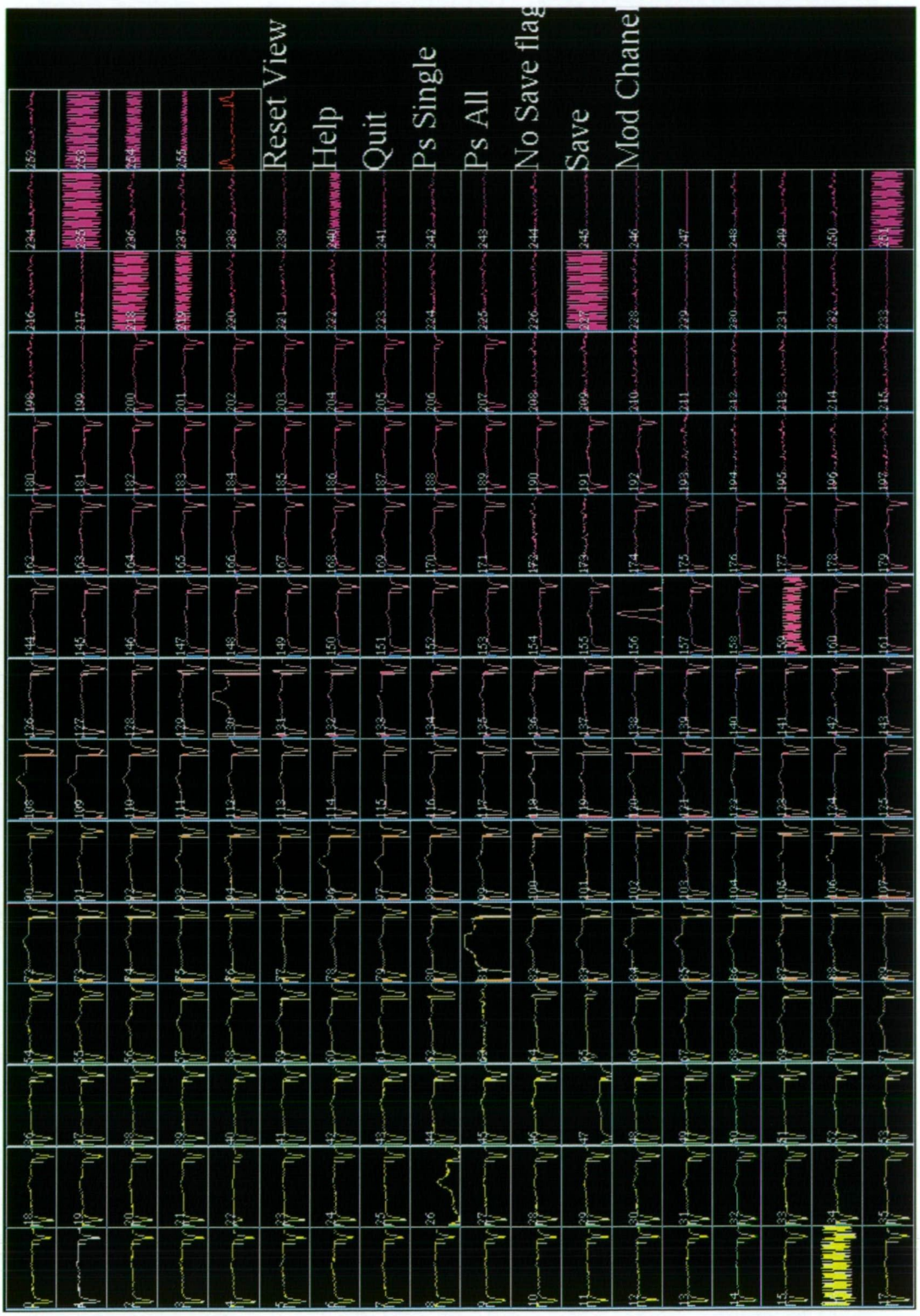


Figure D.2: Display of electrograms, recorded via the 194 electrode array, during epicardial stimulation.

# Appendix E

# Potential Maps

Potential maps of the recording of cardiac activation by point current stimulation is presented here for a particular experiment. In most experiments the epicardial electrode array was located in the left ventricle of the sheep's heart, shown in Figure E.1. Figure E.2 shows a potential map of the propagating depolarising wave, at 20 *ms* after stimulation, for a normal heart. Figure E.3 also shows the depolarising wave at 20 *ms*, but during ischaemia, when the LCX artery was totally occluded, resulting in no blood supply to the right-hand side of the array in Figure E.1. Figure E.4 is at 90 *ms* for ischaemic tissue, showing positive potential over the ischaemic region (ST elevation), and negative potential away from the ischaemic region (ST depression).

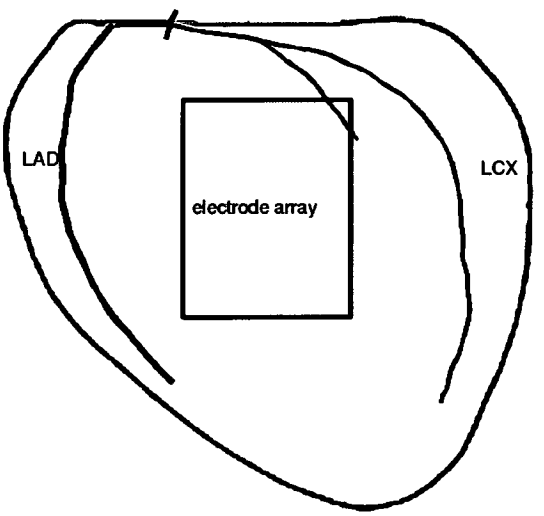


Figure E.1: Diagram of heart showing the placement of the electrode array for cardiac mapping, with the surrounding coronary arteries. For this particular example, the LCX artery is occluded causing an ischaemic area right of the electrode array. Image source: modified image from Taccardi [67].

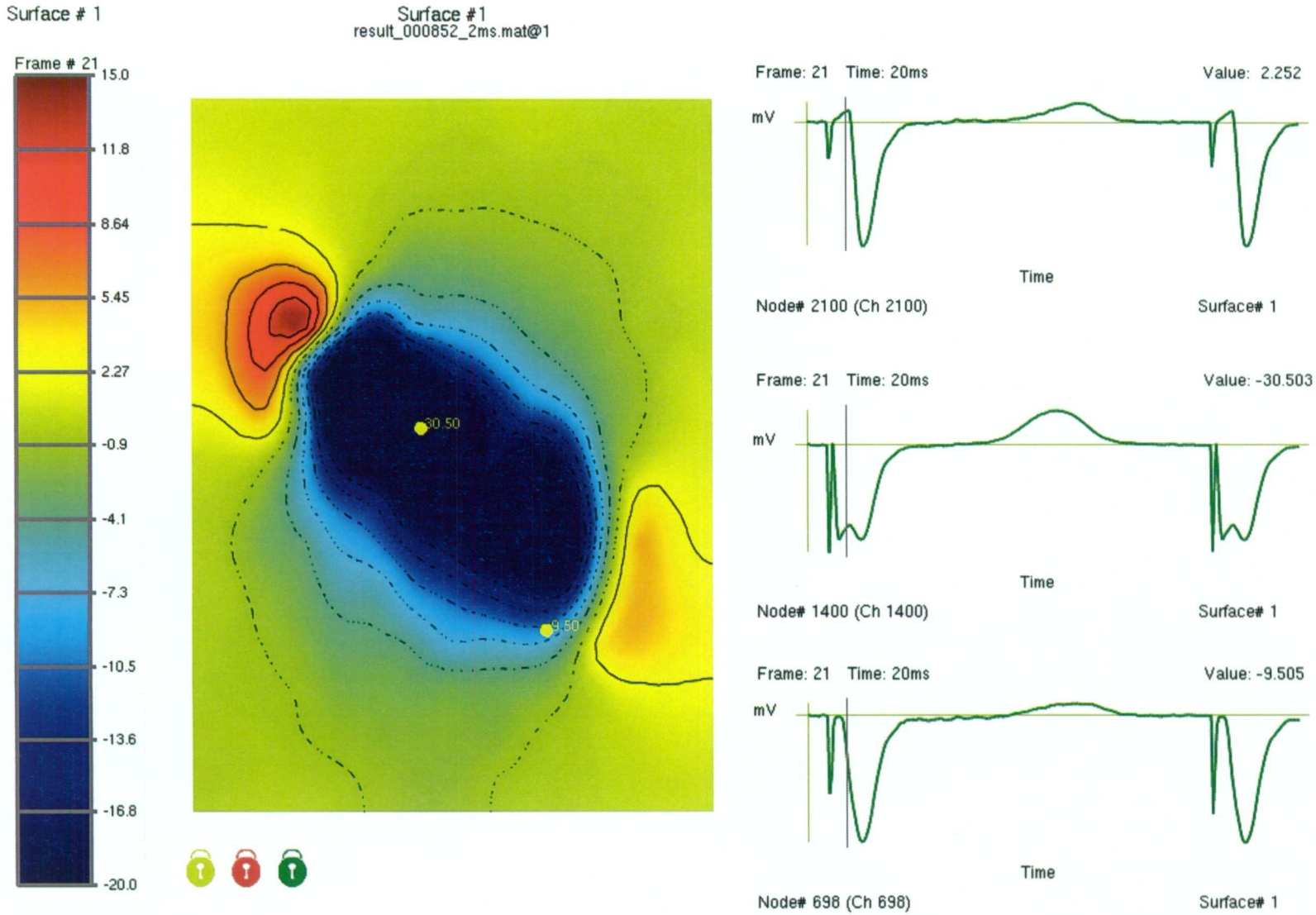


Figure E.2: Potential map at 20 ms after point stimulation, in normal cardiac tissue.

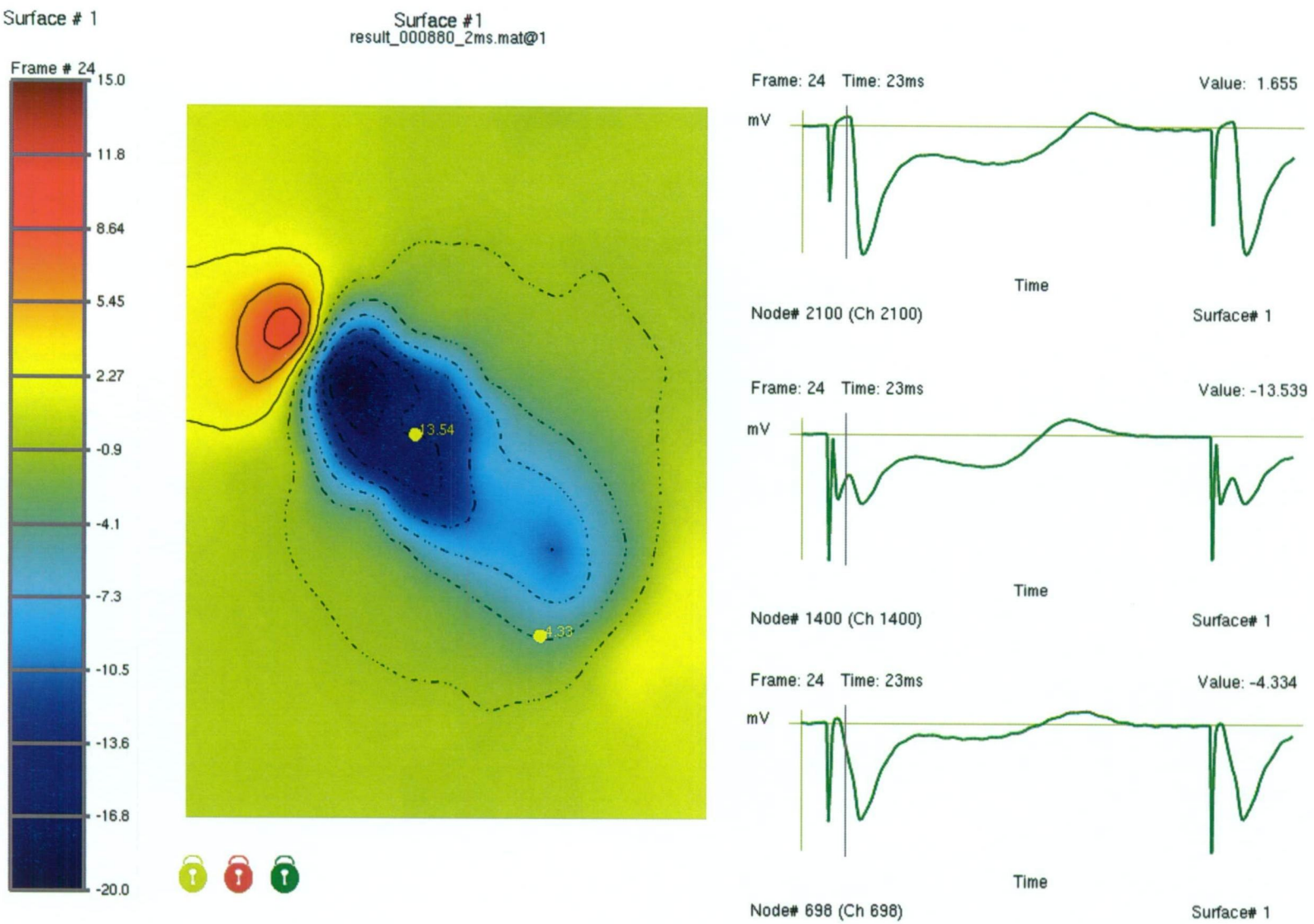


Figure E.3: Potential map at 20 ms after point stimulation, in ischaemic cardiac tissue.

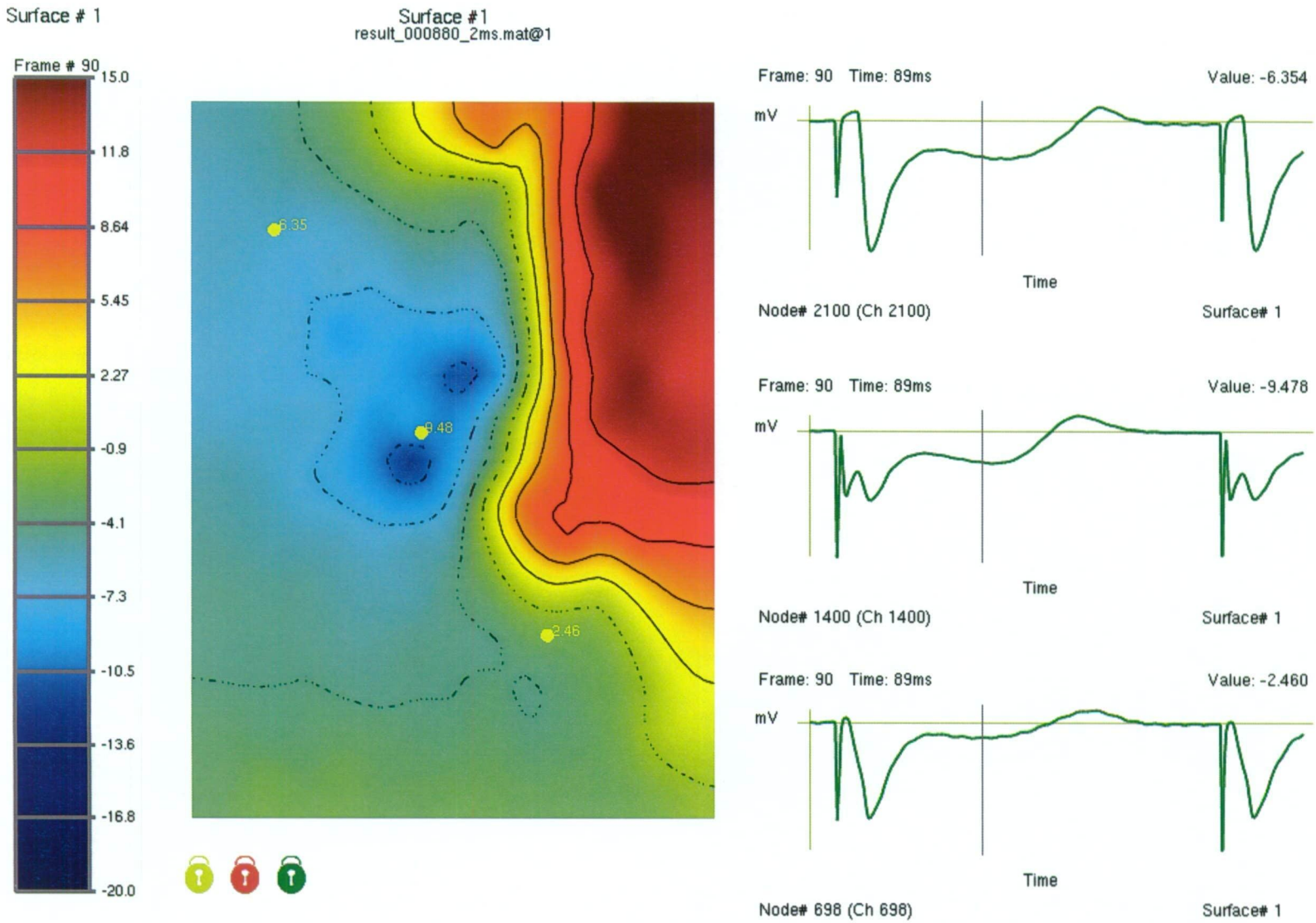


Figure E.4: Potential map at 90 ms after point stimulation, in ischaemic cardiac tissue.

# Appendix F

# Mesh Types

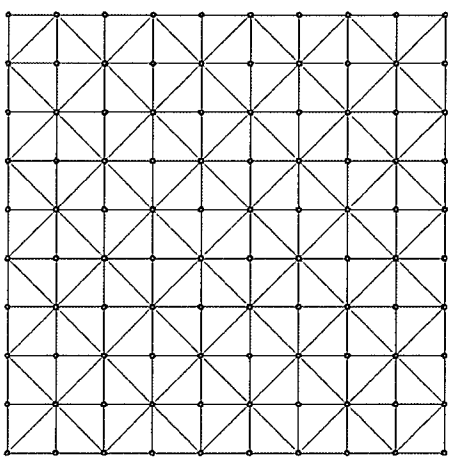

Figure F.1: Triangular mesh used for two-dimensional simulations.

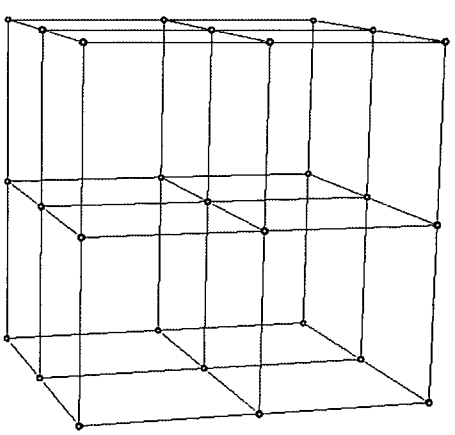

Figure F.2: Hexagonal mesh used for three-dimensional simulations.

# Appendix G

# PEST Control Settings

The PEST software has a number of different settings that can be initialised at the beginning of the parameter estimation process. These settings can have significant effect on the parameter estimation outcome. Here are a few settings:

1. Parameter Transformation: parameters can be transformed to logarithmic. Logarithms have simpler derivatives; and so, transforming parameters to logarithmic may have advantages, such as faster and more stable parameter estimations.

2. Upper and Lower Parameter Bounds: bounds can be defined to set the maximum and minimum values which a parameter is allowed. If the parameter upgrade vector is calculated such that one or more parameters moves beyond its bounds, then the parameter is temporarily held fixed, or adjusted to its allowed bounds.

3. Parameter Change Limits: the amount the parameters are adjusted can have limits as to how much they can change during an optimisation iteration. If a parameter change is too great, it could go over the objective function minimum, causing a prolongation of the estimation process. If the parameter change is too small it may take many iterations to arrive at the minimum.

4. Calculation of Derivatives: the forward difference or the central difference method for calculating derivatives can be set. Choosing the parameter increment for the derivatives calculation is important. A small parameter increment may provide a good approximation for calculating the derivative, but may suffer from round-off effects; a larger derivative may be better in overcoming local minimums in parameter space. The derivative can be taken as the line connecting the difference points, as parabolic, best-fit, or through the two outside points.

# List of Figures

# List of Tables

# Bibliography


[1] C. Y. Li. *A Computer Simulation of ST Segment Shift in Myocardial Ischemia.* PhD thesis, Division of Clinical Sciences, University of Tasmania, 1997.

[2] Bruce Hopenfeld, Jeroen G. Stinstra, and Rob S. Macleod. Mechanism for st depression associated with contiguous subendocardial ischemia. *Journal Cardiovascular Electrophysiology*, 15(10):1200–1206, 2004.

[3] Peter Johnston, David Kilpatrick, and Chuan Yong Li. The importance of anisotropy in modeling st segment shift in subendocardial ischaemia. *IEEE Transactions on Biomedical Engineering*, 48(12):1366–1376, 2001.

[4] Craig S. Henriquez and Alexandra A. Papazoglou. Using computer models to understand the roles of tissue structure and membrane dynamics in arrhythmogenesis. *Proceedings of the IEEE*, 84(3):334–354, 1996.

[5] Bradley J. Roth and Jr. John P. Wilkswo. The effect of externally applied electrical fields on myocardial tissue. *Proceedings of the IEEE*, 84(3):379–391, 1996.

[6] E. Entcheva, N.A. Trayanov, and F.J. Claydon. Patterns of and mechanisms for shock-induced polarization in the heart: a bidomain analysis. *Biomedical Engineering, IEEE Transactions on*, 46(3):260–270, 1999.

[7] N. G. Sepulveda, B. J. Roth, and Jr. Wikswo, J. P. Current injection into a two-dimensional anisotropic bidomain. *Biophysical Journal*, 55(5):987–99, 1989.

[8] M. S. Spach, W. T. Miller, D. B. Geselowitz, R. C. Barr, J. M. Kootsey, and E. A. Johnson. The discontinuous nature of propagation in normal canine cardiac muscle. evidence for recurrent discontinuities of intracellular resistance that affect the membrane currents. *Circulation Research*, 48:39–54, 1981.

[9] Bradley J. Roth. Electrical conductivity values used with the bidomain model of cardiac tissue. *IEEE Transactions on Biomedical Engineering*, 44(4):326–328, 1997.

[10] L. Clerc. Directional differences of impulse spread in trabecular muscle from mammalian heart. *Journal of Physiology*, 255:335–346, 1976.

[11] David E. Roberts, Lawrence T. Hersh, and Allen M. Scher. Influence of cardiac fiber orientation on wavefront voltage, conduction velocity, and tissue resistivity in the dog. *Circulation Research*, 44(5):701–712, 1979.

[12] David E. Roberts and Allen M. Scher. Effect of tissue anisotropy on extracellular potential fields in canine myocardium in situ. *Circulation Research*, 50(3):342–351, 1982.

[13] P. Le Guyander, P. Savard, and R. Trelles. Measurement of myocardial conductivities with a four-electrode technique in the frequency domain. *Proceedings of 19th Annual International Conference of IEEE-EMBS*, pages 2448–2449, 1997.

[14] P. Le Guyander, R. Trelles, and P. Savard. Extracellular measurement of anisotropic bidomain myocardial conductivities. i. theoretical analysis. *Annals of Biomedical Engineering*, 29:862–877, 2001.

[15] W. Krassowska and J. C. Neu. Theoretical versus experimental estimates of the effective conductivities of cardiac muscle. *Computers in Cardiology*, pages 703–706, 1992.

[16] J. G. Stinstra, B. Hopenfeld, and R. S. Macleod. Using models of the passive cardiac conductivity and full heart anisotropic bidomain to study the epicardial potentials in ischemia. *Proceedings of the 26th Annual International Conference of the IEEE EMBS*, pages 3555–3558, 2004.

[17] J. G. Stinstra, B. Hopenfeld, and R. S. Macleod. On the passive cardiac conductivity. *Annals of Biomedical Engineering*, 33:1743–1751, December 2005.

[18] Peter R. Johnston. Tissue conductivity and st depression in a cylindrical left ventricle. *International Journal of Bioelectromagnetism*, 4(2):61–62, 2002.

[19] R. Sadleir and C. Henriquez. Estimation of cardiac bidomain parameters from extracellular measurement: Two dimensional study. *Annals of Biomedical Engineering*, 34:1289–1303, 2006.

[20] http://www.nhf.org.nz/images/Heart%20diagram.jpg.

[21] http://www.nhf.org.nz/images/electrical_conduction.jpg.

[22] D. Durrer, R. T. Van Dam, G. E. Freud, M. J. Janse, F. L Meijler, and R. C. Arzbaecher. Total excitation of the isolated human heart. *Circulation*, 41:899–1024, June 1970.

[23] J. S. Fleming. *Interpreting the Electrocardiogram.* Cox and Wyman Ltd, London, Fakenham and Reading, 1979.

[24] Ph. Bourlas, E. Giakoumakis, and G. Papakonstantinou. A knowledge acquisition and management system for ecg diagnosis. *In Proceedings of Workshop on Machine Learning in Medical Applications, Advance Course in Artificial Intelligence-ACAI99*, pages 30–36, 1999.

[25] W. T. Miller and D. B. Geselowitz. Simulation studies of the electrocardiogram i. the normal heart. *Circulation Research*, 43:301–314, August 1978.

[26] P. R. Johnston, S. J. Walker, J. A. K. Hyttinen, and D. Kilpatrick. Inverse electrocardiographic transformations: Dependence on the number of epicardial regions and body surface data points. *Mathematical Biosciences*, 120:165–187, 1994.

[27] J. MalmivuoJaakko and R. Plonsey. *Bioelectromagnetism: Principles and Applications of Bioelectric and Biomagnetic Fields.* Oxford University Press, 1995.

[28] P. R. Johnston and D. Kilpatrick. The forward problem of electrocardiology incorporating detailed heart anatomy. *Computational Biomedicine*, pages 191–198, September 1993.

[29] S. J. Walker and D. Kilpatrick. Forward and inverse electrocardiographic calculations using resistor network models of the human torso. *Circulation Research*, 6:504–513, 1987.

[30] F. B. Sachse, C. D. Werner, K. Meyer-Waarden, and O. Dössel. Solving the forward problem in electrocardiography: Analysing the selection of appropriate regions of impedance models. *Computers in Cardiology*, pages 701–704, 1998.

[31] C. Ramanathan and Y. Rudy. Electrocardiographic imaging: I. effect of torso inhomogeneities on body surface electrocardiographic potentials. *Journal of Cardiovascular Electrophysiology*, 12:229–240, 2001.

[32] C. Ramanathan, R. N. Ghanem, P. Jia, K. Ryu, and Y. Rudy. Noninvasive electrocardiographic imaging for cardiac electrophysiology and arrhythmia. *Nature Medicine*, 10:422–428, April 2004.

[33] A. N. Tikhonov and V. Y. Arsenin. *Solutions of Ill-Posed Problems.* VH Winston and Sons, 1977.

[34] J. E. Burnes, B. Taccardi, P. R. Ershler, and Y. Rudy. Noninvasive electrocardiographic imaging of substrate and intramural ventricular tachycardia

in infarcted hearts. *Journal of the American College of Cardiology*, 38:2071–2078, December 2001.

[35] H. S. Oster, B. Taccardi, R. L. Lux, P. R. Ershler, and Y. Rudy. Noninvasive electrocardiographic imaging: Reconstruction of epicardial potentials electrograms and isochrones and localization of single and multiple electrocardiac events. *Circulation*, 96:1012–1024, August 1997.

[36] S. J. Walker, A. J. Bell, M. G. Loughhead, P. S. Lavercombe, and D. Kilpatrick. Spatial distribution and prognostic significance of st segment potential determined by body surface mapping in patients with acute inferior myocardial infarction. *Circulation*, 76:289–297, August 1987.

[37] R. S. MacLeod, R. M. Miller, M. J. Gardner, and B. M Hoaráček. Application of an electrocardiographic inverse solution to localize ischemia during coronary angioplasty. *Journal of Cardiovascular Electrophysiology*, 6:2–18, January 1995.

[38] D. Kilpatrick, A. Bell, and S. J. Walker. Derived epicardial potentials differentiate ischemic st depression from st depression secondary to st elevation in acute inferior myocardial infarction in humans. *American College of Cardiology*, 14:695–702, September 1989.

[39] C. R. Johnston and R. S. MacLeod. Adaptive local regularization methods for the inverse ecg problem. *Progress in Biophysics and Molecular Biology*, 69:405–423, March 1998.

[40] S. J. Walker, P. S. Lavercombe, M. G. Loughhead, and D. Kilpatrick. A body surface mapping system with immediate interactive data processing. *Computers in Cardiology*, page 305, 1983.

[41] S. J. Walker and D. Kilpatrick. Importance of the great vessels in the genesis of the electrocardiogram. *Circulation Research*, 66:1080–1087, April 1990.

[42] D. Kilpatrick and S. J. Walker. A validation of derived epicardial potential distributions by prediction of the coronary artery involved in acute myocardial infarction in humans. *Circulation*, 76:1282–1289, December 1987.

[43] R. C. Barr and M. S. Spach. Inverse calculation of qrs-t epicardial potentials from body surface potential distributions for normal and ectopic beats in the intact dog. *Circulation Research*, 42:661–675, May 1978.

[44] M. S. Spach, R. C. Barr, C. F. Lanning, and P. C. Tucek. Origin of body surface qrs and t wave potentials from epicardial potential distributions in the intact chimpanzee. *Circulation*, 55:268–278, February 1977.

[45] P. Collin-Franzone, L. Guerri, and S. Rovida. Wavefront propagation in an activation model of the anisotropic cardiac tissue: Asymptotic analysis and numerical simulations. *Journal of Mathematical Biology*, 28:121, 1990.

[46] Leslie Tung. *A Bi-Domain Model for Describing Ischemic Myocardial D-C Potentials.* PhD thesis, Massachusetts Institute of Technology, 1978.

[47] O. H. Schmitt. Biological information processing using the concept of interpenetrating domains. In D. P. Zipes and J. Jalife, editors, *Leibovic KN Information Processing in the Nervous System*, pages 325–331. Biophysical Science Group, Minneapolis, Minnesota, 1969.

[48] B. J. Roth. How the anisotropy of the intracellular and extracellular conductivities influences stimulation of cardiac muscle. *J Math Biol*, 30(6):633–46, 1992. Journal Article.

[49] R. C. Penland D. M. Harrild and C. S. Henriquez. Modeling impulse propagation and extracellular potential distributions in anisotropic cardiac tissue using a finite volume element discretization. *Computing and Visualization in Science*, 4:215–226, 2002.

[50] C. S. Henriquez. Simulating the electrical behaviour of cardiac tissue using

the bidomain model. *Critical Reviews in Biomedical Engineering*, 21(1):1–77, 1993.

[51] C. Luo and Y. Rudy. A dynamic model of the cardiac ventricular action potential i. simulations of ionic current and concentration changes. *Circulation Research*, 74:1071–1096, 1994.

[52] C. Luo and Y. Rudy. A dynamic model of the cardiac ventricular action potential ii. after polarizations, triggered activity, and potentiation. *Circulation Research*, 74:1097–1113, 1994.

[53] G. W. Beeler and H. Reuter. Reconstruction of the action potential of myocardial fibres. *Journal of Physiology*, 268:177–210, 1977.

[54] E. J. Vigmond, F. Aguel, and N. A. Trayanova. Computational techniques for solving the bidomain equations in three dimensions. *IEEE Transactions on Biomedical Engineering*, 49:1260–1269, November 2002.

[55] C. S. Henriquez, J. V. Tranquillo, D. Weinstein, E. Hsu, and C. R. Johnston. *Three-dimensional Propagation in Mathematical Models: Integrative Model of the Mouse Heart*, chapter In Cardiac Electrophysiology: From Cell to Bedside, Edited by D. Zipes and J. Jalife, Ch. 30, pages 273–281. Saunders, 4 edition, 2004.

[56] B. J. Roth. The electrical potential produced by a strand of cardiac muscle: A bidomain analysis. *Annals of Biomedical Engineering*, 16:609–637, 1998.

[57] Y. Belhamadia. A time-dependent adaptive remeshing for electrical waves of the heart. *IEEE Transactions in Biomedical Engineering*, 55:443–452, 2008.

[58] S. Puwal and B. J. Rother. Forward euler stability of the bidomain model of cardiac tissue. *IEEE Transactions in Biomedical Engineering*, 54:951–953, 2007.

[59] J. P. Whiteley. An efficient technique for the numerical solution of the bidomain equations. *Annals of Biomedical Engineering*, 36:1398–1408, 2008.

[60] L . Fritz and H. Hutten. Analysis of the impact of fusion beats onto epicardial electrograms based on a bidomain slab model. In *IFMBE Proceedings, World Congress on Medical Physics and Biomedical Engineering 2006*, pages 3428–3431. Springer Berlin Heidelberg, 2007.

[61] I. J. LeGrice, B. H. Smaill, L. Z. Chai, S. G. Edgar, J. B Gavin, and P. J. Hunter. Laminar structure of the heart: Ventricular myocyte arrangement and connective tissue architecture in the dog. *American Journal of Physiology*, 269:H571–H582, 1995.

[62] B. H. Smaill and P. J. Hunter. *Structure and Function of the Diastolic Heart*, chapter in Theory of Heart: Biomechanics, Biophysics, and Nonlinear Dynamics of Cardiac Function, pages 1–29. Springer-Verlag, 1991.

[63] T. Arts, K. D. Costa, J. W. Covell, and A. D. McCulloch. Relating myocardial laminar architecture to shear strain and muscle fiber orientation. *American Journal of Physiology - Heart Circulation and Physiology*, 280:H2222–H2229, 2001.

[64] D. F. Scollan, A. Holmes, R. Winslow, and J. Forder. Histological validation of myocardial microstructure obtained from diffusion tensor magnetic resonance imaging. *American Journal of Physiology - Heart Circulation and Physiology*, 275:H2308–H2318, 1998.

[65] Daniel D. Streeter and David L. Bassett. An engineering analysis of myocardial fiber orientation in pig's left ventricle in systole. *Anatomical Record*, 155:503–512, 1966.

[66] Daniel D. Streeter, Henry M. Spotnitz, Dali P. Patel, John Ross, and Edmund H. Sonnenblick. Fiber orientation in the canine left ventricle during diastole and systole. *Circulation Research*, 24:339–347, 1969.

[67] Bruno Taccardi, Emilio Macchi, Robert L. Lux, Philip R. Ershler, Santa Spaggiari, Silvana Baruffi, and Yonild Vyhmeister. Effect of myocardial fiber direction on epicardial potentials. *Circulation*, 90(6):3076–3090, 1994.

[68] L. Garrido, V. J. Wedeen, K. K. Kwong, U. M. Spencer, and H. L. Kantor. Anisotropy of water diffusion in the myocardium of the rat. *Circulation Research*, 74:789–793, 1994.

[69] P. M. Nielsen, I. J. Le Grice, B. H. Smaill, and P.J. Hunter. Mathematical model of geometry and fibrous structure of the heart. *American Journal of Physiology*, 260:H1365–H1378, 1991.

[70] P. J. Hunter, P. M. Nielsen, B. H. Smaill, I. J. Le Grice, and I. W. Hunter. An anatomical heart model with applications to myocardial activation and ventricular mechanics. *Critical Reviews in Biomedical Engineering*, 20:403–426, 1992.

[71] I. J. LeGrice, P. J. Hunter, and B. H. Smaill. Laminar structure of the heart. *American Journal of Physiology*, 272:H2466–H2467, 1997.

[72] E. A. Sobie, R. C. Susil, and L. Tung. A generalized activating function for predicting virtual electrodes in cardiac tissue. *Biophysical Journal*, 73:1410–1423, 1997.

[73] D. D. Streeter. *Gross Morphology and Fiber Geometry of the Heart*, chapter In R. M. Berne and N. Sperelakis, Handbook of Physiology, Section 2, pages 61–112. American Physiology Society, 1979.

[74] A. A. Young, I. J. LeGrice, M. A. Young, and B. H. Smaill. Extended confocal microscopy of myocardial laminae and collagen network. *Journal of Microscopy*, 192:139–150, 1998.

[75] C. S. Henriquez, A. L. Muzikant, and C. K. Smoak. Anisotropy, fiber curvature, and bath loading effects on activation in thin and thick cardiac

tissue preparations: Simulations in a three-dimensional bidomain model. *Journal of Cardiovascular Electrophysiology*, 7:424–444, May 1996.

[76] E. W. Hsu and C. S. Henriquez. Myocardial fiber orientation mapping using reduced encoding diffusion tensor imaging. *Journal of Cardiovascular Magnetic Resonance*, 3:339–347, 2001.

[77] K. D. Costa, Y. Takayama, A. D. McCulloch, and J. W. Covell. Laminar fiber architecture and three-dimensional systolic mechanics in canine ventricular myocardium. *American Journal of Physiology - Heart and Circulatory Physiology*, 276:H595–H607, 1999.

[78] http://histology-world.com/.

[79] M. McLean and J. Prothero. Determination of relative fiber orientation in heart muscle: Methodological problems. *The Anatomical Record*, 232:459–465, 1992.

[80] L. Geerts, P. Bovendeerd, K. Nicolay, and T. Arts. Characterization of the normal cardiac myofiber field in goat measured with mr-diffusion tensor imaging. *American Journal of Physiology - Heart Circulation and Physiology*, 283:H139–H145, 2002.

[81] W. G. O'Dell and A. D. McCulluch. Imaging three-dimensional cardiac function. *Annual Review of Biomedical Engineering*, 2:431–456, 2000.

[82] E. W. Hsu, A. L. Muzikant, S. A. Matulevicius, R. C. Penland, and C. S. Henriquez. Magnetic resonance myocardial fiber-orientation mapping with direct histological correlation. *American Journal of Physiology - Heart Circulation and Physiology*, 274:H1627–H1633, 1998.

[83] C. C. Van Donkelaar, L. J. G. Kretzers, P. H. M. Bovendeerd, L. M. A. Lataster, K. Nicolay, J. D. Janssen, and M. R. Drost. Diffusion tensor imaging in biomechanical studies of skeletal muscle function. *Journal of Anatomy*, 194:79–88, 1999.

[84] L. Zhukov and A. H. Barr. Heart-muscle fiber reconstruction from diffusion tensor mri. *Proceedings of IEEE Visualization*, pages 597–602, 2003.

[85] P. J. Basser, J. Mattiello, and D. LeBihan. Mr diffusion tensor spectroscopy an imaging. *Biophysical Journal*, 66:259–267, 1994.

[86] F. B. Sachse, C. Henriquez, G. Seemann, C. Riedel, C. D. Werner, R. C. Penland, B. Davis, and E. Hsu. Modeling of fiber orientation in the ventricular myocardium with mr diffusion imaging. *Computers in Cardiology*, 28:617–620, 2001.

[87] N. Kang, J. Zhang, E. S. Carlson, and D. Gembris. White matter fiber tractography via anisotropic diffusion simulation in the human brain. *IEEE Transactions on Medical Imaging*, 24:1127– 1137, 2005.

[88] M. Lazar, D. M. Weinstein, J. S. Tsuruda, K. M. Hasan, K. Arfanakis, M. E. Meyerand, B. Badie, H. A. Rowley, V. Haughton, A. Field, and A. L. Alexander. White matter tractography using diffusion tensor deflection. *Human Brain Mapping*, 18:306–321, 2003.

[89] S. E. Maier and H. Mamata. Diffusion tensor imaging of the spinal cord. *Annals of the New York Academy of Sciences*, 1064:50–60, 2005.

[90] M. Ries, R. A. Jones, F. Basseau, C. T. W. Moonen, and N. Grenier. Diffusion tensor mri of the human kidney. *Journal of Magnetic Resonance Imaging*, 14:42–49, 2001.

[91] B. M. Damon, Z. Ding, A. W. Anderson, A. S. Freyer, and J. C. Gore. Validation of diffusion tensor mri-based muscle fiber tracking. *Magnetic Resonance in Medicine*, 48:97–104, 2002.

[92] T. G. Reese, R. M. Weisskoff, R. N. Smith, B. R. Rosen, R. E. Dinsmore, and V. J. Wedeen. Imaging myocardial fiber architecture in vivo with magnetic resonance. *Magnetic Resonance in Medicine*, 34:786–791, 1995.

[93] P. J. Basser and D. K. Jones. Diffusion-tensor mri: Theory, experimental design and data analysis - a technical review. *NMR Biomedicine*, 15:456–467, 2002.

[94] S. Mori and P. C. M. Van Zijl. Fiber tracking: Principles and strategies - a technical review. *NMR in Biomedicine*, 15:468–480, 2002.

[95] Y. Masutani, S. Aoki, O. Abe, N. Hayashi, and K. Otomo. Mr diffusion tensor imaging: Recent advance and new techniques for diffusion tensor visualization. *European Journal of Radiology*, 46:53–66, 2003.

[96] Stanley S. Rush. Methods of measuring the resistivities of anisotropic conducting media in situ. *Journal of Research of the National Bureau of Standards-C. Engineering and Instrumentation*, 66C(3):217–222, 1962.

[97] Stanley Rush, J. A. Abildskov, and Richard Mcfee. Resistivity of body tissues at low frequencies. *Circulation Research*, 12(1):40–50, 1963.

[98] S. Weidmann. Electrical constants of trabercular muscle from mammalian heart. *Journal of Physiology*, 210:1041–1054, 1970.

[99] R. A Chapman and C. H. Fry. An analysis of the cable properties of frog ventricular myocardium. *Journal of Physiology*, 283:263–282, 1977.

[100] A. G. Kléber and C. B. Riegger. Electrical constants of arterially perfused rabbit papillary muscle. *Journal of Physiology*, 385:307–324, 1987.

[101] P. Le Guyander, P. Savard, and R. Trelles. Measurement of myocardial conductivities with an eight-electrode technique in the frequency domain. *Proceedings of 17th Annual International Conference of IEEE-EMBS*, pages 71–72, 1995.

[102] J. Tsai, J. A. Will, S. H. Van Stelle, H. Cao, S. Tungjitkusolmun, Y. B. Choyand D. Haemmerich, V. R. Vorperian, and J. G. Webster. In-vivo measurements of swine myocardial resistivity. *IEEE Transactions on Biomedical Engineering*, 49:472–483, 2002.

[103] T. J. C. Faes, H. A. Van der Meij, J. C. de Munck, and R. M. Heethaar. The electric resistivity of human tissues (100 hz-10 mhz): A meta-analysis of review studies. *Physiological Measurement*, 20:R1–R10, 1999.

[104] R. C. Barr and R. Plonsey. Electrode systems for measuring cardiac impedances using optical transmembrane potential sensors and interstitial electrodes-theoretical design. *IEEE Transactions on Biomedical Engineering*, 50:925–934, August 2003.

[105] R. Plonsey and R. C. Barr. A critique of impedance measurements in cardiac tissue. *Annals of Biomedical Engineering*, 14:307–322, 1986.

[106] H. P. Schwan. Four-electrode null techniques for impedance measurement with high resolution. *The Review of Scientific Instruments*, 39:481–485, 1968.

[107] H. P. Schwan and C. F. Kay. Specific resistance of body tissues. *Circulation Research*, 4:664–670, 1956.

[108] H. C. Burger and R. van Dongen. Specific electric resistance of body tissues. *Physical Medical Biology*, 5:431–447, 1961.

[109] R. Plonsey and R. Barr. The four-electrode resistivity technique as applied to cardiac muscle. *IEEE Transactions on Biomedical Engineering*, BME-29(7):541–546, 1982.

[110] B. J. Roth. A comparison of two boundary conditions used with the bidomain model of cardiac tissue. *Annals of Biomedical Engineering*, 19:669–678, 1991.

[111] J. J. B. Jack, D. Noble, and R. W. Tsien. *Electric Current Flow in Excitable Cells.* Oxford: Claredon Press, 1983.

[112] A. E. Pollard, W. M. Smith, and R. C. Barr. Feasibility of cardiac microimpedance measurement using multisite interstitial stimulation. *American Journal of Heart Circulation Physiology*, pages H2402–H2411, 2004.

[113] B. M. Johnston, P. R. Johnston, and D. Kilpatrick. A new approach to the determination of cardiac potential distributions: Application to the analysis of electrode configurations. *Mathematical Biosciences*, 202:288–309, August 2006.

[114] J. C. Neu and W. Krassowska. Homogenization of syncytial tissues. *Critical Reviews in Biomedical Engineering*, 21:137–199, 1993.

[115] J. G. Stinstra S. Shome, B. Hopenfeld, and R. S. Macleod. Modeling the passive cardiac electrical conductivity during ischemia. *Medical and biological engineering and computing*, 43:776–782, November 2005.

[116] P. Colli Franzone, L. Guerri, and B. Taccardi. Spread of excitation in a myocardial volume: Simulation studies in a model of anisotropic ventricular muscle activated by point stimulation. *Journal of Cardiovascular Electrophysiology*, 4:144–160, April 1993.

[117] B. Taccardi, S. Veronese, P. Colli Franzone, and L. Guerri. Multiple components in the unipolar electrogram: A simulation study in a three-dimensional model of ventricular myocardium. *Journal of Cardiovascular Electrophysiology*, 9:1062–1084, October 1998.

[118] N. G. Sepulveda, B. J. Roth, and J. P. Wikswo Jr. Current injection into a two-dimensional anisotropic bidomain. *Biophysical Journal*, 55:987–999, 1989.

[119] B. J. Roth. Action potential propagation in a thick strand of cardiac muscle. *Circulation Research*, 68:162–173, 1991.

[120] B. J. Roth and D. L. Beaudoin. Approximate analytical solutions of the bidomain equations for electrical stimulation of cardiac tissue with curving fibers. *Physical Review E*, 67:051925, 2003.

[121] L. F. Pavarino and P. Colli Franzone. *In Domain Decomposition Methods in*

*Science and Engineering: Parallel Solution of Cardiac Reaction-Diffusion Models*, volume 40, pages 669–776. Springer Berlin Heidelberg, 2005.

[122] D. W. Frazier, W. Krassowska, P. Chen, P. D. Wolf, N. D. Danieley, W. M. Smith, and R. E. Ideker. Transmural activations and stimulus potentials in three-dimensional anisotropic canine myocardium. *Circulation Research*, 63:135–146, 1988.

[123] H. Ashikaga, J. H. Omens, N. B. Ingels, and J. W. Covell. Transmural mechanics at the left ventricular epicardial pacing site. *American Journal of Physiology - Heart and Circulatory Physiology*, 286:H2401–H2407, 2004.

[124] I. Libbus and D. S. Rosenbaum. Transmural action potential changes underlying ventricular electrical remodeling. *Journal of Cardiovascular Electrophysiology*, 14:394–402, 2003.

[125] R. Plonsey. Quantitative formulations of electrophysiological sources of potential fields in volume conductors. *IEEE Transactions on Biomedical Engineering*, BME-31(12):868–872, 1984.

[126] D. Kilpatrick and P. R. Johnston. Origin of the electrocardiogram. *IEEE Engineering in Medicine and Biology*, 13:479–486, August/September 1994.

[127] P. Colli Franzone, Luciano Guerri, and Bruno Taccardi. Potential distributions generated by point stimulation in a myocardial volume: Simulation studies in a model of anisotropic ventricular muscle. *Journal of Cardiovascular Electrophysiology*, 4(4):438–458, 1993.

[128] G. Arisi, E. Macchi, C. Corradi, R. L. Lux, and B. Taccardi. Epicardial excitation during ventricular pacing, relative independence of breakthrough sites from excitation sequence in canine right ventricle. *Circulation Research*, 71:840–849, 1992.

[129] S. Baruffi, S. Spaggiari, D. Stilli, E. Musso, and B. Taccardi. *The Importance of Fiber Orientation in Determining the Features of Cardiac Electric*

*Field*, chapter In Z. Antaloczy, pages 89–92. Amsterdam, Excerpta Medica, 1978.

[130] S. Watabe, B. Taccardi, R. L. Lux, and P. R. Ershler. Effect of nontransmural necrosis on epicardial potential fields. correlation with fiber direction. *Circulation*, 82:2115–2127, 1990.

[131] T. Sano, N. Takayama, and T. Shimamoto. Directional differences of conduction velocity in the cardiac ventricular syncytium studied by microelectrodes. *Circulation Research*, 7:262–267, 1959.

[132] Andre G. Kleber, Michiel J. Janse, and Vladimir G. Fast. Normal and abnormal conduction in the heart. In *Handbook of Physiology - The Heart*, volume 1, chapter 12, pages 455–530. Oxford University Press, 2001.

[133] B. Taccardi, R. L. Lux, R. S. MacLeod, P. R. Ershler, T. J. Dustman, M. Scott, Y. Vyhmeister, and Nicole Ingebrigtsen. Ecg waveforms and cardiac electric sources. *Journal of Electrocardiology*, 29:98–100, 1996.

[134] A. L. Muzikant and C. S. Henriquez. Paced activation mapping reveals organization of myocardial fibres: A simulation study. *Journal of Cardiovascular Electrophysiology*, 8(3):281–294, 1997.

[135] H. S. Oster, B. Taccardi, R. L. Lux, P. R. Ershler, and Y. Rudy. Electrocardiographic imaging: Noninvasive characterization of intramural myocardial activation from inverse-reconstructed epicardial potentials and electrograms. *Circulation*, 97:1496–1507, 1998.

[136] S. B. Knisley and W. M. Smith. Experimental techniques for investigating cardiac electrical activity and response to electrical stimuli. *Proceedings of the IEEE*, 84:417–427, March 1996.

[137] P. Colli-Franzone, L. Guerri, and B. Taccardi. Modeling ventricular excitation: Axial and orthotropic anisotropy effects on wavefronts and potentials. *Mathematical Biosciences*, 188:191–205, 2004.

[138] L. V. Corbin and A. M. Scher. The canine heart as an electrocardiographic generator. dependence on cardiac cell orientation. *Circulation Research*, 41:58–67, 1977.

[139] P. Colli-Franzone, L. Guerri, C. Viganotti, E. Macchi, S. Baruffi, S. Spaggiari, and B. Taccardi. Potential fields generated by oblique dipole layers modeling excitation wavefronts in the anisotropic myocardium. comparison with potential fields elicited by paced dog hearts in a volume conductor. *Circulation Research*, 51:330–346, 1982.

[140] R. L. Cooley and R. L. Naff. *Regression Modeling of Ground-Water Flow: U.S. Geological Survey Techniques in Water-Resources Investigation.* USGS Publications, 1990.

[141] M. Tonkin and J. Doherty. A hybrid regularized inversion methodology for highly parameterized environmental models. *Water Resources Research*, 41:W10412, 2005.

[142] M. Douspis, J. G. Bartlett, A. Blachard, and M. Le Dour. Concerning parameter estimation using the cosmic microwave background. *Astronomy and Astrophysics*, 368:1–14, 2001.

[143] Y. Bard. *Nonlinear Parameter Estimation.* Academic Press, 1974.

[144] J. Doherty. *PEST, Model-Independent Parameter Estimation.* Watermark Numerical Computing, user manual: 5th edition edition, 2006.

[145] K. Levenberg. A method for the solution of certain non-linear problems in least squares. *Quarterly of Applied Mathematics*, 2:164–168, 1944.

[146] J. Starmer and F. Starmer. The joy of learning. main ideas, scaffolding, and thinking: building new concepts by modeling: Howto. *http://frank.itlab.us/datamodel/*, 2008.

[147] G. R. Liu and X. Han. *Computational Inverse Techniques in NonDestruction Evaluation.* CRC Press, 2003.

[148] D. W. Marquardt. An algorithm for least-squares estimation of nonlinear parameters. *Journal of the Society of Industrial and Applied Mathematics*, 11:431–441, June 1963.

[149] N. Sun. *Inverse Problems in Groundwater Modeling.* Kluwer Academic Publishers, 1999.

[150] L. R. Townley and J. L. Wilson. Computationally efficient algorithms for parameter estimation and uncertainty propagation in numerical models of groundwater flow. *Water Resources Research*, 21:1851–1860, December 1985.

[151] A. V. Vecchia and R. L. Cooley. Simultaneous confidence and prediction intervals for nonlinear regression models with application to a groundwater flow model. *Water Resources Research*, 23:1237–1250, July 1987.

[152] M. C. Hill. Methods and guidelines for effective model calibration. Technical report, U.S. Geological Survey Water-Resources Investigations Report 98-4005, 1990.

[153] C. L. Lawson and R. J. Hanson. *Solving Least Squares Problems.* Society for Industrial and Applied Mathematics, 1995.

[154] G. A. F. Seber and C. J. Wild. *Nonlinear Regression.* Wiley, 2003.

[155] R. C. Aster, B. Borchers, and C. H. Thurber. *Nonlinear Parameter Estimation.* Elsevier, 2005.

[156] J. Pormann. Cardiowave. *http://cardiowave.duke.edu*, 2005.

[157] J. Pormann. *A Modular Simulation System for the Bidomain Equations.* PhD thesis, Durham, NC: Duke University, 1999.

[158] J. Pormann, C. S. Henriquez, J. A. Board, D. J. Rose, D. M. Harrild, and A. P. Henriquez. Computer simulations of cardiac electrophysiology. *ACM/IEEE*, 2000.

[159] J. Pormann, J. A. Board, D. J. Rose, and C. S. Henriquez. Automated membrane model creation. *Computers in Cardiology*, 27:235–238, 2000.

[160] J. Pormann, J. A. Board, D. J. Rose, and C. S. Henriquez. Large-scale modeling of cardiac electrophysiology. *Computer in Cardiology*, 29:259–262, 2002.

[161] SCIRun: A Scientific Computing Problem Solving Environment. Scientific Computing and Imaging Institute (SCI), http://software.sci.utah.edu/scirun.html, 2002.

[162] R. S. Macleod, D. M. Weinstein, J. D. de St. Germain, D. H. Brooks, C. R. Johnson, and S. G. Parker. Scirun/biopse: Integrated problem solving environment for bioelectric field problems and visualization. In *Proceedings of the Int. Symp. on Biomed. Imag.*, pages 640–643, April 2004.

[163] D. M. Weinstein, S. G. Parker, J. Simpson, K. Zimmerman, and G. Jones. Visualization in the scirun problem-solving environment. In *The Visualization Handbook*, pages 615–632. Edited by C.D. Hansen and C.R. Johnson, Elsevier, 2005.

[164] BioPSE: Problem Solving Environment for modeling, simulation, image processing, and visualization for biomedical computing applications. Scientific Computing and Imaging Institute (SCI), http://software.sci.utah.edu/biopse.html, 2002.

[165] D. M. Weinstein, J. V. Tranquillo, Craig S. Henriquez, and C. R. Johnston. BioPSE case study: Modeling, simulation, and visualization of three dimensional mouse heart propagation. *International Journal of Bioelectromagnetism*, 5(1):314–315, 2003.

[166] T. C. Oppe, W. D. Joubert, and D. R. Kincaid. *NSPCG User's Guide.* Center for Numerical Analysis, The University of Texas at Austin, 1 edition, April 1988.

[167] R. Weber dos Santos and F. Dickstein. *In Functional Imaging and Modeling of the Heart: On the Influence of a Volume Conductor on the Orientation of Currents in a Thin Cardiac Tissue*, volume 2674, pages 111–121. Springer Berlin Heidelberg, 2003.

[168] R. Weber dos Santos, G. Plank, S. Bauer, and E. J. Vigmond. Parallel multigrid preconditioner for the cardiac bidomain model. *IEEE Transactions of Biomedical Engineering*, 51:1960–1968, November 2004.

[169] P. Colli Franzone, L. F. Pavarino, and B. Taccardi. Modeling anisotropic and heterogeneous cardiac models: Parallel simulations. *In "MEDICON 2004, the 10th Mediterranean Conference on Medical and Biological Engineering of the IFMBE*, 6, 2004.

[170] J. P. Keener and K. Bogar. A numerical method for the solution of the bidomain equations in cardiac tissue. *Chaos*, 8:234–241, March 1998.

[171] R. S. MacLeod and C. R. Johnston. Interactive scientific visualization for bioengineering data, 1993.

[172] D. S. Li, A. C. Yong, and D. Kilpatrick. Validation of a subendocardial ischaemic sheep model by intracoronary fluorescent microspheres. *Clinical and Experimental Pharmacology and Physiology*, 23:111–118, 1996.

[173] D. Li, C. Y. Li, A. C. Yong, and D. Kilpatrick. Source of electrocardiographic ST changes in subendocardial ischemia. *Circulation Research*, 82:957–970, 1998.

[174] Li Qin. *Transmyocardial ST Potential in Ischaemic Heart Disease.* PhD thesis, University of Tasmania: School of Medicine, 2005.

[175] E. Macchi, M. Cavalideri, D. Stilli, E. Musso, S. Baruffi, G. Olivetti, P. R. Ershler, R. L. Lux, and B. Taccardi. High-density epicardial mapping during current injection and ventricular activation in rat hearts. *The American Physiological Society*, 275:H1886–H1897, November 1998.

[176] J. M. Rogers, S. B. Melnick, and J. Huang. Fiberglass needle electrodes for transmural cardiac mapping. *IEEE Transactions on Biomedical Engineering*, 49:1639–1641, December 2002.

[177] J. M. Rogers, J. Huang, and S. B. Melnick an R. E. Ideker. Sustained reentry in the left ventricle of fibrillating pig hearts. *Circulation Research*, 92:539–545, March 2003.

[178] B. B. Punske, B. Taccardi, B. Steadman, P. R. Ershler, A. England, M. L. Valencik, J. A. McDonald, and S. E. Litwin. Effect of fiber orientation on propagation: Electrical mapping of genetically altered mouse hearts. *Journal of Electrocardiology*, 38:40–44, 2005.

[179] R. A. Malkin and B. D. Pendley. Construction of a very high-density extracellular electrode array. *American Journal of Physiology*, 279:H437–H442, 2000.

[180] M. R. Neuman. *Chapter 5: Biopotential Electrodes*, chapter In Medical Instrumentation: Application and Design, Editor in Chief, J. G. Webster, pages 183–231. Wiley, New York, 1997.

[181] L. A. Geddes, L. E. Baker, and A. G. Moore. Optimum electrolytic chloriding of silver electrodes. *Medical and Biological Engineering and Computing*, 7:49–56, January 1969.

[182] P. Waller. *256 Channel Switch and Signal Generator Unit.* Central Science Laboratory, University of Tasmania, 2005.

[183] B. M. Johnston and P. R. Johnston. An in-principle method for measuring cardiac tissue fibre rotation. *International Journal of Bioelectromagnetism*, 7:313–315, August 2005.

[184] B. M. Johnston, P. R. Johnston, and D. Kilpatrick. Analysis of electrode configurations for measuring cardiac tissue conductivities and fibre rotation. *Annals of Biomedical Engineering*, 34:986–996, June 2006.

[185] B. M. Johnston and P. R. Johnston. Possible four-electrode configurations for measuring cardiac tissue fiber rotation. *IEEE Transactions on Biomedical Engineering*, 54:547–550, March 2007.

[186] C. Y. Li, W. K. Pluta, and D. Kilpatrick. Field programmable gate array in a fast 256-channel data acquisition system. *Australasian Physical & Engineering Sciences in Medicine*, 20:47–52, 1997.

[187] A. G. Kleber, M. J. Janse, F. J. Wilms-Schopmann, A. A. Wilde, and R. Coronel. Changes in conduction velocity during acute ischemia in ventricular myocardium of the isolated porcine heart. *Circulation*, 73:189–198, 1986.

[188] T. F. Oostendorp, A. Van Oosterom, and G. Huiskamp. Interpolation on a triangulated 3D surface. *Journal of Computational Physics*, 80:331–343, 1989.

[189] R. S. MacLeod, R. L. Lux, and B. Taccardi. Translation of body surface maps between different electrode configurations using a three-dimensional interpolation scheme. *In Proceedings of the International Committee on Electrocardiology, XXth Annual Meeting*, pages 179–182, 1993.

[190] P. R. Johnston and D. Kilpatrick. The effect of conductivity values on ST segment shift in subendocardial ischaemia. *IEEE Transactions on Biomedical Engineering*, 50:150–158, February 2003.

[191] A. L. Muzikant, E. W. Hsu, P. D. Wolf, and C. S. Henriquez. Region specific modeling of cardiac muscle: Comparison of simulated and experimental potentials. *Annals of Biomedical Engineering*, 30:867–883, 2002.

[192] G. Arisi, E. Macchi, S Baruffi, S. Spaggiari, and B. Taccardi. Potential fields on the ventricular surface of the exposed dog heart during normal excitation. *Circulation Research*, 52:706–715, 1983.

[193] R. A. FitzHugh. Impulses and physiological states in theoretical models of nerve membrane. *Biophysical Journal*, 1:445–466, 1961.

[194] J. M. Rogers and A. D. McCulloch. A collocation-galerkin finite element model of cardiac action potential propagation. *IEEE Transactions on Biomedical Engineering*, 41:743–757, August 1994.

[195] F. Fenton and A. Karma. Vortex dynamics in three-dimensional continuous myocardium with fiber rotation: Filament instability and fibrillation. *Chaos*, 8:20–47, March 1998.

[196] R. A. Oliver and W. Krassowska. Reproducing cardiac restitution properties using the fenton-karma membrane model. *Annal of Biomedical Engineering*, 33:907–911, July 2005.

[197] A. M. Goodman, R. A. Oliver, C. S. Henriquez, and P. D. Wolf. A membrane model of electrically remodelled atrial myocardium derived from in vivo measurements. *Europace*, 7:S135–S145, 2005.

[198] P. Colli Franzone, L. Guerri, M. Pennacchio, and B. Taccardi. Anisotropic mechanisms for multiphasic unipolar electrograms: Simulation studies and experimental recordings. *Annals of Biomedical Engineering*, 28:1326–1342, 2000.

[199] P. J. Hunter and B. H. Smaill. The analysis of cardiac function: A continuum approach. *Progress in Biophysics and Molecular Biology.*, 52:101–164, 1988.

[200] D. A. Hooks, K. A. Tomlinson, S. G. Marsden, I. J. LeGrice, B. H. Smaill, A. J. Pullan, and P. J. Hunter. Cardiac microstructure: Implications for electrical propagation and defibrillation in the heart. *Circulation Research*, 91:331–338, 2002.

[201] B. B. Punske, R. L. Lux, R. S. MacLeod, P. R. Ershler, T. J. Dustman, Y. Vyhmeister, B. Taccardi, and N. E. Harrison. Experimental study and

removal of the drift of the reference potential from the unipolar electrogram. *Proceedings of The First Joint BMES/EMBS Conference*, page 303, Oct 1999.

[202] M. S. Spach, W. P. Silberberg, J. P. Boineau, R. C. Barr, E. C. Long, T. M. Gallie, J. B. Gabor, and A. G. Wallace AG. Body surface isopotential maps in normal children ages 4 to 14 years. *American Heart Journal*, 72:640–652, 1966.

[203] P. Colli Franzone and L. Guerri. Spreading of excitation in 3-D models of the anisotropic cardiac tissue i: Validation of the eikonal model. *Mathematical Biosciences*, 113:145–209, 1993.

[204] P. Colli-Franzone, L. Guerri, and B. Taccardi. On the polyphasic character of simulated and experimental electrograms. *Biomedizinische Technik*, 46:16–19, 2001.